Mass Spectrometry-Based Studies of Synthetic and Natural Macromolecules

Gillian R. Hilton MChem (Hons)

A thesis submitted for the degree of Doctor of Philosophy

University of Warwick

Department of Biological Sciences

December 2009

Dedicated to my parents, Ian and Maureen, without their encouragement and support none of this would have been possible

Table of Contents

Chapter 3. Materials and Methods

List of Figures

List of Tables

Acknowledgements

"Gillian. If it was meant to be easy - everyone would do it" - Maureen Hilton

I was once advised that undertaking a PhD was similar to riding the Big Dipper rollercoaster in Blackpool. I (and all the others that ride with me) would experience highs and lows throughout the PhD but at the end it would be all worthwhile. I would like to take this opportunity to thank all of those people that have taken this PhD journey with me. I will be eternally indebted to them for all their help and encouragement over the last three years.

I would like to begin by expressing my gratitude to my academic supervisor Prof. Jim Scrivens for giving me the opportunity to undertake this PhD. His support, advice and continual encouragement have been invaluable over the last three years. Thank you to my industrial supervisor Dr Tony Jackson (AzkoNobel) because without his guidance I would not have undertaken this PhD. I thank Tony for his infectious enthusiasm about polymer chemistry and for his endless knowledge and teaching on the subject. The work was financially supported by the EPSRC, AzkoNobel and the Intertek Measurement Science Group, Wilton. I thank all the staff at Intertek, Wilton especially Malcolm Beckett, Jayne Heron, Richard Jennings and Duncan Robertson for their willing assistance.

Thanks to all members of the Scrivens Group, past and present, in particular Charlie, Vib and Sue for their helpful discussions and for providing an enjoyable working environment. Thank you to the Structural Biology Group but especially Dr Narinder Sanghera for her patience and tuition regarding the prion project. I will also be forever grateful and appreciative to Prof. Keith Jennings for his unfaltering wisdom, for sharing his extensive knowledge of mass spectrometry, for his help with the finer grammatical details within the thesis, and for all of his help and advice.

My special thanks go to Dr Kostas Thalassinos. He was my amazing post-doc, great sounding-board for new ideas, trusted advisor (I finally concede he was almost always 99.9% correct) and has become a true friend.

The prion protein work has been supported by many colleagues and collaborators who I would like to thank. Dr Teresa Pinheiro and Dr Claudia Blindauer (University of Warwick), Dr Andy Gill (University of Edinburgh) and my American collaborators Megan Grabenauer, Thomas Wyttenbach and Mike Bowers (UCSB).

I have been blessed with a greater number of friends that I am able to list, but I would like to thank them for contributing to the maintenance of my sanity. Particular mention must go to Siân, Tom, Beth and Mike (York) and members of the Leamington hockey club but especially Emma and Tom for all the fun adventures we have shared.

Finally my biggest thank you goes to my brother and parents who have always supported me, encouraged me throughout my career and believed in my abilities even when they didn't understand what I did! Everything that I have achieved, I owe to their unconditional love.

Declaration

I hereby declare that this thesis, submitted in partial fulfilment of the requirements for the degree of Doctor of Philosophy and entitled "Mass Spectrometry-Based Studies of Synthetic and Natural Macromolecules", represents my own work and has not been previously submitted to this or any other institution for any degree, diploma or other qualification. Work undertaken by my collaborators is explicitly stated where appropriate.

Gillian R. Hilton

December 2009

Summary

Originally established as an analytical technique in the fields of physics and chemistry, mass spectrometry has recently become an essential tool in biological research. Advances in ionisation methods and novel types of instrumentation have led to the development of mass spectrometry for the analysis of a wide variety of biological samples. The work presented here describes the use of mass spectrometry to characterise a variety of synthetic and natural macromolecules.

Transmissible spongiform encephalopathies (TSEs), also known as prion diseases, are a class of fatal, infectious neurodegenerative diseases that affect both humans and animals. Prion proteins are unprecedented infectious pathogens that cause a group of invariably fatal neurodegenerative diseases by means of an entirely novel mechanism. Ion mobility mass spectrometry (IM-MS) was used to probe the conformation of a variety of different prion proteins in the gas-phase. It was shown that IM-MS could distinguish between two recombinant structures representative of normal cellular prion protein, PrP^{C} and the pathogenic scrapie form (PrP^{Sc}). The structure of the full-length prion protein was probed by means of IM-MS. A comparison of the estimated cross-sections of truncated prion protein constructs and full-length constructs suggested that the N-terminal flexible tail was associated with the core structure. Metal binding to two different prion protein constructs was investigated. It was observed that copper coordination to the N-terminal fragment could induce conformational changes in the octarepeat fragment. These changes were relatively small and could not be measured in the full-length prion protein. The data suggested that minor structural changes in the N-terminal could stimulate endocytosis via a minor, undetected, conformational change in the C-terminal domain.

IM-MS was used as a high resolution separation technique to distinguish between mixtures of isobaric synthetic polymers. It was observed that the resolving power of IM-MS/MS was insufficient to resolve the higher molecular weight oligomers. In comparison, gel permeation chromatography (GPC)-nuclear magnetic resonance (NMR) spectroscopy (GPC-NMR) analysis of the same isobaric mixture could not separate the two components. It was observed that IM-MS was better than GPC-NMR at separating isobaric poly(ethylene glycol) mixtures, especially when taking speed and sensitivity into account.

Abbreviations

One

1D	One-dimensional

Two

2D	Two-dimensional

A

ADC	Analog-to-digital
AIBN	azobisisobutyronitrile
ATD	Arrival time distribution
ATR	Attentuated total reflection

B

BovPrP	Bovine prion protein
BSE	Bovine spongiform encephalopathy

C

CD	Circular dichroism
$CDCl_3$	deuterated chloroform
CI	Chemical ionisation
CID	Collision-induced ionisation
CJD	Creutzfeldt-Jakob disease
CNS	Central nervous system
COSE	Correlated sweep excitation
CRM	Charge residue model
CSF	Cerebrospinal fluid
C-terminus	Carboxyl-terminus
Cu	Copper

CWD	Chronic wasting disease

D

D	Polydispersity
Da	Dalton
DC	Direct current
DCIM	Drift cell ion mobility
DCTB	trans-2-3-(4-tert-butylphenyl)-2-methyl-(2-propenylidene)-malononitrile
DEFRA	Department for environment, food and rural affairs
DESI	Desorption electrospray ionisation

E

E. coli	Escherichia coli
ECD	Electron capture dissociation
EHSS	Exact hard sphere scattering
EI	Electron impact
EM	Electron microscopy
EO	Ethylene oxide
EPR	Electron paramagnetic resonance
ePrP	Elk prion protein
ER	Endoplasmic reticulum
ESI	Electrospray ionisation
ETD	Electron transfer dissociation

F

FAB	Fast atom bombardment
FFI	Fatal familial insomnia
FID	Free induction decay
FT-ICR	Fourier transform-ion cyclotron resonance

FTIR	Fourier transform infrared
FWHM	Full width half heigth maximum

G

GABA	gamma-aminobutyric acid
GPC	Gel permeation chromatography
GPI	Glycosyl phosphatidylinositol
GSS	Gerstmann-Sträussler-Scheinker

H

His	Histidine
HuPrP	Human prion protein

I

IEM	Ion evaporation model
IM	Ion mobility
IM-MS	Ion mobility mass spectrometry
IMS	Ion mobility spectrometry
IR	Infrared
IU	Infectious units

L

LC	Liquid chromatography

M

m/z	mass-to-charge
MALDI	Matrix assisted laser desorption/ionisation
MCP	Microchannel plate
MCT	Mercury cadmium telluride
Mn	Manganese

M_n	number-average molecular weight
MoPrP	Mouse prion protein
MS	Mass spectrometry
MS/MS	Tandem mass spectrometry
MSG	Measurement Science Group
M_w	weight-average molecular weight

N

n-ESI	nano-Electrospray ionisation
NMR	Nuclear magnetic resonance
N-terminal	Amino-terminal

O

oa-ToF	orthogonal acceleration time-of-flight
OvPrP	Ovine prion protein

P

PA	Projection approximation
PD	Parkinson's disease
PDB	Protein data bank
PE	Poly(ethylene)
PEEK	Poly(ether ether ketone)
PEG	Poly(ethylene glycol)
pg	Picogram
PIPLC	Phosphatidylinositol specific phospholipase C
PMCA	Protein misfolding cyclic amplification
PMMA	Poly(methyl methacrylate)
PP	Poly(propylene)
PPG	Poly(propylene glycol)
PRNP	Prion protein gene
Prnp	Knockout mice lacking the PrP gene

PrP	Prion protein
PrP*	Partially folded prion protein intermediate
PrP27-30	Truncated prion protein
PrP^{C}	Normal cellular prion protein
PrP^{Sc}	Scrapie pathogenic prion protein
PS	Poly(styrene)
PSD	Post source decay
PSPr	Proteinase-sensitive prionopathy
PTMEG	Poly(tetra methylene glycol)

Q

QQQ	Triple quadrupole
Q-ToF	Quadrupole time-of-flight

R

RF	Radio frequency
ROS	Reactive oxygen species

S

SDS	Sodium dodecyl sulphate
SEC	Size exclusion chromatography
SHaPrP	Syrian hamster prion protein
SIMS	Secondary ion mass spectrometry
SLD	Soft laser desorption
SOD	Superoxide dismutase

SWIFT	Stored waveform inverse Fourier transform

T

TDC	Time-to-digital
TM	Trajectory model
ToF	Time-of-flight
TSE	Transmissible spongiform encephalopathy
T-Wave	Travelling-Wave

U

UV	Ultra violet

V

v-CJD	variant-Creutzfeldt-Jakob disease

W

X

XPS	X-ray photoelectron spectroscopy

Z

Zn	Zinc

Chapter 1

Introduction to Mass Spectrometry

1.1 Foundations of mass spectrometry

The ability to make precise mass measurements is fundamental to all scientific investigations. The use of scales to measure the weight of an object was first depicted in the hieroglyphics of the ancient Egyptians. Since this initial description there has been a considerable advance in the design and use of scales and balances in daily life and within the scientific community. Mass spectrometry is an elegant example of the progress that has been made in the measurement of mass.

During the latter half of the nineteenth century, aided by the development of increasingly reliable vacuum pumps, chemists and physicists in various European countries endeavoured to understand the nature of electrical discharges through rarefied gases. In 1876 Eugene Goldstein extended the studies of Johann Wilhelm Hittorf (who described experiments on discharges in gases at low pressures) and was the first person to use the term cathode rays. The nature of these cathode rays remained unclear. It was initially believed that the rays were either atoms or molecules that had picked up a charge. Goldstein, however, demonstrated that the cathode rays could travel in a straight line over distances far greater than the mean free paths of atomic and molecular species. Consequently, he and others considered that the rays were electromagnetic in nature (Jennings 2009).

Years later the cathode ray problem was eventually resolved by Joseph John (J. J.) Thomson. He showed that cathode rays were composed of particles which, in relation to the hydrogen atom, had a charge to mass ratio of approximately 1/1800. These particles were named electrons. In 1906 J. J. Thomson was awarded the Nobel Prize for Physics for his theoretical and experimental investigations on the conduction of electricity by gases. His pioneering work leading to the discovery of the electron (Thomson 1899) led to the creation of the first mass spectrometer, called a parabola spectrograph. This new technology allowed Thomson to separate the isotopes of neon (Thomson 1911); the first observation of non-radioactive isotopes. Francis W. Aston inspired by the discoveries and work of Thomson designed and built a new mass spectrometer. This new instrument had improved resolution which could discriminate between the isotopes in lighter elements such as neon and chlorine (Aston 1919a; Aston 1919b; Aston 1920). Aston was awarded the

Chemistry Nobel prize in 1922 and eventually discovered over 200 non-radioactive isotopes after building an improved instrument in 1927.

Mass spectrometry has been transformed since the initial studies of J. J. Thomson. The technique has experienced crucial developments in ionisation methods; it has been coupled to other separation techniques including gas chromatography, liquid chromatography and, of important relevance to this thesis, ion mobility spectrometry. The recent developments in mass spectrometry have led to entirely new instrument designs and applications. It is now considered an essential analytical tool for chemists and structural biologists alike.

1.2 What is a mass spectrometer?

Mass spectrometry (MS) is a powerful analytical technique that offers both high selectivity and sensitivity. A mass spectrometer is a device that can measure the mass-to-charge ratio (*m/z*) of an ion in the gas phase. This is achieved by ionising the sample, separating these ions according to their *m/z* and subsequently detecting and recording their relative abundance. Figure 1.1 shows a schematic of the four essential components within a modern mass spectrometer: sample introduction/ionisation, mass analysis, ion detection and a computer system. The analyte is introduced into the mass spectrometer and ionised in the ion source. These ions are resolved in the mass analyser according to their *m/z*. A detector registers the ions at each value of *m/z* and a computer system records the resulting data and presents it in an accessible format. Variations in each of the component parts of the instrument give rise to a wide range of types of mass spectrometer.

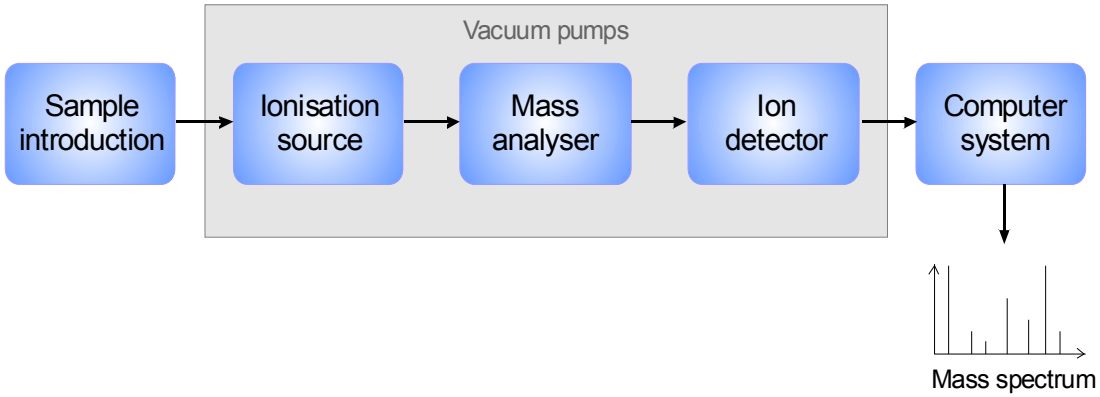

Figure 1.1: Schematic block diagram of a mass spectrometer.

Mass spectrometers and MS-based techniques are used throughout the industrial world to analyse and identify a variety of different substances. These include flavours, fragrances, natural products, pollutants, synthetic polymers, pharmaceuticals and metabolites (de Hoffmann and Stroobant 2007). The invention and application of soft ionisation techniques such as matrix-assisted laser desorption ionisation (MALDI) and electrospray ionisation (ESI) have allowed significant improvements, and progress, to be made in biochemical MS research. These ionisation methods allow large, polar and thermally liable bio-molecules to be characterised by means of MS.

1.3 Ionisation

Various ionisation techniques can be employed in mass spectrometry analysis. In the early 1980s the ionisation methods of choice were electron impact (EI), chemical ionisation (CI) and fast atom bombardment (FAB). The EI and CI methods require the analyte to be in the gas-phase. These ionisation methods are therefore limited to the analysis of thermally stable and volatile compounds. Electron impact ionisation is widely used to characterise small organic molecules. EI produces $M^{+\cdot}$ ions with significant internal energy that can induce fragmentation. In contrast, CI is a technique that produces MH^+ ions with lower internal energy. The amount of internal energy can, to some extent, be controlled by the careful choice of the reagent ion. The CI ionisation method produces mass spectra that contain fewer fragment

ions than the corresponding EI mass spectrum. Consequently, the two ionisation methods (EI and CI) can provide complementary information.

In general, biological samples such as proteins are polar and thermally liable. This implies that, without prior derivatisation of the sample, ionisation methods such as EI and CI are not suitable to characterise biological samples. The invention of the FAB source in 1981 (Barber, Bordoli et al. 1981) allowed, for the first time, routine MS analysis of polar thermally liable molecules that were up to a few thousand Dalton (Da) in mass. In contrast to the gas-phase ionisation methods, FAB requires the sample to be dissolved in a non-volatile liquid matrix such as glycerol or *m*-nitrobenzylic alcohol. The technique is based on accelerated argon atoms bombarding the surface of a sample:matrix solution to produce ions. These newly formed ions are passed into the mass analyser and then detected. In the 1980s the advantage of the FAB method was that it could produce ions from high molecular weight polar compounds (up to 5000 Da) (El-Aneed, Cohen et al. 2009). The disadvantage of this technology was the need to use a matrix. The presence of matrix-associated chemical noise could often mask the signal of sample ions. This made interpretation of the sample mass spectrum extremely difficult. The use of FAB as the ionisation method of choice for non-volatile and biological samples has been superseded by MALDI and ESI.

1.3.1 Matrix assisted laser desorption/ionisation (MALDI)

MALDI is a soft pulsed ionisation technique. The principal mechanism for MALDI was developed by Karas and co-workers in 1988 (Karas and Hillenkamp 1988). In 1985, however, Koichi Tanaka discovered soft laser desorption (SLD) and later filed a patent for his work as a new ionisation method for use in mass spectrometry. In 2002, Tanaka and John Fenn (the latter invented ESI) were awarded the Nobel Prize in Chemistry for their development of soft desorption ionisation methods for mass spectrometric analyses of biological macromolecules. It is, however, the work of Karas and Hillenkamp that established MALDI as an essential ionisation process for mass spectrometry analysis.

The MALDI technique is based on the sample being mixed with a solvent that is saturated with an organic matrix. The matrix must be able to form a solution with the sample but also contain a chromophore that can absorb radiation at the wavelength of a laser. The matrix must absorb the laser pulse very strongly and act as a proton donor to help the formation of the MH^+ ions (in most cases). The matrix is also essential to protect, dilute and isolate analyte molecules from one another by the formation of a solid solution upon evaporation of the solvent (Karas, Glückmann et al. 2000). In addition, the solid-solution matrix can shield the analyte from the direct laser ablation and absorb any excess energy. The choice of matrix depends on the properties of the analyte. Aromatic acids with an unsaturated substituent, that conjugates with the ring, are good matrix candidates because of their absorption characteristics. For example the most common matrices chosen to aid ionisation are α-cyano-4-hydroxycinnamic acid (CHCA) for peptide analysis, sinapinic acid (3,5-dimethoxy-4-hydrocinnamic acid) is used for protein characterisation and DCTB (trans-2-3-(4-tert-butylphenyl)-2-methyl-(2-propenylidene)-malononitrile) is commonly employed to analyse synthetic polymers. Alkali and transition metal salts are also added to the DCTB matrix to aid the cationisation of synthetic polymers. The analyte:matrix:salt mixture is subsequently spotted onto a stainless steel MALDI plate and allowed to dry. The solvent evaporation can produce a crystal that contains a homogenous dispersion of analyte and matrix molecules. The crystal is ablated with short pulses of a nitrogen laser at wavelength 337 nm. The irradiation from the laser is absorbed by the matrix molecules which cause them to vibrate. As a consequence, the analyte:matrix lattice disintegrates and a plume of desorbed and ionised molecules is generated. The proposed ion formation process is summarised in Figure 1.2.

Several hypotheses have been outlined to explain the MALDI ionisation process (Zenobi and Knochenmuss 1998). The most widely accepted theory is the ion formation mechanism. In this mechanism it is proposed that, in the gas-phase, protons are transferred from the energetically excited matrix molecules to the analyte whilst in the desorption plume (see Figure 1.2). Singly charged species resulting from the attachment of a proton (or cation in the presence of an alkali/transition metal salt) are the most commonly formed MALDI ion species. Another ion

formation mechanism proposed by Karas and co-workers is the "lucky-survivor" model (Karas, Glückmann et al. 2000). The "lucky-survivor" theory states that large charged analyte:matrix clusters are formed in the initial laser ablation. These highly charged clusters cannot survive in the plume and instantly undergo charge reduction, via neutralisation reactions from electrons trapped in the matrix, to generate charge states +1 and 0. The singly charged ions are the only ions that have a sufficiently low neutralisation cross-section to survive in the desorption plume (Karas, Glückmann et al. 2000).

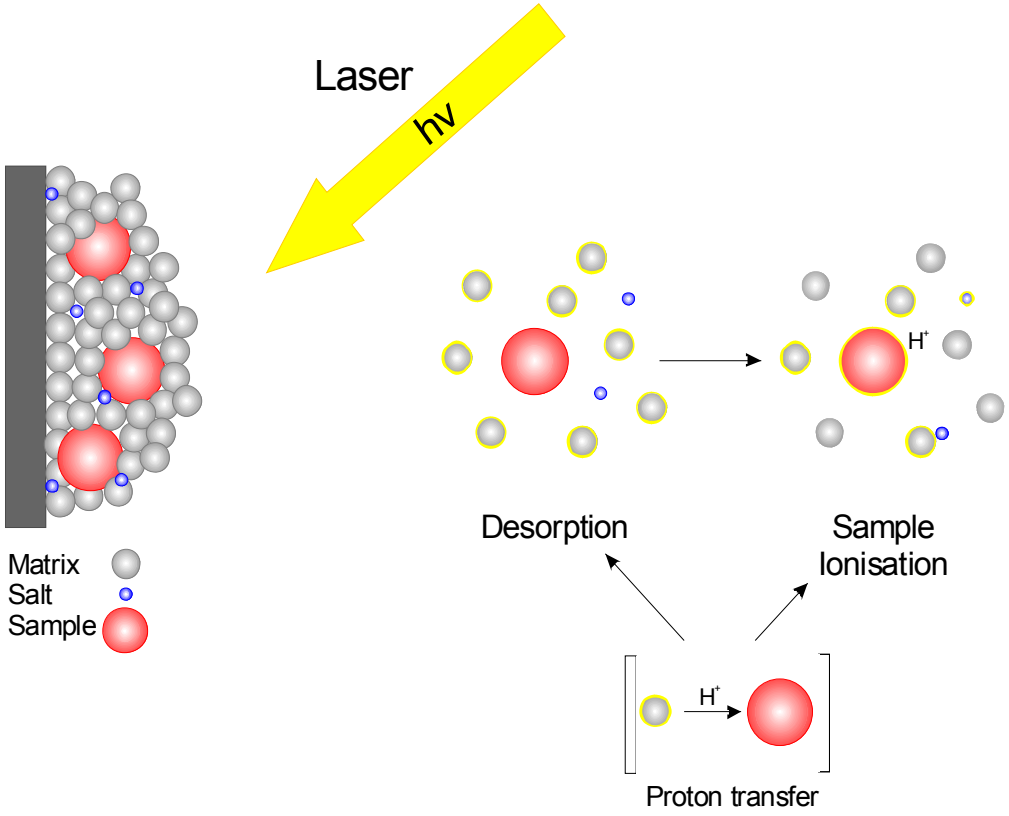

Figure 1.2: Schematic representation of the proposed MALDI ionisation process.

1.3.2 Electrospray ionisation (ESI)

In contrast to the pulsed laser ablation mechanism of MALDI, ESI is a continuous ionisation process. The technique requires the sample to be dissolved in a suitable aqueous/organic solvent system prior to the solution being sprayed into the ion source. The particular solvent system that is used is dependant on the compound class and the ionisation mode required (i.e. positive or negative ion mode). For example, positive ion mode ESI-MS analysis requires a sample to be dissolved in an

aqueous solution that contains varying concentrations of organic solvent (such as methanol or acetonitrile) and acid. This solution can contain a mixture of single- or multiply- protonated sample molecules. The solution is then sprayed through a capillary needle. The capillary needle is held at a high electrical potential with respect to the entrance of the mass spectrometer. This electric field induces a charge accumulation at the liquid surface, located at the end of the capillary, to form a Taylor cone. At a critical point the liquid breaks away, from the tip of the Taylor cone, to form highly charged droplets. The creation of a Taylor cone reduces the charge-to-surface ratio of the newly formed droplet. The droplet's release is facilitated by a nebulising gas (usually nitrogen) which flows around the outside of the capillary and directs the droplet towards the mass spectrometer. There are two proposed mechanisms that describe the production of gas-phase ions from aqueous charged droplets; these are the ion evaporation model (IEM) and the charge residue model (CRM) (see Figure 1.3). The IEM suggests that once airborne, the charge repulsion in the droplet can exceed the surface tension (known as the Rayleigh limit) and the solvent molecules evaporate. The reduction in droplet size increases the surface charge density and therefore increases the charge repulsion forces (Coulombic forces). This charge repulsion creates a Coulombic explosion which causes the droplet to divide. Ions within these newly formed droplets are desorbed into the gas-phase and enter the mass spectrometer. It is believed that ions with a relatively low *m/z* value are preferentially formed by means of this mechanism (Kebarle 2000). In contrast, the CRM suggests that once airborne the charge repulsion in the droplet can exceed the Rayleigh limit; solvent molecules evaporate and the droplet can fragment by means of a Coulombic explosion. This process is continuously repeated until a single, multiply-charged, analyte ion is produced. It has been suggested that the CRM is the dominant mechanism for multiply charged ions at a high *m/z* ratio (Kebarle 2000). Figure 1.3 illustrates the two proposed mechanisms of the ion formation within the ESI process. The main advantage of ESI is that for instruments of limited *m/z* range the multiple charges allow one to observe ions of a higher mass at lower *m/z* values. This permits mass spectrometer systems which have limited *m/z* range analysers to characterise higher molecular weight materials.

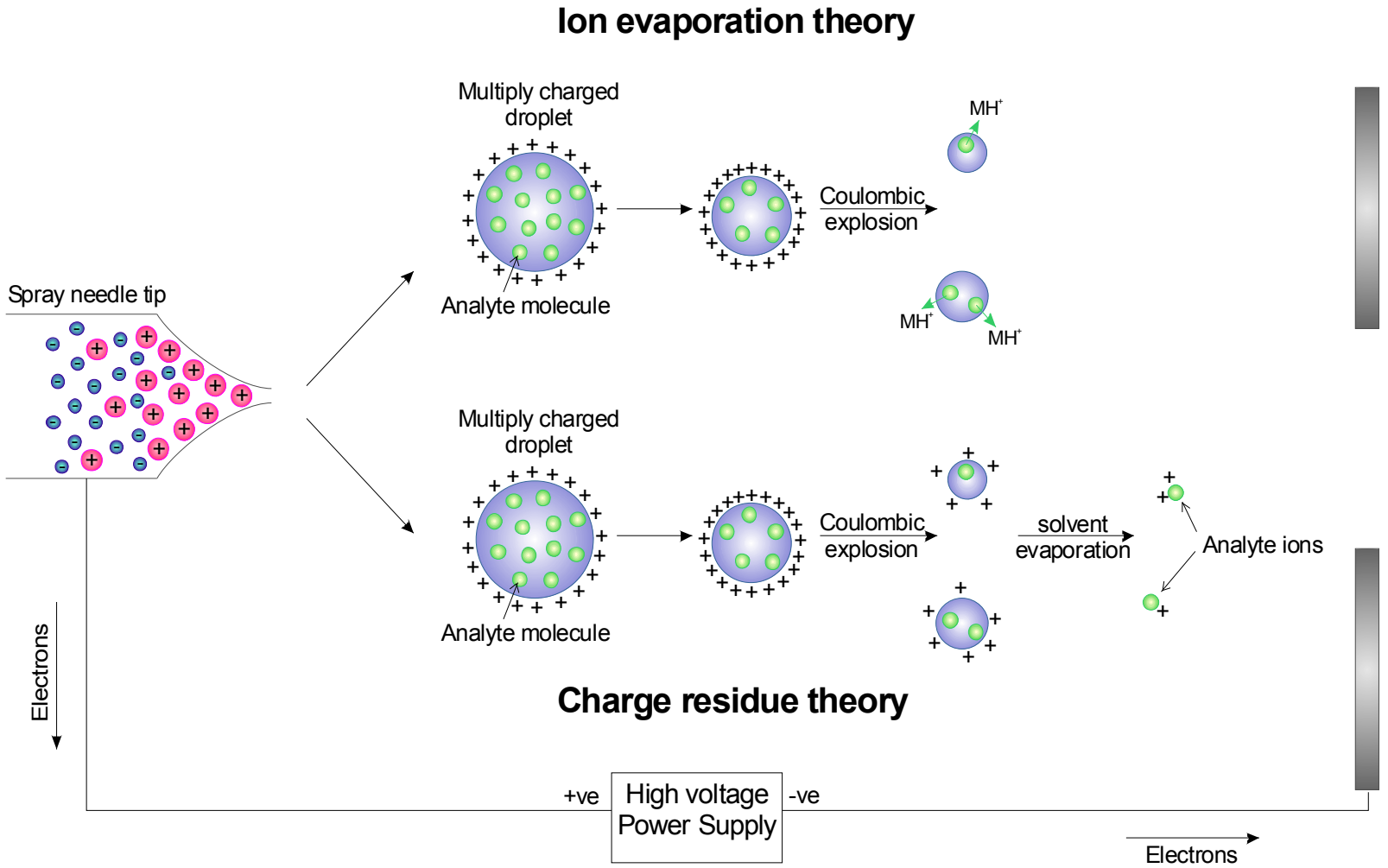

Figure 1.3: Schematic representation of the two proposed ESI ionisation mechanisms. Adapted from (Kebarle 2000)

1.4 Mass analysers

Once ions have been produced, in the ion source, they are separated according to their *m/z* ratio in the mass analyser. There are many different types of mass analyser but, in general, analysers can be classified as those that can scan, detecting ions of each *m/z* in turn, and those that detect ions of all *m/z* simultaneously. A scanning mass analyser, such as a quadrupole or magnetic sector, can successively detect ions of different *m/z* over a period of time. In contrast, analysers such as the time-of-flight (ToF) mass analyser, the ion trap and the ion cyclotron resonance instrument, allow the simultaneous detection of all ions. All mass analysers share three main characteristics: an upper mass limit, transmission efficiency and resolving power. The upper mass limit determines the highest *m/z* value that can be measured. The transmission efficiency is defined by the ratio of the number of ions that reach the detector and the number of ions that are produced in the ion source. The resolving power of a mass analyser is described as its ability to distinguish between two adjacent ions that are of similar mass. Conventional MS resolution is defined as ($m/\Delta m$) at a certain *m/z* ratio with the value calculated at full-width half-height maximum (FWHM) of the peak.

1.4.1 Quadrupole mass analyser

The principle of the quadrupole mass analyser was first described by Paul and Steinwedel in 1953 (Paul and Steinwedel 1953). The analyser consists of four parallel rods that are circular or hyperbolic in cross-section. These rods are arranged as two pairs of electrically connected rods. A combination of direct current (DC) and alternating radio frequency (RF) potentials are applied to each pair of rods. This produces a complex oscillating motion of ions as they transverse the mass analyser. These oscillating electric potentials can focus the trajectory of the ions towards the centre of the quadrupole mass analyser. The motion of the ions depends on the electric field they experience. If the quadrupole mass analyser is operated in scanning mode, (both DC and RF voltages are applied to the rods) ions of a specific *m/z* value will have a stable trajectory. This will allow their passage through the analyser and into the detector. The remaining ions, of different *m/z* values, will either collide into the four parallel rods or be lost at the walls of the analyser. If

suitable RF voltages are applied to all four parallel rods, all ions will have a stable trajectory and can successfully pass through the mass analyser to be detected. A variety of multipole mass filters have been developed based on the quadrupole RF-only method. These include a hexapole (six parallel rods) and an octapole (eight parallel rods). The multipole mass filter device is often placed in series with other mass analysers.

1.4.2 Time-of-Flight (ToF) mass analyser

The first commercial linear ToF instrument was based on the concepts and designs of Wiley and M^{c} Laren in 1955 (Wiley and McLaren 1955). The ToF mass analyser is classified as a simultaneous transmission device. It measures the *m/z* of an ion according to the time it takes to transverse a field-free region. The ToF analyser requires the ions to be produced in bundles and is therefore the ideal mass analyser for pulsed ion sources such as MALDI. These ion bundles are accelerated by a potential (V_s) which provides each ion with a fixed amount of initial kinetic energy. After acceleration the ions enter a field-free region, known as the flight tube, where they travel a distance (d) at a velocity inversely proportional to the square root of their mass (see Equation 1.4). The *m/z* ratio can be calculated by measuring the time it takes an ion to transverse the flight tube from the ion source to the detector. An ion with a mass (m) and a total charge (q = ze) has a kinetic energy.

$$\frac{mv^2}{2} = qV_s = zeV_s = E_k$$

Equation 1.1

where v is velocity, V_s is the applied potential, z is the number of charges, e is the electronic charge. The time taken to transverse the flight tube is given by.

$$t = \frac{d}{v}$$

Equation 1.2

Replacing v with its value from Equation 1.1 gives.

$$t^2 = \frac{m}{z\left(\frac{d^2}{2V_s e}\right)}$$

Equation 1.3

Rearranging Equation 1.3 assuming v is a constant gives.

$$t = \sqrt{\frac{m}{z} \times constant}$$

Equation 1.4

Equation 1.4 suggests that the *m/z* can be calculated from measuring the time (de Hoffmann and Stroobant 2007). The general concept of the ToF mass analyser is that the larger the mass of an ion the longer the time required for it to transverse the flight tube.

The advantage of a linear ToF mass analyser is high sensitivity and high mass range. In principle, the mass range does not have an upper mass limit. The major disadvantage of the linear ToF is the poor resolution. Factors such as the length of the flight tube, the volume of space where the ions are formed and the variation of initial kinetic energy of the individual ions, can all affect the resolving power. Ions with the same *m/z* ratio but with different initial kinetic energies will transverse the flight tube at different velocities. This will result in each ion reaching the detector at a slightly different time which can create a broad ion peak. This peak broadening phenomena can be reduced by means of delayed pulsed extraction (Vestal, Juhasz et al. 1995). An extraction pulse is applied to the ions after a certain time delay (ranging from hundreds of nanoseconds to several microseconds) (de Hoffmann and Stroobant 2007). As a result, more kinetic energy is transferred to ions that have remained in the ion source compared to ions that are further away from the ion source. The delayed pulse extraction technique attempts to balance the initial kinetic energy within a bundle of ions, reducing peak broadening at the detector.

Mass resolution is also proportional to ion flight time. The longer the flight tube, in theory, the better the resolution. Modern ToF instruments achieve higher mass resolution by means of a reflectron. The reflectron is composed of a series of ring electrodes (Mamyrin, Karataev et al. 1973). These electrodes are an optic device that can act as an electrostatic ion mirror. The reflectron can reflect ions back down the flight tube which effectively doubles their flight path (see Figure 1.4). Ions with higher initial kinetic energy can travel further into the reflectron ring electrodes than ions with less initial energy. Ions with the same *m/z* value but different initial kinetic energy should reach the detector at the same time. Figure 1.4 shows a schematic representation of the reflectron mechanism. A compromise is made when employing an ion reflectron. Although the mass resolution of the ions will be improved, there is a potential loss in sensitivity and a reduction in the upper mass limits that can be measured.

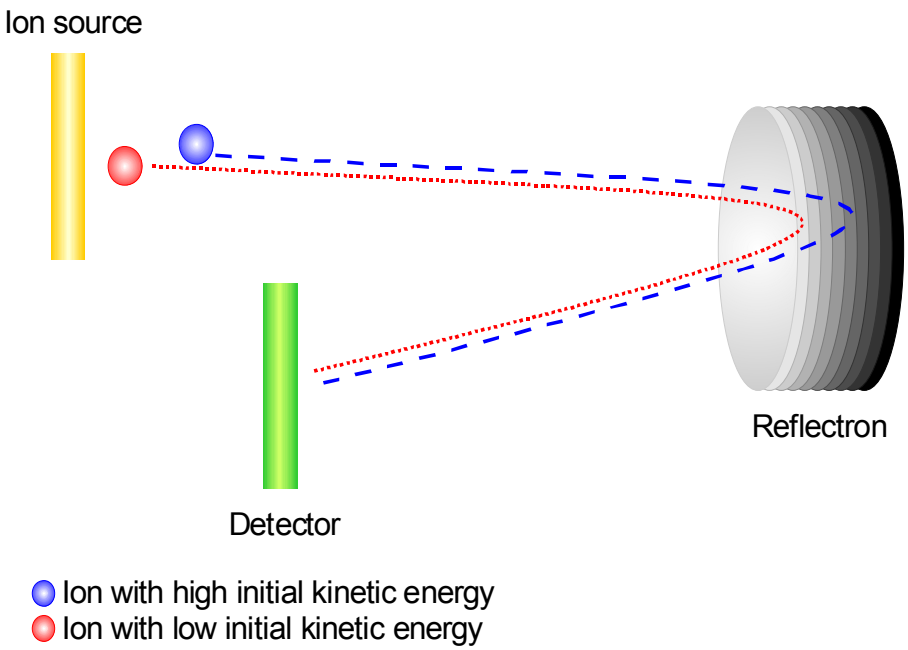

Figure 1.4: Schematic representation of a ToF mass analyser equipped with a reflectron. Both ions have the same mass but different initial kinetic energies. The ion with the highest initial kinetic energy (blue) will travel further into the reflectron in comparison to the ion with less initial kinetic energy (red). Both ions will reach the detector simultaneously.

1.5 Detectors

A variety of different mass spectrometer detectors can be employed. The method is based on detecting an ion beam from the mass analyser and transforming this information into a usable signal. Detectors can be classified into one of two categories. These are direct measurement, such as a Faraday cage, which measure the direct charge that reaches the detector, or detectors that increase the intensity of the signal, such as electron- or photon-multipliers and array detectors (de Hoffmann and Stroobant 2007).

The electron and photon multiplier detectors are based on an ion (positive or negative) colliding with a plate (conversion dynode) to create an emission of secondary electrons. These newly generated electrons are accelerated so that they collide with a continuous-dynode. These collisions create enough energy to dislodge more electrons from successive dynodes. This process is repeated until a cascade of electrons is produced which generates an electrical current. The electric current is passed through a resistor to generate a voltage that can then be amplified. In this approach an amplification of up to 10^7, of the original signal, can be obtained (de Hoffmann and Stroobant 2007).

An array detector, such as microchannel plate (MCP) detector, contains an array of parallel miniature electron multiplier channels which are typically placed at an 8° angle to the surface of the plate (Wiza 1979) (see Figure 1.5). The internal diameter of the electron multiplier channel is coated with a semi-conducting material. Upon the ion beam colliding with the semi-conductive material secondary electrons are emitted. In a similar mechanism to the electron multiplier, a cascade of newly generated electrons is created and the number of electrons can be amplified by 10^5 – 10^8 (de Hoffmann and Stroobant 2007). A single ion reaching the MCP detector will affect a few channels only; therefore the multiple channels can detect several different ions simultaneously. Figure 1.5 shows a schematic representation of an electron multiplier channel. Great care needs to be taken not to saturate the MCP detector with ion signals because the channels must have time to recover (dead time)

before they can detect new signals. If the MCP detector becomes saturated with a large signal, it will not be able to detect any smaller signal which may follow directly afterwards. The array detector is ideally suited to ionisation methods such as MALDI and ESI which can produce hundreds of ions that must be analysed simultaneously.

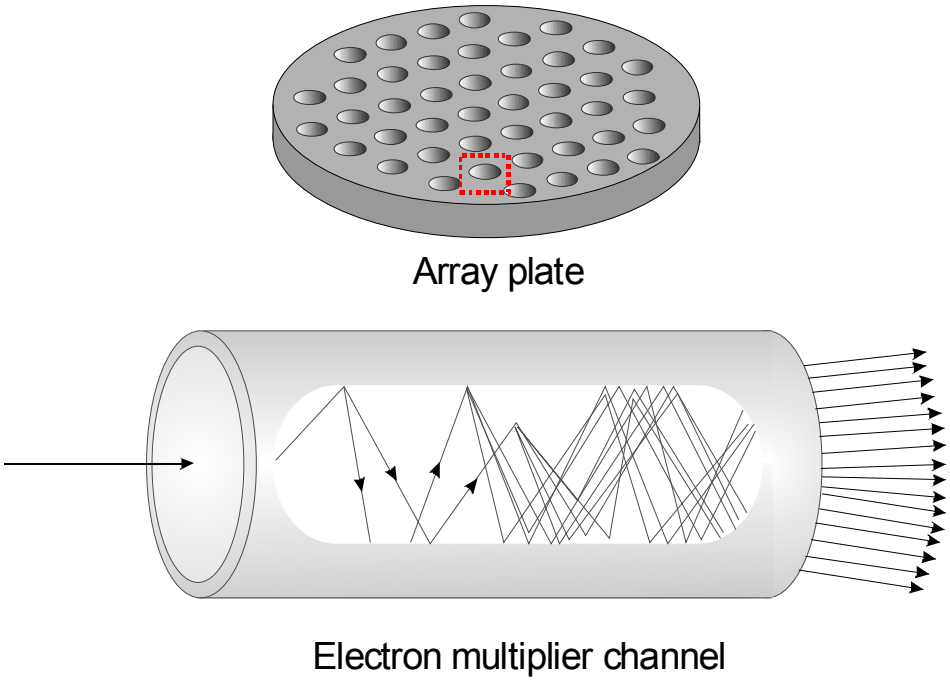

Figure 1.5: Schematic representation of an array plate and the electron multiplication within one of the channels. Adapted from (de Hoffmann and Stroobant 2007).

In modern mass spectrometry the most commonly used detector is either an analog-to-digital (ADC) or a time-to-digital (TDC) detector. Both ACD and TDC detectors use a multiplier, such as a MCP detector, as a first stage. An ADC detector registers the ion current produced from the mass analyser, amplifies the signal and removes high frequency noise using a filter. The voltage derived from the ion current is then plotted on a *m/z* scale with respect to previously acquired calibrated data. In contrast, a TDC detector records the time at which an ion strikes the detector and sums the signal from all individual acquisitions to create the observed mass spectrum (de Hoffmann and Stroobant 2007). TCD detectors have the advantage of greater speed of detection, whereas ADC detectors have an improved dynamic range.

1.6 Tandem mass spectrometry

To perform tandem mass spectrometry (MS/MS) at least two mass analysis steps are required. Common configurations of instrumentation include the hybrid Q-ToF (quadrupole mass analyser coupled to a ToF instrument), ToF-ToF mass analysers and the triple quadrupole (QQQ) mass analyser. MS/MS experiments can take place in either time (Iontrap, Orbitrap, Fourier transform ion cyclotron resonance (FT-ICR-MS)) or in space (Q-ToF, ToF-ToF, QQQ). In time MS/MS experiments are performed by a sequence of events within an ion storage device whereas at least two physically distinct mass analysers are required to conduct in space experiments. Both methods require the fragmentation of a selected ion (precursor ion) within the first mass analyser to allow the second mass analyser to characterise the fragment ions (product ions) produced.

In the 1960s Jennings (Jennings 1968) and McLafferty (McLafferty and Bryce 1967) pioneered collision-induced dissociation (CID). This technique is based on a precursor ion colliding with an inert gas. The translational energy from the collisions is converted into internal energy which is rapidly distributed throughout the ion. Consecutive collisions increase the internal energy to induce fragmentation. Interpretation of the resulting product ion mass spectrum can determine sequence and/or structural information about the precursor ion. The production of peptide fragment ions by means of CID has been well characterised. The nomenclature to describe the product ions was proposed by Roepstorff, Fohlmann and extended by Biemann (Biemann 1992; Roepstorff and Fohlman 1984). The fragmentation pathway of particular synthetic polymer systems is described in Chapter 6 and 7.

A different and nonergodic process, namely electron capture dissociation (ECD), can also be used to achieve the fragmentation of peptides and certain types of synthetic polymers (Cerda, Horn et al. 1999; Syka, Coon et al. 2004). The production of fragment ions by means of ECD is, however, limited to the use in FT-ICR-MS instruments. Complementary to this technique is electron transfer dissociation (ETD). The mechanisms of reactions initiated by ETD are not well understood and

several different processes resulting from an initial electron transfer or proton abstraction can occur. The ECD and ETD mechanisms have been extensively used to investigate the position of post translation modifications (PTMs) (Mehlhorn, Groth et al. 1996). In contrast to CID, ECD and ETD are site-specific reactions; fragmentation occurs along the peptide backbone and leaves little excess energy for further fragmentation such as PTM loss. In general, CID sensitivity is much higher than that obtained from ECD and ETD.

1.7 Ion mobility mass spectrometry

Ion mobility spectrometry (IMS) is a well-established analytical technique that is used throughout the industrial world to characterise explosives, drugs and chemical welfare agents. Invented in the 1970s IMS, also known as plasma chromatography or ion chromatography, is a technique that separates ions based on their mobility through an inert gas (Cohen and Karasek 1970; Karasek 1974). In the constraints of a drift tube, the ions migrate through a counter flowing buffer gas under the influence of a weak electric field. A constant electric field (E), produced by a series of ring electrodes, propels the ions through the drift tube whilst collisions with the buffer gas decelerate the motion of these ions. This process creates a quasi-constant velocity v_d. The ions collide with the buffer gas and separation occurs according to their mass, charge and shape. Compact ions with small collision cross-sections will drift more quickly than extended ions. The measurement of this mobility yields information about the rotationally-averaged cross-section of each ion (i.e. whether it is compact or extended). The ion mobility K is the ratio of v_d to the electric field strength E.

$$K = \frac{v_d}{E}$$

Equation 1.5

The ion mobility is expressed as the reduced mobility (K_0) of an ion under standard temperature T_0 and pressure P_0 (T_0 273 K and P_0 760 Torr).

$$K_0 = K\frac{PT_0}{TP_0} = K\frac{P \times 273}{T \times 760}$$

Equation 1.6

Using kinetic theory (Mason and McDaniel 1988) the reduced mobility K_0 can be related to the collision cross-section of the ion species by means of the following equation.

$$K_0 = \frac{3ze}{16N_0} \times \frac{1}{\sigma}\sqrt{\left(\frac{2\pi}{\mu k_B T}\right)}$$

Equation 1.7

where z is the number of charges, e is the electronic charge, N_0 the buffer gas number density at standard temperature and pressure, σ is the average collision integral or collision cross-section, μ the reduced mass of the buffer gas and ion, k_B is the Boltzmann constant and T is the effective temperature.

The average collision cross-section can be obtained from the average of all possible collision geometries (Clemmer and Jarrold 1997). Several models have been proposed to calculate the exact average collision cross-section. The simplest method is the projection approximation (PA) which replaces the cross-section of an ion with its projection (shadow) and averages the projections created by every orientation of the ion. The PA is an adequate approximation for small molecules but can underestimate the cross-section of proteins when interactions with the buffer gas become important (Scarff, Thalassinos *et al.* 2008). The trajectory method (TM) gives the most reliable estimate, incorporating all interactions, but is computationally intense. A compromise is to use a third model, the exact hard sphere scattering (EHSS) method. This ignores electrostatic interactions so requires substantially less computational time, and can calculate cross-sections to within a few percent of values obtained by the TM (Jarrold 1998).

1.7.1 Instrumentation

Two different types of ion mobility instrumentation have been developed; travelling wave (T-Wave) ion mobility and drift-cell ion mobility (DCIM) mass spectrometry. Both techniques can be coupled to a range of ion sources, such as ESI and MALDI, and mass analysers. Different configurations of mass analysers have been used to perform mass analysis including quadrupole mass analysers (Shelimov, Clemmer *et al.* 1997a), ToF mass analysers (Srebalus, Li et al. 1999) and FT-ICR spectrometers (Bluhm, Gillig et al. 2000).

To date, the majority of DCIM-MS instruments have been designed, developed and built in-house. The number of these instruments is limited because of the mechanical, electrical, engineering and software expertise required to build each instrument. Recently, however, a DCIM device has been incorporated into a commercial instrument (McCullough, Kalapothakis et al. 2008) and a drift cell was added into a commercial Q-ToF hybrid instrument (Thalassinos, Slade et al. 2004). This instrument benefited from the ability of the ToF mass analyser to acquire mass spectra on a time scale significantly faster (microseconds) than the time required for mobility separation (milliseconds). The ToF mass analyser allowed a large number of mass spectra, typically 200, to be obtained during a single mobility separation. The DCIM-MS approach has been used to study a variety of different compounds including carbon clusters (von Helden, Hsu et al. 1991; von Helden, Hsu et al. 2002), synthetic polymers (Gidden, Bowers *et al.* 2002; Gidden, Jackson *et al.* 1999; Gidden, Wyttenbach *et al.* 1999; Gidden, Wyttenbach *et al.* 2000), proteins (Shelimov, Clemmer *et al.* 1997a; Wyttenbach, von Helden *et al.* 1996) and peptides (Kaleta and Jarrold 2003). von Helden and co-workers describe a method in which the theoretical cross-section of a molecule can be related to its equivalent experimental value (von Helden, Wyttenbach et al. 1995). Their approach involves the use of molecular mechanics/dynamics calculations to generate three-dimensional structures which can be minimised, by means of specific programs (Wyttenbach, Helden et al. 1997). These programs can determine the lowest-energy conformations and so calculate their respective theoretical cross-sections. The calculations have been shown to be in excellent agreement with experimental data (Wyttenbach, von Helden et al. 1996).

In contrast to DCIM, T-Wave technology uses a series of transient DC voltages to propel ions through a stacked-ring ion guide. RF voltages are applied to consecutive ring electrodes to stabilise the trajectory of the ions (Pringle, Giles *et al.* 2007a). The electrodes in the stacked-ring ion guide are arranged orthogonally to the ion transmission axis. Opposite RF phases are applied to alternating adjacent rings to create a radially-confining effective potential barrier. This reduces ion loss by diffusion. Figure 1.6 shows a schematic representation of the stacked-ring ion guide. Ions are propelled through the stacked-ring ion guide by a superimposed DC potential. This DC potential moves across electrode pairs, the length of the stacked-ring ion guide, at regular time intervals. A stacked-ring ion guide that contains 61 electrode pairs has a DC potential repeat pattern of six. This suggests that a DC potential can be applied to the 1st and 7th pair of electrodes, then a pulse is applied to the 2nd and 8th pair of electrodes and so on across the electrode rings. This pattern of pulsed DC voltages generates a sequence of travelling waves.

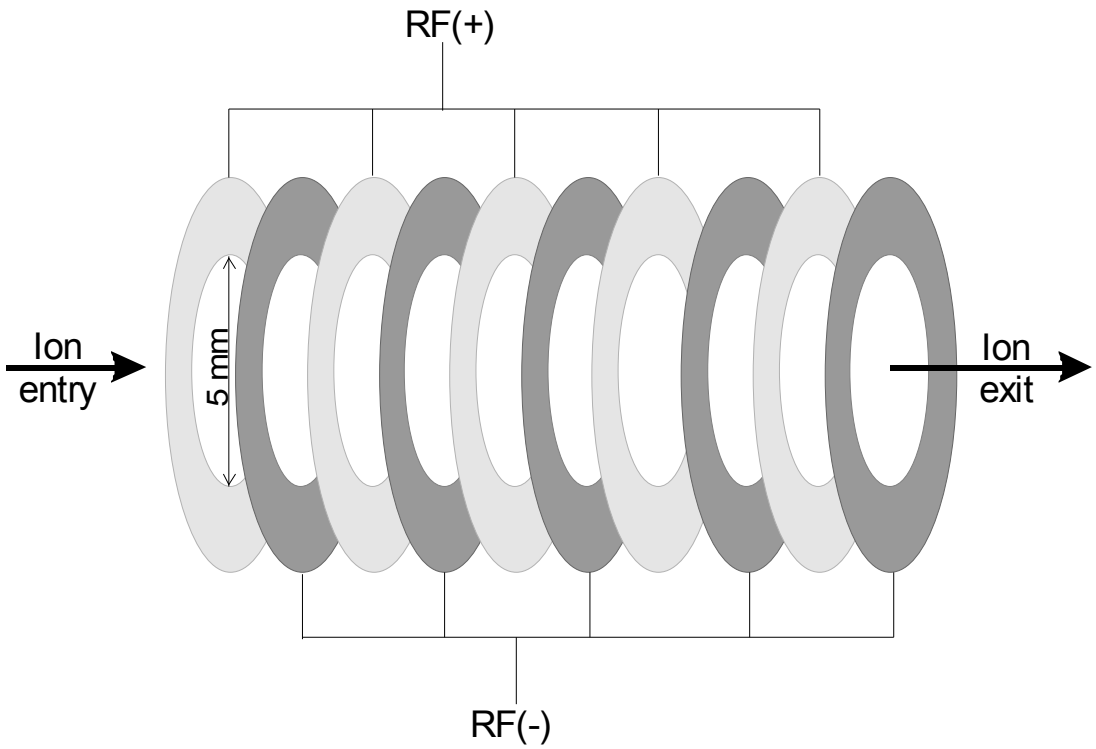

Figure 1.6: A schematic representation of the stacked ring ion guide region within a T-Wave device.

T-Wave technology has been integrated into a Q-ToF instrument to create the commercially available Synapt HDMS system (Waters, Manchester, UK). Figure 1.7 shows a schematic of the Synapt instrument (Pringle, Giles *et al.* 2007a). The instrument comprises three T-Wave enabled stacked ion guides: trap; IM cell and transfer region. The trap and transfer regions are 100 mm long and consist of 31 electrode pairs. A DC-only potential is applied to the last pair of electrodes in the trap ion guide. This voltage is periodically modulated to create an ion gate/packet prior to their entry into the IM cell. The mobility cell is 185 mm long and contains 61 electrode pairs. The flow of buffer gas within the mobility cell can be optimised for each sample and a maximum pressure of 1 mbar can be sustained (Pringle, Giles *et al.* 2007a). In contrast to the trap region, the transfer region has a T-Wave voltage applied to the stacked-ring ion electrodes. This T-Wave voltage allows the ions that have been separated in the mobility cell to be carried through the transfer region and into the detector. The orthogonal acceleration-ToF mass analyser acquisition time is synchronised with the gated release of ion packets from the trap region into the mobility cell. These ion packets are released every 100 μs. For each ion packet, 200 orthogonal acceleration pushes (mass spectra) are measured by the ToF mass analyser. This synchronisation allows both the arrival time distribution (ATD) information and mass spectral data to be obtained simultaneously. The process is repeated until a mass spectrum with the desired signal-to-noise is obtained.

The T-Wave device has a number of potential advantages when compared to DCIM approaches. These include high sensitivity and the ability to collect mass spectra data and ATD information simultaneously. Another advantage of the T-Wave device is that CID experiments can be performed in either or both of the trap and transfer region. This allows a variety of different experiments to be performed. The physical principles behind DCIM are well characterised and data obtained can be used to measure the absolute collision cross-section of an ion. Mobility separation obtained by means of the T-Wave technology depends on a number of different variables including complex ion trajectories, collisions with the buffer gas and the time-dependent, non-uniform electric field of the T-Wave cell. Due to these T-Wave features, absolute collision cross-sections of an ion cannot be obtained directly from mobility measurements. In order to compare the results from the two mobility

techniques a calibration method for the T-Wave technology has been developed (Ruotolo, Benesch *et al.* 2008; Thalassinos, Grabenauer *et al.* 2009). This calibration produces an estimated cross-section based on the measurement of the mobility of reference standards of known cross-sections obtained under similar experimental conditions.

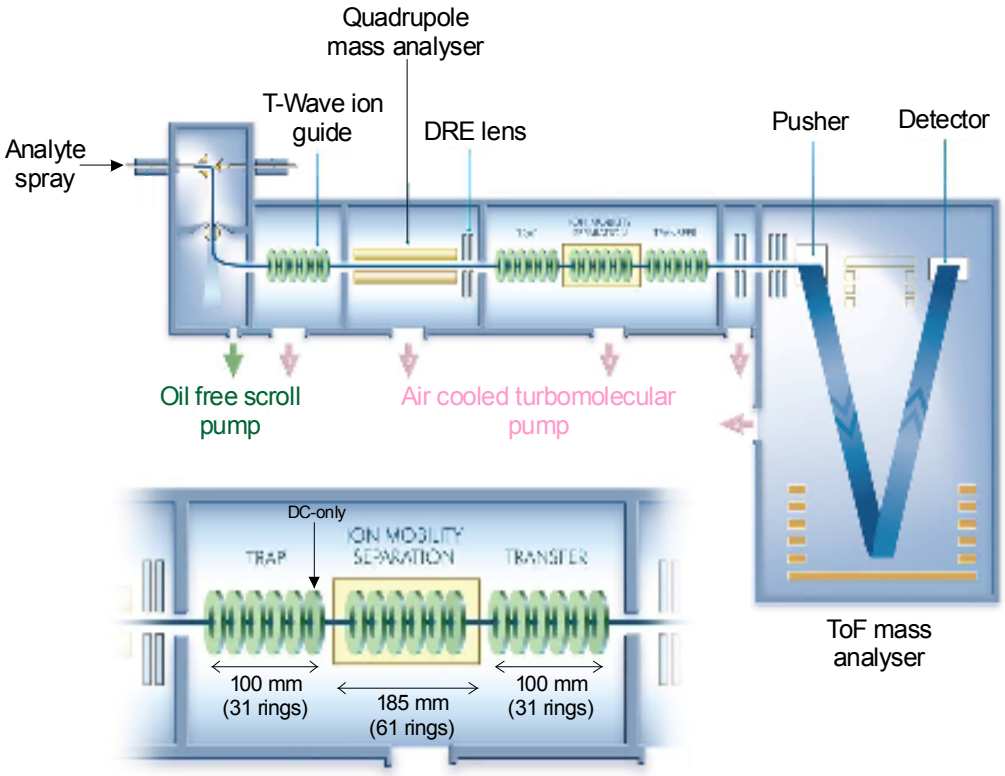

Figure 1.7: Schematic representation of the Synapt. (Inset). Enlargement of the T-Wave ion mobility device. Adapted from (Pringle, Giles et al. 2007b).

1.7.2 T-Wave calibration

Several approaches have been proposed to calibrate data obtained by means of the T-Wave device (Ruotolo, Benesch et al. 2008; Thalassinos, Grabenauer et al. 2009). The majority of these calibration methods require the mobility measurement of known standards, by means of the T-Wave device, to create a calibration curve from which the estimated cross-section of unknown compounds can be derived. A universal calibration method has yet to be established. To create a successful calibration, standards of known absolute cross-sections obtained by means of a DCIM-MS are used (Clemmer; Valentine, Anderson et al. 1997; Valentine, Counterman et al. 1999). The calibration method used throughout this body of work has been developed within the Scrivens research group (Thalassinos, Grabenauer et al. 2009; Thalassinos and Scrivens 2009) and is described below.

1. Measure arrival time in scan (scan number (n))
2. Convert to time (multiply by pusher time)

$$t_d = n \times pusher\ time\ (ms)$$

Equation 1.8

3. Correct for *m/z* independent time of flight

The independent time of flight is related to the T-Wave velocity and is the time an ion spends in the mobility region (t_m) and transfer region (t_t). The time is calculated for each ion electrode pair. For example the mobility cell contains 61 electrode pairs therefore the independent time of flight of an ion in the mobility cell is $61 \times t_m$. The transfer region contains 31 electrode pairs ($31 \times t_t$). The independent time an ion spends in the mobility cell and transfer region must be subtracted from the drift time (t_d). At the wave velocity 300 m s^{-1}, the values for t_m and t_t are equal to 10 µs therefore [(61 × 10) + (31 × 10)] µs = 920 µs. The corrected drift time (t'_d) can be calculated from the following equation.

$$t'_d = t_d - 920$$

Equation 1.9

4. Correct for *m/z* dependent time of flight

At 1000 *m/z*, the time taken for an ion to transverse the ToF mass analyser flight tube is 44 μs and the transit time from being expelled from the transfer region to the ToF mass analyser is 41 μs. The addition of these two times is equal to 85 μs. This value must be subtracted from the drift time. The corrected effective drift time (t''_d) is proportional to the square root of the *m/z* value.

$$t''_d = t'_d - \sqrt{\frac{m/z}{1000}} \times 0.085$$

Equation 1.10

5. Obtain calibration coefficients from published absolute cross-section data (σ). Correct the published cross-section by taking into account the reduced mass and charge state. Where e is the charge on the ion, m_i is the mass of the ion and m_n is the mass of the mobility gas.

$$\sigma' = \frac{\sigma}{e\sqrt{\left(\frac{1}{m_i} + \frac{1}{m_n}\right)}}$$

Equation 1.11

6. Plot σ' against t''_d.
7. Fit appropriate curve to data points either a power series fit ($y = \mathbf{A}x^{\mathbf{B}}$) or a linear series fit (when $y = \mathbf{A}x + \mathbf{B}$).
8. Calculate **A** and **B** from the gradient.
9. Convert T-Wave experimental mobility data into estimated cross-sections by calculating either a power fit (Equation 1.12) or a linear fit (Equation 1.13).

$$\sigma = t''^{B}_{d} \times A \times e \times \sqrt{\left(\frac{1}{m_i} \times \frac{1}{m_n}\right)}$$

Equation 1.12

$$\sigma = [(t''_d \times A) + B] \times e \times \sqrt{\left(\frac{1}{m_i} \times \frac{1}{m_n}\right)}$$

Equation 1.13

The T-Wave height, wave velocity and pressure of buffer gas within the mobility cell can all affect an ion's ATD but these parameters do not affect the calibration. It is therefore essential that data from the calibration standard is obtained under the same conditions as the unknown compound (Leary, Schenauer *et al.* 2009). Figure 1.8 shows a plot of the corrected effective drift time (t''_d) vs the corrected published absolute cross-sections used to create a calibration. A recent study showed that a valid T-Wave device calibration requires the corrected arrival times of the calibration standards to bracket those of the unknown sample (Shvartsburg and Smith 2008). Furthermore, it was observed that a power series is appropriate for calibrating large compounds such as proteins whereas a linear relationship has been found to be more appropriate for smaller molecules such as peptides (Thalassinos, Grabenauer et al. 2009).

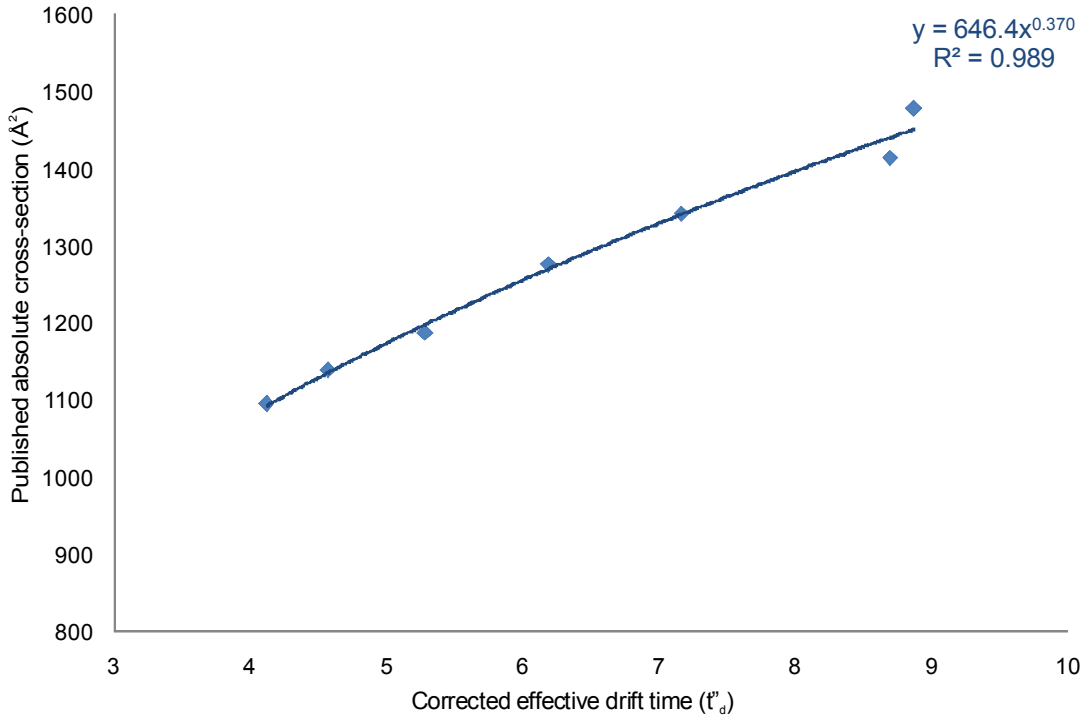

Figure 1.8: An example plot of the corrected effective drift time (t''_d) of equine myoglobin vs the corrected published absolute cross-sections. The power series fit is displayed. This is the type of plot used in the T-Wave calibration.

1.8 Classical tools of structural biology

The properties of a compound, in particular proteins, are largely determined by its structure. The secondary structure, defined as the local conformation of the protein's backbone and the tertiary structure, the three-dimensional fold of the protein, can be determined by means of a variety of biophysical techniques. Techniques such as circular dichroism (CD) and infrared spectroscopy are used to characterise the secondary structure of proteins, whereas X-ray crystallography and nuclear magnetic resonance (NMR) spectroscopy are the classical biophysical methods used to determine the tertiary structure of a protein. All of these techniques measure the population-average structure in solution and can provide complementary information to mass spectrometry data.

1.8.1 Circular dichroism (CD)

CD is recognised as a valuable technique for examining the structure of proteins in solution. It is an absorption spectroscopy technique based on measuring the absorbance signal of circularly polarised light. Plane polarised light consists of two circularly polarised light components of equal magnitude; one rotates in a counter-clockwise direction (left handed) and the other in a clockwise direction (right handed). CD refers to the differential absorption of these two components. A CD signal is observed when an optically active chromophore is either chiral because of its structure, it is covalently linked to the chiral centre in the molecule or it is placed in an asymmetrical environment by virtue of the three-dimensional structure adopted by the molecule (Kelly, Jess et al. 2005). The CD technique is based on measuring the difference in absorbance between the two circularly polarised components.

Proteins and peptides are optically active because they possess two different types of asymmetry; configurational and conformational. Amino acid residues, except glycine, have optical activity because of their intrinsic L-chirality about the α-carbon atom. The secondary structure of proteins also contributes to the optical activity. The near-ultra violet (UV) CD region (wavelength 250-300 nm) detects the optical activity of aromatic side chains in phenylalanine, tyrosine and tryptophan. In this

region the chromophores are sensitive to the overall tertiary structure of the protein. The secondary structure of a peptide or protein can be determined by means of far-UV CD spectroscopy (wavelength < 250 nm). The far-UV CD spectra of a protein can yield information about the asymmetric features of the amino acid backbone. Common types of secondary structure, adopted by peptides and proteins, give rise to distinctive features in a far-UV CD spectrum (see Figure 1.9).

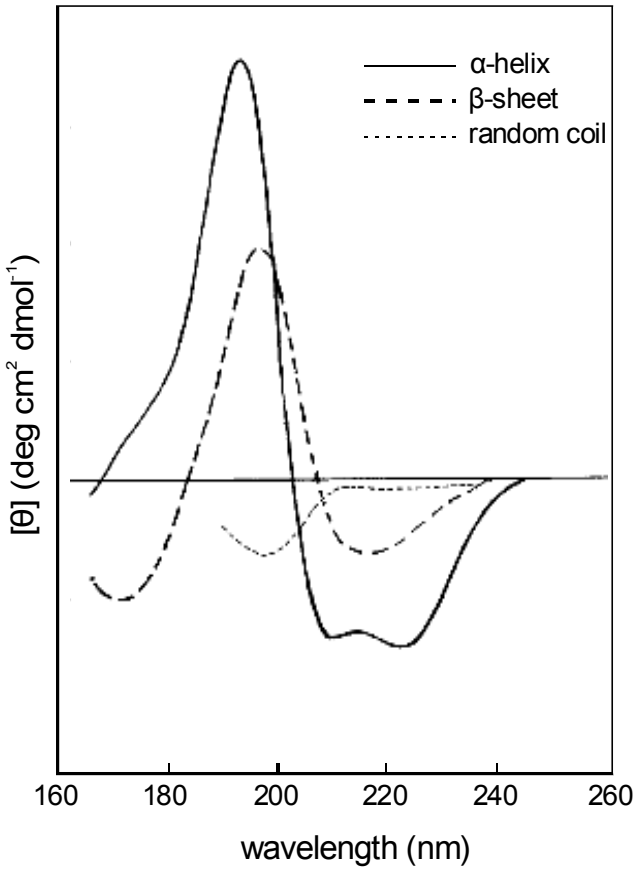

Figure 1.9: Far-UV CD spectra associated with the various types of secondary structure. Solid line α-helix, dashed line β-sheet and dotted line random coil structure. Taken from (Kelly, Jess et al. 2005).

Figure 1.9 shows a far-UV CD spectrum associated with various types of secondary structure. An α-helical structural motif is characterised by two negative absorbance bands at ~222 nm and 208 nm and a positive band at 190 nm. The far-UV CD spectrum of a β-sheet rich protein will have a negative band at 216 nm and a random coil structure is characterised by a negative band near 200 nm.

1.8.2 Infrared (IR) spectroscopy

The infrared region in the electromagnetic spectrum encompasses wavelengths 0.78 – 300 μm (wavenumber $1.3 \times 10^4 – 3.3 \times 10^1$ cm^{-1}). The absorption of IR radiation does not create an electronic transition in a molecule (as in CD spectroscopy); instead small changes between discrete quantised vibrational energy levels are induced. Molecules that have a charge separation either across the whole molecule or across a specific bond possess a permanent dipole moment. An atom's position within a molecule fluctuates continuously because of the various types of molecular vibrations that are possible. These vibrations can be classified as either bending or stretching motions and can give rise to a transient dipole moment. There must be a change in the permanent or transient dipole moment, during a vibration, for a molecule to absorb IR radiation and be classified as IR-active. When a molecule vibrates, a regular fluctuation in the dipole moment occurs which allows the dipole moment to interact with the electrical field associated with the IR radiation. If the frequency of the IR radiation is the same as that of the vibration for which there is a change in dipole moment, a quantum of vibrational energy is absorbed by the molecule. This results in a change in the molecule's vibrational amplitude and the radiation is absorbed (Skoog and Leary 1992). An IR spectrum is a representation of a sample's vibrational frequency fingerprint. Molecules absorb IR radiation at characteristic wavelengths determined by their atomic composition and bond structure. Consequently, each molecule will produce a unique IR absorption spectrum.

IR spectroscopy is widely used to determine the secondary structure of peptides and proteins (Pelton and McLean 2000). The IR spectra of peptides and proteins can exhibit a number of amide bands, each of which represent a different vibration of the

peptide group (Goormaghtigh, Cabiaux et al. 1990). Nine characteristic amide bands are observed in the IR spectra of proteins but the dominant species is from the amide I (1600-1700 cm^{-1}) band. This band represents the vibration frequencies of a C=O stretch, C-N stretch and N-H bend within a peptide group. Goormaghtigh and co-workers found that the wavenumber of the amide I band could suggest the secondary structure of the protein. They observed that predominantly α-helical conformations had an amide I band at 1655 cm^{-1}, whereas β-sheet rich structures gave a maximum at 1630 cm^{-1} in the IR spectrum (Goormaghtigh, Cabiaux et al. 1990).

1.8.3 Nuclear magnetic resonance (NMR) spectroscopy

The three-dimensional structure of a protein can be determined by means of NMR spectroscopy. Two-dimensional (2D) NMR spectroscopy data can describe the inter-atomic distances between specific protons that are <5 Å apart in a protein of known sequence, that contains ≤ 250 amino acid residues (Voet and Voet 1995). NMR spectroscopy is the technique of choice to study the three-dimensional structure of proteins that have a molecular weight ≤ 30, 000 Da and do not form crystals. In addition to the average three-dimensional structure, NMR can provide information on a wide array of short-lived transient conformational states (Pelton and McLean 2000). A disadvantage of NMR spectroscopy is that the sample may have to be chemically modified to incorporate isotopes that give NMR signals such as ^{13}C and ^{15}N. The resulting one-dimensional (1D) and 2D NMR spectrum of a biological macromolecule can be complex and obtaining resonance assignments is non-trivial (Pelton and McLean 2000).

1.8.4 X-ray crystallography

X-ray crystallography is a spectroscopy technique based upon the measurement of emission, absorption, scattering fluorescence and diffraction of X-rays striking a crystal. These measurements provide information on the position of atoms within a crystal and allow the three-dimensional structure to be determined (Skoog and Leary 1992). Proteins that do not form crystals cannot be analysed by means of X-ray crystallography.

1.8.5 Mass spectrometry

Mass spectrometry, in particular ESI-MS, is the ideal tool to characterise heterogeneous populations of soluble protein species that differ in their *m/z* ratio. When coupled to IMS, MS analysis of proteins can provide information on minor species within a complex mixture whilst also offering the means to monitor the appearance and disappearance of individual species during a reaction. This feature is unique to MS and is therefore an advantage over the complementary classical biophysical techniques mentioned above. The small amounts of sample required, the ability to maintain non-covalent interactions in the gas-phase and the fast time-scale of data acquisition suggest that ESI-MS is a technique of choice to characterise protein and synthetic polymer structure.

1.9 Conserved solution-phase structure in the gas-phase

The question of whether or not the solution-phase structure is conserved in the gas-phase is a hotly debated topic. There is a common belief amongst structural biologists that the gas-phase structure cannot be equivalent to the solution-phase structure because, in the absence of solvent, all hydrophobic/hydrophilic interactions that stabilise the structure are removed. The wooden carving entitled "Sky and Water I" by the graphical artist Escher represents the solution-phase structure/gas-phase structure discussion (see Figure 1.10); where the fish represent that solution-phase structure and the birds resemble the equivalent gas-phase structure. In addition, it is debated whether the *in vitro* protein structure, that has been obtained without the presence of a crowding agent, is relevant to the protein's *in vivo* structure (Ellis 2001). Indeed, there is evidence to suggest that thermodynamic and kinetic properties of macromolecules are dramatically different in the cell than those experienced in an uncrowded solution in the test tube (Ellis 2001). To date, solution-phase NMR and solid-phase X-ray crystallography are the best tools a structural biologist has to observe the structure of a biological system. It is therefore assumed that the structures observed by means of these techniques are relevant to the biological form.

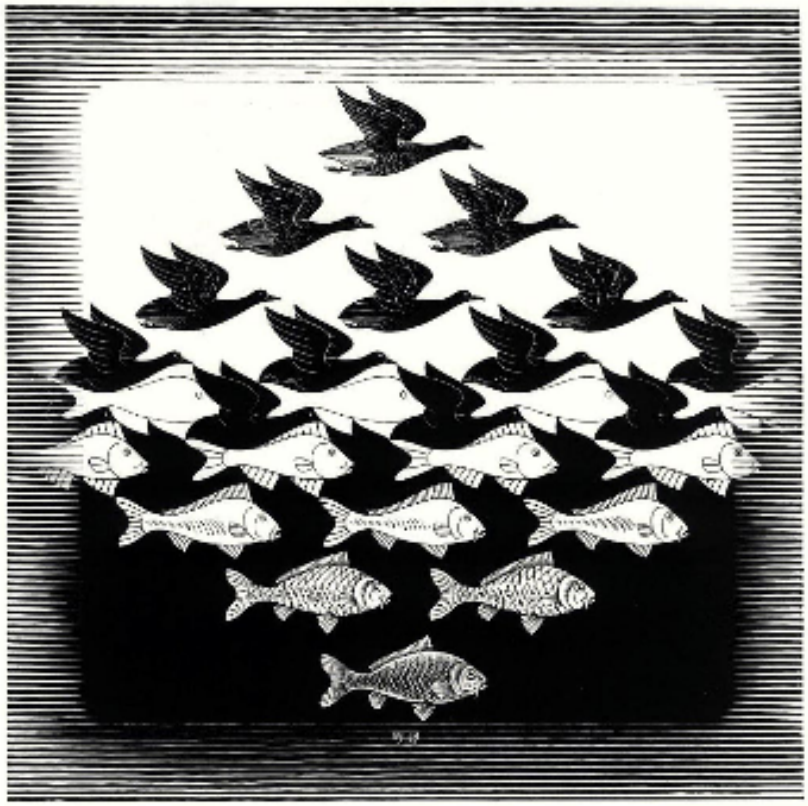

Figure 1.10: Wooden carving entitled "Sky and Water I" by M.C. Escher (1930). This carving is representative of the conserved solution-phase structure to the gas-phase structure debate.

A recent study showed that the published X-ray and NMR cross-sections could be related to the estimated collisional cross-section determined by means of IM-MS (Scarff, Thalassinos et al. 2008). This suggests that IM-MS is a technique that can be used to investigate the three-dimensional structure of a protein and that the results obtained are similar to those attained by means of X-ray crystallography and NMR spectroscopy (see section 1.7). It has been suggested that the gas-phase structure can be related to the solution phase structure (Shelimov, Clemmer *et al.* 1997b). The time-scale required for a gas-phase structure to rearrange, to account for its environment, is 30-60 ms (Badman, Myung *et al.* 2005). The IM-MS experiments, undertaken on the T-Wave device and many DCIM instruments, operate within a 15-30 ms time frame (Wyttenbach, Grabenauer *et al.* 2009). This limits the opportunity for the sample solution-phase structures to rearrange within the gas phase. Shelimov and co-workers observed that in the absence of solvent a protein's conformation

became more compact. They proposed that the intramolecular interactions present, in the protein structure, can make the protein pack more tightly and can cause the polar side chains to collapse onto the protein surface. It was reported that the gas-phase structure had a 10-16% decrease in the cross-section compared its solution phase counterpart (Shelimov, Clemmer *et al.* 1997b). It is therefore assumed that the gas-phase structure is similar to the observed *in vitro* solution-phase structure.

1.10 Aims and objectives

Ion mobility mass spectrometry is a relatively new area of research. The first T-Wave device, incorporated into the Synapt HDMS system, was developed by Waters, Manchester, UK and was commercially available in January 2007. Because of this new instrumentation, extensive method development was required to evaluate the potential of this technique as the new method of choice for characterising the three-dimensional structure of a compound.

The present project was focussed on using ion mobility mass spectrometry to characterise synthetic and natural macromolecules and to relate their structure to observed properties and function. Two different systems were studied; synthetic polymers and recombinant prion proteins. Investigations using synthetic polymers as the sample set were as part of a CASE Award project. These studies were conducted, in part, at the industrial site of Intertek MSG (formerly ICI Measurement Science Group), under the supervision of Dr. Tony Jackson. Structural studies of recombinant prion protein were partially funded by the department for environment, food and rural affairs (DEFRA). The aim of this work was to develop and evaluate a mass spectrometry-based method to distinguish between the prion isoforms and assess the technique's ability to be used as an ante-mortem diagnostic test.

The aims of this project were to:

1. Utilise the novel ion mobility mass spectrometry (IM-MS) technique to study the structure of the prion protein. Further elucidate the structural properties of normal cellular prion protein by means of IM-MS to distinguish this from a pathogenic scrapie form (Chapter 4). Characterise full-length prion protein and compare its structural properties to the truncated prion protein counterpart (Chapter 4). Compare and contrast the structural stability of various mammalian prion protein species. (Chapter 4).

2. Confirm or challenge previous characterisation of the metal binding sites in the prion protein by means of IM-MS. (Chapter 5).

3. Analyse the structural properties of synthetic polymer mixtures by means of gel permeation chromatography (GPC) coupled to NMR spectroscopy and IM-MS. (Chapter 7).

1.11 Research papers

The research involved in this project has already resulted in seven peer reviewed and published papers with others in preparation.

Hilton, G. R.[*], Thalassinos, K.[*], Grabenauer, M., Sanghera N., Slade, S. E., Wyttenbach T., Robinson P. J., Pinherio T. J. T., Scrivens, J. H and Bowers, M. T **Structural Analysis of Prion Proteins by means of Drift Cell and Travelling Wave Ion Mobility Mass Spectrometry.** Accepted. Journal of the American Society for Mass Spectrometry (2009).

[*]joint first author

Hilton, G. R., Thalassinos, K., Sanghera N., Blindauer C. A., Pinherio T. J. T., Gill A. C., and Scrivens, J. H. **Conformational Studies of Copper Coordination in Full-Length and N-terminal Fragments of Prion Proteins.** Submitted. Biochemistry (2009).

Thalassinos, K., Grabenauer, M., Slade, S. E., **Hilton, G. R**., Bowers, M. T. and Scrivens, J. H. **Characterisation of Phosphorylated Peptides Using Travelling Wave-Based and Drift Cell Ion Mobility Mass Spectrometry.** Analytical Chemistry (2009) 81: 248–254

Hilton, G. R., Jackson, A. T., Thalassinos, K. and Scrivens, J. H. **Structural Analysis of Synthetic Polymer Mixtures using Ion Mobility and Tandem Mass Spectrometry**. Analytical Chemistry (2008) 80: 9720–9725

Scarff, C. A., Thalassinos, K., **Hilton, G. R**. and Scrivens, J. H. **Travelling Wave Ion Mobility Mass Spectrometry Studies of Protein Structure: Biological Significance and Comparison with X-ray Crystallography and Nuclear Magnetic Resonance Spectroscopy Measurements.** Rapid Communications in Mass Spectrometry (2008) 22: 3297-3304

Williams, J. P., **Hilton, G. R**., Thalassinos, K., Jackson, A. T. and Scrivens, J. H. **The Rapid Characterisation of Poly(ethylene glycol) Oligomers using Desorption Electrospray Ionisation Tandem Mass Spectrometry Combined with Novel Product Ion Peak Assignment Software.** Rapid Communications in Mass Spectrometry (2007) 21: 1693-1704

Thalassinos, K., Jackson, A. T., Williams, J. P., **Hilton, G. R**., Slade, S. E. and Scrivens, J. H. **Novel Software for the Assignment of Peaks from Tandem Mass Spectrometry Spectra of Synthetic Polymers.** Journal of the American Society for Mass Spectrometry (2007) 18: 1324-1331

1.12 Conference Papers (Peer Reviewed)

Hilton, G. R., Thalassinos, K., Sanghera, N., Slade, S.E., Pinheiro, T.J.T. and Scrivens J.H. Travelling Wave Ion Mobility Mass Spectrometry-based Conformational Studies of Prion Protein - Comparison of Recombinant Truncated

Mouse and Syrian Hamster. 57th ASMS Conference on Mass Spectrometry & Allied Topics, Philadelphia, Pennsylvania (2009)

Scrivens, J. H. **Hilton, G. R.,** Thalassinos, K., Slade, S. E., Sanghera, N., Grabenauer M., Pinheiro, T. J., Bowers, M. T. Utilising Ion Mobility Mass Spectrometry as a Diagnostic Tool for Differentiating Conformational Variants of Prion Proteins. Joint Funders' Transmissible Spongiform Encephalopathies Workshop, University of Warwick, Warwick UK (2008)

Hilton, G. R., Thalassinos, K., Slade, S. E., Sanghera, N., Blindauer, C. A., Pinheiro, T. J., Bowers, M. T. and Scrivens, J. H. Travelling wave ion mobility mass spectrometry-based conformational studies of prion protein - effects of metal cation binding and buffer gas. BMSS 30th Annual Meeting University of York, York UK (2008)

Slade, S. E., Thalassinos, K., **Hilton, G. R.,** Pinheiro, T., Blindauer, C. A., Bowers, M. T. and Scrivens, J. Travelling wave ion mobility mass spectrometry-based conformational studies of prion protein – effects of metal cation binding and buffer gas. 56th ASMS Conference on Mass Spectrometry & Allied Topics Denver, Colorado (2008)

Thalassinos, K., **Hilton, G. R.,** Slade, S. E., Grabenauer, M., Bowers, M. T. and Scrivens, J. H. Improved characterisation of phosphorylated peptides utilising travelling wave-based and drift cell ion mobility mass spectrometry with molecular modelling studies. 56th ASMS Conference on Mass Spectrometry & Allied Topics Denver, Colorado (2008)

Thalassinos, K., **Hilton, G. R.,** Slade, S. E., Pinheiro, T. J., Blindauer, C. A. and Scrivens, J. H. Use of a travelling wave-based ion mobility mass spectrometry approach to study metal binding to the prion protein. ASMS Sanibel Conference on Ion Mobility and Related Emerging Areas Daytona Beach, Florida (2008)

Thalassinos, K., **Hilton, G. R.,** Slade, S. E., Sanghera, N., Robinson, P., Pinheiro, T. J. T., Bowers, M. T. and Scrivens, J. H. Use of a travelling wave based ion mobility

mass spectrometry approach to resolve prion proteins of varying conformations. Prion 2007 Edinburgh Scotland (2007)

Hilton, G. R., Williams, J. P., Holland, R. J., Thalassinos, K., Jackson, A. T. and Scrivens, J. H. Enhanced information content of direct desorption experiments utilising reactive DESI combined with ion mobility mass spectrometry and tandem mass spectrometry. 54th Annual American Society for Mass Spectrometry Conference Indianapolis, U.S.A. (2007)

1.13 Oral Presentations

Hilton, G. R., Jackson, A. T, Slade, S. E., Scrivens, J. H. Comparison of Electron Transfer Dissociation and Collision-Induced Dissociation Fragmentation of Multiply Charged Polyethers. 57th ASMS Conference on Mass Spectrometry & Allied Topics, Philadelphia, Pennsylvania (2009)

Hilton, G. R., Thalassinos, K., Slade, S. E., Sanghera, N., Blindauer, C. A., Pinheiro, T. J., Bowers, M. T. and Scrivens, J. H. Travelling wave ion mobility mass spectrometry-based conformational studies of prion protein - effects of metal cation binding and buffer gas. BMSS 30th Annual Meeting University of York, York UK (2008)

1.14 Invited Oral Presentations

Hilton, G. R., Thalassinos, K., Jackson, A. T, Scrivens, J. H. Microstructural studies of synthetic polymers. 42nd IUPAC Congress, Glasgow, Scotland, UK (2009)

1.15 References

Aston, F. W. (1919a). Neon. *Nature* **104**, 334.

Aston, F. W. (1919b). A positive-ray spectrograph. *Philosophical Magazine* **38**, 707-715.

Aston, F. W. (1920). Isotopes and Atomic Weights. *Nature* **105**, 617-619.

Badman, E. R., Myung, S. and Clemmer, D. E. (2005). Evidence for Unfolding and Refolding of Gas-Phase Cytochrome c Ions in a Paul Trap. *Journal-American Society for Mass Spectrometry* **16**, 1493-1497.

Barber, M., Bordoli, R. S., Sedgwick, R. D. and Tyler, A. N. (1981). Fast atom bombardment of solids (FAB): a new ion source for mass spectrometry. *Journal of the Chemical Society Chemical Communications* **7**, 325–327.

Biemann, K. (1992). Mass spectrometry of peptides and proteins. *Annual Review of Biochemistry* **61**, 977-1010.

Bluhm, B. K., Gillig, K. J. and Russell, D. H. (2000). Development of a Fourier-transform ion cyclotron resonance mass spectrometer-ion mobility spectrometer. *Review of Scientific Instruments* **71**, 4078-4086.

Cerda, B. A., Horn, D. M., Breuker, K., Carpenter, B. K. and McLafferty, F. W. (1999). Electron capture dissociation of multiply-charged oxygenated cations. A nonergodic process. *European Journal of Mass Spectrometry* **5**, 335-338.

Clemmer, D. E. http://www.indiana.edu/~clemmer/.

Clemmer, D. E. and Jarrold, M. F. (1997). Ion Mobility Measurements and their Applications to Clusters and Biomolecules. *Journal of Mass Spectrometry* **32**, 577-592.

Cohen, M. J. and Karasek, F. W. (1970). Plasma chromatrography TM-new dimension for gas chromatography and mass spectrometry. *Journal of Chromatographic Science* **8**, 330-337.

de Hoffmann, E. and Stroobant, V. (2007). Mass Spectrometry Principles and Applications. *John Wiley & Sons*.

El-Aneed, A., Cohen, A. and Banoub, J. (2009). Mass Spectrometry, Review of the Basics: Electrospray, MALDI, and Commonly Used Mass Analyzers. *Applied Spectroscopy Reviews* **44**, 210-230.

Ellis, R. J. (2001). Macromolecular crowding: obvious but underappreciated. *Trends Biochem Sci* **26**(10): 597-604.

Gidden, J., Bowers, M. T., Jackson, A. T. and Scrivens, J. H. (2002). Gas-phase conformations of cationized poly(styrene) oligomers. *Journal of the American Society for Mass Spectrometry* **13**, 499-505.

Gidden, J., Jackson, A. T., Scrivens, J. H. and Bowers, M. T. (1999). Gas phase conformations of synthetic polymers: poly (methyl methacrylate) oligomers cationized by sodium ions. *International Journal of Mass Spectrometry* **188**, 121-130.

Gidden, J., Wyttenbach, T., Batka, J. J., Weis, P., Bowers, M. T., Jackson, A. T. and Scrivens, J. H. (1999). Poly (ethylene terephthalate) oligomers cationized by alkali ions: structures, energetics, and their effect on mass spectra and the matrix-assisted laser desorption/ionization process. *Journal of the American Society for Mass Spectrometry* **10**, 883-895.

Gidden, J., Wyttenbach, T., Jackson, A. T., Scrivens, J. H. and Bowers, M. T. (2000). Gas-Phase Conformations of Synthetic Polymers: Poly(ethylene glycol), Poly(propylene glycol), and Poly(tetramethylene glycol). *Journal of the American Chemical Society* **122**, 4692-4699.

Goormaghtigh, E., Cabiaux, V. and Ruysschaert, J. M. (1990). Secondary structure and dosage of soluble and membrane proteins by attenuated total reflection Fourier-transform infrared spectroscopy on hydrated films. *European Journal of Biochemistry* **193**, 409-20.

Jarrold, M. F. (1998). Unfolding, Refolding, and Hydration of Proteins in the Gas Phase. *Accounts of Chemical Research* **32**, 360-367.

Jennings, K. R. (1968). Collision-induced decompositions of aromatic molecular ions. *International Journal of Mass Spectrometry and Ion Physics* **1**, 227-235.

Jennings, K. R. (2009). The Foundations of Mass Spectrometry in Europe - The First Fifty Years, University of Warwick.

Kaleta, D. T. and Jarrold, M. F. (2003). Noncovalent Interactions between Unsolvated Peptides: Dissociation of Helical and Globular Peptide Complexes. *The Journal of Physical Chemistry B* **107**, 14529-14536.

Karas, M. and Hillenkamp, F. (1988). Laser desorption ionization of proteins with molecular masses exceeding 10,000 daltons. *Analytical Chemistry* **60**, 2299-2301.

Karas, M., M. Glückmann and J. Schäfer (2000). Ionization in matrix-assisted laser desorption/ionization: singly charged molecular ions are the lucky survivors.

Journal of Mass Spectrometry **35**(1): 1-12.**Karasek, F. W.** (1974). Plasma chromatography. *Analytical Chemistry* **46**, 710A-720a.

Kebarle, P. (2000). A brief overview of the present status of the mechanisms involved in electrospray mass spectrometry. *Journal of Mass Spectrometry* **35**, 804-817.

Kelly, S. M., Jess, T. J. and Price, N. C. (2005). How to study proteins by circular dichroism. *Biochimia et Biophysica Acta* **1751**, 119-39.

Leary, J. A., Schenauer, M. R., Stefanescu, R., Andaya, A., Ruotolo, B. T., Robinson, C. V., Thalassinos, K., Scrivens, J. H., Sokabe, M. and Hershey, J. W. B. (2009). Methodology for Measuring Conformation of Solvent-Disrupted Protein Subunits using T-WAVE Ion Mobility MS: An Investigation into Eukaryotic Initiation Factors. *Journal of the American Society for Mass Spectrometry* **20**, 1699-1706.

Mamyrin, B. A., Karataev, V. L., Shmikk, D. V. and V.A., Z. (1973). The mass reflectron, a new non-magnetic time-of-flight spectrometer with high resolution. *Soviet Physics JETP* **37**, 45-48.

Mason, E. A. and McDaniel, E. W. (1988). Transport properities of ions in gases. *New York: Wiley*.

McCullough, B. J., Kalapothakis, J., Eastwood, H., Kemper, P., MacMillan, D., Taylor, K., Dorin, J. and Barran, P. E. (2008). Development of an Ion Mobility Quadrupole Time of Flight Mass Spectrometer. *Analytical Chemistry* **80**, 6336-6344.

McLafferty, F. W. and Bryce, T. A. (1967). Metastable-Ion characteristics: Characterization of Isomeric molecules. *Chemical Communications*1215.

Mehlhorn, I., Groth, D., Stockel, J., Moffat, B., Reilly, D., Yansura, D., Willett, W. S., Baldwin, M., Fletterick, R., Cohen, F. E., Vandlen, R., Henner, D. and Prusiner, S. B. (1996). High-level expression and characterization of a purified 142-residue polypeptide of the prion protein. *Biochemistry* **35**, 5528-37.

Paul, W. and Steinwedel, H. (1953). Ein neues Massenspektrometer ohne Magnetfeld (A new mass spectrometer without magnetic field). *Zeitschrift fur Naturforschung*448-450.

Pelton, J. T. and McLean, L. R. (2000). Spectroscopic Methods for Analysis of Protein Secondary Structure. *Analytical Biochemistry* **277**, 167-176.

Pringle, S. D., Giles, K., Wildgoose, J. L., Williams, J. P., Slade, S. E., Thalassinos, K., Bateman, R. H., Bowers, M. T. and Scrivens, J. H. (2007a). *International Journal of Mass Spectrometry* **261**, 1.

Pringle, S. D., Giles, K., Wildgoose, J. L., Williams, J. P., Slade, S. E., Thalassinos, K., Bateman, R. H., Bowers, M. T. and Scrivens, J. H. (2007b). An investigation of the mobility separation of some peptide and protein ions using a new hybrid quadrupole/travelling wave IMS/oa-ToF instrument. *International Journal of Mass Spectrometry* **261**, 1-12.

Roepstorff, P. and Fohlman, J. (1984). Proposal for a common nomenclature for sequence ions in mass spectra of peptides. *Biomedical Mass Spectrometry* **11**, 601.

Ruotolo, B. T., Benesch, J. L., Sandercock, A. M., Hyung, S. J. and Robinson, C. V. (2008). Ion mobility-mass spectrometry analysis of large protein complexes. *Nature Protocol* **3**, 1139-52.

Scarff, C. A., Thalassinos, K., Hilton, G. R. and Scrivens, J. H. (2008). Travelling wave ion mobility mass spectrometry studies of protein structure: biological significance and comparison with X-ray crystallography and nuclear magnetic resonance spectroscopy measurements. *Rapid Communications in Mass Spectrometry* **22**, 3297-3304.

Shelimov, K. B., Clemmer, D. E., Hudgins, R. R. and Jarrold, M. F. (1997a). Protein Structure in Vacuo: Gas-Phase Conformations of BPTI and Cytochrome c. *Journal of the American Chemical Society* **119**, 2240-2248.

Shelimov, K. B., Clemmer, D. E., Hudgins, R. R. and Jarrold, M. F. (1997b). Protein Structure in Vacuo: Gas-Phase Conformations of BPTI and Cytochrome c. *Journal- American Chemical Society* **119**, 2240-2248.

Shvartsburg, A. A. and Smith, R. D. (2008). Fundamentals of Traveling Wave Ion Mobility Spectrometry. *Analytical Chemistry* **80**, 9689-9699.

Skoog, D. A. and Leary, J. J. (1992). Principles of instrumental analysis. *Saunders College Publishing*.

Srebalus, C. A., Li, J., Marshall, W. S. and Clemmer, D. E. (1999). Gas-Phase Separations of Electrosprayed Peptide Libraries. *Analytical Chemistry* **71**, 3918-3927.

Syka, J. E., Coon, J. J., Schroeder, M. J., Shabanowitz, J. and Hunt, D. F. (2004). Peptide and protein sequence analysis by electron transfer dissociation

mass spectrometry. *Proceedings of the Natational Academy of Sciences U S A* **101**, 9528-33.

Thalassinos, K., Grabenauer, M., Slade, S. E., Hilton, G. R., Bowers, M. T. and Scrivens, J. H. (2009). Characterization of Phosphorylated Peptides Using Traveling Wave-Based and Drift Cell Ion Mobility Mass Spectrometry. *Analytical Chemistry* **81**, 248-254.

Thalassinos, K. and Scrivens, J. H. (2009). Applications of Traveling Wave Ion Mobility Mass Spectrometry. *CRC Press*.

Thalassinos, K., Slade, S. E., Jennings, K. R., Scrivens, J. H., Giles, K., Wildgoose, J., Hoyes, J., Bateman, R. H. and Bowers, M. T. (2004). Ion mobility mass spectrometry of proteins in a modified commercial mass spectrometer. *International Journal of Mass Spectrometry* **236**, 55-63.

Thomson, J. J. (1899). On the Masses of the Ions in Gases at Low Pressures. *Philosophical Magazine* **48**, 547-567.

Thomson, J. J. (1911). Rays of Positive Electricity. *Philosophical Magazine* **6**, 752-67.

Valentine, S. J., Anderson, J. G., Ellington, A. D. and Clemmer, D. E. (1997). Disulfide-Intact and -Reduced Lysozyme in the Gas Phase: Conformations and Pathways of Folding and Unfolding. *The Journal of Physical Chemistry B* **101**, 3891-3900.

Valentine, S. J., Counterman, A. E. and Clemmer, D. E. (1999). A database of 660 peptide ion cross sections: use of intrinsic size parameters for bona fide predictions of cross sections. *Journal of the American Society for Mass Spectrometry* **10**, 1188-1211.

Vestal, M. L., Juhasz, P. and Martin, S. A. (1995). Delayed Extraction Matrix-assisted Laser Desorption Time-of-flight Mass Spectrometry. *Rapid Communications In Mass Spectrometry* **9**, 1044.

Voet, D. and Voet, J. G. (1995). Biochemistry. *John Wiley & Sons*

von Helden, G., Hsu, M.-T., Kemper, P. R. and Bowers, M. T. (1991). Structures of carbon cluster ions from 3 to 60 atoms: Linears to rings to fullerenes. *The Journal of Chemical Physics* **95**, 3835-3837.

von Helden, G., Hsu, M. T., Gotts, N. and Bowers, M. T. (2002). Carbon cluster cations with up to 84 atoms: structures, formation mechanism, and reactivity. *The Journal of Physical Chemistry* **97**, 8182-8192.

von Helden, G., Wyttenbach, T. and Bowers, M. T. (1995). Inclusion of a MALDI ion source in the ion chromatography technique: conformational information on polymer and biomolecular ions. *International Journal of Mass Spectrometry and Ion Processes* **146-147**, 349-364.

Wiley, W. C. and McLaren, I. H. (1955). Time-of-Flight Mass Spectrometer with Improved resolution. *Review of Scientific Instruments* **26**, 1150-1157.

Wiza, J. L. (1979). Microchannel plate detectors. *Nuclear Instruments and Methods* **162**, 587-601.

Wyttenbach, T., Grabenauer, M., Thalassinos, K., Scrivens J. H and Bowers, M. T. (2009). The Effect of Calcium Ions and Peptide Ligands on the Stability of the Calmodulin Dumbbell Structure. *Submitted*.

Wyttenbach, T., Helden, G. v., Batka, J. J. J., Carlat, D. and Bowers, M. T. (1997). Effect of the long-range potential on ion mobility measurements. *Journal of the American Society for Mass Spectrometry* **8**, 275-282.

Wyttenbach, T., von Helden, G. and Bowers, M. T. (1996). Gas-Phase Conformation of Biological Molecules: Bradykinin. *Journal of the American Chemical Society* **118**, 8355-8364.

Zenobi, R. and Knochenmuss, R. (1998). Ion formation in MALDI mass spectrometry. *Mass Spectrometry Reviews* **17**, 337-366.

Chapter 2
Introduction to the Prion Protein

2.1 Transmissible spongiform encephalopathies

Transmissible spongiform encephalopathies (TSEs), also known as prion diseases, are a class of fatal, infectious neurodegenerative diseases that affect both humans and animals. Examples of prion diseases include bovine spongiform encephalopathy (BSE) in cattle, chronic wasting disease (CWD) in deer, scrapie in sheep, and kuru and Creutzfeldt-Jakob disease (CJD) in humans (Collinge and Palmer 1992).

The neurodegenerative disease kuru was discovered in the members of the Fore tribe, Papua-New Guinea in the late 1950s. As part of their funeral ceremonies the tribe practised ritualistic cannibalism to pay their respects to the dead and the spiritual world. In particular, women and children ate the internal viscera including the central nervous system (CNS) of the deceased relative whilst the men consumed less infectious material such as the skeletal muscle. As a consequence of this ritual the tribal people started to develop pronounced symptoms such as tremors, fevers and cerebellar ataxia until death occurred months later. Unable to explain these incidents the Fore tribe concluded that this was the work of sorcery; the physician Carleton Gajdusek and co-workers, however, believed the symptoms were indicative of a spongiform encephalopathy, now known as kuru (Gajdusek 1977). It was observed that the neuropathology of kuru resembled scrapie and CJD (Hadlow 1959a; Klatzo, Gajdusek *et al.* 1959) and that CJD could be transmitted after intracerebral inoculation of human brain extracts into apes (Hadlow 1959b). The agent that linked these diseases was at the time still unknown.

TSEs came to prominence in the 1980s-90s when an epidemic of BSE in the UK caused the death of many hundreds of cattle (Brown, Will et al. 2001; Dabaghian, Mortimer et al. 2004; Khamsi 2006). In the 1980s the UK government changed the rendering and livestock feeding practices to allow protein-rich nutritional supplements, from rendered TSE infected animals, to be fed to healthy cattle. This change in regulation resulted in a rapid amplification of BSE to epidemic proportions in the UK cattle population and led to the introduction of infected meat-products into the human food-chain. A new TSE, designated variant CJD (v-CJD), subsequently

appeared in humans and was linked to the consumption of BSE-infected material from cattle (Collinge 1999). The social and economic impact of this epidemic and evidence that another epidemic could occur (d'Aignaux, Cousens et al. 2001; Valleron, Boelle et al. 2001) has led to a new urgency in the study of TSE diseases.

2.2 Discovery of PrP

It was initially believed that a "slow virus" was the cause of kuru and scrapie because of the extended incubation period for both of these diseases. The transmissibility of kuru was reported in 1966 when the passage of the disease was observed in chimpanzee models (Gajdusek, Gibbs et al. 1966) and later studies showed that CJD could also be transmitted to chimpanzees following intracerebral inoculation (Gibbs, Gajdusek et al. 1968). The cause of these diseases was still unknown when it was noted that scrapie, kuru and CJD could cause death to the host without provoking an immune system response to a "foreign agent". Investigations into the scrapie reagent showed that it was extremely resistant to ionising and ultraviolet (UV) radiation (Alper, Cramp *et al.* 1967; Alper, Haig *et al.* 1966; Latarjet, Muel *et al.* 1970). This observation stimulated numerous hypotheses concerning the nature of the infectious agent ranging from a small DNA virus to a polysaccharide but it was eventually shown to be a protein (Prusiner 1999).

2.3 What is a prion?

Stanley Prusiner was awarded the Nobel Prize for Physiology or Medicine in 1997 for his discovery of prions – a new biological principle of infection. He describes prions as unprecedented infectious pathogens that cause a group of invariably fatal neurodegenerative diseases by means of an entirely novel mechanism (Prusiner 1998). Although the precise molecular details of the mechanism are not clearly known, it is thought that the key event in prion diseases is the conversion of the normal cellular form of the prion protein, PrP^{C} to a pathogenic scrapie form (PrP^{Sc}). Prion diseases may be present as genetic, infectious or sporadic disorders.

2.3.1 Is a prion a virus?

Prions and viruses share many similar features; both can stimulate a process to produce more pathogen. Both can cause disease by accumulating in an infected host and both can exist as different strains. In contrast to viruses, which are encoded by a viral genome, prions lack a nucleic acid genome and are composed of an alternative isoform of a cellular protein. Prions are nonimmunogenic because the host is tolerant to PrP^{Sc} because of its exposure to the native PrP^{C} (Prusiner 1999; Williamson, Peretz *et al.* 1996). The same cannot be said for viruses whose presence as a foreign body in the host usually provokes a reaction from the immune system. Unlike viruses, prions do not have a consistent structure and can exist in multiple molecular forms. Viruses, however, usually have a single molecular form which can vary by having distinct ultra-structural morphologies. It is believed that different strains of the prion occur through conformational changes in PrP^{Sc} while viral strains arise from distinct differences in the nucleic acid sequence. Investigations have been conducted to elucidate if nucleic acids are present in the infectious material (Kellings, Meyer et al. 1992; Kellings, Prusiner et al. 1994; Manuelidis, Sklaviadis et al. 1995) but to date no evidence has been found to suggest that the prion is a type of virus. Experiments which altered or destroyed the nucleic acids/viruses, thought to be responsible for the prion disease, retained scrapie infectivity (Prusiner 1982). In contrast, infectivity was dramatically reduced using methods that modified or destroyed the protein structure (Gabizon, McKinley et al. 1988; Soto and Castilla 2004). These observations led to the "protein-only" hypothesis, which states that the scrapie causing agent is devoid of nucleic acid and seems to be composed exclusively of a modified protein (Prusiner 1982).

Genetic studies have shown that knockout mice lacking the PrP gene ($Prnp^{0/0}$) were resistant to scrapie infection. These mice developed normally. They were unable to propagate new infectious particles and showed no sign of scrapie clinical symptoms (Bueler, Fischer et al. 1992). Once the gene encoding PrP was restored the mice became susceptible to PrP disease again. Other evidence to support the "protein-only" hypothesis was the successful propagation of infectivity in neuroblastoma cells (Race, Fadness *et al.* 1987; Rubenstein, Carp *et al.* 1984) in which cells containing PrP^{C} were chronically infected with brain homogenate and infectivity was monitored

for several months. Since the absence of PrP^C expression does not provoke disease, it is likely that scrapie-causing diseases are a consequence of PrP^{Sc} accumulation rather than inhibition of PrP^C function (Bueler, Fischer et al. 1992).

2.4 Human TSE diseases

2.4.1 Inherited

Familial CJD, Gerstmann-Sträussler-Scheinker (GSS) syndrome and fatal familiar insomnia (FFI) are the three dominant genetically determined phenotypes of inherited TSEs. Familial prion diseases are inherited in an autosomal dominant manner and are linked to mutations in the human prion protein (*PRNP*) gene (Crowther 2002). Several hypotheses have been outlined which suggest that mutations in *PRNP* can destabilise the PrP^C structure and could facilitate the conversion of PrP^C to PrP^{Sc} (Cohen, Pan *et al.* 1994; Harrison, Bamborough *et al.* 1997; Huang, Gabriel *et al.* 1994). Up to 14% of familiar CJD patients have died from the disease due to mutations in *PRNP* (Windl, Dempster et al. 1996). These mutations can vary from several point mutations to insertions in the octarepeat region with inconclusive evidence, from neuropathology studies, to connect specific mutations to the corresponding disease phenotype. The mutation E200K has been identified as a contributing factor to the high incidence of familial CJD in Slovakia, Poland, Germany, Tunisia, Greece, Libya, and Chile and within certain ethnic sub-groups (Goldfarb, Brown et al. 1991).

Slow progressive cerebellar ataxia is a characteristic clinical symptom of GSS syndrome and typically begins when a patient is 50-60 years in age. Unlike familial CJD, a common *PRNP* mutation, P102L, has been described and found to be reproducibly associated with transmission of GSS in up to 40% of cases (Hsiao, Baker et al. 1989). In more recent years a variety of other GSS *PRNP* mutations and their associated phenotypes have been discovered, however, P102L and G131V mutations are still believed to account for the majority of incidents (Collins, McLean et al. 2001).

2.4.2 Sporadic

Sporadic CJD accounts for the majority of TSE disease cases in humans to date with a worldwide incidence rate of 1 in every 1,000,000 people per year (Chesebro 2003). Data from the United Kingdom CJD surveillance unit, over a 19 year period, indicates that there are no links in the incidence rate of sporadic CJD with any other forms of the disease (see Figure 2.1). The cause of sporadic CJD remains uncertain as mutations in the *PRNP* gene have not been found. One theory suggests that a somatic mutation occurs in *PRNP* which could stimulate a rare spontaneous conversion of PrP^{C}, present in the brain, to PrP^{Sc} which would result in disease (Prusiner 1998). This non-mutating spontaneous conversion theory could explain the different clinical symptoms and brain histology observed in patients with sporadic CJD to those with other forms of the disease (Will, Ironside et al. 1996). Alternative theories suggest that sporadic CJD results from a switch to a neurovirulence in a silent ubiquitous strain of the CJD agent (Kimberlin 1990) or that the normally harmless form of PrP^{C} can actually be harmful in a small number of genetically susceptible individuals (Collee and Bradley 1997).

2.4.3 Iatrogenic

Iatrogenic CJD has arisen as a complication of neurosurgery usually as a result of inadequate sterilisation of neurological surgical electrodes or from instrumentation that has been previously contaminated (Soto 2004). It has also been associated with treatments involving the transmission of human-cadaveric pituitary-derived growth hormone and gonadotrophins, dura mater and corneal grafting (Soto 2004). In 2004 a novel case of preclinical v-CJD was reported in a patient who had received a blood transfusion from an asympotomatic carrier of v-CJD. The blood donor later developed and died from v-CJD with the recipient of the blood transfusion also showing clinical symptoms of v-CJD before their death (from a non-neurological disorder) five years later (Peden, Head et al. 2004). There is other evidence to suggest that v-CJD can be transmitted via blood transfusion. Houston *et al.* showed that blood donated from a pre-symptomatic BSE infected sheep into other healthy sheep could induce BSE infection (Houston, Foster et al. 2000). Further studies also suggest that blood taken from animals during the pre-clinical and clinical stages of

BSE infection can transmit the infection through blood transfusion (Hunter, Foster et al. 2002). This has raised concerns over the safeguarding of the blood supply, with potentially many asympotomatic carriers unknowingly donating blood. The development of a non-invasive highly sensitive preclinical diagnostic test for prion diseases is highly desirable not only to stop the spread of the disease but may also lead to better clinical outcomes in the future.

Kuru was the first human TSE disease shown to be caused by the prion protein (Gajdusek 1977). In the 1960s, as a consequence of their ritualistic cannibalism, kuru reached epidemic proportions in the members of the Fore tribe of Papua-New Guinea. It was found that the disease was more prevalent in women and children (Klatzo, Gajdusek et al. 1959) and this was later concluded to be due to their preferred consumption of the brain and CNS from the deceased relative. The cessation of the Fore tribe's cannibalistic rituals in the 1950s decreased the incident rate of historic kuru, some cases have been reported, however, in older tribal members (≥40 years of age) of the contemporary Fore survivors (Mead, Stumpf et al. 2003). Factors contributing to the later onset of the disease have been associated with the older age at exposure to the infectious material and the concentration of prion agent present in the ingested material. It has also been noted that methionine homozygosity at codon 129 of *PRNP* can increase the risk of contracting kuru at a younger age with homozygous sufferers tending to have shorter incubation and gestation periods of the disease than their heterozygote counterparts.(Cervenakova, Goldfarb et al. 1998; Lee, Brown et al. 2001).

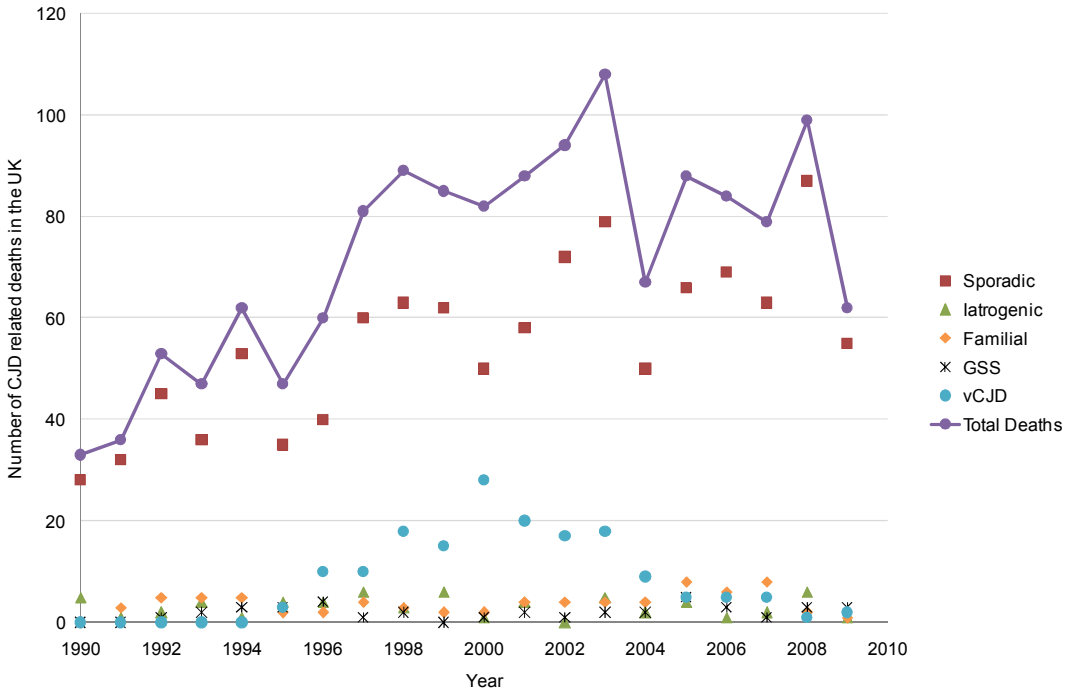

Figure 2.1: The number of people referred to the National Creutzfeldt-Jakob disease surveillance unit which have confirmed or suspected cases of CJD in Britain since 1990. Taken from (CJD) last updated 7th December 2009.

2.4.4 Variant CJD

In 1996 the first case of new variant-CJD (v-CJD) was reported in Britain following the population's exposure to BSE-infected food-stuffs (Will, Ironside et al. 1996). In contrast to sporadic CJD, patients with v-CJD are much younger in age at the time of death (median age at death 65 years and 29 years old respectively) (Will, Ironside et al. 1996) and experience distinctly different psychiatric symptoms to that of sporadic CJD, such as dysphoria, anxiety, insomnia and withdrawal (Spencer, Knight et al. 2002). After the initial presentation of psychiatric or behavioural symptoms, the gestation period of v-CJD can be several months or years. The incidence rate of v-CJD in the UK has been on the decline since 2000 (see Figure 2.1) scientists believe, however, that a possible new epidemic could occur in the next 10-15 years (see Figure 2.2). To date, all cases of v-CJD have been in patients who are methionine homozygotes at codon 129, the only exception being a heterozygous (methionine/valine (MV)) patient diagnosed with preclinical v-CJD in 2004 (Peden, Head et al. 2004). This finding has major implications for future estimations of

numbers of v-CJD cases in the UK, as the heterozygote genotype constitutes the largest genetic subgroup in the population (Hilton, Ghani et al. 2004).

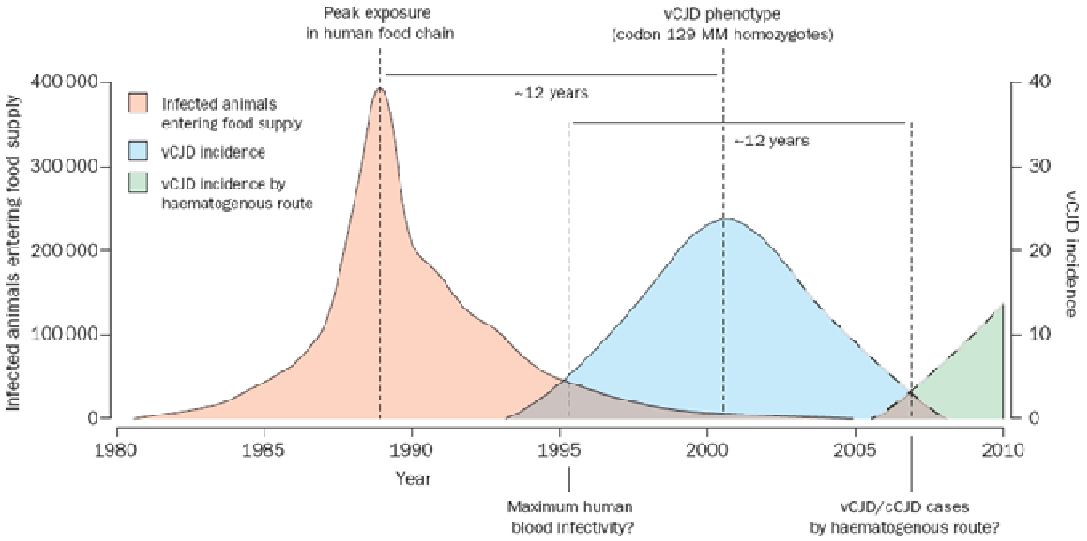

Figure 2.2: Profile of BSE-infected cattle in the British human food chain (red) and the subsequent predicted profile of v-CJD (blue and green). Taken from (Collins, Lawson et al. 2004).

2.5 Codon 129

It has been postulated that a polymorphism at codon 129 can determine a patient's susceptibility to sporadic, iatrogenic and variant forms of CJD (Chesebro 2003). Experiments were conducted in which transgenic mice carrying three different genotypes of human codon 129, MM, MV and VV, were inoculated with v-CJD. The results of these experiments suggested that the greatest transmission efficiency of the disease occurred in HuMM mice (Bishop, Hart et al. 2006). This implies that homozygosity for methionine at codon 129 could lead to an earlier onset of TSE-related pathological features and clinical disease compared to their heterozygous genotype counterparts. It has also been suggested that this heterozygous subgroup could also have a different incubation period after exposure to either primary infection of the BSE agent or as a secondary infection by blood transfusion (Peden, Head et al. 2004). Codon 129 MV and VV individuals currently constitute 51% and 11% of the UK population respectively (Hilton, Ghani et al. 2004) and the

potentially prolonged incubation period in these individuals, who could be asymptomatic carriers of v-CJD, makes predicting a new v-CJD epidemic a difficult task (d'Aignaux, Cousens *et al.* 2001; Mead, Poulter *et al.* 2009; Valleron, Boelle *et al.* 2001).

2.6 Protein conformational disorders

Protein misfolding, aggregation and accumulation in the brain, to instigate neuronal apoptosis, are common causes of a diverse range of neurodegenerative diseases. During the onset of neurodegenerative diseases a patient's skilled movements, emotions, cognition, memory and numerous other abilities can all be affected (Martin 1999). Protein conformational disorders are attributed to many common neurodegenerative diseases including Alzheimer's disease, Parkinson's disease, Huntington's disease (and related polyglutamine disorders including several forms of spinocerebellar ataxia), TSEs and amyotrophic lateral sclerosis (Soto 2003). Although all of these diseases have distinct clinical symptoms and disease progression they also share similarities. The onset of the majority of these neurodegenerative diseases appears later in life (usually $\geq$ 50 years old). Most can be sporadic and/or inherited, their pathology is characterised by neuronal loss and synaptic abnormalities (Martin 1999) and there is recent evidence to suggest that the accumulation of aggregates formed by the different proteins take the same molecular form (Soto 2003) (see Figure 2.3). The mechanism of protein misfolding for all these diseases is still not fully understood however, and structural studies have shown that in general it is a self propagating conformational change from a predominantly α-helical state to a β-sheet rich isoform. Kinetic studies have also revealed that the aggregation of Aβ (Alzheimer's disease), α-synuclein (Parkinson's disease), huntingtin (Huntington's disease) and PrP involve systematic amyloidosis following a seeding/nucleation mechanism, which can act as a template for further oligomer/aggregate growth. The proposed similarities in the molecular pathways, protein misfolding, aggregation and neuronal death have given hope that a common therapeutic strategy to treat all of these illnesses can be developed (Soto 2003).

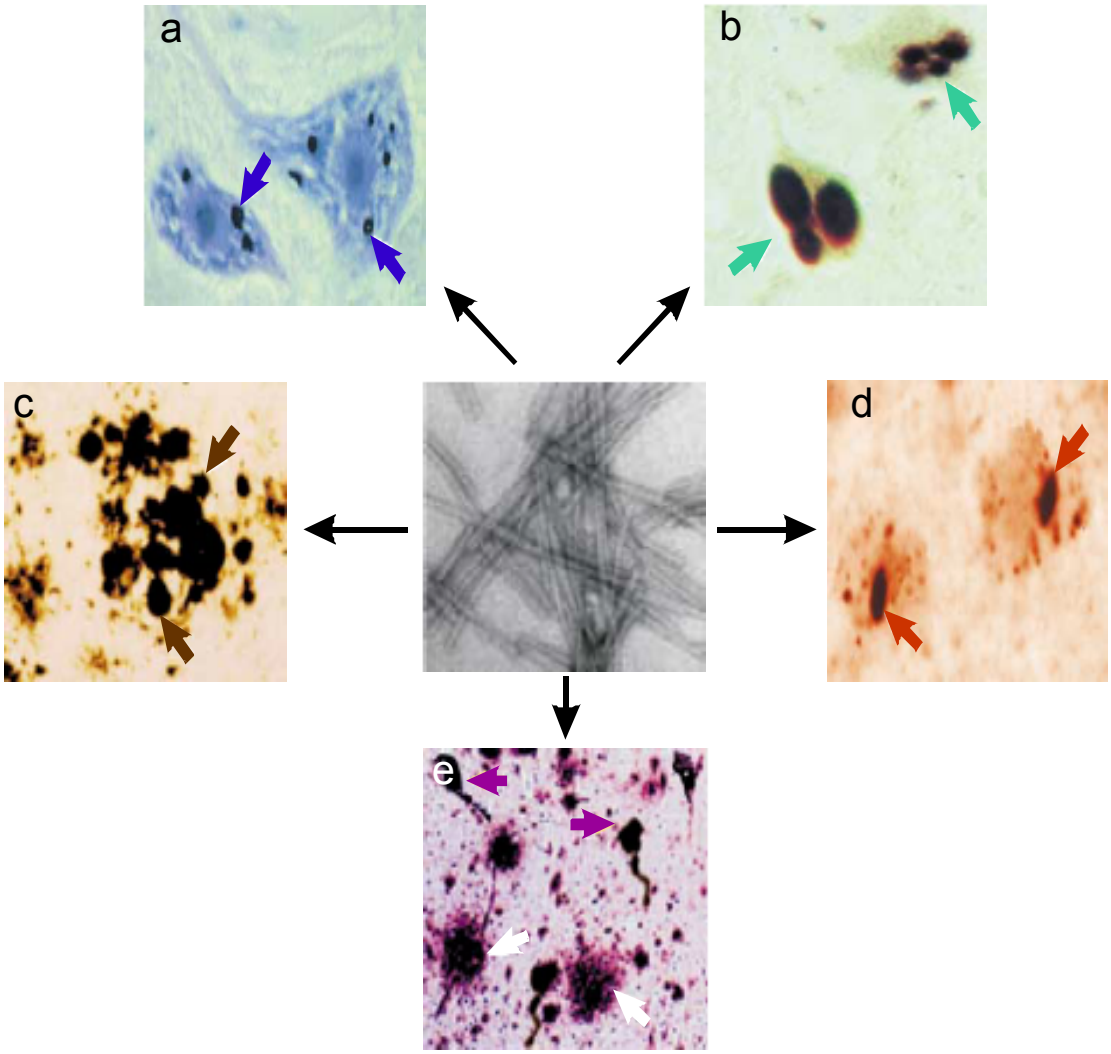

Figure 2.3: Images of cerebral aggregates in neurodegenerative diseases. Different protein compositions show similar ultrastructure of deposits and appear to be mainly composed of a network of fibriluar polymers. (a and b), Intracytoplasmic aggregates are typically present in neurons of people affected by (a) amyotropic lateral sclerosis (b) and Parkinson's disease. (c), Extracellular prion amyloid plaques are located in different brain regions and are present in some cases of transmissible spongiform encephalopathy. (d), Intranuclear inclusions of huntingtin are observed in Huntington's disease. (e), Extracellular amyloid plaques (white arrows) and intracytoplasmic neurofibrillary tangles (purple arrows) are the pathological signature of Alzheimer's disease. Adapted from (Soto 2003).

2.6.1 Parkinson's disease

There is evidence to suggest that α-synuclein behaves like a prion protein and that Parkinson's disease (PD) could be classed as a prion disorder (Desplats, Lee et al. 2009; Olanow and Prusiner 2009) (see Figure 2.4). Parkinson's disease is an age-related neurodegenerative disease affecting approximately one in 500 people in the UK and 4 million people worldwide per year (Parkinsons). The disease is characterised by a loss of dopamine neurons and the appearance of inclusion bodies in the Lewy bodies of the brain. The cause of cell death and the appearance of these inclusion bodies in PD patients is not known, but there are suggestions that proteolytic stress followed by the accumulation of misfolded proteins, in particular α-synuclein, could be a major contributing factor (McNaught, Olanow et al. 2001). α-Synuclein is a 140 amino acid synaptic protein which can adopt an α-helical conformation when bound to a cell membrane. At increased concentrations of α-synuclein the protein can misfold to form a β-sheet rich conformational isoform. These β-sheet rich structures readily polymerise, which can interfere with proteasomal and lysosomal functions (Cuervo, Stefanis *et al.* 2004; Snyder, Mensah *et al.* 2003), and further accumulation of the protein can lead to the formation of fibrils (see Figure 2.4b). Protein aggregates formed in both prion and Parkinson's disease can promote the misfolding of wild-type proteins in unaffected cells and can extend the disease process. It has been observed that α-synuclein spreads in a sequential manner, beginning in the lower brainstem dorsal motor nucleus and extending to the upper brainstem nuclei and cerebral hemispheres (Braak, Del Tredici et al. 2003), and the proposed similarity to the prion protein mechanism (see Figure 2.4) could account for the PD pathological findings. It has therefore been speculated that PD is a prion protein disease resulting from an increased production of α-synuclein which in turn promotes a conformational change in the protein to form toxic oligomers, aggregates and eventually leads to cell death (Olanow and Prusiner 2009).

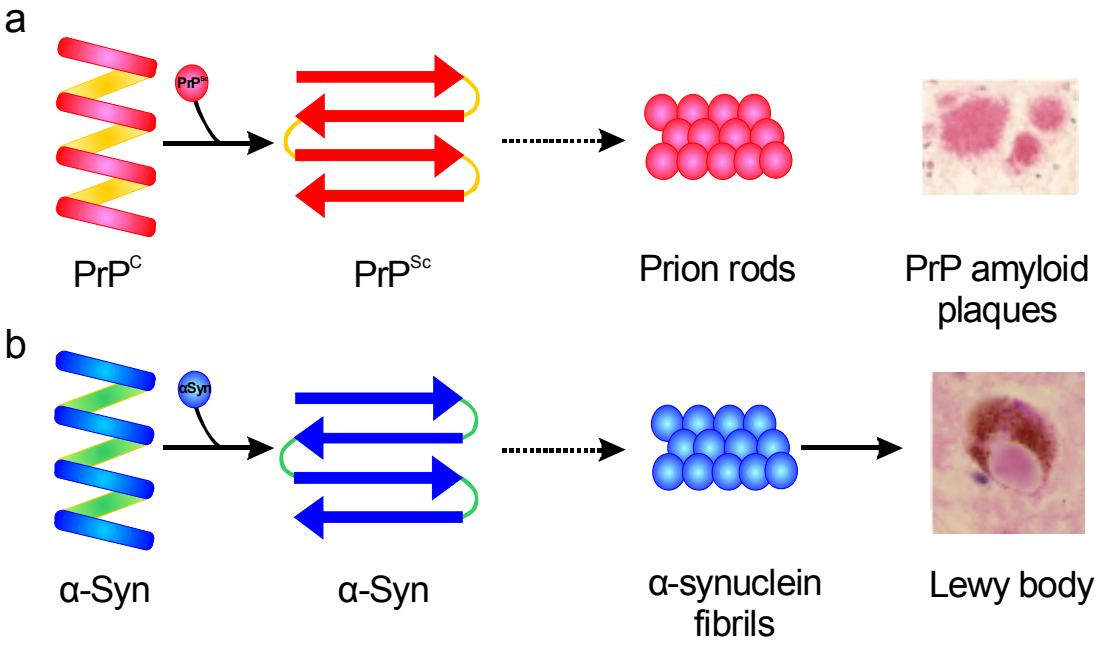

Figure 2.4: Schematic representation illustrating the similarities between PrP in prion diseases and α-synuclein protein in Parkinson's disease. (a), PrP^{C} is predominantly α-helical and resides on the surface of cell membranes. It undergoes a misfolding process to form a β-sheet rich conformation. These β-sheet rich isoforms can aggregate into rods that coalesce to form amyloid plaques. (b), α-Synuclein adopts a largely α-helical conformation when bound to a cell membrane. It can undergo a misfolding event to create a β-sheet rich conformational isoform. The β-sheet rich proteins can polymerise into fibrils which are associated to the formation of Lewy bodies. Adapted from (Olanow and Prusiner 2009).

2.7 Properties of PrP

The PrP isoforms have very different biochemical properties and the ability to distinguish between these could help in the identification of infectious prion disorders.

- PrP^{C} and PrP^{Sc} have an identical amino acid primary sequence with no evidence to suggest modifications that could differentiate between PrP^{C} and PrP^{Sc}.
- PrP^{C} is readily soluble in non-denaturing conditions whereas PrP^{Sc} is insoluble in detergents (Meyer, McKinley et al. 1986).
- PrP^{C} is fully degraded in the presence of the common protease, proteinase K. In contrast PrP^{Sc} is partially resistant to proteinase K digestion with cleavage just after the octarepeat region to form the truncated fragment named PrP 27-30 (amino acid residues 90-231)(Meyer, McKinley *et al.* 1986; Oesch, Westaway *et al.* 1985).
- When intact on the cell surface, PrP^{C} can be removed by phosphatidylinositol-specific phospholipase C (PIPLC) (Caughey, Race *et al.* 1989; Stahl, Borchelt *et al.* 1987) whereas PrP^{Sc} cannot. This suggests that the PrP^{Sc} polypeptide chain is interacting with the cell surface to prevent a successful PIPLC cleavage (Safar, Ceroni *et al.* 1991; Stahl, Borchelt *et al.* 1990).
- PrP^{C} has a half life of 3-6 hours (Borchelt, Scott *et al.* 1990; Caughey, Race *et al.* 1989; Caughey and Raymond 1991; Yedidia, Horonchik *et al.* 2001) before it is catabolised, secreted or released from the cell surface, once accumulated on the cell membrane, however PrP^{Sc} cannot be removed or recycled by the cell.
- PrP^{Sc} can form aggregates and amyloid fibrils in brain tissue which can be stained with Congo red dye (Prusiner, McKinley et al. 1983), in contrast PrP^{C} exists as a monomeric form and does not form aggregates.
- The secondary structure of the two isoforms dramatically differs. Syrian hamster PrP^{C} and PrP^{Sc} were purified under non-denaturing conditions and their secondary structure was measured by Fourier-transform infrared (FTIR) spectroscopy and circular dichroism (CD). These measurements showed that monomeric PrP^{C} has a high α-helix content (42%) with little β-sheet (3%)

present whereas, oligomeric PrP^{Sc} has a higher proportion of β-sheet (43%) content than α-helical (30%) (see table 2.1) (Pan, Baldwin et al. 1993) (Safar, Roller et al. 1993). To date other biochemical characterisation methods have not identified any covalent differences between PrP^{C} and PrP^{Sc} indicating that the isoforms differ only in their conformation.

Table 2.1: Percentage content of secondary structure of purified SHaPrP determined from deconvolution and curve fitting of FTIR amide 1' bands (Pan, Baldwin et al. 1993)

Structure	PrP^{C} (23-231)	PrP^{Sc} (23-231)	PrP (90-231)
α-helix	42	30	21
β-sheet	3	43	54
Turn	32	11	9
Coil	23	16	16

All of these properties are useful to aid the identification of PrP^{Sc} and in some cases can be used as a surrogate marker for prion disease but the lack of some or all of these characteristics does not relate to a lack of prion infectivity. For example, resistance to partial proteinase K digestion has been demonstrated to be an effective tool for detecting PrP^{Sc}, recent studies, however, have shown that not all PrP^{Sc} molecules possess protease resistance, and different species or prion strains can exhibit different degrees of protease resistance (Hsiao, Groth et al. 1994; Telling, Parchi et al. 1996).

2.8 Structure

The mammalian PrP gene encodes for a protein containing approximately 250 amino acid residues. PrP^{C} is a glycosyl phosphatidylinositol (GPI)-linked glycoprotein and contains two N-linked glycosylation sites (Aguzzi and Heikenwalder 2006). Like other GPI-linked proteins PrP can attach to the cell's plasma membrane which is enriched with insoluble detergent domains that are rich in cholesterol and

sphingolipids, referred to as lipid rafts (Brown and Rose 1992; Naslavsky, Stein *et al.* 1997; Taraboulos, Scott *et al.* 1995; Vey, Pilkuhn *et al.* 1996). The mature PrP^C structure is similar throughout the mammalian species. These similarities include a long flexible N-terminal tail (residues 23-124), and secondary structural characteristics such as three α-helices and two-stranded anti-parallel β-sheets which are located in close proximity to the first α-helix (see Figure 2.5). In the majority of mammalian species, the second β-sheet and the third α-helix are connected by an extremely flexible large loop, it has been shown in deer and elk, however, that this loop region is rigid (Gossert, Bonjour et al. 2005). The carboxyl terminus (C-terminus) of PrP^C is stabilised by a disulphide bond, between cysteine residues 179 and 214 (in humans), which links α-helices two and three. Twenty-three residues are removed from the C-terminus during the addition of the GPI-anchor, so that the protein can be anchored to the cell membrane.

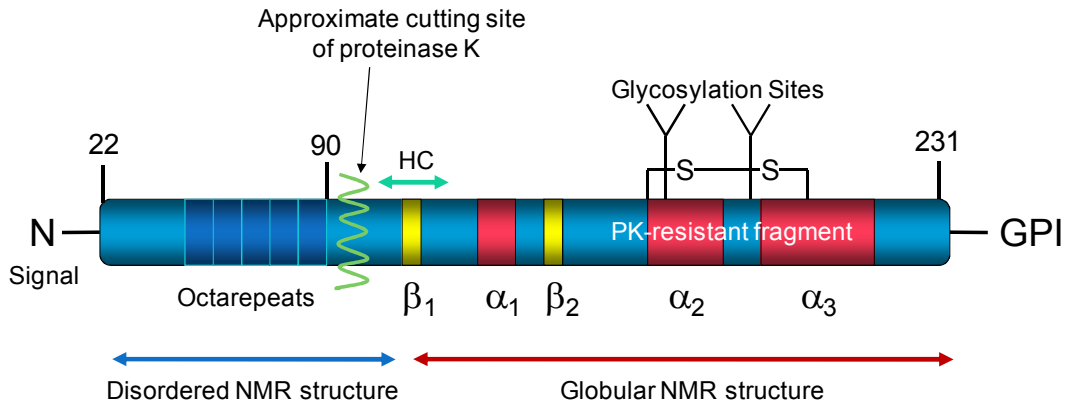

Figure 2.5: Schematic representation illustrating the structural features of the cellular prion protein. There is a signal peptide, residues 1-22, at the N-terminus. The green wavy line represents the approximate cleavage site by proteinase K. The green arrow shows the hydrophobic core region. The secondary structure regions are highlighted in yellow for β-sheet and red for α-helices. The glycosyl phosphatidylinositol (GPI) anchor is located at the C-terminus. Adapted from (Aguzzi and Heikenwalder 2006).

A signal peptide consisting of 22 amino acids (the amino-terminal) is cleaved during the biosynthesis of PrP, producing a protein of ~230 amino acid residues. The unstructured N-terminal region of PrP contains two defined highly conserved regions. The first region, known as the octarepeat region, consists of five repeat

units each of which contains a highly conserved eight amino acid sequence. The second region is downstream of these octarepeat peptides and contains a region of highly conserved hydrophobic amino acid residues referred to as the hydrophobic core. Within this region is a palindromic repeat (AGAAAAGA) which is conserved between all species implying that it has an important functional or structural role. From spectroscopic data it was predicted that amino acids 23-124 in the unstructured N-terminal flexible tail may possess some secondary structure when present in membrane-rich environments (Morillas, Swietnicki et al. 1999). Proteinase K digestion of PrP^{Sc} removes ~ 67 N-terminal residues to produce a truncated form of PrP which corresponds to amino acids 90-231 (PrP 27-30) (Meyer, McKinley *et al.* 1986; Oesch, Westaway *et al.* 1985). (See Figure 2.6)

Mammalian PrP contains five copies of the octarepeat sequence, with the exception of bovine PrP which contains an additional repeat unit. The octarepeat sequence, $(PHGG[G]WGQ)_n$ where the square brackets denote the non-conserved residues, is highly conserved throughout all species suggesting that it has a functional role. The repeating sequence in the chicken hexarepeat unit, $(PGYPHN)_n$, is dramatically different to that in mammals. Previous studies have shown that copper binds to the histidine residues in the octarepeat motif with a saturation stoichiometry of one copper per histidine residue (Brown, Qin et al. 1997). This suggests that PrP^{C} could bind copper ions and aid the transportation of these ions into the cell.

PrP^{C} and glycosylated PrP^{C}, purified from cattle brains, have similar tertiary structures (Hornemann, Schorn et al. 2004). This observation suggests that neither the attachment of N-linked glycans nor the GPI-anchor has an influence on the overall conformation of the prion. Circular dichroism (CD) spectroscopy studies, however, suggest that structural modifications do occur in PrP^{C} when it is GPI-anchored to the cell surface. This implies that the prion can interact with the cell plasma membrane (Morillas, Swietnicki et al. 1999). The two glycosylation sites (residues asparagine Asn181 and Asn197 in humans) can be non-, mono- or di-glycosylated in both the full-length and truncated PrP^{C}. Varieties of N-glycans can

attach to PrP^C with different glycan combinations found to be differentially distributed throughout the CNS.

2.8.1 NMR structure of recombinant PrP

The three-dimensional structure of recombinant PrP proteins expressed in *E. coli* has been determined by nuclear magnetic resonance (NMR) spectroscopy. The structure of the refolded recombinant α-helical conformation is believed to resemble that of PrP^C. The first structure to be solved was the truncated recombinant mouse fragment MoPrP(121-231) (Riek, Hornemann et al. 1996). It showed the presence of three α-helices (helix 1, 2 and 3) and two stranded anti-parallel β-sheets connected to helix 2 and 3 via a disulphide bond. The twisted V-shaped structure formed by the longest helices (helix 2 and 3) forms a scaffold onto which the short β-sheet and helix 1 are anchored (see Figure 2.7a). This structure revealed that there is a global domain for residues 125-228 and a short flexible chain end at residues 229-230. Further studies using full-length constructs showed that the N-terminal fragment, residues 23-120, has features of a flexible random coil-like polypeptide (Riek, Hornemann et al. 1997). The actual positions/structure of this flexible tail have never been defined because of missing assignments caused by residues moving and exchange-broadening in the NMR spectrum. The truncated NMR structure of recombinant Syrian hamster PrP, SHaPrP(90-231), was solved soon after the mouse structure was published (James, Liu et al. 1997). The structure was in good agreement with previous FTIR (Pan, Baldwin et al. 1993) studies with the results showing that of the 142 resolvable residues, 63 were present in α-helices (44%) and 6 residues comprised the short anti-parallel β-sheets (6%). See Table 2.2 to for a comparison of secondary structure percentage

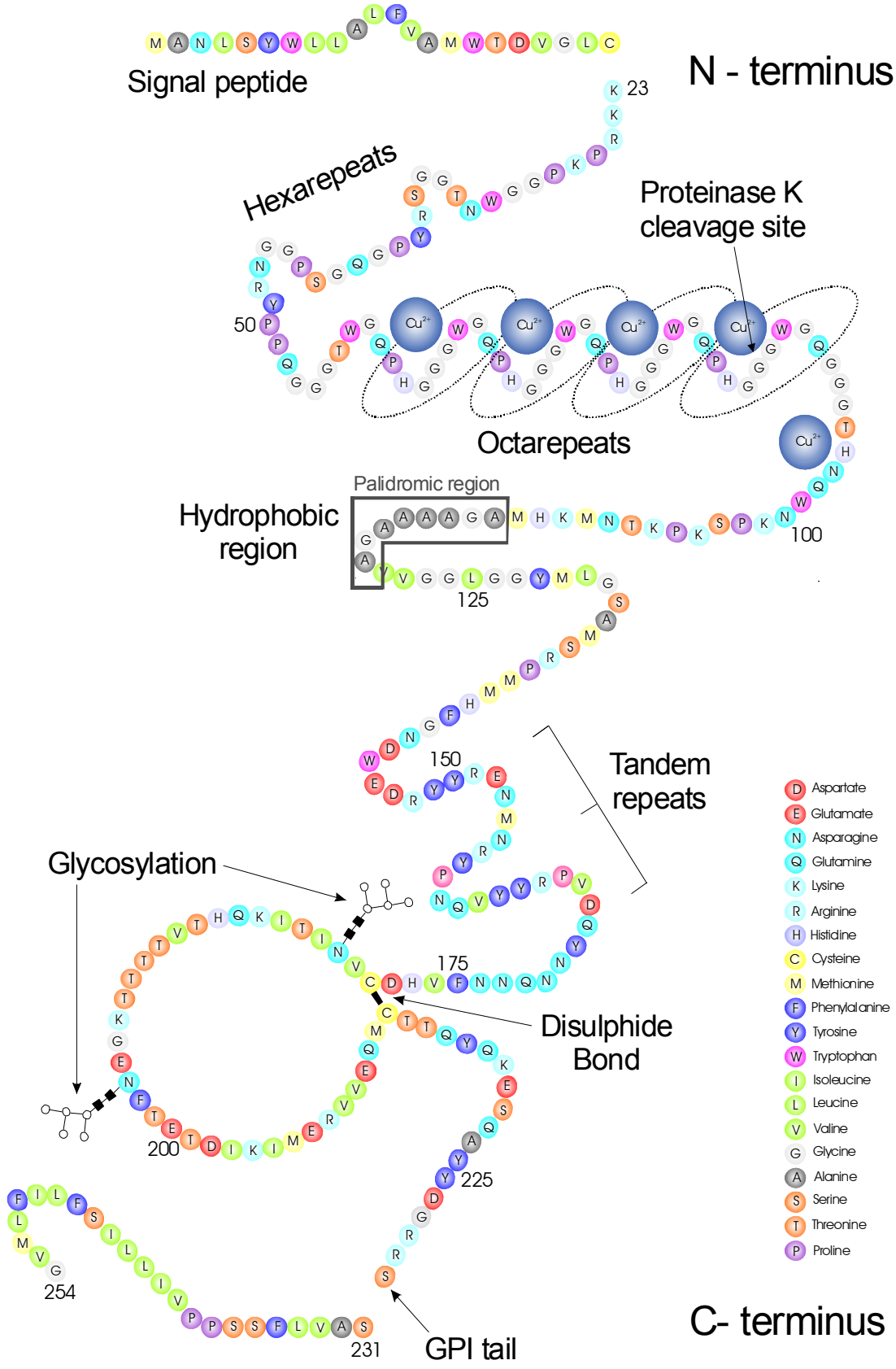

Figure 2.6: Schematic representation of the Syrian hamster prion protein. The major structural features are shown including the copper binding sites.

The NMR structures of truncated and/or full-length recombinant prion proteins from mouse (Hornemann, Korth *et al.* 1997; Riek, Hornemann *et al.* 1996; Riek, Hornemann *et al.* 1997), Syrian hamster (Donne, Viles et al. 1997; James, Liu et al. 1997; Liu, Farr-Jones et al. 1999), chicken (Calzolai, Lysek et al. 2005), turtle (Calzolai, Lysek et al. 2005), frog (Calzolai, Lysek et al. 2005), cat (Lysek, Schorn et al. 2005), dog (Lysek, Schorn et al. 2005), pig (Lysek, Schorn et al. 2005), sheep (Lysek, Schorn et al. 2005), cow (Lopez Garcia, Zahn et al. 2000) , elk (Gossert, Bonjour et al. 2005), vole (Christen, Perez et al. 2008), wallaby (Christen, Hornemann et al. 2009) and human (Zahn, Liu et al. 2000) have been published. The NMR structures show that the secondary structure is highly conserved throughout the mammalian species (see Table 2.2) with three α-helices (labelled helix 1, 2 and 3) and two β-strands (S1 and S2) always present. The numbers of amino acid residues creating helix 1 and β-strands S1, S2 are conserved throughout the mammalian species each containing 12 residues and 3 residues respectively. The lengths of helix 2 and 3, however, differ dramatically with mouse having the shortest α-helices (14 residues helix 2 and 17 residues helix 3) compared to voles and humans which consist of 22 residues in helix 2 and 28 residues in helix 3 respectively. It is thought that these differences in the tertiary structure could contribute to the species barrier (see Section 2.11)

A comparison of truncated recombinant mouse (MoPrP), hamster (SHaPrP), elk (ePrP) and human PrP (HuPrP) NMR structures show that the three-dimensional structure is similar (see Figure 2.7b). This similarity is expected because of the high sequence identity between the proteins. There are local differences between the backbone conformations of the four proteins especially in helix 3 and the nearby loop between β-sheet S2 and helix 2. In elk (vole and wallaby also) residues 165-175 define a 3_{10}-helical turn in the loop connecting β-strand 2 to the helix 2 (Christen, Hornemann *et al.* 2009; Christen, Perez *et al.* 2008; Gossert, Bonjour *et al.* 2005). This feature is in contrast with the mouse, hamster, human and all other mammalian PrP structures where a disordered loop region has been observed. Helix 3, in MoPrP, ends at residue 217 and a kink is observed in segment 219-222 before the chain forms a helix-like turn, whereas a regular α-helix is formed in SHaPrP, ePrP and HuPrP (Zahn, Liu et al. 2000). This kink can be seen in Figure 2.7b.

Differences in the helix 3 and loop residues 165-175 are of specific interest as there is a hypothesis that this is the binding site for protein X which may aid the conversion of PrP^{C} to PrP^{Sc}. (See Section 2.9 for protein X explanation).

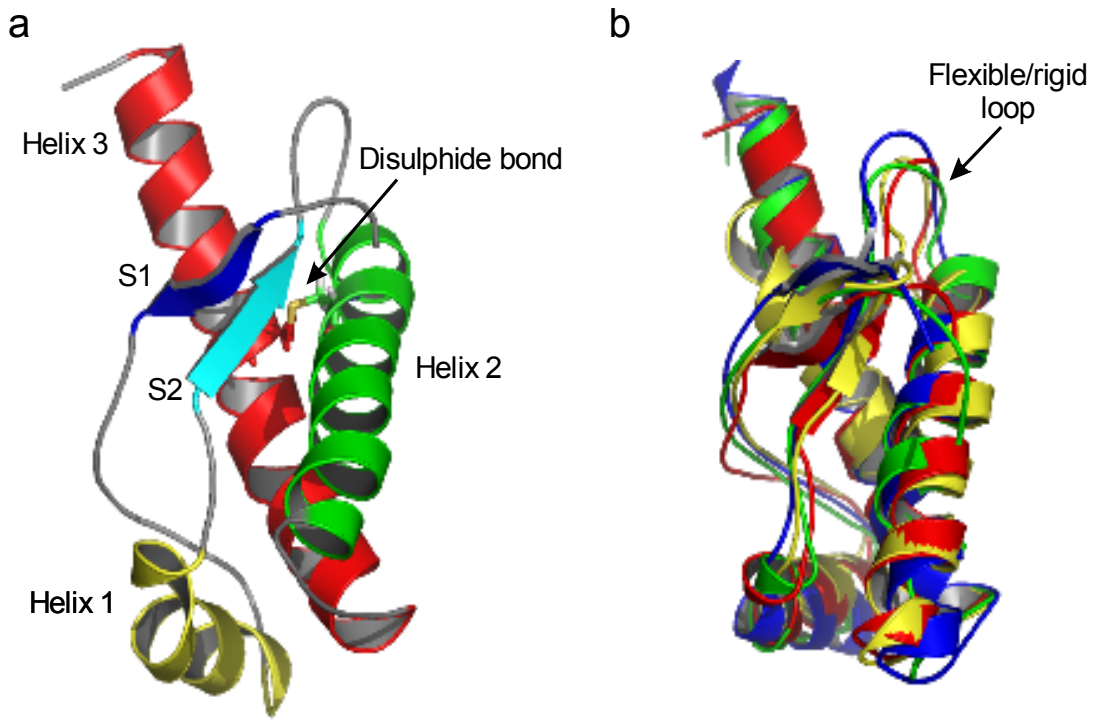

Figure 2.7: Representations of the three-dimensional structures of cellular prion proteins. (a). Cartoon representation of the NMR structure of recombinant SHaPrP(90-231) in aqueous solution indicating the positions of the three α-helices (Helix 1,2 and 3) and the two anti-parallel β-strands (S1 and S2), drawn in Pymol. (b) Superposition of the NMR structures of the polypeptide segment 121-231 of SHaPrP (red), MoPrP (yellow), HuPrP (blue) and ePrP (green). Structures have been superimposed to obtain the best fit of the polypeptide backbone residues 124-228. The flexible loop region has been highlighted.

Table 2.2: The positions and lengths of α-helices (1, 2 and 3) and β-strands (S1 and S2) in the NMR structures of a variety of recombinant PrP mammalian species.

Mammal	PrP Construct	Helix 1	Helix 2	Helix 3	S1	S2	pH
Syrian Hamster	SHa(29-231)	144-156	172-193	200-227	137-140*	160-163	5.2
Syrian Hamster	SHa(90-231)	144-156	172-193	200-227	129-131	161-163	5.2
Human	h(23-230)	144-154	173-194	200-228	128-131	161-164	4.5
Human	h(90-230)	144-154	173-194	200-228	128-131	161-164	4.5
Mouse	m(23-231)	144-154	179-193	200-217	128-131	161-164	4.5
Mouse	m(121-231)	144-154	179-193	200-217	128-131	161-164	4.5
Cow	b(23-230)	144-154	173-194	200-226	128-131	161-164	4.5
Red-eared slider turtle	t(121-225)	144-154	174-188	200-226	128-131	161-164	4.5
Bank Vole	bv(121-231)	144-156	172-194	200-225	128-131	161-164	4.5
Tammar Wallaby	tw(121-231)	144-153	172-189	200-226	128-131	160-163	4.5
Cat	f(121-231)	144-154	174-194	200-226	128-131	161-164	4.5
Dog	c(121-231)	144-154	174-194	200-226	128-131	161-164	4.5
Pig	sc(121-231)	144-154	174-194	200-226	128-131	161-164	4.5
Sheep	ov[H168](121-231)	144-154	174-194	200-226	128-131	161-164	4.5
Elk	e(121-231)	144-155	172-190	200-225	128-131	160-163	4.5

***The NMR data did not suggest a β-sheet between residues 128/129-131 as observed in all other species, instead a β-sheet was proposed to be located at residues 137-140. This may reflect the poor resolving power of the technique as the β-sheet is very small and essential residues could not be detected (Gossert, Bonjour et al. 2005). Alternatively it could indicate that there is a different native conformation for this protein. The full-length structures are only partially assigned because of missing assignments caused by residues moving and exchange-broadening in the NMR spectrum.

2.8.2 Structure of PrP^{Sc}

A variety of conflicting structures for PrP^{Sc} have been proposed but to date no NMR structures of PrP^{Sc} have been published. This could be due to the difficulties in purifying the protein and its propensity to aggregate. A model structure for PrP^{Sc}, residues 108-217 only, has been proposed in which the unstructured N-terminal tail and helix 1 are in β-sheet conformations. The overall structure of this model contains a four-stranded β-sheet with one face covered by two α-helices (Huang, Prusiner et al. 1995) (see Figure 2.8b). NMR structural studies of a reduced short-lived intermediate state, namely reduced β-PrP*, have been performed (Hosszu, Trevitt et al. 2009). This structure showed that helix 1 and 3 have the same α-helical characteristics as PrP^{C}, whereas helix 2 exhibited little evidence of having any α-helical features. From these results it was proposed that helix 2 is the region likely to interact with PrP^{Sc} and transform into β-sheets – this is in contrast to the previous model. Negative stained electron crystallography has been used to characterise 2D crystals of two infectious variants of the prion protein (Wille, Michelitsch et al. 2002). The 2D crystal diffraction patterns suggest that PrP 27-30 can adopt a parallel β-helical fold. When these constraints were applied to modelling studies the result was a protein conformation with the C-terminal α-helices and glycosylation sites on the periphery of the oligomer and the highly flexible N-linked sugars pointing above and below the plane of the oligomer. This was the only conformation which could fit into the electron micrscopy (EM) density observed and be compatible with the amount of β-sheet structure observed by FTIR studies (see Figure 2.8 a and c).

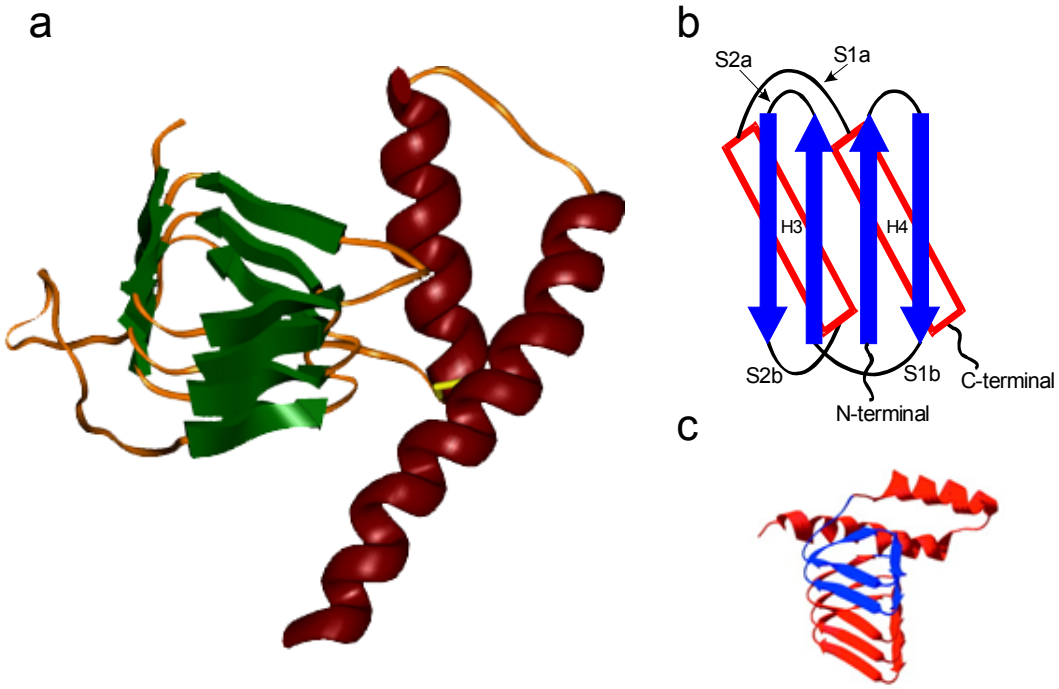

Figure 2.8: Representation of the three-dimensional structures of plausible scrapie prion proteins. (a) PrP^{Sc} model of SHaPrP(90-231) created from FTIR data (Pan, Baldwin et al. 1993). (b) Plausible tertiary structure model for $HuPrP^{Sc}$(108-217) adapted from (Huang, Prusiner et al. 1995). (c) Model created from EM data showing the side-view of β-helical model of PrP27-30 taken from (Wille, Michelitsch et al. 2002).

2.9 Conversion

The biosynthesis pathway of PrP^{C} begins in the endoplasmic reticulum (ER) and is directed to the cell membrane by a signal peptide. After its release from the ER the PrP^{C} journeys through the Golgi apparatus where glycosylation and the addition of the GPI moiety take place (Caughey 1991). It takes approximately 60 minutes for the mature PrP^{C} to cycle from the Golgi apparatus to its final position which is GPI-anchored onto the cell membrane where it is predominantly located in specialised detergent-resistant microdomains known as caveolae. Once at the cell surface the half life of PrP^{C} is between 3-6 hours (Borchelt, Scott *et al.* 1990; Caughey, Race *et al.* 1989; Caughey and Raymond 1991; Yedidia, Horonchik *et al.* 2001) in which time it will be either catabolised/secreted or released from the cell surface (see Figure 2.9).

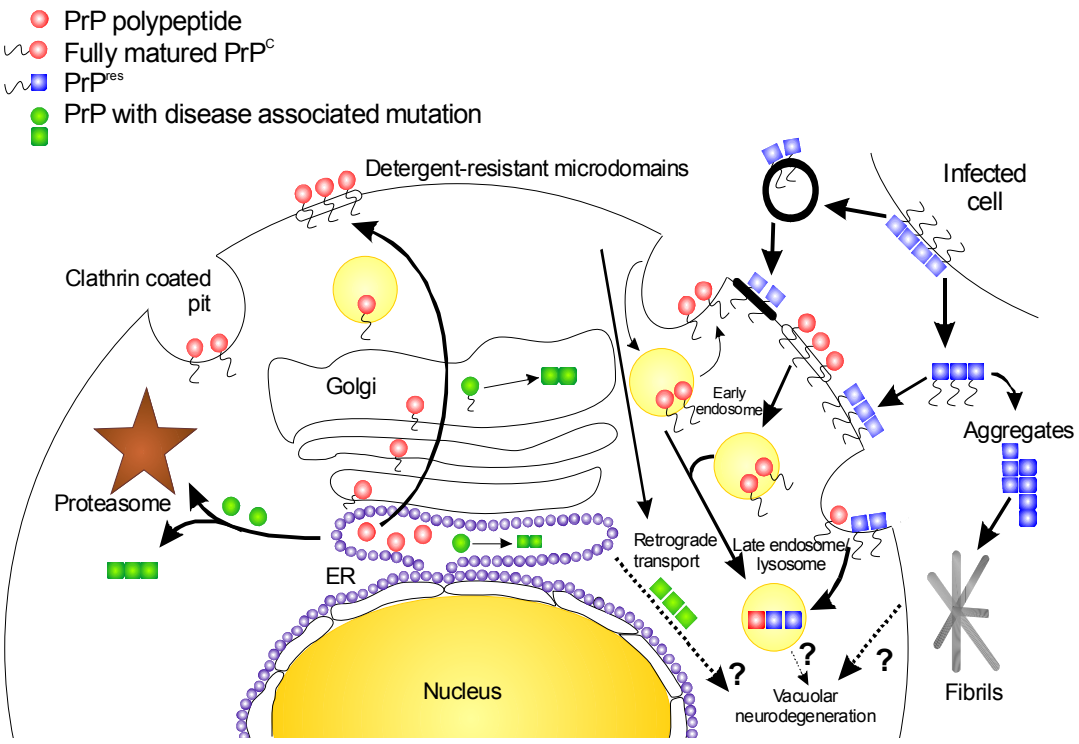

Figure 2.9: Schematic representation of the proposed PrP^{C} synthesis and cell turn-over pathway for the conversion of PrP^{C} into PrP^{Sc}. Adapted from (Collins, Lawson et al. 2004).

The exact conversion site for PrP^{C} to PrP^{Sc} is not known. It is believed to occur by a post-translational modification (glycosylation) once PrP^{C} reaches the cell membrane. In scrapie infected cells, PrP^{C} molecules destined to become PrP^{Sc} exit the cell surface before conversion into PrP^{Sc} (Prusiner 1996). PrP^{C} can then re-enter the cell using a subcellular compartment in caveolae or early endosomes. PrP^{C} can migrate to late endosomes of lysosomes via caveolae-containing endocytic structures and can be either converted into PrP^{Sc} or partially degraded under non-acidic conditions. PrP^{Sc} is trimmed at the amino acid terminus in an acidic compartment in scrapie-infected cultured cells, to form PrP 27-30 (Prusiner 1996) (see Figure 2.10). PrP^{Sc} can accumulate in the cytosol to form aggregates which are resistant to protease digestion. The minimal number of residues required for PrP to transmit disease has

been investigated. Rogers *et al* used *in vitro* mutagenesis studies to show that the deletion of residues 23-88 or the removal of the GPI-anchor did not alter the synthesis of PrP^{Sc} (Rogers, Yehiely et al. 1993).

In contrast to previous studies (Caughey 1991), it has been observed that glycosylation of PrP^{C} is not essential for the formation of PrP^{Sc}. The presence of bulky oligosaccharides is thought to interfere with the conversion of PrP^{C} to PrP^{Sc}. In circumstances where glycosylation was prevented, the rate of PrP^{Sc} synthesis actually increased (Lehmann and Harris 1997; Taraboulos, Scott *et al.* 1995)

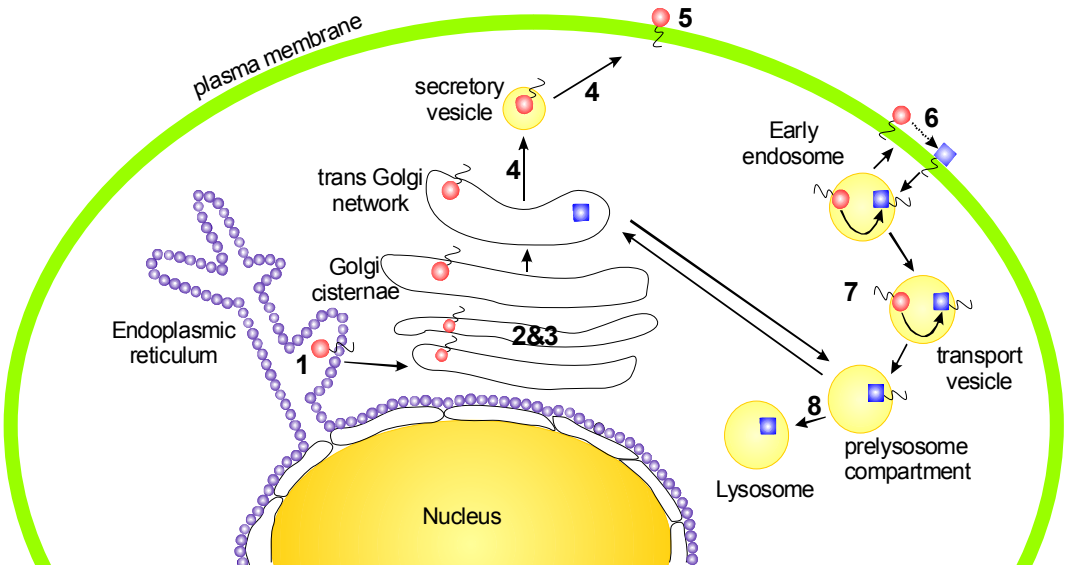

Figure 2.10: Schematic representation showing the probable sites of PrP^{Sc} formation.

1. N-terminal of PrP^{C} is cleaved
2. Glycosylation and GPI moiety added
3. Removal of the C-terminal domain
4. Transport to cell membrane
5. GPI-anchored to cell membrane and remains here between 3-6 hours before being recycled
6. Post-translation modification of PrP^{C} to PrP^{Sc}
7. PrP^{C} transportion into cell via caveolae and converted to PrP^{Sc} or degraded
8. N-terminus trimmed to leave PrP27-30

2.9.1 Models of conversion

Two different models have been postulated for the conversion of PrP^{C} to PrP^{Sc} with the exact mechanism still not fully understood. Both models predict that the infectious protein interacts with endogenous PrP^{C} to induce a conformational change generating PrP^{Sc}.

2.9.2 Template-assisted model

In this model the hypothesis is that PrP^{Sc} can act as a seed or template in the conversion of host PrP^{C} to PrP^{Sc} (Jarrett and Lansbury 1993; Prusiner 1996; Weissmann 1996). It is postulated that spontaneous fluctuations in the PrP^{C} structure can form a partially folded protein intermediate named PrP* (Ceciliani and Pergami 2001; Weissmann 1999). For partial unfolding to occur an external catalyst such as a chaperone or an unknown protein (referred to as protein X) may be required. This metastable intermediate has potentially been identified, in the refolding of PrP 27-30 from a denatured state, by fluorescence and CD spectroscopy (Safar, Roller et al. 1994). Exogenously introduced PrP^{Sc} can interact with this intermediate to induce a conformational change in PrP^{C} to yield further PrP^{Sc} structures (see Figure 2.11a and b). Mechanistic analyses have shown that the PrP conversion is induced by PrP^{Sc} aggregates or polymers and not by soluble, monomeric forms of PrP (Caughey, Kocisko et al. 1995). The presence of the PrP* intermediate state is proposed to lower the activation energy required for a spontaneous conversion of the predominantly α-helical protein form to a β-sheet rich structure. For this mechanism to be successful a small amount of PrP* would have to be present in normal brain tissue which would normally undergo an insignificant rate of conversion to PrP^{Sc}. In the case of infectious prion diseases, exogenous PrP^{Sc} could act as a template for the reaction with the PrP* and promote the conversion of PrP* to PrP^{Sc} (Ceciliani and Pergami 2001). In genetically inherited diseases such as familial CJD and GSS, mutations in the gene sequence could help destabilise the PrP^{C} structure thereby increasing the population of the PrP* intermediate and enhancing the rate of the spontaneous PrP^{C} to PrP^{Sc} conversion (Cohen, Pan *et al.* 1994; Harrison, Bamborough *et al.* 1997; Huang, Gabriel *et al.* 1994). This proposed model is a first-order reaction with the only rate limiting step being the

transition of PrP^{C} to PrP^{Sc}. It has been speculated that this conversion occurs by the initial binding of PrP^{Sc} to PrP^{C}, via a localised site close in proximity to the C-terminal end of the third helix. This then slowly converts PrP^{C} into the infectious form of PrP^{Sc} (Bessen, Raymond *et al.* 1997; Caughey, Kocisko *et al.* 1995; DebBurman, Raymond *et al.* 1997; Horiuchi and Caughey 1999). There is evidence to support that this conversion is a first order reaction. Scrapie incubation time period studies suggest that the level of PrP^{C} expression is inversely proportional to the incubation period. (Carlson, Ebeling *et al.* 1994; Prusiner, Scott *et al.* 1990).

2.9.3 Nucleated Polymerisation model

In this model it is proposed that PrP^{C} and PrP^{Sc} are in a reversible equilibrium with PrP^{C} as the strongly favoured structure. The PrP^{Sc} structure can be stabilised, and the equilibrium reversed, when additional monomeric PrP^{Sc} units are attached to create a crystal-like seed model (Weissmann 1999). In the absence of this rare crystal-like seed or pre-existing aggregates the conversion between PrP^{C} and PrP^{Sc} is reversible. The crystal-like seed or complex aggregates can act as a stable nucleus and promote the rapid addition of further monomeric PrP^{Sc} units (Brown, Goldfarb et al. 1991; Jarrett and Lansbury 1993). This addition of monomeric units continues until large aggregates are formed which can then fragment to create new crystal-like seeds and allow the reaction cycle to start again (see Figure 2.11b). This rapid fragmentation process to create a new seed would account for the exponential conversion rate observed (Weissmann 1999). The rate limiting step of this reaction would be the formation of the stable nucleus and therefore this conversion model would be a multi-step high order reaction (Jarrett and Lansbury 1993). It is believed that yeast prion propagation and conventional amyloid fibril formation occur by this nucleated polymerisation mechanism (Caughey 2001).

Conversion studies *in vitro* have shown the mechanism to have many similar features to the nucleation polymerisation model. These similarities include the requirement to exceed a critical protein concentration prior to the formation of aggregates and the observation of a lag phase in kinetic experiments, equivalent to

the slow addition of monomeric PrP^{Sc} units, suggests a higher order reaction (Jarrett and Lansbury 1993).

An alternative theory is that the conversion of PrP^{C} to PrP^{Sc} could be a combination of both models. Horwich *et al*, propose that the conversion mechanism could be a hybrid of both the template-assisted and the nucleation polymerisation model whereby a nucleation seed is initially formed which can then catalyse the conformational change in PrP^{C} to PrP^{Sc} (Horwich and Weissman 1997).

2.10 Prion strains

The concept of the prion strain emerged when observations that distinct versions of prion diseases, which differ in their symptomatic and biochemical properties, could occur in the same species without a change in the PrP gene being detected (Dickinson and Meikle 1971). It was speculated that strain-specific properties of prions could be encoded by the PrP genome but to date there has been no significant evidence to support this hypothesis (Weissmann 1991). An alternative theory is that PrP^{Sc} can exist in a variety of distinct pathological conformations each of which can act as a template for the conversion of PrP^{C}; this template can impart the new novel conformation resulting in an accumulation of the distinct pathological strain. There is evidence from the yeast Sup35 prion model that strain phenotypes can be encoded in for a variety of different conformations all of which are stable against chaotropic salts and heat. (King and Diaz-Avalos 2004; Tanaka, Chien et al. 2004; Tanaka, Collins et al. 2006)

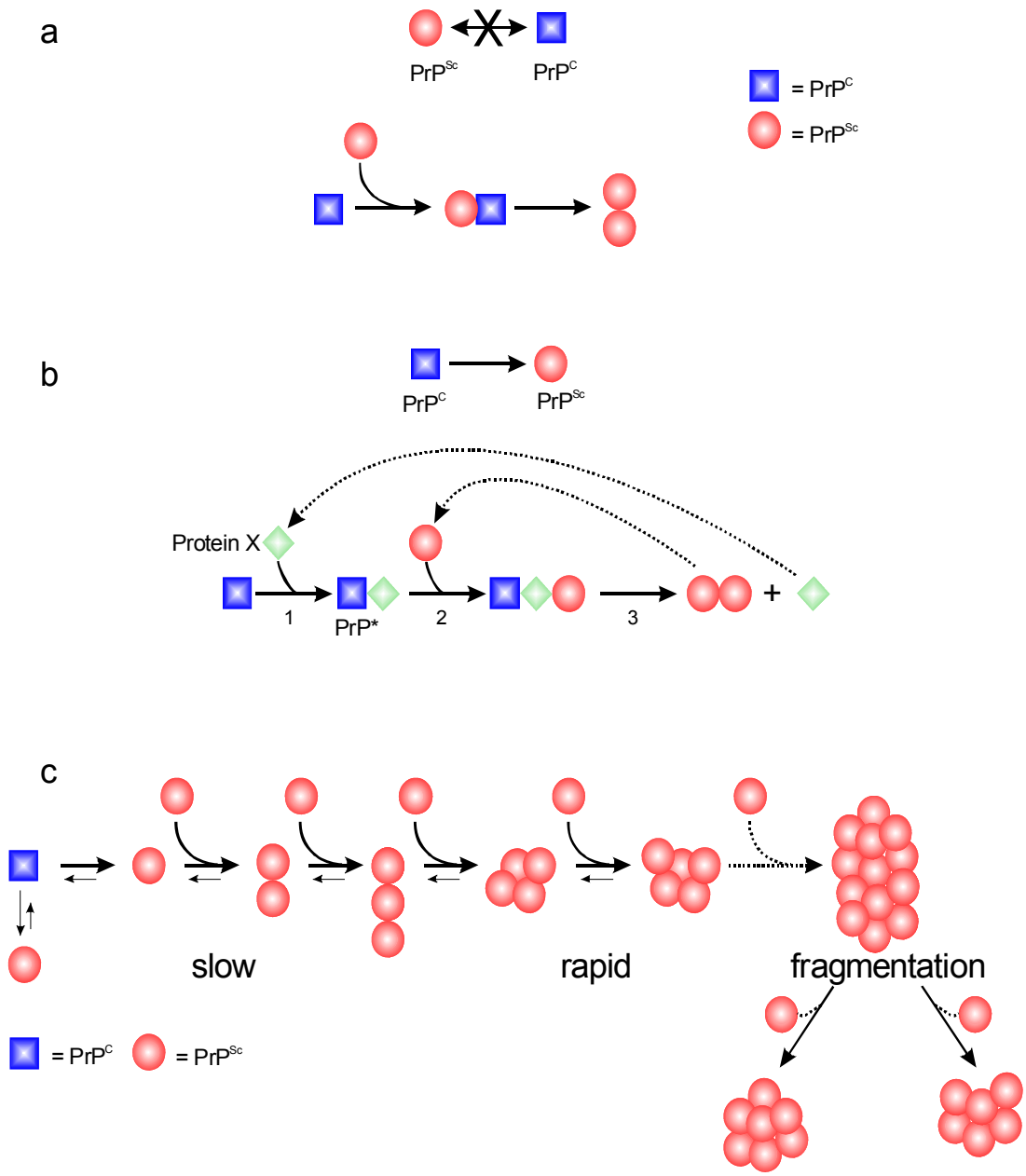

Figure 2.11: Schematic representations of the various proposed models of conversion. (a) **The "refolding" model**. The conformational change is kinetically controlled, a high activation energy barrier preventing spontaneous conversion at detectable rates. Interaction with exogenously introduced PrP^{Sc} causes PrP^{C} to undergo an induced conformational change to yield PrP^{Sc}. This reaction may involve extensive unfolding and refolding of the protein to explain the postulated high energy barrier and could be dependent on an enzyme or chaperone. Adapted from (Weissmann 1999). **Template assisted model**. **1**. In the initial step PrP^{C} binds to protein X to form a complex. **2**. PrP^{Sc} interacts with the new PrP*/protein X complex. **3**. PrP* is converted to PrP^{Sc}, releasing protein X and forming a PrP^{Sc} dimer. Adapted from (Weissmann 1999). **Nucleated polymerisation model of PrP^{Sc} formation.** PrP^{C} and PrP^{Sc} are in a reversible equilibrium strongly favouring PrP^{C}. PrP^{Sc} is stabilised

when several monomeric PrP^{Sc} units add together to form aggregates or crystal-like seed structures. Seed formation is a rare event; once a seed is present, monomer addition can ensue at a rapid rate. It is believed that the aggregates are continuously fragmented to account for the exponential conversion rates. Adapted from (Ceciliani and Pergami 2001; Weissmann 1999).

2.11 Species barrier

There are suggestions that differences in the PrP amino acid sequence are the major contributing factor to a transmission species barrier (Kocisko, Priola *et al.* 1995; Prusiner 1995; Prusiner, Scott *et al.* 1990; Raymond, Bossers *et al.* 2000; Scott, Kohler *et al.* 1992). There is a high sequence identity between bovine and ovine PrP with differences in only seven amino acid positions; in comparison the differences between bovine and human differ by more than 30 amino acid positions (Figure 2.12). Two pairs of uniquely shared amino acid substitutions have been identified in the PrP gene sequence of cattle and great apes (including humans) (Krakauer, Pagel et al. 1996). Speculations that these unique substitutions allow the successful transmission of BSE across the species barrier, in the form of v-CJD, and may also have prevented the transmission of scrapie to humans (Krakauer, Pagel et al. 1996). Alternatively, it is postulated that similarities in the secondary and tertiary structure of PrP molecules can enable a successful transmission of a TSE agent (Caughey, Raymond *et al.* 1998; Safar, Wille *et al.* 1998; Telling, Parchi *et al.* 1996).

The apparent sporadic transmission of scrapie suggests there are limiting factors which prevent the successful transmission of PrP across the species barrier. Scrapie in sheep can exist in a variety of strains, but only a select few can be readily transmitted to other sheep and goats. In contrast, BSE appears to be caused by a single strain and can be transmitted to humans (v-CJD) as well as cattle. It has been previously described that a single amino acid substitution in the host/donor PrP can have a profound effect on targeting the TSE strains in the CNS of the recipient species and can alter the disease pathology of a specific TSE agent (Barron, Thomson et al. 2001). NMR structural analysis of recombinant human (Zahn, Liu et al. 2000), hamster (Donne, Viles et al. 1997) and mouse (Riek, Hornemann et al. 1997) PrP identified significant sequence differences in the α-helix 3 region and the

loop residues 167-171 and it is has been suggested that these differences could alter the species specificity (see Figure 2.7b). A small number of residues, located from codon 101 to 143, were found to be central to the prion species barrier (Schatzl, Da Costa et al. 1995). Residues that are considered important for the species barrier have been mapped onto the three-dimensional structure of PrP (Riek, Hornemann et al. 1996). These residues were found to be part of the hydrophobic core region or are located on the surface of the protein. It was implied that the positions of these residues could destabilise the structure or influence the protein's ligand binding properties. Barron *et al*. (Barron, Thomson et al. 2001) demonstrated that a single mutation in the N-terminal flexible region of PrP could allow the efficient transmission of a strain of the agent across the species barrier to animals that would not have normally have succumbed to the disease. It is likely that the key domain(s) within a protein and the strain of the infectious agent are important contributing factors to the species barrier. Understanding prion strains and the species barrier is of paramount importance with respect to the BSE epidemic in Britain.

2.12 Function

The physiological role of PrP^{C} is still debated, with data suggesting a number of possible functions including immunoregulation, signal transduction, synaptic transmission, antioxidant action, cell adhesion, copper binding and many others (Aguzzi and Polymenidou 2004; Choi, Kanthasamy et al. 2006). Studies have shown that knockout mice lacking the PrP gene ($Prnp^{0/0}$) develop and behave normally and showed no sign of scrapie clinical symptoms (Bueler, Fischer et al. 1992). In comparison to the control mice, PrP-null mice have shown brain abnormalities in the structure of the hippocampus (Collinge, Whittington et al. 1994), have an altered circadian rhythm and disrupted sleep patterns (Tobler, Gaus et al. 1996). Further $Prnp^{0/0}$ studies showed that the synaptosomal fractions of the wild type mouse brain, and cultured cell lines, contained more copper than their knockout counterparts.

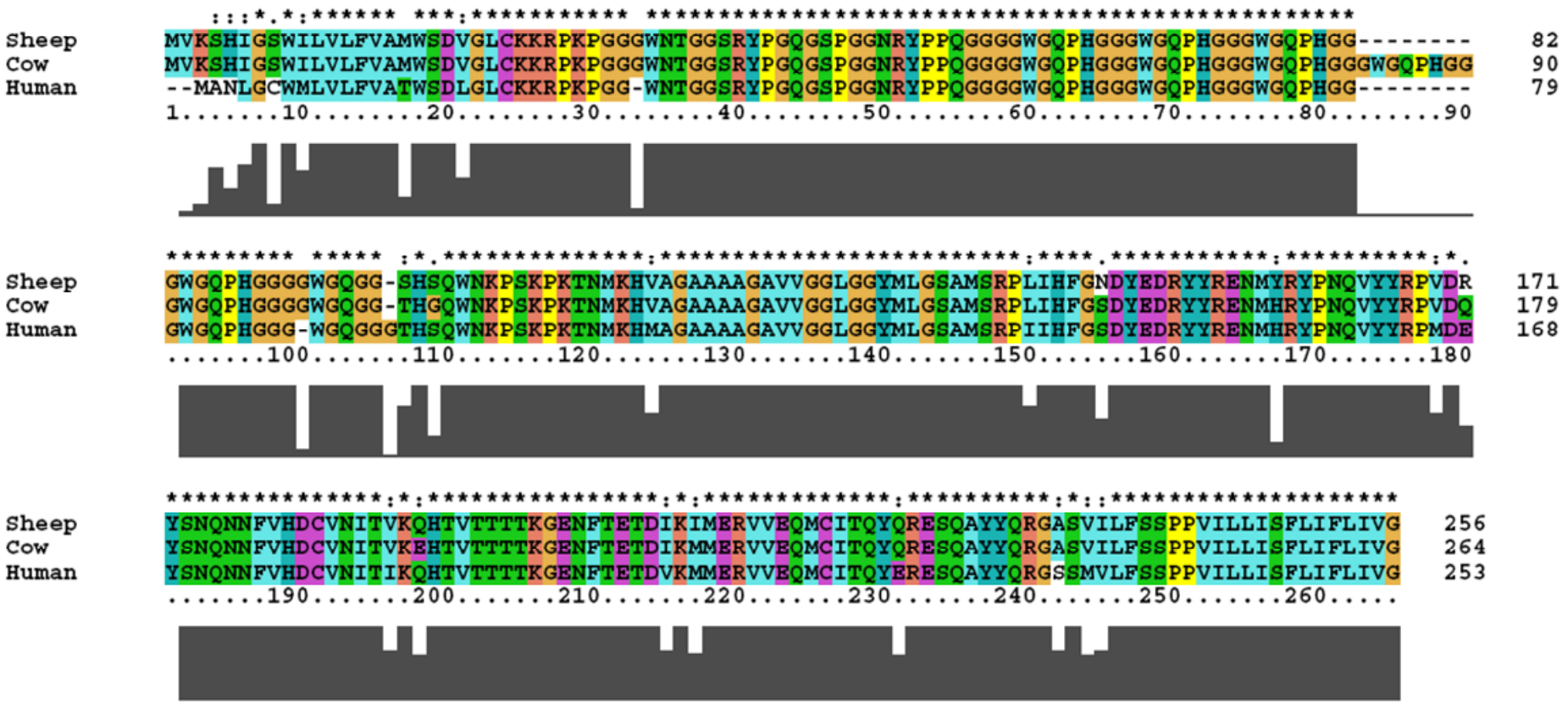

Figure 2.12: Sequence alignment for human, bovine and ovine PrP. Residues aligned using the nearest neighbour fit in Cluster.

One possible protective physiological function of PrP^C is as an antioxidant. It has been reported that Cu^{2+} can bind to the N-terminal of the protein, as a response to oxidative stress, to induce endocytosis of PrP^C (Linden, Martins *et al.* 2008; Vassallo and Herms 2003). Copper is an essential element for life and has numerous roles within the human body including acting as a catalyst in the transportation of iron, synthesis of collagen, coagulation of blood (Linder and Hazegh-Azam 1996) and, of particular significant to prion research, the synthesis of neurotransmitters (Georgieff 2007). Copper located in synapses can play an important role in the gamma-aminobutyric acid (GABA) feedback system and glutamate uptake (Gabrielsson, Robson et al. 1986). It is widely accepted that PrP^C can bind copper in a cooperative manner and there is some indication that it is involved in the homeostasis of copper within the body (Brown, Qin et al. 1997; Viles, Cohen et al. 1999). In CJD patients, the levels of copper located in the brain are significantly decreased with similar effects/changes also observed in mice infected with scrapie.

The highest concentration of PrP^C is found in brain tissue. If PrP^C is consumed it is intestinally digested where it can be absorbed into the blood and transported to lymphoid fluids. After this initial transportation, PrP^C can be replicated at sites including the spleen, muscles, tonsils, appendix and a region in the intestines known as the Peyer's patch (see Figure 2.13). These newly replicated prions are then transported to the brain by the peripheral nerves where they cross the brain-blood barrier and accumulate in brain (Aguzzi and Heikenwalder 2006). PrP^C can also be expressed in neurons and glia, which would account for the high PrP^C dosage located in brain tissues. Due to its GPI-anchored location on the cell surface it is believed PrP^C may have a functional role in cell adhesion and recognition, ligand uptake, or transmembrane signalling.

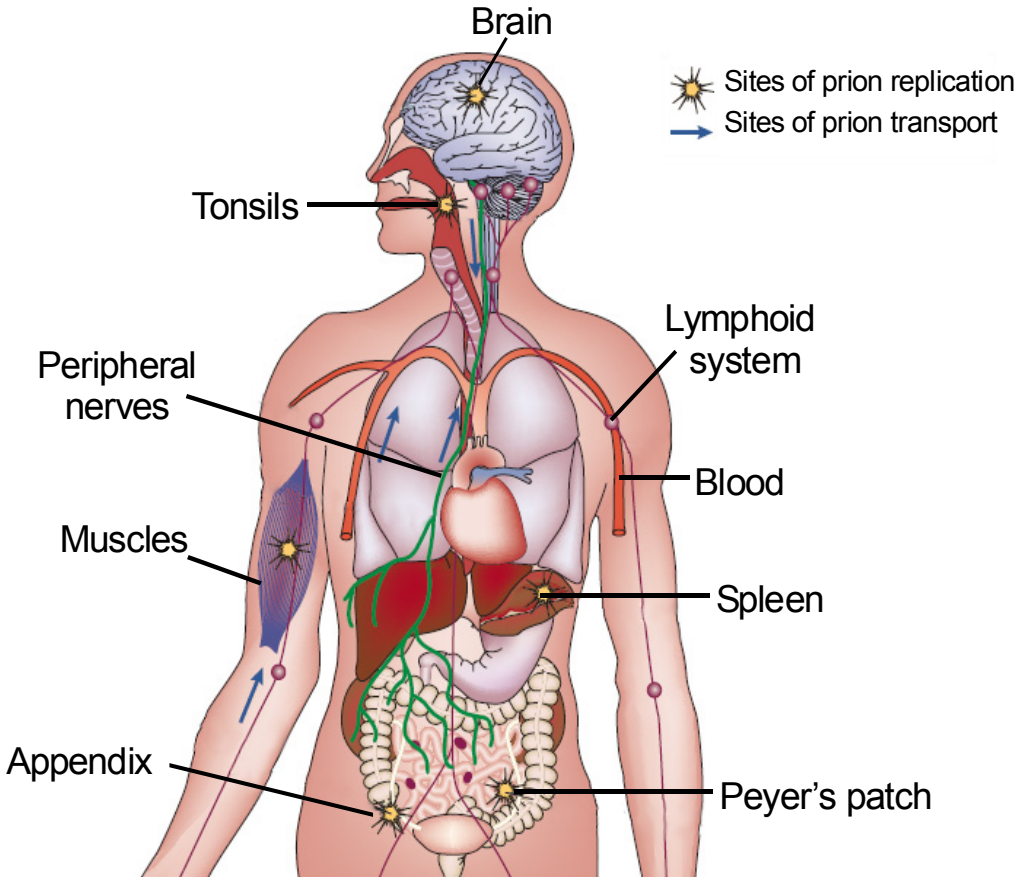

Figure 2.13: Schematic representation of the human tissues and blood involved in the propagation and transport of prions. Orally ingested prions are intestinally absorbed and transported to the blood and lymphoid fluids. After a peripheral replication step prions are primarily transported to the brain via the peripheral nerves. The prions cross the blood-brain barrier to accumulate in brain tissues. Adapted from (Aguzzi and Heikenwalder 2006).

2.13 What causes cell death?

It is debated whether the accumulation of PrP^{Sc} or the loss of PrP^{C} function is the actual cause of cell death in prion diseases. Experiments show that PrP^{Sc} accumulation in the brain and the resulting extracellular aggregates/amyloid fibrils, can promote nerve cell loss and lead to neuronal death (Forloni, Angeretti et al. 1993). Conversely, it has been shown that PrP peptides can induce lipid vesicle fusion and it is believed that it is this PrP fusogenic property which causes neuronal death by destabilising the cellular membrane (Pillot, Lins et al. 1997). There is also a hypothesis that PrP^{C} can influence the activity of Cu/Zn superoxide dismutase which is important in the cell's defence against oxidative stress (Brown, Schulz-

Schaeffer et al. 1997). The conversion of PrP^{C} to PrP^{Sc} leads to this oxidative stress defence being lost allowing neurons to be exposed to increased oxidative stress levels.

2.14 Clinical diagnosis

2.14.1 PrP concentration in blood

The concentration of PrP^{Sc} in plasma and red blood cells is estimated to be approximately 5-10 fold lower than in the buffy coat. The buffy coat contains leukocytes and platelets and contributes to 1% of the whole blood cell and can be separated from the red and white blood cells by centrifugation. Using rodent models, infectivity studies have shown that during the incubation period of prion disease the maximum concentration of PrP^{Sc} in the buffy coat, in circulating blood, is 5-10 infectious units (IU) mL^{-1}. At the onset of disease the concentration of PrP^{Sc} increases to approximately 100 IU mL^{-1} (Soto 2004). One picogram (pg) of PrP^{Sc} is estimated to contain 100 IU, therefore the estimated concentration of PrP^{Sc} in the buffy coat is expected to be 1 pg mL^{-1} (~3 x 10^{-14} M) and 0.1 pg mL^{-1} (~3 x 10^{-15} M) during the symptomatic and pre-symptomatic phases respectively (Soto 2004). The concentration of PrP^{Sc} is an order of magnitude lower in whole blood, so that a blood test from pre-symptomatic patients would have to detect PrP^{Sc} in the femtomolar concentration range (Soto 2004). For a feasible pre-symptomatic blood assay to be developed PrP^{Sc} would either have to be concentrated or amplified prior to analysis.

2.14.2 Current post-mortem tests

Brain histology assays are the most accurate method for identifying TSEs in post-mortem samples; however, this procedure can be labour-intensive, expensive and has an extremely low throughput. After the BSE crisis in Britain, the European Commission approved five tests for the post-mortem detection of BSE in cattle (see Table 2.3). The majority of these tests are designed to detect PrP 27-30 after the sample has been subjected to proteinase K digestion. A disadvantage of using this physical property as a diagnostic test is the evidence for a new proteinase-sensitive

prionopathy (PSPr) which is detergent insoluble but sensitive to protease digestion. The current approved tests cannot detect this new prionopathy which accounts for 3% of all sporadic CJD cases in humans and an unknown number in cattle (Gambetti, Dong et al. 2008). The majority of these tests are either labour–intensive or have a potentially high false-positive rate at the biologically relevant prion concentrations. It is unlikely that these tests would successfully diagnose pre-symptomatic disease due to their restricted detection limits. An ante-mortem test is required to prevent pre-clinical BSE cattle from entering the food chain and to safeguard the blood supply from asympotomatic carriers donating blood.

Table 2.3: Summary of European Commission approved post-mortem tests for the detection of altered and infectious PrP isoforms in cattle brains (Soto 2004).

Technique	Principle	Detection limit (pmol)	Advantages	Disadvantages
Prionics-Check Western test	Gel electrophoresis and Western blot	5.0-20	Good reproducibility, low rate of false-positives	Low throughput, low sensitivity. Dependent on proteinase K digestion
Enfer test	Enzyme-linked immunosorbent assay (ELISA)	1.0-10	Rapid and simple	Potential for false-positives. Dependent on proteinase K digestion
CEA/Biorad test	Sandwich ELISA using two different monoclonal antibodies	0.5-2.0	High sensitivity	Long and labour-intensive. Potential for false-positives. Dependent on

				proteinase K digestion
Prionics-Check LIA test	Sandwich ELISA using two different antibodies to detect proteinase K resistance	1.0-5.0	Rapid, automated and simple	Variability depending on sample preparation. Potential for false-positives. Dependent on proteinase K digestion
Conformational-dependent immunoassay	Differential antibody-binding to native and denatured PrP	0.5-5.0	High sensitivity. Independent of proteinase K digestion	Complicated, time consuming and labour intensive

2.14.3 Pre-mortem tests

The effective treatment of TSE sufferers requires a pre-clinical diagnostic test to be developed. It is known that by the time a patient is exhibiting clinical symptoms the brain alterations are too extensive to be reversed and therapeutic treatment is no longer an option. It has been shown in animal models that early treatment of TSEs can delay the onset of disease thereby extending their life expectancy (Soto 2004). Animal infectivity bioassays are methods which directly measure the presence of prions and the infectious PrP^{Sc} agent. Widespread use of these invasive bioassays is limited as it can take months or years to obtain a result. Recent developments have seen research into non-invasive diagnostic tests which include analysis of bodily fluids, tonsil tissue following a tonsillectomy, and screening of appendicectomy samples. The screening of 16,703 patients revealed that three appendicectomy samples showed lymphoreticular accumulation of prion protein but this pathology could not be related to v-CJD (Hilton, Ghani et al. 2004). Other research has led to the development of three putative PrP^{Sc}-specific antibodies that discriminate between PrP^{C} and PrP^{Sc} (Paramithiotis, Pinard et al. 2003; Serbec, Bresjanac et al. 2004; Zou,

Zheng et al. 2004). Further work is required to analyse the sensitivity and specificity of these antibodies before a diagnostic test can be developed. An alternative strategy to increase the sensitivity for PrP^{Sc} is first to concentrate or amplify the sample prior to detection. Protein misfolding cyclic amplification (PMCA) is an *in vitro* technique that mimics the replication of prions *in vivo* (Saborio, Permanne et al. 2001). Samples are subjected to cycles of incubation and sonication in the presence of PrP^{C} which accelerates the replication of PrP^{Sc} in the sample and can lead to a several-million fold increase in sensitivity (Saa, Castilla et al. 2006). PMCA experiments have been used successfully to detect PrP^{Sc} in pre-clinical hamster blood (Saa, Castilla et al. 2006).

2.15 Aims

The aim of this work is to develop and evaluate a mass spectrometry-based method to distinguish between the prion isoforms and assess the technique's potential to be used as an ante-mortem diagnostic test.

2.16 References

Aguzzi, A. and Heikenwalder, M. (2006). Pathogenesis of prion diseases: current status and future outlook. *Nature Reviews Microbiology* **4**, 765-75.

Aguzzi, A. and Polymenidou, M. (2004). Mammalian prion biology: one century of evolving concepts. *Cell* **116**, 313-27.

Alper, T., Cramp, W. A., Haig, D. A. and Clarke, M. C. (1967). Does the agent of scrapie replicate without nucleic acid? *Nature* **214**, 764-6.

Alper, T., Haig, D. A. and Clarke, M. C. (1966). The exceptionally small size of the scrapie agent. *Biochemical and Biophysical Research Communications* **22**, 278-84.

Barron, R. M., Thomson, V., Jamieson, E., Melton, D. W., Ironside, J., Will, R. and Manson, J. C. (2001). Changing a single amino acid in the N-terminus of murine PrP alters TSE incubation time across three species barriers. *Embo Journal* **20**, 5070-8.

Bessen, R. A., Raymond, G. J. and Caughey, B. (1997). In situ formation of protease-resistant prion protein in transmissible spongiform encephalopathy-infected brain slices. *Journal of Biological Chemistry* **272**, 15227-31.

Bishop, M. T., Hart, P., Aitchison, L., Baybutt, H. N., Plinston, C., Thomson, V., Tuzi, N. L., Head, M. W., Ironside, J. W., Will, R. G. and Manson, J. C. (2006). Predicting susceptibility and incubation time of human-to-human transmission of vCJD. *Lancet Neurology* **5**, 393-8.

Borchelt, D. R., Scott, M., Taraboulos, A., Stahl, N. and Prusiner, S. B. (1990). Scrapie and cellular prion proteins differ in their kinetics of synthesis and topology in cultured cells. *Journal of Cell Biology* **110**, 743-52.

Braak, H., Del Tredici, K., Rub, U., de Vos, R. A., Jansen Steur, E. N. and Braak, E. (2003). Staging of brain pathology related to sporadic Parkinson's disease. *Neurobiology of Aging* **24**, 197-211.

Brown, D. A. and Rose, J. K. (1992). Sorting of GPI-anchored proteins to glycolipid-enriched membrane subdomains during transport to the apical cell surface. *Cell* **68**, 533-44.

Brown, D. R., Qin, K. F., Herms, J. W., Madlung, A., Manson, J., Strome, R., Fraser, P. E., Kruck, T., vonBohlen, A., SchulzSchaeffer, W., Giese, A.,

Westaway, D. and Kretzschmar, H. (1997). The cellular prion protein binds copper in vivo. *Nature* **390**, 684-687.

Brown, D. R., Schulz-Schaeffer, W. J., Schmidt, B. and Kretzschmar, H. A. (1997). Prion protein-deficient cells show altered response to oxidative stress due to decreased SOD-1 activity. *Experimental Neurology* **146**, 104-12.

Brown, P., Goldfarb, L. G. and Gajdusek, D. C. (1991). The new biology of spongiform encephalopathy: infectious amyloidoses with a genetic twist. *Lancet* **337**, 1019-22.

Brown, P., Will, R. G., Bradley, R., Asher, D. M. and Detwiler, L. (2001). Bovine spongiform encephalopathy and variant Creutzfeldt-Jakob disease: background, evolution, and current concerns. *Emerging Infectious Diseases* **7**, 6-16.

Bueler, H., Fischer, M., Lang, Y., Bluethmann, H., Lipp, H. P., DeArmond, S. J., Prusiner, S. B., Aguet, M. and Weissmann, C. (1992). Normal development and behaviour of mice lacking the neuronal cell-surface PrP protein. *Nature* **356**, 577-82.

Calzolai, L., Lysek, D. A., Perez, D. R., Guntert, P. and Wuthrich, K. (2005). Prion protein NMR structures of chickens, turtles, and frogs. *Proceeding of the Natational Academy of Sciences U S A* **102**, 651-5.

Carlson, G. A., Ebeling, C., Yang, S. L., Telling, G., Torchia, M., Groth, D., Westaway, D., DeArmond, S. J. and Prusiner, S. B. (1994). Prion isolate specified allotypic interactions between the cellular and scrapie prion proteins in congenic and transgenic mice. *Proceeding of the Natational Academy of Sciences U S A* **91**, 5690-4.

Caughey, B. (1991). Cellular metabolism of normal and scrapie-associated forms of PrP. *Seminars in Virology* **2**, 189-196.

Caughey, B. (2001). Interactions between prion protein isoforms: the kiss of death? *Trends Biochemical Sciences* **26**, 235-42.

Caughey, B., Kocisko, D. A., Raymond, G. J. and Lansbury, P. T., Jr. (1995). Aggregates of scrapie-associated prion protein induce the cell-free conversion of protease-sensitive prion protein to the protease-resistant state. *Chemistry and Biology* **2**, 807-17.

Caughey, B., Race, R. E., Ernst, D., Buchmeier, M. J. and Chesebro, B. (1989). Prion protein biosynthesis in scrapie-infected and uninfected neuroblastoma cells. *Journal of Virology* **63**, 175-81.

Caughey, B. and Raymond, G. J. (1991). The scrapie-associated form of PrP is made from a cell surface precursor that is both protease- and phospholipase-sensitive. *Journal of Biological Chemistry* **266**, 18217-23.

Caughey, B., Raymond, G. J. and Bessen, R. A. (1998). Strain-dependent differences in beta-sheet conformations of abnormal prion protein. *Journal of Biological Chemistry* **273**, 32230-5.

Ceciliani, F. and Pergami, P. (2001). Infective proteins: the prion puzzle. *Current Protein and Peptide Science* **2**, 191-204.

Cervenakova, L., Goldfarb, L. G., Garruto, R., Lee, H. S., Gajdusek, D. C. and Brown, P. (1998). Phenotype-genotype studies in kuru: implications for new variant Creutzfeldt-Jakob disease. *Proceeding of the Natational Academy of Sciences U S A* **95**, 13239-41.

Chesebro, B. (2003). Introduction to the transmissible spongiform encephalopathies or prion diseases. *British Medical Bulletin* **66**, 1-20.

Choi, C. J., Kanthasamy, A., Anantharam, V. and Kanthasamy, A. G. (2006). Interaction of metals with prion protein: possible role of divalent cations in the pathogenesis of prion diseases. *Neurotoxicology* **27**, 777-87.

Christen, B., Hornemann, S., Damberger, F. F. and Wuthrich, K. (2009). Prion protein NMR structure from tammar wallaby (Macropus eugenii) shows that the beta2-alpha2 loop is modulated by long-range sequence effects. *Journal of Molecular Biology* **389**, 833-45.

Christen, B., Perez, D. R., Hornemann, S. and Wuthrich, K. (2008). NMR structure of the bank vole prion protein at 20 degrees C contains a structured loop of residues 165-171. *Journal of Molecular Biology* **383**, 306-12.

CJD http://www.cjd.ed.ac.uk/.

Cohen, F. E., Pan, K.-M., Huang, Z., Baldwin, M., Fletterick, R. J. and Prusiner, S. B. (1994). Structural Clues to Prion Replication. *Science* **264**, 530-531.

Collee, J. G. and Bradley, R. (1997). BSE: a decade on--Part I. *Lancet* **349**, 636-41.

Collinge, J. (1999). Variant Creutzfeldt-Jakob disease. *Lancet* **354**, 317-23.

Collinge, J. and Palmer, M. S. (1992). Prion diseases. *Current Opinion in Genetics and Development* **2**, 448-54.

Collinge, J., Whittington, M. A., Sidle, K. C., Smith, C. J., Palmer, M. S., Clarke, A. R. and Jefferys, J. G. (1994). Prion protein is necessary for normal synaptic function. *Nature* **370**, 295-7.

Collins, S., McLean, C. A. and Masters, C. L. (2001). Gerstmann-Straussler-Scheinker syndrome,fatal familial insomnia, and kuru: a review of these less common human transmissible spongiform encephalopathies. *Journal of Clinical Neuroscience* **8**, 387-97.

Collins, S. J., Lawson, V. A. and Masters, C. L. (2004). Transmissible spongiform encephalopathies. *Lancet* **363**, 51-61.

Crowther, D. C. (2002). Familial conformational diseases and dementias. *Human Mutation* **20**, 1-14.

Cuervo, A. M., Stefanis, L., Fredenburg, R., Lansbury, P. T. and Sulzer, D. (2004). Impaired degradation of mutant alpha-synuclein by chaperone-mediated autophagy. *Science* **305**, 1292-5.

d'Aignaux, J. N., Cousens, S. N. and Smith, P. G. (2001). Predictability of the UK variant Creutzfeldt-Jakob disease epidemic. *Science* **294**, 1729-31.

Dabaghian, R. H., Mortimer, P. P. and Clewley, J. P. (2004). Prospects for the development of pre-mortem laboratory diagnostic tests for Creutzfeldt-Jakob disease. *Reviews in Medical Virology* **14**, 345-61.

DebBurman, S. K., Raymond, G. J., Caughey, B. and Lindquist, S. (1997). Chaperone-supervised conversion of prion protein to its protease-resistant form. *Proceeding of the Natational Academy of Sciences U S A* **94**, 13938-43.

Desplats, P., Lee, H. J., Bae, E. J., Patrick, C., Rockenstein, E., Crews, L., Spencer, B., Masliah, E. and Lee, S. J. (2009). Inclusion formation and neuronal cell death through neuron-to-neuron transmission of alpha-synuclein. *Proceeding of the Natational Academy of Sciences U S A* **106**, 13010-5.

Dickinson, A. G. and Meikle, V. M. (1971). Host-genotype and agent effects in scrapie incubation: change in allelic interaction with different strains of agent. *Molecular and General Genetics* **112**, 73-9.

Donne, D. G., Viles, J. H., Groth, D., Mehlhorn, I., James, T. L., Cohen, F. E., Prusiner, S. B., Wright, P. E. and Dyson, H. J. (1997). Structure of the recombinant full-length hamster prion protein PrP(29-231): the N terminus is

highly flexible. *Proceeding of the Natational Academy of Sciences U S A* **94**, 13452-7.

Forloni, G., Angeretti, N., Chiesa, R., Monzani, E., Salmona, M., Bugiani, O. and Tagliavini, F. (1993). Neurotoxicity of a prion protein fragment. *Nature* **362**, 543-6.

Gabizon, R., McKinley, M. P., Groth, D. and Prusiner, S. B. (1988). Immunoaffinity purification and neutralization of scrapie prion infectivity. *Proceeding of the Natational Academy of Sciences U S A* **85**, 6617-21.

Gabrielsson, B., Robson, T., Norris, D. and Chung, S. H. (1986). Effects of divalent metal ions on the uptake of glutamate and GABA from synaptosomal fractions. *Brain Research* **384**, 218-23.

Gajdusek, D. C. (1977). Unconventional viruses and the origin and disappearance of kuru. *Science* **197**, 943-60.

Gajdusek, D. C., Gibbs, C. J. and Alpers, M. (1966). Experimental transmission of a Kuru-like syndrome to chimpanzees. *Nature* **209**, 794-6.

Gambetti, P., Dong, Z., Yuan, J., Xiao, X., Zheng, M., Alshekhlee, A., Castellani, R., Cohen, M., Barria, M. A., Gonzalez-Romero, D., Belay, E. D., Schonberger, L. B., Marder, K., Harris, C., Burke, J. R., Montine, T., Wisniewski, T., Dickson, D. W., Soto, C., Hulette, C. M., Mastrianni, J. A., Kong, Q. and Zou, W. Q. (2008). A novel human disease with abnormal prion protein sensitive to protease. *Annual Neurology* **63**, 697-708.

Georgieff, M. K. (2007). Nutrition and the developing brain: nutrient priorities and measurement. *American Journal of Clinical Nutrition* **85**, 614S-620.

Gibbs, C. J., Jr., Gajdusek, D. C., Asher, D. M., Alpers, M. P., Beck, E., Daniel, P. M. and Matthews, W. B. (1968). Creutzfeldt-Jakob disease (spongiform encephalopathy): transmission to the chimpanzee. *Science* **161**, 388-9.

Goldfarb, L. G., Brown, P., Mitrova, E., Cervenakova, L., Goldin, L., Korczyn, A. D., Chapman, J., Galvez, S., Cartier, L., Rubenstein, R. and et al. (1991). Creutzfeldt-Jacob disease associated with the PRNP codon 200Lys mutation: an analysis of 45 families. *European Journal of Epidemiology* **7**, 477-86.

Gossert, A. D., Bonjour, S., Lysek, D. A., Fiorito, F. and Wuthrich, K. (2005). Prion protein NMR structures of elk and of mouse/elk hybrids. *Proceeding of the Natational Academy of Sciences U S A* **102**, 646-50.

Hadlow, W. J. (1959a). Myopathies of livestock. *Laboratory Investigation* **8**, 1478-98.

Hadlow, W. J. (1959b). SCRAPIE AND KURU. *The Lancet* **274**, 289-290.

Harrison, P. M., Bamborough, P., Daggett, V., Prusiner, S. B. and Cohen, F. E. (1997). The prion folding problem. *Current Opinion in Structural Biology* **7**, 53-9.

Hilton, D. A., Ghani, A. C., Conyers, L., Edwards, P., McCardle, L., Ritchie, D., Penney, M., Hegazy, D. and Ironside, J. W. (2004). Prevalence of lymphoreticular prion protein accumulation in UK tissue samples. *Journal of Pathology* **203**, 733-9.

Horiuchi, M. and Caughey, B. (1999). Specific binding of normal prion protein to the scrapie form via a localized domain initiates its conversion to the protease-resistant state. *Embo J* **18**, 3193-203.

Hornemann, S., Korth, C., Oesch, B., Riek, R., Wider, G., Wuthrich, K. and Glockshuber, R. (1997). Recombinant full-length murine prion protein, mPrP(23-231): purification and spectroscopic characterization. *FEBS Lett* **413**, 277-81.

Hornemann, S., Schorn, C. and Wuthrich, K. (2004). NMR structure of the bovine prion protein isolated from healthy calf brains. *EMBO Reports* **5**, 1159-64.

Horwich, A. L. and Weissman, J. S. (1997). Deadly conformations--protein misfolding in prion disease. *Cell* **89**, 499-510.

Hosszu, L. L., Trevitt, C. R., Jones, S., Batchelor, M., Scott, D. J., Jackson, G. S., Collinge, J., Waltho, J. P. and Clarke, A. R. (2009). Conformational Properties of {beta}-PrP. *Journal of Biological Chemistry* **284**, 21981-90.

Houston, F., Foster, J. D., Chong, A., Hunter, N. and Bostock, C. J. (2000). Transmission of BSE by blood transfusion in sheep. *Lancet* **356**, 999-1000.

Hsiao, K., Baker, H. F., Crow, T. J., Poulter, M., Owen, F., Terwilliger, J. D., Westaway, D., Ott, J. and Prusiner, S. B. (1989). Linkage of a prion protein missense variant to Gerstmann-Straussler syndrome. *Nature* **338**, 342-5.

Hsiao, K. K., Groth, D., Scott, M., Yang, S. L., Serban, H., Rapp, D., Foster, D., Torchia, M., Dearmond, S. J. and Prusiner, S. B. (1994). Serial transmission in rodents of neurodegeneration from transgenic mice expressing mutant prion protein. *Proceeding of the Natational Academy of Sciences U S A* **91**, 9126-30.

Huang, Z., Gabriel, J. M., Baldwin, M. A., Fletterick, R. J., Prusiner, S. B. and Cohen, F. E. (1994). Proposed three-dimensional structure for the cellular prion protein. *Proceeding of the Natational Academy of Sciences U S A* **91**, 7139-43.

Huang, Z., Prusiner, S. B. and Cohen, F. E. (1995). Scrapie prions: a three-dimensional model of an infectious fragment. *Folding and Design* **1**, 13-9.

Hunter, N., Foster, J., Chong, A., McCutcheon, S., Parnham, D., Eaton, S., MacKenzie, C. and Houston, F. (2002). Transmission of prion diseases by blood transfusion. *Journal of General Virology* **83**, 2897-905.

James, T. L., Liu, H., Ulyanov, N. B., Farr-Jones, S., Zhang, H., Donne, D. G., Kaneko, K., Groth, D., Mehlhorn, I., Prusiner, S. B. and Cohen, F. E. (1997). Solution structure of a 142-residue recombinant prion protein corresponding to the infectious fragment of the scrapie isoform. *Proceeding of the Natational Academy of Sciences U S A* **94**, 10086-91.

Jarrett, J. T. and Lansbury, P. T., Jr. (1993). Seeding "one-dimensional crystallization" of amyloid: a pathogenic mechanism in Alzheimer's disease and scrapie? *Cell* **73**, 1055-8.

Kellings, K., Meyer, N., Mirenda, C., Prusiner, S. B. and Riesner, D. (1992). Further analysis of nucleic acids in purified scrapie prion preparations by improved return refocusing gel electrophoresis. *Journal of General Virology* **73 (Pt 4)**, 1025-9.

Kellings, K., Prusiner, S. B. and Riesner, D. (1994). Nucleic acids in prion preparations: unspecific background or essential component? *Philos Trans R Soc Lond B Biol Sci* **343**, 425-30.

Khamsi, R. (2006). Prion disease: the shape of things to come. *Nature* **439**, 134-5.

Kimberlin, R. H. (1990). Bovine spongiform encephalopathy. Taking stock of the issues. *Nature* **345**, 763-4.

King, C. Y. and Diaz-Avalos, R. (2004). Protein-only transmission of three yeast prion strains. *Nature* **428**, 319-23.

Klatzo, I., Gajdusek, D. C. and Zigas, V. (1959). Pathology of Kuru. *Laboratory Investigations* **8**, 799-847.

Kocisko, D. A., Priola, S. A., Raymond, G. J., Chesebro, B., Lansbury, P. T., Jr. and Caughey, B. (1995). Species specificity in the cell-free conversion of prion protein to protease-resistant forms: a model for the scrapie species barrier. *Proceeding of the Natational Academy of Sciences U S A* **92**, 3923-7.

Krakauer, D. C., Pagel, M., Southwood, T. R. and Zanotto, P. M. (1996). Phylogenesis of prion protein. *Nature* **380**, 675.

Latarjet, R., Muel, B., Haig, D. A., Clarke, M. C. and Alper, T. (1970). Inactivation of the scrapie agent by near monochromatic ultraviolet light. *Nature* **227**, 1341-3.

Lee, H. S., Brown, P., Cervenakova, L., Garruto, R. M., Alpers, M. P., Gajdusek, D. C. and Goldfarb, L. G. (2001). Increased susceptibility to Kuru of carriers of the PRNP 129 methionine/methionine genotype. *Journal of Infectious Diseases* **183**, 192-196.

Lehmann, S. and Harris, D. A. (1997). Blockade of glycosylation promotes acquisition of scrapie-like properties by the prion protein in cultured cells. *Journal of Biological Chemistry* **272**, 21479-87.

Linden, R., Martins, V. R., Prado, M. A., Cammarota, M., Izquierdo, I. and Brentani, R. R. (2008). Physiology of the prion protein. *Physiol Rev* **88**, 673-728.

Linder, M. C. and Hazegh-Azam, M. (1996). Copper biochemistry and molecular biology. *American Journal of Clinical Nutrition* **63**, 797S-811.

Liu, H., Farr-Jones, S., Ulyanov, N. B., Llinas, M., Marqusee, S., Groth, D., Cohen, F. E., Prusiner, S. B. and James, T. L. (1999). Solution structure of Syrian hamster prion protein rPrP(90-231). *Biochemistry* **38**, 5362-77.

Lopez Garcia, F., Zahn, R., Riek, R. and Wuthrich, K. (2000). NMR structure of the bovine prion protein. *Proceeding of the Natational Academy of Sciences U S A* **97**, 8334-9.

Lysek, D. A., Schorn, C., Nivon, L. G., Esteve-Moya, V., Christen, B., Calzolai, L., von Schroetter, C., Fiorito, F., Herrmann, T., Guntert, P. and Wuthrich, K. (2005). Prion protein NMR structures of cats, dogs, pigs, and sheep. *Proceeding of the Natational Academy of Sciences U S A* **102**, 640-5.

Manuelidis, L., Sklaviadis, T., Akowitz, A. and Fritch, W. (1995). Viral particles are required for infection in neurodegenerative Creutzfeldt-Jakob disease. *Proceeding of the Natational Academy of Sciences U S A* **92**, 5124-8.

Martin, J. B. (1999). Molecular basis of the neurodegenerative disorders. *New England Journal of Medicine* **340**, 1970-80.

McNaught, K. S., Olanow, C. W., Halliwell, B., Isacson, O. and Jenner, P. (2001). Failure of the ubiquitin-proteasome system in Parkinson's disease. *Nature Reviews Neuroscience* **2**, 589-94.

Mead, S., Poulter, M., Uphill, J., Beck, J., Whitfield, J., Webb, T. E., Campbell, T., Adamson, G., Deriziotis, P., Tabrizi, S. J., Hummerich, H., Verzilli, C., Alpers, M. P., Whittaker, J. C. and Collinge, J. (2009). Genetic risk factors for variant Creutzfeldt-Jakob disease: a genome-wide association study. *Lancet Neurol* **8**, 57-66.

Mead, S., Stumpf, M. P., Whitfield, J., Beck, J. A., Poulter, M., Campbell, T., Uphill, J. B., Goldstein, D., Alpers, M., Fisher, E. M. and Collinge, J. (2003). Balancing selection at the prion protein gene consistent with prehistoric kurulike epidemics. *Science* **300**, 640-3.

Meyer, R. K., McKinley, M. P., Bowman, K. A., Braunfeld, M. B., Barry, R. A. and Prusiner, S. B. (1986). Separation and properties of cellular and scrapie prion proteins. *Proceeding of the Natational Academy of Sciences U S A* **83**, 2310-4.

Morillas, M., Swietnicki, W., Gambetti, P. and Surewicz, W. K. (1999). Membrane environment alters the conformational structure of the recombinant human prion protein. *Journal of Biological Chemistry* **274**, 36859-65.

Naslavsky, N., Stein, R., Yanai, A., Friedlander, G. and Taraboulos, A. (1997). Characterization of detergent-insoluble complexes containing the cellular prion protein and its scrapie isoform. *Journal of Biological Chemistry* **272**, 6324-31.

Oesch, B., Westaway, D., Walchli, M., McKinley, M. P., Kent, S. B., Aebersold, R., Barry, R. A., Tempst, P., Teplow, D. B., Hood, L. E. and et al. (1985). A cellular gene encodes scrapie PrP 27-30 protein. *Cell* **40**, 735-46.

Olanow, C. W. and Prusiner, S. B. (2009). Is Parkinson's disease a prion disorder? *Proceeding of the Natational Academy of Sciences U S A* **106**, 12571-2.

Pan, K. M., Baldwin, M., Nguyen, J., Gasset, M., Serban, A., Groth, D., Mehlhorn, I., Huang, Z., Fletterick, R. J., Cohen, F. E. and et al. (1993). Conversion of alpha-helices into beta-sheets features in the formation of the scrapie prion proteins. *Proceeding of the Natational Academy of Sciences U S A* **90**, 10962-6.

Paramithiotis, E., Pinard, M., Lawton, T., LaBoissiere, S., Leathers, V. L., Zou, W. Q., Estey, L. A., Lamontagne, J., Lehto, M. T., Kondejewski, L. H., Francoeur, G. P., Papadopoulos, M., Haghighat, A., Spatz, S. J., Head, M., Will, R., Ironside, J., O'Rourke, K., Tonelli, Q., Ledebur, H. C.,

Chakrabartty, A. and Cashman, N. R. (2003). A prion protein epitope selective for the pathologically misfolded conformation. *Nature Medicine* **9**, 893-9.

Parkinsons www.parkinsons.org.uk.

Peden, A. H., Head, M. W., Diane, L. R., Jeanne, E. B. and James, W. I. (2004). Preclinical vCJD after blood transfusion in a PRNP codon 129 heterozygous patient. *The Lancet* **364**, 527-529.

Pillot, T., Lins, L., Goethals, M., Vanloo, B., Baert, J., Vandekerckhove, J., Rosseneu, M. and Brasseur, R. (1997). The 118-135 peptide of the human prion protein forms amyloid fibrils and induces liposome fusion. *Journal of Molecular Biology* **274**, 381-93.

Prusiner, S. B. (1982). Novel proteinaceous infectious particles cause scrapie. *Science* **216**, 136-44.

Prusiner, S. B. (1995). The prion diseases. *Scientific American* **272**, 48-51, 54-7.

Prusiner, S. B. (1996). Molecular biology and pathogenesis of prion diseases. *Trends Biochemical Science* **21**, 482-7.

Prusiner, S. B. (1998). Prions. *Proceeding of the Natational Academy of Sciences U S A* **95**, 13363-83.

Prusiner, S. B. (1999). Prion Biology and Diseases, Cold Spring Harbour Laboratory Press.

Prusiner, S. B., McKinley, M. P., Bowman, K. A., Bolton, D. C., Bendheim, P. E., Groth, D. F. and Glenner, G. G. (1983). Scrapie prions aggregate to form amyloid-like birefringent rods. *Cell* **35**, 349-58.

Prusiner, S. B., Scott, M., Foster, D., Pan, K. M., Groth, D., Mirenda, C., Torchia, M., Yang, S. L., Serban, D., Carlson, G. A. and et al. (1990). Transgenetic studies implicate interactions between homologous PrP isoforms in scrapie prion replication. *Cell* **63**, 673-86.

Race, R. E., Fadness, L. H. and Chesebro, B. (1987). Characterization of scrapie infection in mouse neuroblastoma cells. *Journal of General Virology* **68 (Pt 5)**, 1391-9.

Raymond, G. J., Bossers, A., Raymond, L. D., O'Rourke, K. I., McHolland, L. E., Bryant, P. K., 3rd, Miller, M. W., Williams, E. S., Smits, M. and Caughey, B. (2000). Evidence of a molecular barrier limiting susceptibility of humans, cattle and sheep to chronic wasting disease. *Embo J* **19**, 4425-30.

Riek, R., Hornemann, S., Wider, G., Billeter, M., Glockshuber, R. and Wuthrich, K. (1996). NMR structure of the mouse prion protein domain PrP(121-321). *Nature* **382**, 180-2.

Riek, R., Hornemann, S., Wider, G., Glockshuber, R. and Wuthrich, K. (1997). NMR characterization of the full-length recombinant murine prion protein, mPrP(23-231). *FEBS Lett* **413**, 282-8.

Rogers, M., Yehiely, F., Scott, M. and Prusiner, S. B. (1993). Conversion of truncated and elongated prion proteins into the scrapie isoform in cultured cells. *Proceeding of the Natational Academy of Sciences U S A* **90**, 3182-6.

Rubenstein, R., Carp, R. I. and Callahan, S. M. (1984). In vitro replication of scrapie agent in a neuronal model: infection of PC12 cells. *Journal of General Virology* **65 (Pt 12)**, 2191-8.

Saa, P., Castilla, J. and Soto, C. (2006). Presymptomatic detection of prions in blood. *Science* **313**, 92-4.

Saborio, G. P., Permanne, B. and Soto, C. (2001). Sensitive detection of pathological prion protein by cyclic amplification of protein misfolding. *Nature* **411**, 810-3.

Safar, J., Ceroni, M., Gajdusek, D. C. and Gibbs, C. J., Jr. (1991). Differences in the membrane interaction of scrapie amyloid precursor proteins in normal and scrapie- or Creutzfeldt-Jakob disease-infected brains. *Journal of Infectious Diseases* **163**, 488-94.

Safar, J., Roller, P. P., Gajdusek, D. C. and Gibbs, C. J., Jr. (1993). Conformational transitions, dissociation, and unfolding of scrapie amyloid (prion) protein. *Journal of Biological Chemistry* **268**, 20276-84.

Safar, J., Roller, P. P., Gajdusek, D. C. and Gibbs, C. J., Jr. (1994). Scrapie amyloid (prion) protein has the conformational characteristics of an aggregated molten globule folding intermediate. *Biochemistry* **33**, 8375-83.

Safar, J., Wille, H., Itri, V., Groth, D., Serban, H., Torchia, M., Cohen, F. E. and Prusiner, S. B. (1998). Eight prion strains have PrP(Sc) molecules with different conformations. *Nature Medicine* **4**, 1157-65.

Schatzl, H. M., Da Costa, M., Taylor, L., Cohen, F. E. and Prusiner, S. B. (1995). Prion protein gene variation among primates. *Journal of Molecular Biology* **245**, 362-74.

Scott, M. R., Kohler, R., Foster, D. and Prusiner, S. B. (1992). Chimeric prion protein expression in cultured cells and transgenic mice. *Protein Science* **1**, 986-97.

Serbec, V. C., Bresjanac, M., Popovic, M., Hartman, K. P., Galvani, V., Rupreht, R., Cernilec, M., Vranac, T., Hafner, I. and Jerala, R. (2004). Monoclonal Antibody against a Peptide of Human Prion Protein Discriminates between Creutzfeldt-Jacob's Disease-affected and Normal Brain Tissue. *Journal of Biological Chemistry* **279**, 3694-3698.

Snyder, H., Mensah, K., Theisler, C., Lee, J., Matouschek, A. and Wolozin, B. (2003). Aggregated and monomeric alpha-synuclein bind to the S6' proteasomal protein and inhibit proteasomal function. *Journal of Biological Chemistry* **278**, 11753-9.

Soto, C. (2003). Unfolding the role of protein misfolding in neurodegenerative diseases. *Nature Reviews Neuroscience* **4**, 49-60.

Soto, C. (2004). Diagnosing prion diseases: needs, challenges and hopes. *Nature Reviews Microbiology* **2**, 809-19.

Soto, C. and Castilla, J. (2004). The controversial protein-only hypothesis of prion propagation. *Nature Medicine* **10 Suppl**, S63-7.

Spencer, M. D., Knight, R. S. and Will, R. G. (2002). First hundred cases of variant Creutzfeldt-Jakob disease: retrospective case note review of early psychiatric and neurological features. *British Medical Journal* **324**, 1479-82.

Stahl, N., Borchelt, D. R., Hsiao, K. and Prusiner, S. B. (1987). Scrapie prion protein contains a phosphatidylinositol glycolipid. *Cell* **51**, 229-40.

Stahl, N., Borchelt, D. R. and Prusiner, S. B. (1990). Differential release of cellular and scrapie prion proteins from cellular membranes by phosphatidylinositol-specific phospholipase C. *Biochemistry* **29**, 5405-12.

Tanaka, M., Chien, P., Naber, N., Cooke, R. and Weissman, J. S. (2004). Conformational variations in an infectious protein determine prion strain differences. *Nature* **428**, 323-8.

Tanaka, M., Collins, S. R., Toyama, B. H. and Weissman, J. S. (2006). The physical basis of how prion conformations determine strain phenotypes. *Nature* **442**, 585-9.

Taraboulos, A., Scott, M., Semenov, A., Avrahami, D., Laszlo, L. and Prusiner, S. B. (1995). Cholesterol depletion and modification of COOH-terminal targeting

sequence of the prion protein inhibit formation of the scrapie isoform. *Journal of Cell Biology* **129**, 121-32.

Telling, G. C., Parchi, P., DeArmond, S. J., Cortelli, P., Montagna, P., Gabizon, R., Mastrianni, J., Lugaresi, E., Gambetti, P. and Prusiner, S. B. (1996). Evidence for the conformation of the pathologic isoform of the prion protein enciphering and propagating prion diversity. *Science* **274**, 2079-82.

Tobler, I., Gaus, S. E., Deboer, T., Achermann, P., Fischer, M., Rulicke, T., Moser, M., Oesch, B., McBride, P. A. and Manson, J. C. (1996). Altered circadian activity rhythms and sleep in mice devoid of prion protein. *Nature* **380**, 639-42.

Valleron, A. J., Boelle, P. Y., Will, R. and Cesbron, J. Y. (2001). Estimation of epidemic size and incubation time based on age characteristics of vCJD in the United Kingdom. *Science* **294**, 1726-8.

Vassallo, N. and Herms, J. (2003). Cellular prion protein function in copper homeostasis and redox signalling at the synapse. *Journal of Neurochemistry* **86**, 538-44.

Vey, M., Pilkuhn, S., Wille, H., Nixon, R., DeArmond, S. J., Smart, E. J., Anderson, R. G., Taraboulos, A. and Prusiner, S. B. (1996). Subcellular colocalization of the cellular and scrapie prion proteins in caveolae-like membranous domains. *Proceeding of the Natational Academy of Sciences U S A* **93**, 14945-9.

Viles, J. H., Cohen, F. E., Prusiner, S. B., Goodin, D. B., Wright, P. E. and Dyson, H. J. (1999). Copper binding to the prion protein: structural implications of four identical cooperative binding sites. *Proceeding of the Natational Academy of Sciences U S A* **96**, 2042-7.

Weissmann, C. (1991). A 'unified theory' of prion propagation. *Nature* **352**, 679-83.

Weissmann, C. (1996). The Ninth Datta Lecture. Molecular biology of transmissible spongiform encephalopathies. *FEBS Lett* **389**, 3-11.

Weissmann, C. (1999). Molecular Genetics of Transmissible Spongiform Encephalopathies. *Journal of Biological Chemistry* **274**, 3-6.

Will, R. G., Ironside, J. W., Zeidler, M., Cousens, S. N., Estibeiro, K., Alperovitch, A., Poser, S., Pocchiari, M., Hofman, A. and Smith, P. G. (1996). A new variant of Creutzfeldt-Jakob disease in the UK. *Lancet* **347**, 921-5.

Wille, H., Michelitsch, M. D., Guenebaut, V., Supattapone, S., Serban, A., Cohen, F. E., Agard, D. A. and Prusiner, S. B. (2002). Structural studies of the scrapie prion protein by electron crystallography. *Proceeding of the Natational Academy of Sciences U S A* **99**, 3563-8.

Williamson, R. A., Peretz, D., Smorodinsky, N., Bastidas, R., Serban, H., Mehlhorn, I., DeArmond, S. J., Prusiner, S. B. and Burton, D. R. (1996). Circumventing tolerance to generate autologous monoclonal antibodies to the prion protein. *Proceeding of the Natational Academy of Sciences U S A* **93**, 7279-82.

Windl, O., Dempster, M., Estibeiro, J. P., Lathe, R., de Silva, R., Esmonde, T., Will, R., Springbett, A., Campbell, T. A., Sidle, K. C., Palmer, M. S. and Collinge, J. (1996). Genetic basis of Creutzfeldt-Jakob disease in the United Kingdom: a systematic analysis of predisposing mutations and allelic variation in the PRNP gene. *Human Genetics* **98**, 259-64.

Yedidia, Y., Horonchik, L., Tzaban, S., Yanai, A. and Taraboulos, A. (2001). Proteasomes and ubiquitin are involved in the turnover of the wild-type prion protein. *Embo J* **20**, 5383-91.

Zahn, R., Liu, A., Luhrs, T., Riek, R., von Schroetter, C., Lopez Garcia, F., Billeter, M., Calzolai, L., Wider, G. and Wuthrich, K. (2000). NMR solution structure of the human prion protein. *Proceeding of the Natational Academy of Sciences U S A* **97**, 145-50.

Zou, W. Q., Zheng, J., Gray, D. M., Gambetti, P. and Chen, S. G. (2004). Antibody to DNA detects scrapie but not normal prion protein. *Proceeding of the Natational Academy of Sciences U S A* **101**, 1380-5.

Chapter 3

Materials and Methods

This chapter is divided into two sections. The first section describes the expression and purification of recombinant prion proteins and the characterisation methods used to study their structure. The second section describes the materials and methods used to characterise synthetic polymers.

3.1 Prions

3.2 Material Suppliers

All chemical reagents were of analytical grade and obtained from the following sources unless otherwise stated:

- American Type Culture Collection (USA)
- BHD Lab Supplies (UK)
- Bio-rad Laboratories (UK)
- Fisher Scientific (UK)
- Fluka Chemika (UK)
- GE Healthcare (UK)
- Melford Laboratories Ltd (UK)
- Merck kGaA (Germany)
- Qiagen (UK)
- Sigma Aldrich (UK)

Dialysis tubing with a 7000 molecular weight cut-off was obtained from Medicell International Ltd (London, UK). Spin columns with a 10,000 molecular weight cut-off were obtained from Millipore Corporate (Watford, UK). Coomassie protein assay reagents and molecular weight markers were obtained from Pierce (Illinois, USA). All other chemicals were purchased from Sigma-Aldrich (Poole, UK) unless otherwise stated.

3.3 Safety

All recombinant PrP expression procedures were carried out in a containment level three laboratory. Recombinant PrP was expressed in *Escherichia coli* and all cells were harvested and disrupted whilst in the containment level three laboratory. The recombinant PrP was solubilised in 8 M GdnHCl and filtered through a 0.22 μM membrane before it was removed from the containment laboratory. Further protein purification was carried out under a class II hood. Decontamination and disposal of waste was carried out in accordance to the Health and Safety Executive guidelines

"Precautions for work with human and animal transmissible spongiform encephalopathies".

3.4 Expression, purification, and refolding SHaPrP(90-231)

Recombinant Syrian hamster prion protein SHaPrP(90–231) was expressed using an alkaline phosphatase promoter in a protease-deficient strain of *E. coli* 27C7 as described by Mehlhorn *et al* (Mehlhorn, Groth et al. 1996). The prion protein was purified from inclusion bodies and refolded into an α-helical structure (α-SHaPrP(90-231)) under oxidising conditions, as previously described (Sanghera and Pinheiro 2002).

The conversion of α-SHaPrP(90-231) to β-sheet-rich structures was carried out using a similar protocol to that described by Martins *et al*., (Martins, Frosoni et al. 2006). 100 μM of recombinant α-SHaPrP(90-231) in 5 mM ammonium formate, pH 5.5 buffer was incubated at 70 °C for 24 hr.

3.5 Expression, purification, and refolding SHaPrP(23-231)

The plasmid (pTrc) encoding full-length SHaPrP(23-231) was transformed into in *E. coli* strain BL21* Rosetta. Transformed cells were grown in 1 L of Terrific Broth supplemented with 100 μg/mL ampicillin and 35 μg/mL chlorampenicol until an absorbance of 0.6 at 600 nm was reached. Protein expression was induced by the addition of isopropyl thio-β-D-galactoside to a final concentration of 1 mM and the cultures were grown for a further 4 hours. The recombinant protein accumulated in inclusion bodies within the cytoplasm. The protocol for the purification of PrP was adapted from Bocharova *et al.,* (Bocharova, Breydo et al. 2005). Briefly, the cells were harvested by centrifugation at 4000 rpm for 30 min at 4 °C and re-suspended in cell lysis buffer; 50 mM Tris / 1 mM EDTA / 100 mM NaCl, pH 8.0 containing 0.2 mg/mL lysozyme, 1 mg / mL deoxycholic acid and 10 μg / mL DNase. Cells were lysed by stirring at 4 °C for 3 hours and centrifuged at 15000 rpm for 15 mins to

isolate the inclusion bodies containing PrP. The inclusion bodies were solubilised in buffer consisting of 8 M urea / 10 mM TrisHCl / 100 mM sodium phosphate containing 10 mM β-mercaptoethanol, pH 8.0 and centrifuged at 15000 rpm for 15 mins to remove insoluble material. The solublised inclusion bodies were applied to a Ni-NTA column (Qiagen) and eluted with 8 M urea, 10 mM Tris / HCl, 100 mM sodium phosphate and 10 mM β-mercaptoethanol, pH 4.5. Fractions containing PrP, as identified on SDS PAGE gels, were pooled and diluted 2 fold with 50 mM HEPES, pH 8.0 buffer containing 8 M urea and 10 mM DTT and incubated overnight at 4 °C. PrP was further purified by application to a cation exchange column (SP-Sepharose, Amersham Biosciences) and eluted with a 50 mM HEPES buffer, pH 8.0 containing 8 M urea and 1.5 M NaCl. Fractions containing PrP were pooled and diluted to 0.1 – 0.5 mg/mL with 50 mM HEPES buffer containing 8 M urea and oxidised using a 5 M excess of Cu^{2+}. The protein solution was stirred overnight and refolded the following day by dialysis into four changes of 5 mM MES, pH 5.0 containing 10 mM EDTA. Protein was concentrated and PrP concentration was determined spectrophotometrically using an extinction coefficient of ε_{280} 61,240 mol^{-1} dm^3 cm^{-1}.

3.6 Expression, purification, and refolding Mouse and Ovine PrP

Expression and purification of MoPrP(90-231), MoPrP(23-231) and OvPrP(23-231) were carried out by Dr Narinder Sanghera (Department of Biological Sciences, University of Warwick, UK). The plasmid (pET 23a) encoding MoPrP was transformed into in *E. coli* strain BL21* Rosetta and recombinant ovine prion protein was expressed using an alkaline phosphatase promoter in a protease-deficient strain of *E. coli* 1B 392. The expression and purification procedure was the same as the full-length SHaPrP(23-231) described above.

3.7 Synthesis and purification of bovine octapeptide (BovPrP(57-101)

The synthetic peptide was provided by Dr Andrew Gill (Neuropathogenesis Division, Roslin Institute, University of Edinburgh, UK). All work was undertaken in the proteomics facility of the Institute for Animal Health and a brief description of the procedure is described below. A model peptide mimicking the N-terminal octapeptide repeat region of PrP was synthesised by standard Fmoc-chemistry by means of an automated pioneer synthesiser (Perseptive Biosystems). The peptide sequence was $(GGGWGQPH)_5GGGGW$. After synthesis, peptides were purified on a reversed-phase C18 HPLC column, lyophilised and checked for identity and purity by means of ESI-MS and ESI-MS/MS.

3.8 Characterisation of purified recombinant PrP

Various analytical methods were used to study the purity and secondary structure of the refolded recombinant samples.

3.8.1 SDS-polyacrylamide gel electrophoresis

The sample purity and molecular weight of the recombinant proteins were analysed by means of 15% mini polyacrylamide gels. Each sample was mixed with sample buffer and heated to 100°C for 5 min until denatured. All gels were visualised using Coomassie brilliant blue. The presence of a single protein band on the gel, within the correct molecular weight range, suggested a high purity of the sample (see Figure 3.1). The exact molecular weight of the prion protein was determined by means of mass spectrometry.

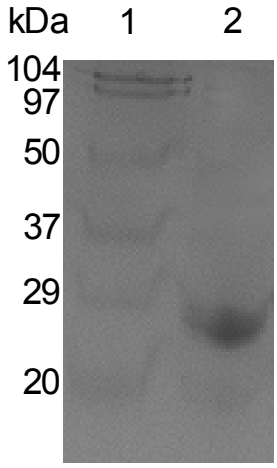

Figure 3.1: Coomassie stained 15% polacrylamide gel. Lane: (1) Molecular weight standards. (2) Purified SHaPrP(23-231).

3.8.2 Infrared spectroscopy

The secondary structure of the refolded proteins was analysed by means of infrared spectroscopy. Attenuated total reflection (ATR) Fourier transform infrared (FTIR) spectra were acquired on a Bruker Vector 22 spectrometer equipped with a liquid nitrogen cooled mercury cadmium telluride (MCT) detector (Bruker, Coventry, UK). Spectra were recorded at room temperature at a nominal resolution of 4 cm^{-1} in the range 4000–1000 cm^{-1}. The spectral contribution of atmospheric water was minimised by the continuous purging of the sample chamber with dried air (Jun-Air; Kent, UK). Residual water vapour peaks were subtracted using reference spectra and baseline correction was applied when necessary. The internal reflection element was a germanium ATR plate (50 x 20 x 2 mm) with an aperture angle of 45°, yielding 25 internal reflections.

A 50 μL aliquot of sample containing ~ 10 μM SHaPrP(90-231) in 5 mM ammonium formate buffer, pH 5.5 was deposited on the ATR plate. A thin hydrated protein film was obtained by slowly evaporating the excess water under a stream of N_2 gas. All ATR FTIR spectra were collected after a short period of H_2O/D_2O exchange in order to aid the analysis of protein secondary structure (Goormaghtigh, Cabiaux et al. 1990). Deposited protein films were subjected to a stream of D_2O-saturated nitrogen gas for 10 minutes.

3.8.3 Circular dichroism

Far-UV (190–260 nm) CD spectra of SHaPrP(90-231), SHaPrP(23-231), MoPrP(90-230), MoPrP(23-230), OvPrP(23-231) (10 μM) and were measured on a JASCO J-815 spectropolarimeter using 1 mm pathlength quartz cuvettes. Typically, a scanning rate of 100 nm/min, a time constant of one second, and a bandwidth of 1.0 nm were used. Spectra were measured at 20 ± 0.2 ˚C, with a resolution of 0.5 nm, and 16 scans were averaged per spectrum. The buffer background was subtracted from the final spectra. Samples were analysed immediately after recombinant α-SHaPrP(90-231) and α-MoPrP(90-230) in 5 mM ammonium formate, pH 5.5 buffer were incubated at 70 °C for 24 hr to determine the secondary structure. β-sheet rich SHaPrP(90-231) and MoPrP(90-230) spectra were recorded before and after 15 min sonication in a bath sonicator. The direct CD measurements (θ, in millidegrees), were converted into molar ellipticity [θ]/deg cm^2 $dmol^{-1}$.

3.8.4 Electron microscopy

Stock solutions of β SHaPrP(90-231) were diluted to a protein concentration of 50 μg/mL in 5 mM ammounium formate buffer, pH 5.0, applied to EM grids coated with carbon film, and stained with 2 % uranyl acetate. The samples were viewed in a Philips CM120 electron microscope equipped with a LaB6 filament and a voltage of 100 kV. Images were acquired at a magnification of 45,000.

3.8.5 Mass Spectrometry

All the parameters listed for mass spectrometry analysis of the prion protein and synthetic polymers are the optimised conditions. The following parameters are for the analysis of recombinant truncated and full-length PrP only.

3.8.5.1 T-Wave Ion Mobility-Mass Spectrometry.

All IM-MS experiments were performed in a hybrid quadrupole-ion mobility-orthogonal acceleration time-of-flight (oa-ToF) mass spectrometer (Synapt HDMS, Waters, Manchester, UK). The instrument was equipped with a nanoflow electrospray ion source and operated at a source temperature of 90°C. The sample solutions were introduced into the source region of the instrument by direct infusion ESI. The cone voltage was optimised at 40V for ESI-MS experiments. A detailed explanation of the Synapt HDMS technology has been described elsewhere (Pringle, Giles et al. 2007). Briefly, the machine comprises of three travelling wave (T-Wave) enabled stacked ion guides: trap; IM cell and transfer. The trap ion guide is used to accumulate ions and releases these as ion packets into the IM cell for mobility separation. The transfer ion guide is used to convey the mobility-separated ions to the oa-ToF mass analyser (Pringle, Giles et al. 2007). The pressure in the T-Wave IM cell was 0.55 mbar in these experiments, with nitrogen employed as the mobility gas. The T-Wave height and velocity were set at 9 V and 300 m/s respectively.

After a release of a packet of ions from the Trap T-Wave the ToF analyser recorded 200 orthogonal acceleration pushes (mass spectra) with the pusher frequency set at 90 μs. This resulted in each IM experiment being performed over an 18.0 ms time frame. The ToF analyser was tuned in V-optic mode for an operating resolution of 7,000 (FWHM). Mass spectra were acquired at an acquisition rate of two spectra/s with an interscan delay of 100 ms. Data acquisition and processing were carried out using MassLynx™ (v4.1) software (Waters Corp., Milford, MA, USA). The resulting mass spectra were analysed and their corresponding masses were deconvoluted using maximum entropy (MaxEnt 1) which is an algorithm part of the MassLynx™ (v4.1) software.

3.8.5.2 Electrospray Ionisation-Mass Spectrometry

All ESI-MS experiments were performed in a quadrupole orthogonal acceleration-time-of-flight (Q oa-ToF) mass spectrometer (Q-ToF I, Waters, Manchester, UK). The instrument was equipped with a nanoflow electrospray ion source and operated at a source temperature of 90°C. The sample solutions were introduced into the source region of the instrument by direct infusion. The cone voltage was optimised at 40 V.

The ToF analyser was tuned in V-optic mode for an operating resolution of 5,000 (FWHM). Mass spectra were acquired at an acquisition rate of two spectra/s with an interscan delay of 100 ms. Data acquisition and processing were carried out using MassLynx™ (v4.0) software (Waters Corp., Milford, MA, USA).

3.8.5.3 Sample Preparation (ESI)

Ammonium formate was obtained from Sigma-Aldrich (Gillingham, UK). All recombinant protein samples were diluted to a concentration of 10 μM in 10 mM ammonium formate pH 5.5. The protein was analysed at two pH values pH 5.5 and pH 7.0. The pH of each sample was increased to pH 7.0 using 0.1% ammonia solution. ESI-MS analysis was performed by infusing a solution of recombinant PrP samples at pH 5.5 and pH 7.0. Samples high in β-sheet content were sonicated for 15 min prior to ESI-MS analysis and were sprayed immediately.

3.9 Metal ion coordination experiments

Expression and purification of the recombinant proteins and peptide are described above.

3.9.1 Circular dichroism

Far-UV (190–260 nm) CD spectra of SHaPrP(23-231) (10 μM) and BovPrP (57-101) (20 μM) were measured on a JASCO J-815 spectropolarimeter using 1 mm path length quartz cuvettes. Typically, a scanning rate of 100 nm/minute, a time constant of one second, and a bandwidth of 1.0 nm were used. Spectra were measured at 20 ± 0.2 ˚C, with a resolution of 0.5 nm, and 16 scans were averaged per spectrum. The buffer background was subtracted from the final spectra. The direct CD measurements (θ, in millidegrees), were converted into molar ellipticity [θ]/deg cm^2 $dmol^{-1}$.

3.9.2 T-Wave Ion Mobility-Mass Spectrometry.

All IM-MS experiments were performed in a hybrid quadrupole-ion mobility-orthogonal acceleration time-of-flight (oa-ToF) mass spectrometer (Synapt HDMS, Waters, Manchester, UK). The instrument was equipped with a nanoflow electrospray ion source and operated at a source temperature of 90°C. The sample solutions were introduced into the source region of the instrument by direct infusion ESI. The cone voltage was optimised at 40V for ESI-MS experiments. A detailed explanation of the Synapt HDMS technology has been described elsewhere (Pringle, Giles et al. 2007). The pressure in the T-wave IM cell was 0.55 mbar in SHaPrP (23-231) experiments and 0.64 mbar for BovPrP (57-101), with nitrogen employed as the mobility gas. The T-Wave height and velocity were set at 9 V and 300 m/s, respectively.

After a release of a packet of ions from the Trap T-Wave the ToF analyser recorded 200 orthogonal acceleration pushes (mass spectra) with the pusher frequency set at 90 μs. This resulted in each IM experiment being performed over an 18.0 ms time frame. The ToF analyser was tuned in V-optic mode for an operating resolution of 7,000 (FWHM). Mass spectra were acquired at an acquisition rate of two spectra/s

with an interscan delay of 100 ms. Data acquisition and processing were carried out using MassLynx™ (v4.1) software (Waters Corp., Milford, MA, USA). The resulting mass spectra were analysed and their corresponding masses were deconvoluted using a maximum entropy (MaxEnt 1) algorithm part of the MassLynx™ (v4.1) software.

3.9.3 Electrospray Ionisation-Mass Spectrometry

All ESI-MS experiments were performed in a quadrupole orthogonal acceleration-time-of-flight (Q oa-ToF) mass spectrometer (Global, Waters, Manchester, UK). The instrument was equipped with a nanoflow electrospray ion source and operated at a source temperature of 90°C. The sample solutions were introduced into the source region of the instrument by direct infusion. The cone was optimised at 40 V for ESI-MS experiments.

The ToF analyser was tuned in V-optic mode for an operating resolution of 7,000 (FWHM). Mass spectra were acquired at an acquisition rate of two spectra/s with an interscan delay of 100 ms. Data acquisition and processing were carried out using MassLynx™ (v4.1) software (Waters Corp., Milford, MA, USA). The resulting mass spectra were analysed and their corresponding masses were deconvoluted using a maximum entropy (MaxEnt 1) algorithm part of the MassLynx™ (v4.1) software

3.9.4 Sample Preparation (ESI)

SHaPrP(23-231) samples were diluted to a concentration of 10 μM in 10 mM ammonium formate pH 5.5 and the pH of the protein sample was increased to pH 7.0 using 0.1% ammonia solution. BovPrP(57-101) samples were diluted to a concentration of 20 μM in 10 mM ammonium formate pH 7.0. Copper sulphate solutions were prepared at three different concentrations 100 mM, 300 mM and 500 mM in 10 mM ammonium formate pH 7.0. These stock dilutions were mixed with the protein and peptide respectively to give a stoichiometric ratio of 1:1, 1:3 and 1:5 PrP:Cu^{2+}. Manganese chloride solutions were prepared at three different

concentrations 100 mM, 500 mM and 1 M in 10 mM ammonium formate pH 7.0. These stock dilutions were mixed with the protein to give a stoichiometric ratio of 1:1, 1:5, 1:10 and 1:20 PrP:Mn^{2+}. Nano-ESI-IM-MS analysis was performed by directly infusing a solution of SHaPrP(23-231) or BovPrP(57-101) pH 7.0 into the spectrometer.

3.9.5 T-Wave cross-section calibration

Methods to create a cross-section calibration for the T-Wave Synapt have been previously published (Ruotolo, Benesch *et al.* 2008; Ruotolo, Giles *et al.* 2005; Scarff, Thalassinos *et al.* 2008; Scrivens J. H 2006; Wildgoose J.L 2005). The calibration was performed following an in-house procedure as described in Thalassinos *et al*. (Thalassinos, Grabenauer et al. 2009). In brief, equine myoglobin and rabbit haemoglobin were diluted to a concentration of 10 μM in 50% aqueous acetonitrile/ 0.1% formic acid (Mallinckrodt Baker Inc., Phillipsburg, NJ, USA) and analysed against values obtained from drift-time ion mobility mass spectrometry (DTIMS) studies (Clemmer). The arrival times obtained were corrected to exclude time spent outside of the T-Wave mobility cell. Mass-independent time spent in the transfer region and mass-dependent time spent between the transfer region and time-of-flight mass analyser were subtracted. Normalised cross-sections (corrected for charge and reduced mass) were then plotted against corrected arrival times to create a calibration with a power series fit for myoglobin and a linear series fit for haemoglobin peptides. The rotationally averaged collisional cross-sections were estimated for all recombinant proteins and peptides (with and without metal ions coordinated). For the truncated and full-length prion proteins studied here, the relationship between corrected arrival times and published arrival times is best approximated by a power fit. When calibrating the Synapt with smaller molecules such as peptides, BovPrP(57-101), a linear relationship has been found to be more appropriate (Thalassinos, Grabenauer et al. 2009). An Excel spreadsheet, downloaded from (http://www2.warwick.ac.uk/fac/sci/bio/research/jscrivens/), was used to calculate the estimated cross-section of the proteins and peptide.

3.10 Polymers

3.10.1 Ion Mobility-Mass Spectrometry/Mass Spectrometry

All IM-MS/MS experiments were performed in a hybrid quadrupole-ion mobility-orthogonal acceleration time-of-flight (oa-ToF) mass spectrometer (Synapt HDMS, Waters, Manchester, UK). The instrument was equipped with a nanoflow electrospray ion source and operated at a source temperature of 90°C. The sample solutions were introduced into the source region of the instrument by direct infusion ESI. The cone voltage was optimised between 40 and 70 V for ESI-MS/MS experiments and the collision energy was ramped between 45 and 110 eV during the acquisition. A detailed explanation of the Synapt HDMS technology has been described elsewhere (Pringle, Giles et al. 2007). Ions were mass selected using the quadrupole prior to MS/MS experiments. All MS/MS experiments were performed in the T-Wave transfer region after ion mobility separation. The pressure in the T-wave IM cell was 0.58 mbar for all PEG samples, with nitrogen employed as the mobility gas. The T-Wave height and velocity were set at 9 V and 300 m/s respectively. The pressure in the T-wave IM cell was 0.58 mbar for all PPG samples, with nitrogen employed as the mobility gas. The T-Wave height and velocity were set at 11 V and 450 m/s respectively.

The ToF analyser recorded 200 orthogonal acceleration pushes (mass spectra) with the pusher frequency set at 64 μs. This resulted in each IM experiment being performed over a 12.8 ms time frame. The total IM acquisition time for the data shown was combined and averaged over 1 minute. The ToF analyser was tuned in V-optic mode for an operating resolution of 7,000 (FWHM). Mass spectra were acquired at an acquisition rate of two spectra/s with an interscan delay of 100 ms. Data acquisition and processing were carried out using MassLynx™ (v4.1) software (Waters Corp., Milford, MA, USA).

3.10.2 Electrospray Ionisation-Mass Spectrometry/Mass Spectrometry

All ESI-MS/MS experiments were performed in a quadrupole orthogonal acceleration-time-of-flight (Q oa-ToF) mass spectrometer (Q-ToF I, Waters,

Manchester, UK). The instrument was equipped with a nanoflow electrospray ion source and operated at a source temperature of 80°C. The sample solutions were introduced into the source region of the instrument by direct infusion. The cone was optimised at 70 V for ESI-MS/MS experiments. Argon was used as the collision gas with a collision energy of 60 V for all spectra shown in Chapter 7.

The ToF analyser was tuned in V-optic mode for an operating resolution of 5,000 (FWHM). Mass spectra were acquired at an acquisition rate of two spectra/s with an interscan delay of 100 ms. Data acquisition and processing were carried out using MassLynx™ (v4.0) software (Waters Corp., Milford, MA, USA).

3.10.3 Sample Preparation (ESI)

PEG 1000, PEG mono-oleate, PEG bis(2-ethyl hexanoate), Brij 76 (stearyl alcohol initiated PEG), PPG monobutyl ether and PPG bis(2-aminopropyl ether) were all obtained from Sigma-Aldrich (Gillingham, UK). Lithium chloride and methanol were also obtained from Sigma-Aldrich. All samples were dissolved in 50% aqueous methanol to a concentration of 100 ng/μL. Lithium chloride was dissolved in 50% aqueous methanol to a concentration of 1 mg/mL. ESI-MS/MS analysis of individual polyether samples was performed by infusing a solution of a mixture of sample with lithium chloride at a ratio of 10:1 (sample:salt, *v*/*v*).

PEG 1000 and PEG mono-oleate were dissolved in 50% aqueous methanol to a concentration of 200 ng/μL and 500 ng/μL respectively. PEG bis(2-ethyl hexanoate) and Brij 76 were dissolved in 50% aqueous methanol to a concentration of 100 ng/μL and 500 ng/μL respectively. PPG monobutyl ether and PPG bis(2-aminopropyl ether) were dissolved in 50% aqueous methanol to a concentration of 100 ng/μL. ESI-IM-MS/MS analysis of polyether mixtures was performed by infusing a solution of samples with lithium chloride at a ratio of 10:10:1 (sample:sample:salt, *v*/*v*/*v*).

3.10.4 MALDI-MS

All samples were analysed, prior to ESI-MS characterisation, by MALDI-MS. MALDI-MS experiments were performed in a MALDI micro MX instrument (Waters MS Technologies, UK). The instrument was operated in reflection mode to obtain a resolution of 9000 FWHM.

3.10.5 Sample Preparation (MALDI)

Sodium trifluoroacetate, DCTB (trans-2-3-(4-tert-butylphenyl)-2-methyl-(2-propenlidene)-malononitrile) and anhydrous tetrahydrofuran were obtained from Sigma-Aldrich (Gillingham, UK). All solutions were prepared at a concentration of 10 mg/mL. The polymer and matrix were dissolved in anhydrous tetrahydrofuran and mixed in a 1:20 ratio (*v*/*v*). This solution was then mixed with sodium trifluoroacetate in tetrahydrofuran, in a 100:1 ratio (*v*/*v*), prior to deposition of approximately 0.5 μL on the sample stage.

3.10.6 NMR

NMR spectra were recorded for PEG 1000, PEG mono-oleate, PEG bis(2-ethyl hexanoate), Brij 76, PPG monobutyl ether and PPG bis(2-aminopropyl ether) in an Eclipse 500 MHz NMR spectrometer (JEOL, Welwyn, UK), operating at 500 MHz and 125 MHz for acquisition of ^{1}H and ^{13}C spectra respectively. The solvent used for all experiments was deuterated chloroform ($CDCl_3$) and the data were generated in 5 mm (external diameter) NMR tubes. The data from all six samples indicated that the structures of those polymers were as expected from the supplier.

3.10.7 On-line GPC-NMR Measurements

A detailed explanation of the on-line GPC-NMR conditions has been described elsewhere (Robertson, Heron *et al.* 2004). Briefly, the gel permeation chromatography (GPC) equipment consisted of a Gilson 305 pump, a Rheodyne injector provided with a 100 μL sample loop and two PLgel columns in series; firstly a PLgel 7.5 mm i.d. x 300 mm column particle size 5 μm pore type 500 Å followed by a PLgel 7.5 mm i.d. x 300 mm column particle size 5 μm pore type 100 Å (Polymer Laboratories Ltd, Shropshire, UK). Degassed $CDCl_3$ was employed as the mobile phase and solvent for the sample preparation. The ^2H resonance of $CDCl_3$ was utilised as the field frequency lock. The eluent flow rate was optimised at 0.7 mL min^{-1}.

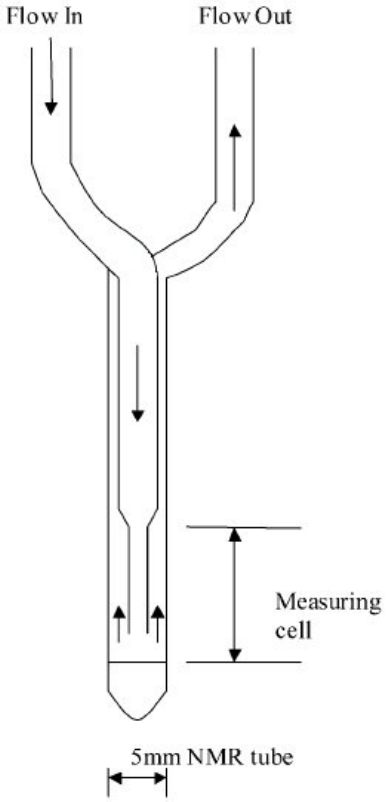

Figure 3.2: Schematic representation of the 5 mm diameter NMR flow cell (Robertson, Heron *et al.* 2004).

On-line NMR measurements were performed by means of a JEOL-Eclipse 500 MHz NMR spectrometer (JEOL, Welwyn, UK). A 5 mm quartz NMR tube was used as the flow cell with a detection cell volume of approximately 220 μL (see Figure 3.2) (Robertson, Heron et al. 2004). The flow cell was connected to the GPC outlet by a PEEK capillary (0.25 mm i.d. x 2.7 m). The temperature of the flow cell was set at 20 °C. A summary of the NMR experimental conditions can be found in Table 3.1.

Table 3.1: Summary of NMR experimental conditions

Parameter	**Value**
Sample Temperature	20 °C
Frequency	500 MHz
Pulse width	~ 45° tip angle
Spectral width	5000 Hz
Pulse delay	0.1 s
Acquisition time	0.17 s
Typical number of scans per slice	4
X points	8192
Typical Y points	200-400
Observation nucleus	^{1}H

3.11 References

Bocharova, O. V., Breydo, L., Salnikov, V. V. and Baskakov, I. V. (2005). Copper(II) inhibits in vitro conversion of prion protein into amyloid fibrils. *Biochemistry* **44**, 6776-87.

Clemmer, D. E. http://www.indiana.edu/~clemmer/.

Goormaghtigh, E., Cabiaux, V. and Ruysschaert, J. M. (1990). Secondary structure and dosage of soluble and membrane proteins by attenuated total reflection Fourier-transform infrared spectroscopy on hydrated films. *European Journal of Biochemistry* **193**, 409-20.

Martins, S. M., Frosoni, D. J., Martinez, A. M., De Felice, F. G. and Ferreira, S. T. (2006). Formation of soluble oligomers and amyloid fibrils with physical properties of the scrapie isoform of the prion protein from the C-terminal domain of recombinant murine prion protein mPrP-(121-231). *Journal of Biological Chemistry* **281**, 26121-8.

Mehlhorn, I., Groth, D., Stockel, J., Moffat, B., Reilly, D., Yansura, D., Willett, W. S., Baldwin, M., Fletterick, R., Cohen, F. E., Vandlen, R., Henner, D. and Prusiner, S. B. (1996). High-level expression and characterization of a purified 142-residue polypeptide of the prion protein. *Biochemistry* **35**, 5528-37.

Pringle, S. D., Giles, K., Wildgoose, J. L., Williams, J. P., Slade, S. E., Thalassinos, K., Bateman, R. H., Bowers, M. T. and Scrivens, J. H. (2007). *International Journal of Mass Spectrometry* **261**, 1.

Robertson, D. F., Heron, J. E. and Beckett, M. C. (2004). On-Line Gel Permeation Chromatography/Nuclear Magnetic Resonance of Complex Polymer Formulations. *Applied Spectroscopy* **58**, 1122-1127.

Ruotolo, B. T., Benesch, J. L., Sandercock, A. M., Hyung, S. J. and Robinson, C. V. (2008). Ion mobility-mass spectrometry analysis of large protein complexes. *Nature Protocol* **3**, 1139-52.

Ruotolo, B. T., Giles, K., Campuzano, I., Sandercock, A. M., Bateman, R. H. and Robinson, C. V. (2005). Evidence for macromolecular protein rings in the absence of bulk water. *Science* **310**, 1658-61.

Sanghera, N. and Pinheiro, T. J. (2002). Binding of prion protein to lipid membranes and implications for prion conversion. *Journal of Molecular Biology* **315**, 1241-56.

Scarff, C. A., Thalassinos, K., Hilton, G. R. and Scrivens, J. H. (2008). Travelling wave ion mobility mass spectrometry studies of protein structure: biological significance and comparison with X-ray crystallography and nuclear magnetic resonance spectroscopy measurements. *Rapid Communications in Mass Spectrometry* **22**, 3297-3304.

Scrivens J. H, T. K., Hilton G. R, Slade S. E, Pinheiro T.J.T, Bateman R. H, Bowers M. T, (2006). *Proc. 55th ASMS Conf. Mass Spectrometry and Allied Topics*, Indianapolis.

Thalassinos, K., Grabenauer, M., Slade, S. E., Hilton, G. R., Bowers, M. T. and Scrivens, J. H. (2009). Characterization of Phosphorylated Peptides Using Traveling Wave-Based and Drift Cell Ion Mobility Mass Spectrometry. *Analytical Chemistry* **81**, 248-254.

Wildgoose J.L, G. K., Pringle S. D, Koeniger S. J, Valentine R. H, Bateman R. H, Clemmer D. E (2005). *Proc. 54th ASMS Conf. Mass Spectrometry and Allied Topics*, Seattle.

Chapter 4
Results: Structural Studies of Prion Proteins

4.1 Introduction

Various analytical methods have been used for the structural characterisation of prions extracted from *in vivo* material and recombinant proteins. Spectroscopic techniques such as CD, FTIR, NMR spectroscopy and electron paramagnetic resonance (EPR) spectroscopy are widely used in prion research. The use of mass spectrometry to analyse the primary structure of PrP and post-translational modifications is well documented (Back, Sanz *et al.* 2002; Maras B. 2004; Onisko, Dynin *et al.* 2007; Principe, Maras *et al.* 2008; Pushie, Ross *et al.* 2007; Qin, Yang *et al.* 2002; Requena, Groth *et al.* 2001; Whittal, Ball *et al.* 2000). When MS is combined with soft ionisation methods, such as ESI, detailed molecular structural information can be obtained. An additional analytical challenge is introduced when MS is used to analyse proteins that are differing in structure, but isobaric in molecular weight. Recent developments in the field of MS have seen the coupling of ion mobility spectrometry (IMS) to MS instruments (Thalassinos and Scrivens 2009). This has led to the development of a powerful methodology which provides a potential technique to investigate the different structures of PrP with the prospect of developing a future diagnostic test for prion diseases.

A combination of ESI with ion mobility has been used to generate information on the conformations of recombinant prion proteins. Prions from three different mammalian species were studied: Syrian hamster, mouse and ovine. The truncated prion samples were either α-helical in structure, representative of PrP^{C}, or refolded to a β-sheet rich construct; a property similar to PrP^{Sc}. Separation of α-helical and β-sheet rich PrP 27-30 isomers, with the same nominal *m/z* ratio but differing secondary structure, was possible using ion mobility. In conjunction with the Bowers Group (UCSB, California, US), computer modelling studies of full-length proteins were performed and the theoretical cross-sections were compared to experimental data. The α-helical full-length proteins were analysed and a comparison of the stabilities and unfolding mechanisms of the various species was made.

4.2 Results and Discussion

For all materials and methods please refer to Chapter 3.

4.3 Syrian hamster PrP (SHaPrP)

During its short life span (3-6 hours) (Borchelt, Scott *et al.* 1990; Caughey, Race *et al.* 1989; Caughey and Raymond 1991; Yedidia, Horonchik *et al.* 2001) the prion protein can experience two different pH environments; a mildly acidic environment, whilst cycling within the cell, and a neutral environment when it is GPI-anchored to the cell membrane. The prion conformational isoforms studied were α-helical SHaPrP(90-231) and β-sheet rich SHaPrP(90-231) at physiological pH 5.5 and pH 7.0. Both conformational isoforms have the same nominal *m/z* ratio but differ in their secondary structure. MS alone is not able to resolve oligomers with the same nominal *m/z* ratio, regardless of their shape. Figure 4.1 shows the mass spectra of α-helical SHaPrP(90-231) and β-sheet rich SHaPrP(90-231) at pH 5.5. A comparison of the MS spectra indicates the charge state envelope distributions of the two data sets are similar and that the samples are devoid of contamination. The labels on the peaks (7+, 8+ etc) indicate the *m/z* ratio of the ion species. The deconvoluted peak (see insets) derived from each sample corresponded to the predicted molecular mass of oxidised SHaPrP(90-231), 16240 Da. This is considered to be more biologically relevant than its reduced counterpart (Hosszu, Trevitt *et al.* 2009; Prusiner 1998). This is because the oxidised construct is structured due to the presence of a disulphide bond. This disulphide bond has been observed in both conformational isoforms.

The conversion of PrP^C, a protein that is predominantly α-helical, to a β-sheet-rich isoform that has a propensity to aggregate, is the key molecular event in prion diseases. Recombinant prion protein can be refolded into a monomeric α-helical conformer α SHaPrP(90-231) or to a β-sheet-rich structure. Refolding of PrP under oxidising non-denaturing conditions at pH 5.5 yields an α SHaPrP(90-231) isoform. This isoform shows a characteristic far-UV CD spectrum with well defined minima at 208 nm and 222 nm (Figure 4.2a) and also a FTIR spectrum containing a symmetrical amide I band with a maximum at ~1660 cm^{-1} (Figure 4.2b). The CD

and FTIR results are consistent with a protein containing a significant amount of α-helical structure. Incubation of α SHaPrP(90-231) at 70 °C for 24 hrs induces a

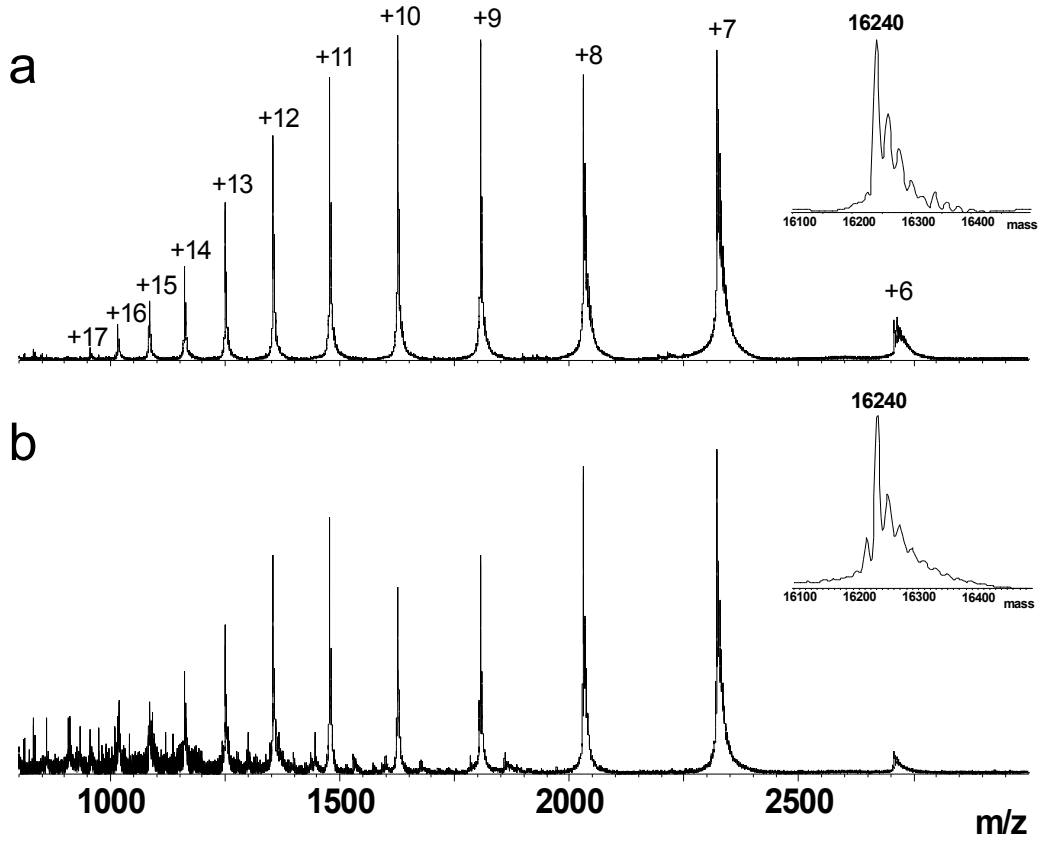

Figure 4.1(a): Mass spectrum of α SHaPrP(90-231) at pH 5.5. Inset: Deconvoluted mass of the oxidised protein. (b) Mass spectrum of β SHaPrP(90-231) at pH 5.5. Inset: Deconvoluted mass of the oxidised protein.

structural transition from a protein that is mainly α-helical to one that has increased β-sheet structure (Martins, Frosoni *et al.* 2006). In contrast to α SHaPrP(90-231), the β-sheet-rich SHaPrP(90-231) isoform produced a far-UV CD spectrum has a minimum at ~ 217 nm (Figure 4.2a), which is indicative of a substantial increase in β-sheet structure. CD data are a representation of the average structure in solution. The β-sheet structure observed by means of CD could contain a variety of monomeric structures as well as β-sheet rich oligomers. The amide I band in the FTIR spectrum of β SHaPrP(90-231) is also significantly different from that of α SHaPrP(90-231), the appearance of a distinct band at 1627 cm^{-1} is characteristic of

β-sheet structure (Figure 4.2b). Examination of the β-sheet-rich isoform of SHaPrP(90-231) under the electron microscope revealed the presence of ordered aggregates. Electron microscopy showed flexible fibrillar type structures of varying lengths with an average diameter of 10 nm (Figure 4.2c). Direct analysis of these β-sheet-rich SHaPrP(90-231) structures by means of ESI-IM-MS was challenging due to the difficulty of obtaining a stable spray. To overcome this problem the sample was sonicated for 15 minutes in a bath sonicator, resulting in lower molecular weight molecules which could then be directly infused into the IM-MS. Analysis of the sonicated β SHaPrP(90-231) sample by means of CD showed no change in the secondary structure of the protein upon sonication (Figure 4.2a) although the EM images suggested that the large protein aggregates were broken into smaller structures (Figure 4.2c).

Several hypotheses have been outlined which suggest that the α-helical PrP can undergo a conformational change to form a variety of β-sheet rich isoforms (Gambetti, Dong *et al.* 2008). The monomeric β-sheet rich PrP sample prepared for this experimental data set is likely to be one of a number of possible structures observed *in vitro* and *in vivo*. It has been observed, by means of CD and EM (Figure 4.2), that the β-sheet rich PrP sample had a propensity to aggregate and form high order oligomers. Monomeric/low oligomeric material is required for nanoflow mass spectrometry analysis, as it was observed that higher order oligomers blocked the sample tip. The formation of monomeric β-sheet rich PrP (after 15 minute sonication) could be considered a transient form of the aggregating protein. Sonication of the prion is used in high order oligomeric seeding experiments such as prion misfolding cyclic amplification (PMCA) experiments which were first described by Castilla *et al.,* 2005 (Castilla, Saa *et al.* 2005). A fast and sensitive approach is required to capture the monomeric β-sheet form, under near native conditions, when the PrP sample has been sonicated.

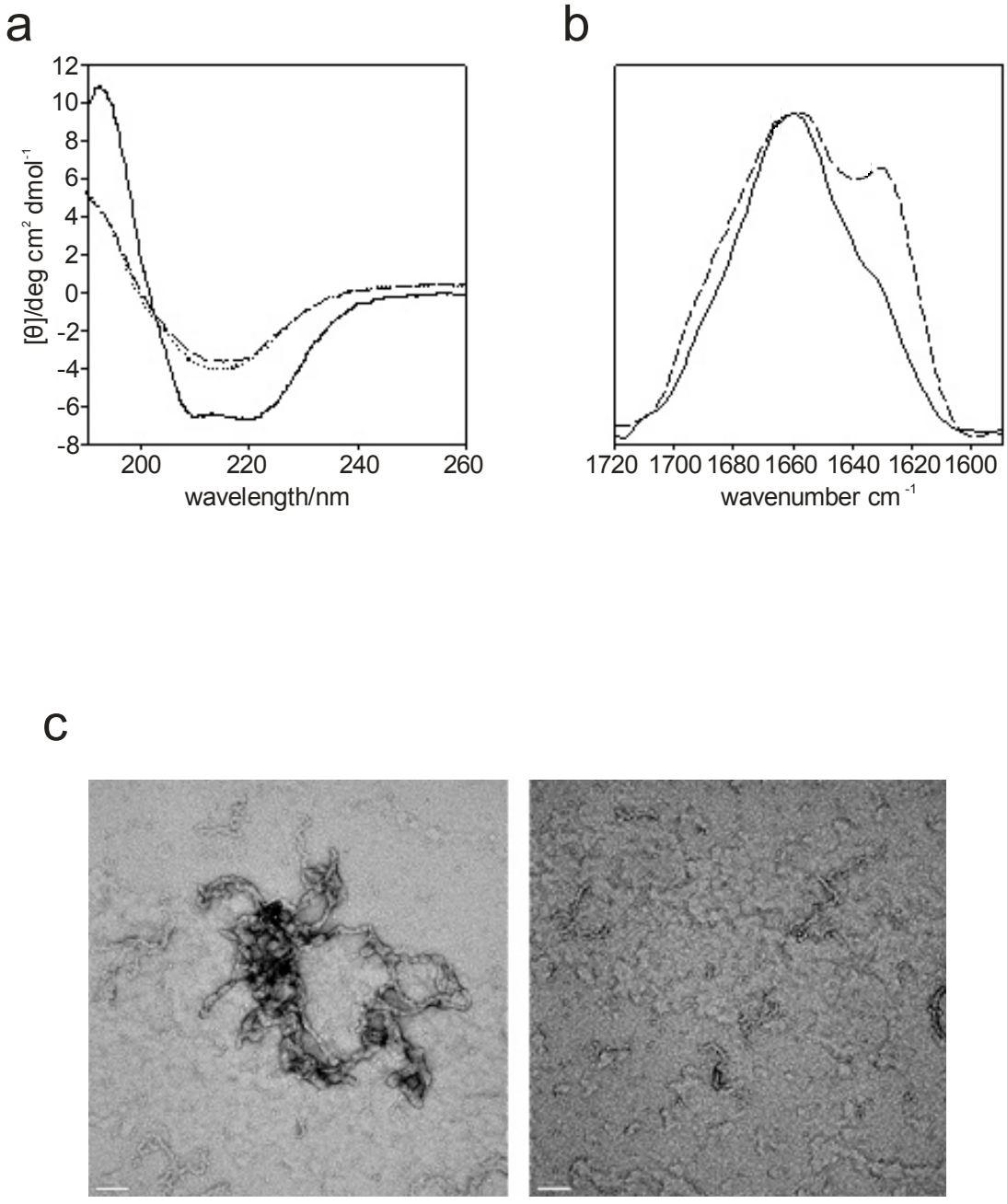

Figure 4.2: Conformational properties of different PrP states. Secondary structure of PrP; (a) Far-UV CD spectra of α-helical PrP (solid line), β-sheet-rich PrP (dashed line) and following sonication (dotted line) and (b) ATR FTIR spectra of α-helical PrP (solid line) and β-sheet-rich PrP (dashed line). (c) Morphology of β-sheet-rich PrP aggregates. Electron micrographs of negatively stained β-sheet-rich PrP aggregates before (left panel) and after sonication (right panel). The bar scale is 50 nm.

The SHaPrP(90-231) samples, rich in β-sheet content, had a propensity to aggregate and were analysed immediately after their conversion from the α-helical form. It was observed that, on average, the sonicated β SHaPrP(90-231) sample started to aggregate after a few minutes of spraying. These aggregates blocked the sample tip and prevented further data from being collected. An advantage of the Synapt is its ability to simultaneously collect mass spectral data and arrival time distribution (ATD) information. This allows data to be collected in a relatively short time scale. The total Synapt IM acquisition time for the data shown was combined and the data were averaged over five minutes enabling high quality data to be obtained before the sample tip blocked. The MS experimental time period is crucial in the maintenance of solution-phase structure. It has been shown that, within a time scale of 30-60 ms, the gas-phase structures of proteins can rearrange as a result of their change in environment (Badman, Myung *et al.* 2005). The Synapt experiments operate within a 15-30 ms time frame (Wyttenbach, Grabenauer *et al.* 2009), which limits the opportunity for the protein solution-phase structures to rearrange within the gas phase.

The conformational isoforms at pH 5.5 were directly infused after ionisation by means of ESI into the Synapt mass spectrometer. Figure 4.3 shows the estimated cross-sections for the +6 to +17 charge states at pH 5.5 and the enlargement is of the data of the +15 to +17 charge states (see inset). Separation of the two isobaric conformational isoforms and their corresponding mass spectra were derived in the same experiment. There are small differences in the estimated cross-sections between the α-helical SHaPrP(90-231) and the β-sheet rich SHaPrP(90-231) from charge states +13 to +17. The charge states of α-helical SHaPrP(90-231) appear to have a smaller rotationally averaged cross-section than that of the β-sheet rich SHaPrP(90-231). Upon the sequential addition of protons the conformational isoforms become less compact in structure. This can be representative of the unfolding structure.

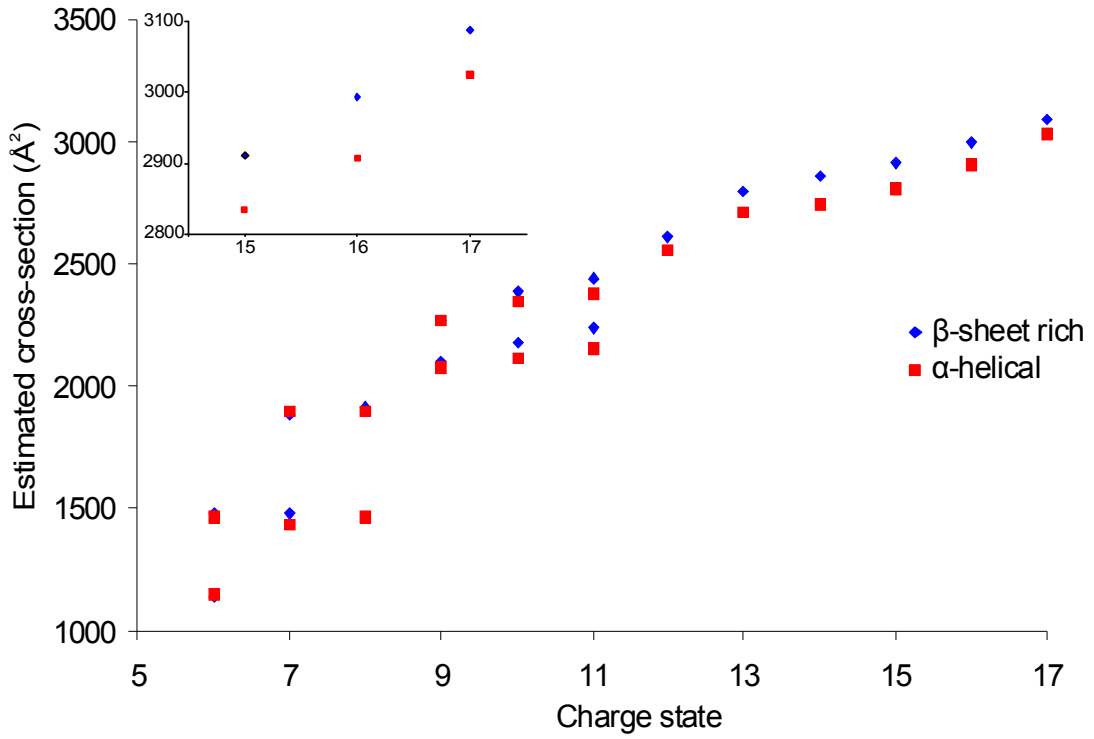

Figure 4.3: Comparison of estimated cross-sections from charge state +6 to +17 for the α-helical (red) and predominantly β-sheet (blue) SHaPrP (90-231), at pH 5.5. Inset: Enlarged image of the +15 to +17 charge states showing the differences in the estimated cross-sections between the α-helical and predominantly β-sheet conformational isoforms.

At the lower charge states, no significant differences in the rotationally-average cross-section were observed. The ATD profiles for individual charge states were examined and showed a clear distinction between the two isomeric samples. Figure 4.4 shows a comparison of the α-helical and β-sheet rich SHaPrP(90-231) ATDs at pH 5.5 for the +9 and +10 charge states. The peaks labelled * were not included in the estimated cross-section plot in Figures 4.3 or 4.5. The ATD for the α-helical PrP charge state +9 (Figure 4.4a) is 60% broader at full-width half-height maximum (FWHM) than that of the β-sheet form. There is also a 40% increase in the intensity of the secondary peak in α-helical species relative to that of the β-sheet ATD. These differences are particularly noticeable when the individual ATDs are overlaid. Similar observations have been made for the +10 charge state see Figure 4.4b. The relatively large width of the α SHaPrP(90-231) ATD suggests that there are multiple conformations present which may have a difference in cross-section of <5%. It is

expected that cross-sections that are greater than 5% in difference would be resolved by this ion mobility approach (Hilton, Jackson *et al.* 2008).

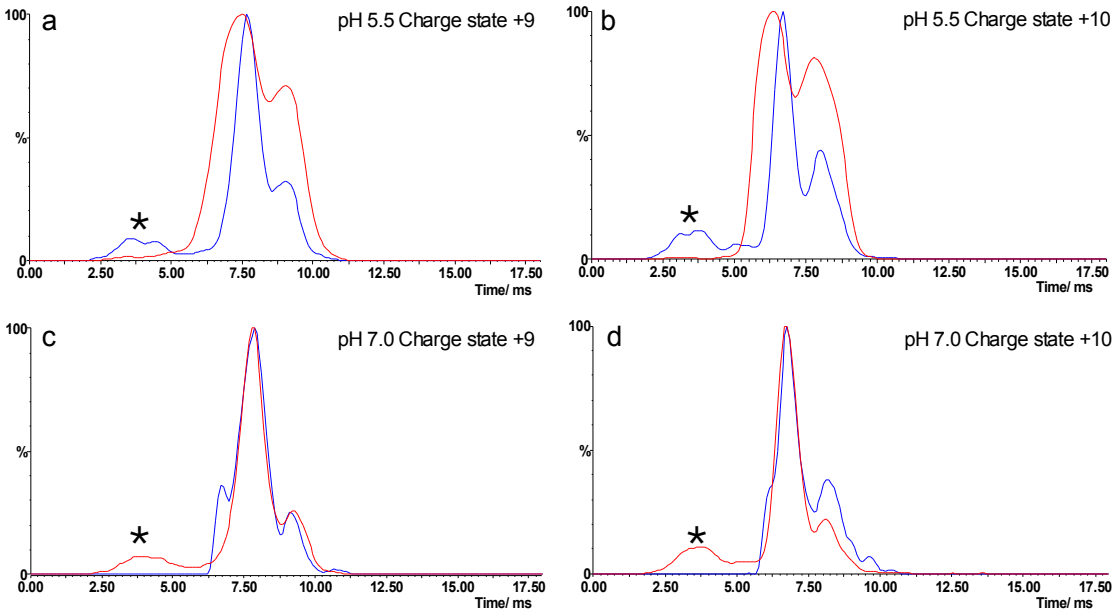

Figure 4.4: Comparison of α-helical (red) and predominantly β-sheet (blue) SHaPrP(90-231) selected arrival time distributions (ATDs) for the +9 and +10 charge state. (a) Overlaid ATDs for the +9 charge state at pH 5.5. (b) Overlaid ATDs for the +10 charge state at pH 5.5. (c) Overlaid ATDs for the +9 charge state at pH 7.0. (d) Overlaid ATDs for the +10 charge state at pH 7.0.

The pH of each sample was increased to pH 7.0 by the addition of a 0.1% ammonia solution and infused into the Synapt mass spectrometer. Figure 4.6 shows the estimated cross-sections for the +6 to +17 charge states obtained at pH 7.0 and the enlargement is of the data of the charge states +15 to +17 (see insets). The degree of protein unfolding, as sequential protons are added, is indicated by an increase in estimated cross-section with increasing charge state. The unfolding of the prion is similar under the two physiological pH conditions. Multiple stable conformations are observed under both pH conditions from charge states +6 to +11. Two conformations were observed for the +8 charge state at pH 7.0 but one conformation dominated and was the only one considered here. At charge states ≥ +12 it was observed that the FWHM of individual ATDs decreased as sequential protons were

added. An instrument performance validation was performed, using equine myoglobin and α-helical SHaPrP(90-231) at pH 7.0, to check the reproducibility and precision of the ATD profiles and estimated cross-sections throughout all the experiments (see Figure 4.5 for myoglobin reproducibility). These validation experiments were performed before any IM-MS conformational isoform studies. The measured experimental variation indicated that the differences observed between α-helical SHaPrP(90-231) pH 5.5 and β-sheet rich SHaPrP(90-231) pH 5.5 were because of differences in the sample conformation rather than experimental error. The differences observed in the conformation disappeared when the pH of the sample was increased.

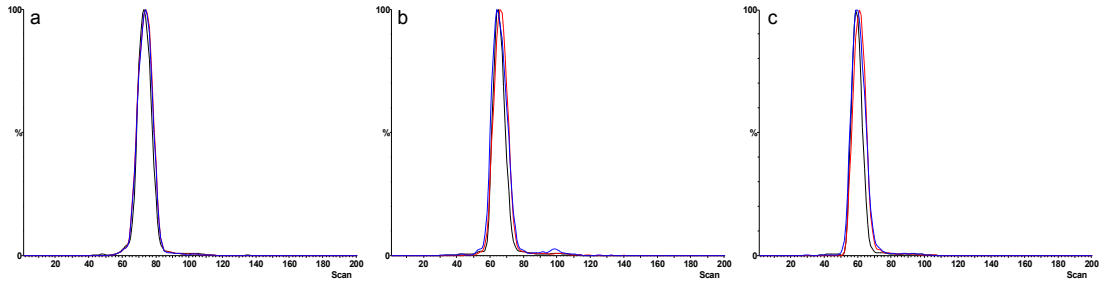

Figure 4.5: Arrival time distributions (ATDs) of equine myoglobin (50% aqueous acetonitrile/ 0.1% formic acid) for charge states +13 (a), +14 (b) and +15 (c). The different colours represent three different instrument performance validation checks over a three month time period. All the ATDs are within ±1 scan number of one another. This reproducibility and precision of the ATD profiles suggests that the differences observed between α-helical SHaPrP(90-231) pH 5.5 and β-sheet rich SHaPrP(90-231) pH 5.5 were because of differences in the sample conformation rather than experimental error.

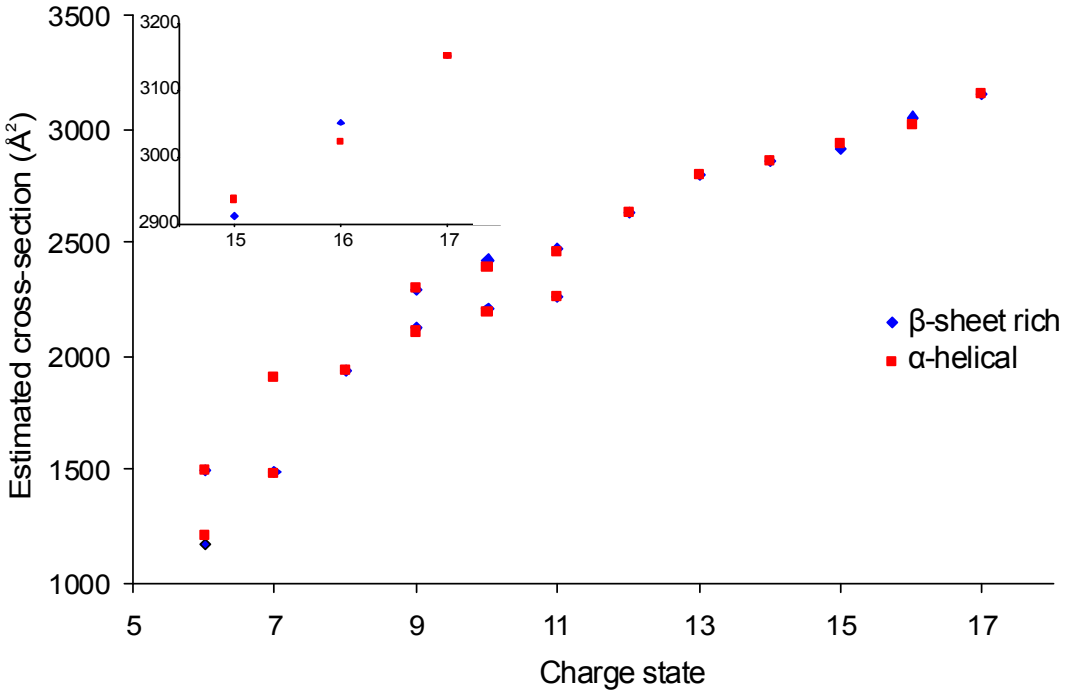

Figure 4.6: Comparison of estimated cross-sections from charge state +6 to +17 for the α-helical (red) and predominantly β-sheet (blue) SHaPrP(90-231), at pH 7.0. Inset: Enlarged image of the +15 to +17 charge states shows no differences in the estimated cross-sections between the α-helical and β-sheet rich conformational isoforms.

Figure 4.6 shows there is no significant difference in the estimated cross-sections between the α-helical and β-sheet rich conformers at pH 7.0. At the higher charge states, +15 to +17, ~100 Å^2 separate the two isoforms at pH 5.5, whereas ≤ 10 Å^2 separates the α- and β- SHaPrP(90-231) at pH 7.0. Examination of the individual ATDs at pH 7.0 revealed there were no differences in the shape, size or intensity of the peaks. Figure 4.4c and d shows a comparison of ATDs for the +9 and +10 charge states which suggest that both isoforms at pH 7.0 have similar conformations to the β-sheet rich SHaPrP(90-231) at pH 5.5.

4.4 Mouse PrP (MoPrP90-230)

Truncated α-helical- and β-sheet-rich mouse prion proteins were studied at pH 5.5 and pH 7.0 by means of IM-MS. Both conformational isoforms have the same nominal *m/z* ratio but differ in their secondary structure, and therefore cannot be separated by MS alone. The same refolding methods and secondary structure characterisation techniques used to monitor the SHaPrP(90-231) isoforms were applied to the mouse protein. Far-UV CD was used to observe the changes in secondary structure between the prion isoforms. The spectra show typical characteristics of an α-helical structure, minima at 208 nm and 222 nm, and a β-sheet structure, minimum at 218 nm, for the refolded isoforms (data not shown). A comparison of the mass spectra for α MoPrP(90-230) and β-sheet rich MoPrP(90-230) at pH 5.5 and pH 7.0 showed that both data sets have a similar charge state envelope distribution observed in all four spectra (data not shown). The resulting data were deconvoluted and revealed that the molecular mass of the sample was 16012 Da. This corresponds to the predicted molecular weight of oxidised MoPrP(90-230) (disulphide bond intact).

The physical properties of the SHaPrP(90-231) and MoPrP(90-230) samples were similar. In both sample sets the β-sheet rich isoform had a propensity to aggregate and was analysed immediately after its conversion from the α-helical form. All samples were pH sensitive and could precipitate if the pH was greater than pH 7.8. Figure 4.7 shows the plot of the estimated cross-sections of α MoPrP(90-230) and β-sheet MoPrP(90-230) at pH 5.5 and pH 7.0. The estimated cross-sections at pH 5.5 range from ~1380 $Å^2$ for the +6 charge state to ~3400 $Å^2$ for the +20 charge state. The ATD for charge state +9 has at least two distinct conformations and the +10 charge state has at least three different conformations in the ATD (see Figure 4.8). All other charge states have one distinct peak in their corresponding ATD. The FWHM at the lower charge states (+6 to +8) was greater than that of the higher charge states (+16 to +20) which suggests that multiple disparate conformations populate the lower charge states. There are small differences in the estimated cross-sections between the α-helical MoPrP(90-230) and the β-sheet rich MoPrP(90-230) in all of the charge states in Figure 4.7. The β-sheet rich MoPrP(90-230) appear to have smaller rotationally averaged cross-sections than the α-helical MoPrP(90-230);

the opposite was observed for the Syrian hamster samples. As was observed for the SHaPrP(90-231) isoforms at pH 5.5, the individual ATDs for MoPrP(90-230) suggest larger differences in their conformations than represented in the estimated cross-section plot. Figure 4.8 shows the individual ATDs for the +7 and +10 charge states for both the α-helical and β-sheet rich MoPrP(90-230) at pH 5.5. Figure 4.8a* were not included in the estimated cross-section plot. When the ATDs of the +7 charge state of the β-sheet rich isoform and the α-helical counterpart were overlaid, it was clear that the former ATD is much narrower (FWHM 29 scans) than the latter (FWHM 38 scans). This suggests that β MoPrP(90-230) is either more compact in structure and/or has fewer disparate conformational populations than α MoPrP(90-230). In contrast the FWHM of the +10 charge state peaks are similar; the notable difference in these ATDs is the arrival time of each conformation. The conformations belonging to the α MoPrP(90-230) have a shorter arrival time and must, therefore, have a smaller cross-section than their β-sheet rich equivalents.

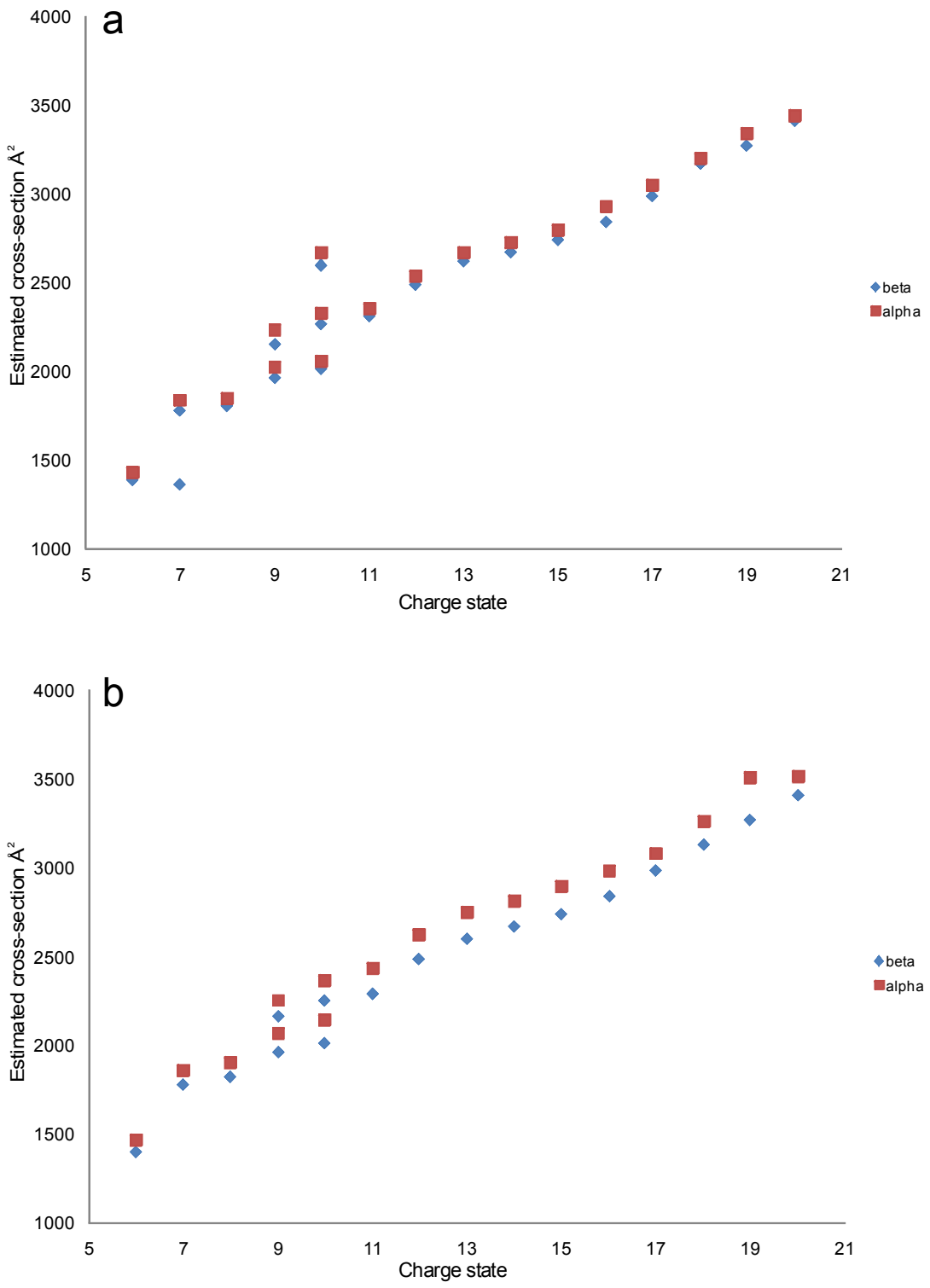

Figure 4.7: Estimated cross-section plot for charge states +6 to +20. (a) Comparison of α MoPrP(90-230) (red) and β-sheet rich MoPrP(90-230)(blue) at pH 5.5. (b) Comparison of α MoPrP(90-230) (red) and β-sheet rich MoPrP(90-230)(blue) at pH 7.0.

The estimated cross-sections for α MoPrP(90-230) and β-sheet rich MoPrP(90-230) at pH 7.0 are shown in Figure 4.7b. They range from ~1450 $Å^2$ for the +6 charge state to ~3500 $Å^2$ for the +20 charge state. These are larger than the cross-sections calculated at pH 5.5 and suggest that the conformations can change because of their pH environment. The number of distinct conformations for each charge state and the unfolding pattern of the protein are similar to those observed in Figure 4.7a. There is an average 5% difference in the estimated cross-section between the α MoPrP(90-230) and β MoPrP(90-230) samples; this is considered significant. From these data it has been deduced that the α-helical isoform has a larger rotationally-averaged cross-section than β-sheet rich MoPrP(90-230). These differences at pH 7.0 were also evident in the individual ATDs (data not shown).

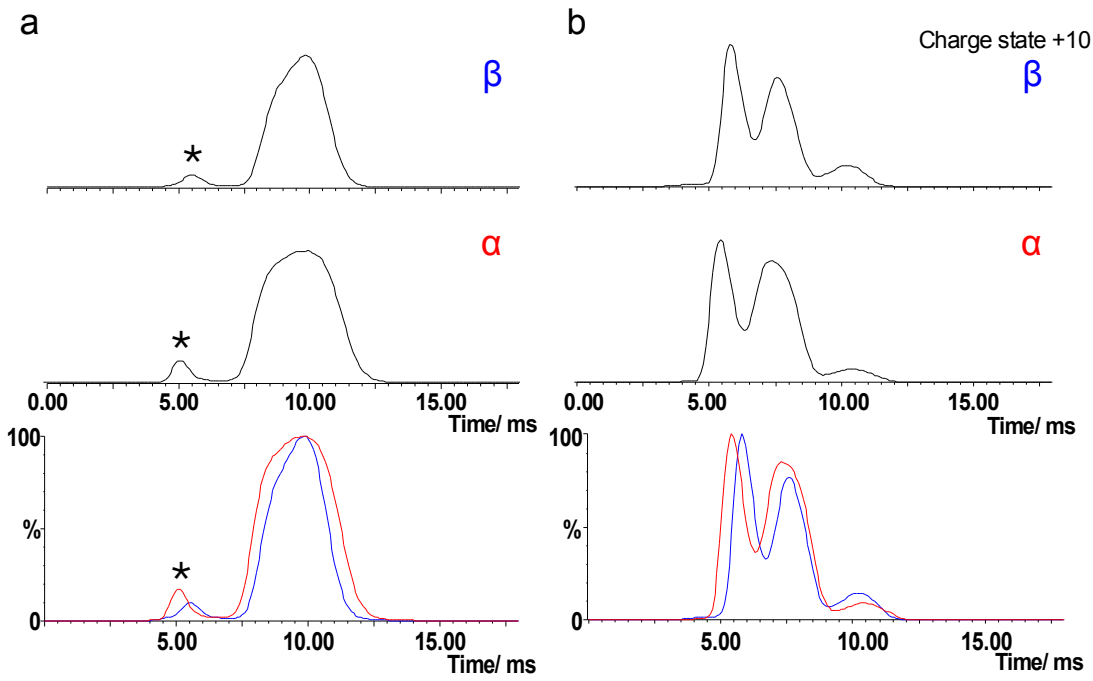

Figure 4.8: The individual arrival time distribution of MoPrP(90-230) at pH 5.5 (a) Charge state +7 β-sheet rich MoPrP(90-230) (blue), α MoPrP(90-230) (red) overlaid α and β-sheet ATD. (b) Charge state +10 β-sheet rich MoPrP(90-230) (blue), α MoPrP(90-230) (red) overlaid α and β-sheet ATD.

4.5 Comparison of SHaPrP(90-231) with MoPrP(90-230)

Both SHaPrP(90-231) and MoPrP(90-230) have been characterised by means of IM-MS. The PrP sequence is highly conserved between the two mammalian species with a difference of only eight different amino acid residues between the sequences. These differences give rise to a difference of 228 Da (1.4%) in mass. Figure 4.3 reveals that the β-sheet rich SHaPrP(90-231) conformation is larger in cross-section than the α-helical isoform at pH 5.5, whereas the opposite observation was made in the mouse data (Figure 4.7a). At pH 7.0, there were no differences between the estimated cross-sections of the α or β-sheet rich SHaPrP(90-231) (Figure 4.6); significant differences, however, were observed between the mouse conformational isoforms with the α-helical conformation, again, having the larger cross-section (Figure 4.7b). Figure 4.9a shows a direct comparison of the α-helical SHaPrP(90-231) and MoPrP(90-230) samples at pH 5.5. On average SHaPrP(90-231) is 5% larger in cross-section, for all charge states, when compared to MoPrP(90-230). This observation is surprising because of the small difference in their primary sequences. SHaPrP(90-231) gives rise to more distinct conformations at the lower charge states, +6 to +10, than the mouse equivalent. A similar observation is reflected in the β-sheet rich samples (see Figure 4.9b) in which a 6% average difference in the estimated cross-sections between the mouse and hamster PrP β-sheet rich samples were measured. There are data to suggest that hamster and mouse PrP fold via different mechanisms (Robinson and Pinheiro 2009). It is believed that the hamster PrP folds via a framework mechanism. This occurs by diffusion-collision and requires the secondary structure to be initially formed, followed by the tertiary structure arrangement. In comparison, the mouse PrP folds because of a nucleation condensation mechanism in which the secondary and tertiary structure form simultaneously and without the presence of a detectable intermediate (Robinson and Pinheiro 2009). The difference between the folding mechanisms, and presumably unfolding mechanisms, could account for the differences in estimated cross-section observed.

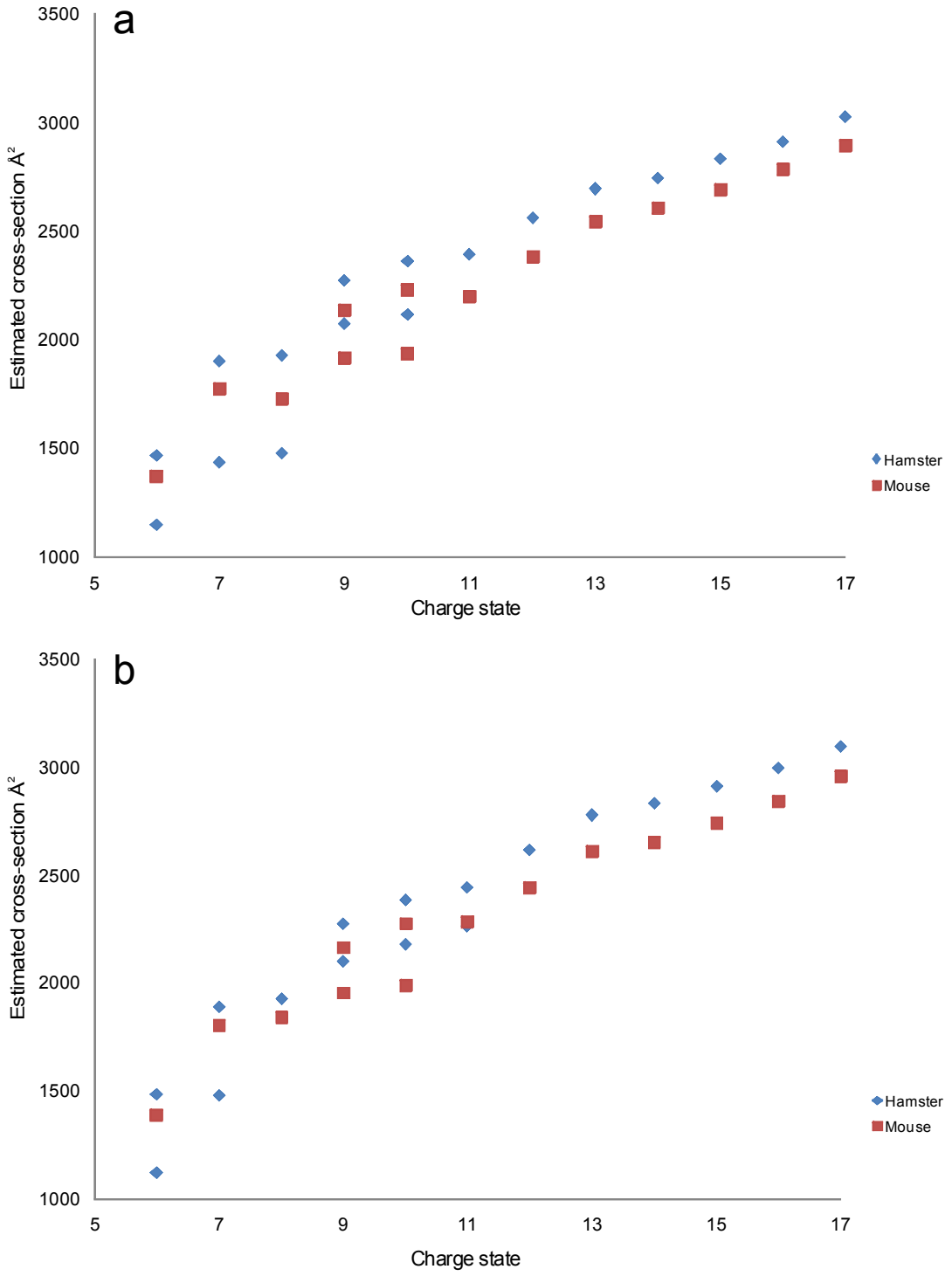

Figure 4.9: Estimated cross-section plot for charge states +6 to +17. (a) Comparison of α MoPrP(90-230) (red) and α SHaPrP(90-231)(blue) at pH 5.5. (b) Comparison of β MoPrP(90-230) (red) and β SHaPrP(90-231)(blue) at pH 5.5.

4.6 Comparison of full-length PrP with truncated PrP

IM-MS was used to observe the estimated cross-sections of recombinant full-length Syrian hamster (SHaPrP(23-231)) and mouse (MoPrP(23-230)). Several attempts were made to convert the full-length α-helical PrP into a β-sheet rich structure; all methods, however, proved unsuccessful (see Table 4.1). Figure 4.10 shows the estimated cross-section plot of α SHaPrP(23-231) at pH 7.0. The estimated cross-sections range from 1871 $Å^2$ for the +9 charge state to 4915 $Å^2$ for the +26 charge state; these are larger than the truncated cross-sections. The lowest and most biologically relevant charge state, +9, has at least two distinct conformations. Charge states +12 to +15 also give rise to at least two distinct conformations. For all the other charge states only one peak was observed in the corresponding ATD. Three different conformational families are observed in Figure 4.10 illustrated by a dotted, solid and dashed box. It is believed that the conformations in each individual family are related, and that the increase in cross-section, with increased charge state, is because of long range Coulombic repulsion (Sinelnikov, Kitova *et al.* 2007). The differences between the conformational families could be related to the different degrees of unfolding. It is likely that the +9 to +15 charge states (dotted box) are the most thermally stable and compact conformations, and that the conformational family illustrated by the solid box could represent a transition-state or partially unfolded protein. Conformational structures of the fully unfolded protein could constitute the third conformational family (dashed box), charge states +20 to+26.

Table 4.1: A list of conditions used to try to convert full-length α-helical PrP into a β-sheet rich structure. All the samples were analysed by means of far-UV CD. A minimum at 217 nm in the far-UV CD spectrum would be indicative of a substantial increase in β-sheet structure.

Conversion conditions	**217 nm minimum?**
Incubation of α SHaPrP(23-231) at 65 °C for 24 hrs	X
Incubation of α SHaPrP(23-231) at 70 °C for 24 hrs	X
Incubation of α SHaPrP(23-231) at 75 °C for 24 hrs	X
Incubation of α SHaPrP(23-231) at 75 °C for 3 hrs repeated twice	X
Incubation of α SHaPrP(23-231) at 85 °C for 1 hr	X
Incubation of α SHaPrP(23-231) at 85 °C for 1 hr repeated four times	X
Incubation of α SHaPrP(23-231) at 85 °C for 24 hrs	X

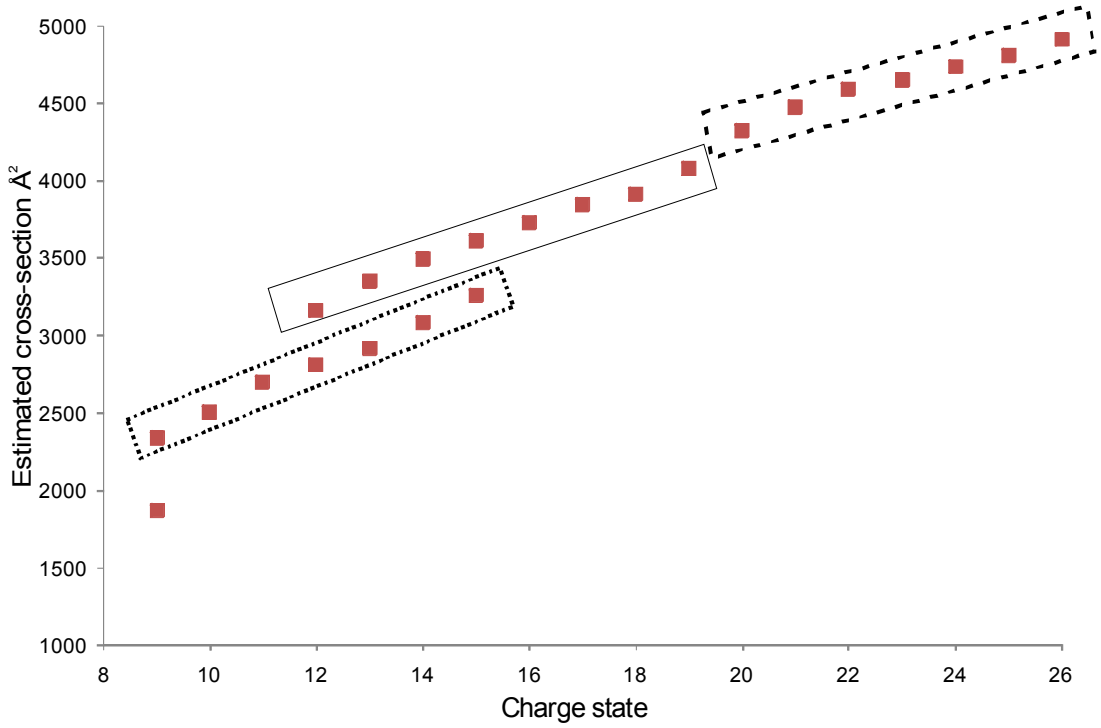

Figure 4.10: Estimated cross-section plot for α SHaPrP(23-231) for charge states +9 to +26. Boxes indicate different conformational families present.

Figure 4.11 shows a comparison of truncated and full-length estimated cross-sections of the hamster PrP at pH 5.5 and pH 7.0. The difference in molecular weight between the two constructs is 6862 Da. Under the two physiological pHs, both constructs show a similarity in their estimated cross-sections from charge states +9 to +15. It has been previously published that the N-terminal region has features of a flexible random coil-like polypeptide which is dissociated from the core truncated structure (Riek, Hornemann *et al.* 1997). At charge states +9 to +15 there are small differences in the estimated cross-section between the truncated and full-length proteins. If both proteins have near-identical structures, it is believed that the estimated cross-section of the full-length construct would proportionally increase in size relative to the truncated protein. The relatively small differences in the estimated cross-sections, for charge states +9 to +15, observed in Figure 4.11 suggest that the N-terminal tail associates with the truncated core. This tail-core association hypothesis indicates that the flexible N-terminal tail is structured. If the N-terminal

flexible tail were not associated with core, it is likely that the rotationally-averaged cross-section would be larger than that observed. A similar observation was made for the comparison of the truncated and full-length mouse PrP constructs and the same tail-core association conclusion was drawn.

A comparison has been made between the experimentally derived estimated cross-sections and theoretical approximations from published NMR structures and in-house computer modelling structures (see Figure 4.11). The structures of truncated Syrian hamster prion and truncated mouse prion determined by means of NMR spectroscopy, which were used for the calculations, are held in the Protein Data Bank (PDB) (Berman, Westbrook *et al.* 2000). All computer modelling studies were performed by UCSB collaborators and their methods are briefly outlined below. The AMBER suite of programs were used to create model structures of SHaPrP(90-231), SHaPrP(23-231), MoPrP(90-230) and MoPrP(23-230) based on information found in the PDB (1b10) and (1AG2) respectively. A simulated annealing protocol was used to minimise these structures and their theoretical cross-sections were calculated by the use of the program MobCal (Mesleh, Hunter *et al.* 1996; Shvartsburg and Jarrold 1996). The computer model structures are shown in Figure 4.12 and as an inset in Figures 4.11. Cross-sections were calculated by means of two different theoretical

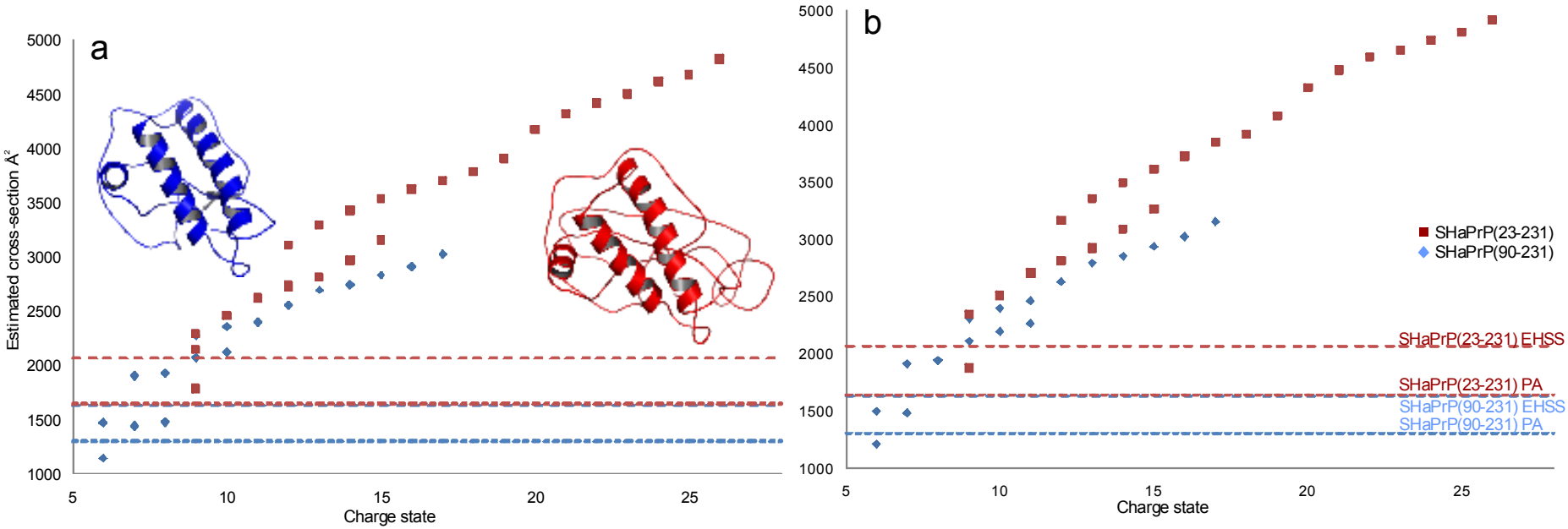

Figure 4.11: Estimated cross-section plot for α SHaPrP(90-231) (blue) and α SHaPrP(23-231) (red). (a) Charge states +6 to +26 estimated cross-sections at pH 5.5. Red dashed and dotted lines theoretical EHSS and PA cross-sections for SHaPrP(23-231), blue dashed and dotted lines theoretical EHSS and PA cross-sections for SHaPrP(90-231). Inset computer model structures used to determine theoretical cross-sections. (b) Charge states +6 to +26 estimated cross-sections at pH 7.0. Red dashed and dotted lines theoretical EHSS and PA cross-sections for SHaPrP(23-231), blue dashed and dotted lines theoretical EHSS and PA cross-sections for SHaPrP(90-231).

approximation approaches, the projection approximation (PA) and the exact hard sphere scattering (EHSS) method. The PA replaces the cross-section of an ion with its projection (shadow) and averages the projections created by every orientation of the ion. This method does not take into account protein-buffer gas interactions and can therefore under-estimate the cross-section of a protein. The EHSS method is similar to the PA method. The EHSS method includes the protein-buffer gas interactions in the cross-section calculation but excludes any electrostatic interactions. It has been observed that the EHSS model can over-estimate a protein's cross-section (Scarff, Thalassinos *et al.* 2008). The PA and EHSS cross-sections for all the hamster and mouse constructs are listed in Tables 4.2 and 4.3. The PA and EHSS cross-sections for hamster PrP are represented as dotted and dashed lines in Figure 4.11. The experimental estimated cross-sections for the lower charge states lie between the PA and EHSS theoretical values. At pH 5.5 three truncated conformations are in agreement with the theoretical values; when the pH is increased two conformations lie in-between the theoretical values at pH 7.0. It is observed from the data set for the full-length prion that the +9 charge state has a compact conformation that is in agreement with the theoretical cross-sections. These observations support the hypothesis that the lowest/lower charge states (under near-native conditions) are representative of the native protein structure. It is believed that the lower charge state conformations are more compact because they have fewer basic residues exposed on the surface when compared to the unfolded conformations of the same protein. Previous work has shown that a gaseous protein's conformation is more compact in cross-section than conformations that have been measured by the means of X-ray crystallography and NMR spectroscopy (Scarff, Thalassinos *et al.* 2008) (Shelimov, Clemmer *et al.* 1997a). The lower charge state estimated cross-sections are smaller than the EHSS model value. In the absence of solvent, polar amino acid side chains can collapse onto the protein surface because of intramolecular interactions (Shelimov, Clemmer *et al.* 1997b). In the gas-phase these interactions can reduce the overall rotationally averaged cross-section of a protein. The gas phase ions are therefore smaller in cross-section than the solution phase EHSS model cross-sections.

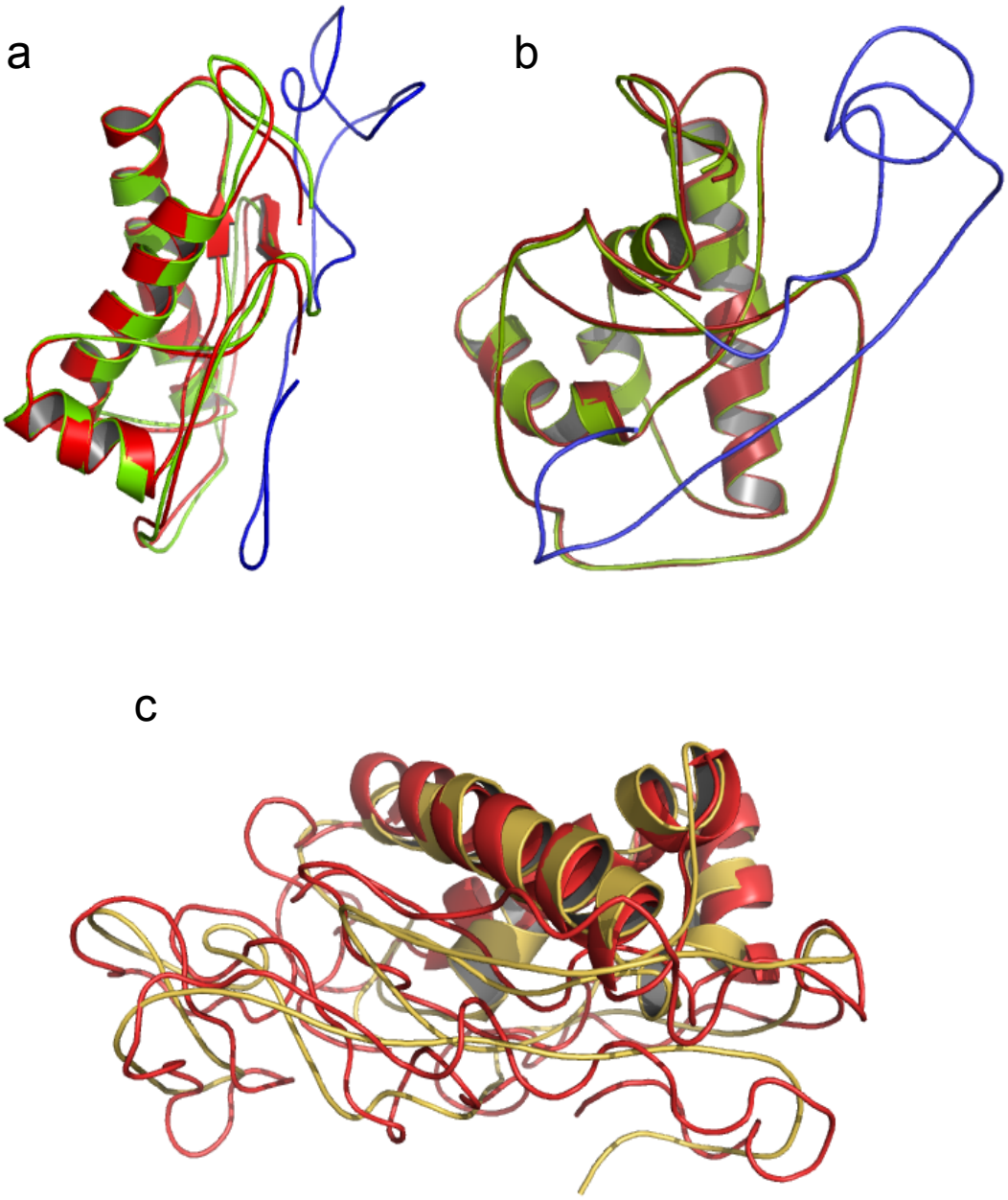

Figure 4.12: Cartoon representation of SHaPrP and MoPrP computer model structures. (a) **SHaPrP.** Red structure SHaPrP(90-231), green structure SHaPrP(23-231) residues 90-231 only and blue structure SHaPrP(23-231) residues 23-89. (b) **MoPrP**. Red structure MoPrP(90-230), green structure MoPrP(23-230) residues 90-230 only and blue structure MoPrP(23-230) residues 23-89. (c) **Structural alignment of cartoon representations**. SHaPrP(23-231) red and MoPrP(23-230) yellow.

Tables 4.2 and 4.3 show that the estimated experimental cross-sections for the hamster and mouse PrP constructs are in good agreement with the calculated theoretical cross-sections. A comparison of the hamster and mouse theoretical values suggests that the mouse PrP protein is larger in cross-section than that of the hamster. The opposite is observed in the experimental estimated cross-sections (see Figure 4.9 and Figure 4.16). The simplistic computer modelling studies did not energy minimise the conformational space surrounding each atom. This suggests that the calculated values could be unrealistically high in energy and, at present, do not represent the prion protein structure in its lowest energy state. The energy states of the individual models have not been optimised which suggests that the model hamster structure could be in a different energy state than the mouse. The potential difference in the modelling energy parameters could explain the opposing observations made between the cross-sections in the experimental and theoretical data. The model structures have compact cross-sections because they are based on the folded PDB NMR core structures. The agreement between the experimental and theoretical data further supports that hypothesis that the lowest experimental charge states are representative of the protein's native structure.

Table 4.2: Theoretical and experimental estimated cross-sections for the lowest charge state at physiological pH for Syrian hamster PrP.

Constructs	**SHaPrP(90-231)**		**SHaPrP(23-231)**	
Calculated cross-section	**pH 5.5**	**pH 7.0**	**pH 5.5**	**pH 7.0**
PA	1302 $Å^2$	1302 $Å^2$	1641 $Å^2$	1641 $Å^2$
EHSS	1626 $Å^2$	1626 $Å^2$	2065 $Å^2$	2065 $Å^2$
Experimental	1466 $Å^2$	1496 $Å^2$	1784 $Å^2$	1871 $Å^2$

Table 4.3: Theoretical and experimental estimated cross-sections for the lowest charge state at physiological pH for Mouse PrP.

Constructs	MoPrP(90-230)		MoPrP(23-230)	
Calculated cross-section	**pH 5.5**	**pH 7.0**	**pH 5.5**	**pH 7.0**
PA	1335 Å^2	1335 Å^2	1703 Å^2	1703 Å^2
EHSS	1676 Å^2	1676 Å^2	2158 Å^2	2158 Å^2
Experimental	1431 Å^2	1467 Å^2	1895 Å^2	2151 Å^2

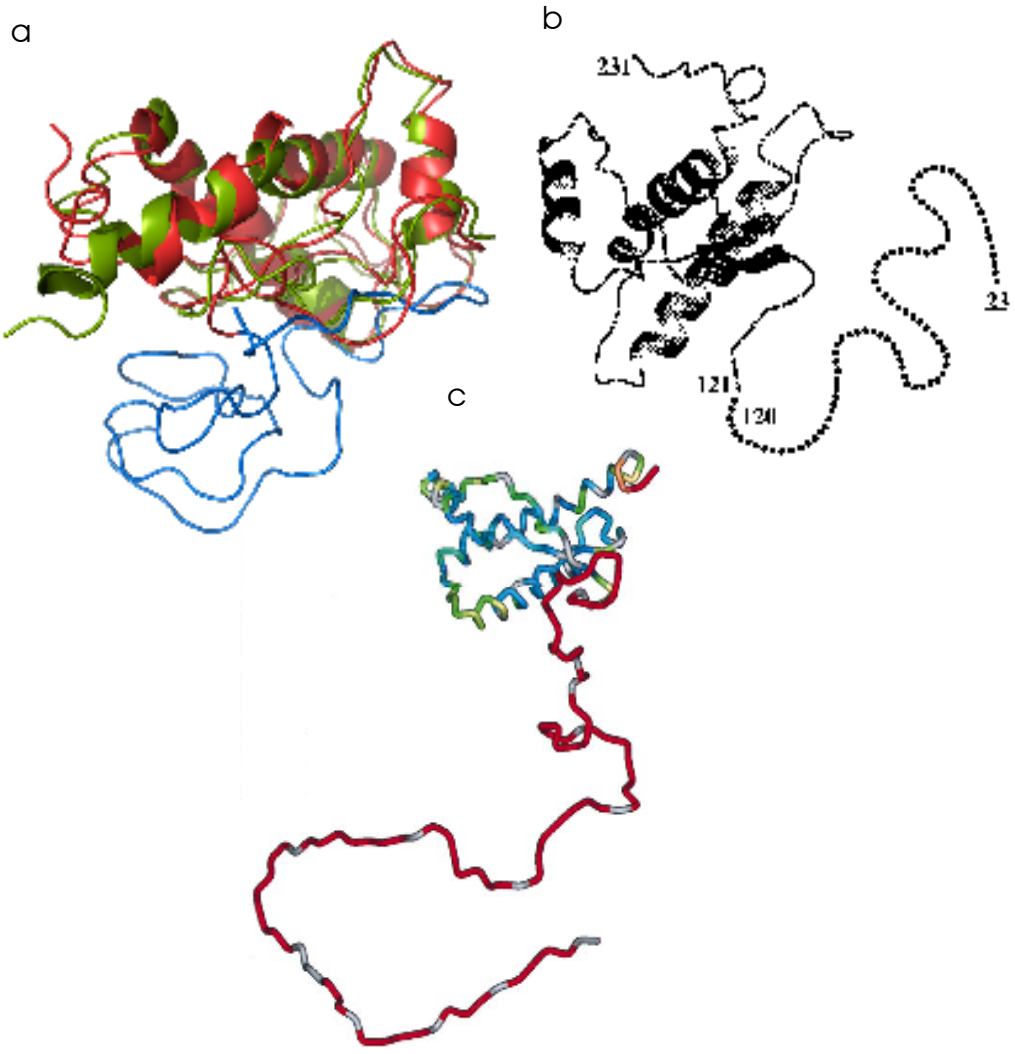

Figure 4.13: Cartoon representation of SHaPrP(23-231) computer model structure. Red structure SHaPrP(90-231), green structure SHaPrP(23-231) residues 90-231 only and blue structure SHaPrP(23-231) residues 23-89. (b) and (c) Previously published proposed structure for full-length PrP. Taken from (Riek, Hornemann *et al.* 1997) and (Donne, Viles *et al.* 1997) respectively.

4.7 Models

Figure 4.12 shows the model structures used to calculate the theoretical cross-section of the hamster and mouse PrP protein as listed in Tables 4.2 and 4.3. In Figure 4.12a and b the red structure represents the truncated protein amino acid residues 90-231, the green structure represents the residues 90-231 in the full-length protein (23-231) and the blue structure represents residues 23-89 in the flexible N-terminal tail. The red and green structures are very similar. This suggests that the addition of the N-terminal flexible tail does not affect the position or structure of the core protein residues. The full-length protein models, for both the hamster and mouse PrP, show that the flexible N-terminal tail can associate with the core structure. These models are in stark contrast to previous speculations which imply that the flexible N-terminal tail is unstructured and do not associate with the core structure (see Figure 4.13 for model comparison) (Donne, Viles *et al.* 1997; Riek, Hornemann *et al.* 1997). It is postulated that if the structure of the full-length protein was similar to that proposed by Riek *et al,* (Riek, Hornemann *et al.* 1997) and Donne *et al,* (Donne, Viles *et al.* 1997) (Figure 4.13), then the rotationally averaged cross-section of the protein would be considerably larger than that of the truncated protein. Experimental data suggest that the estimated cross-section of the two protein constructs are similar. The models in Figure 4.12 also suggest that the N-terminal flexible tail has some structure. The tail in both protein models appear to be twisted and contain several loop regions – the latter observation is particularly notable in the hamster model. Figure 4.12c shows a comparison of the hamster and mouse prions full-length model structures. The full-length hamster structure is illustrated in red and the corresponding mouse structure is shown in yellow. It is observed that the model structures are highly conserved and the individual N-terminal flexible tails have a similar ordered structure. As previously discussed these are simplified model structures and may differ from the protein's *in vivo* structure.

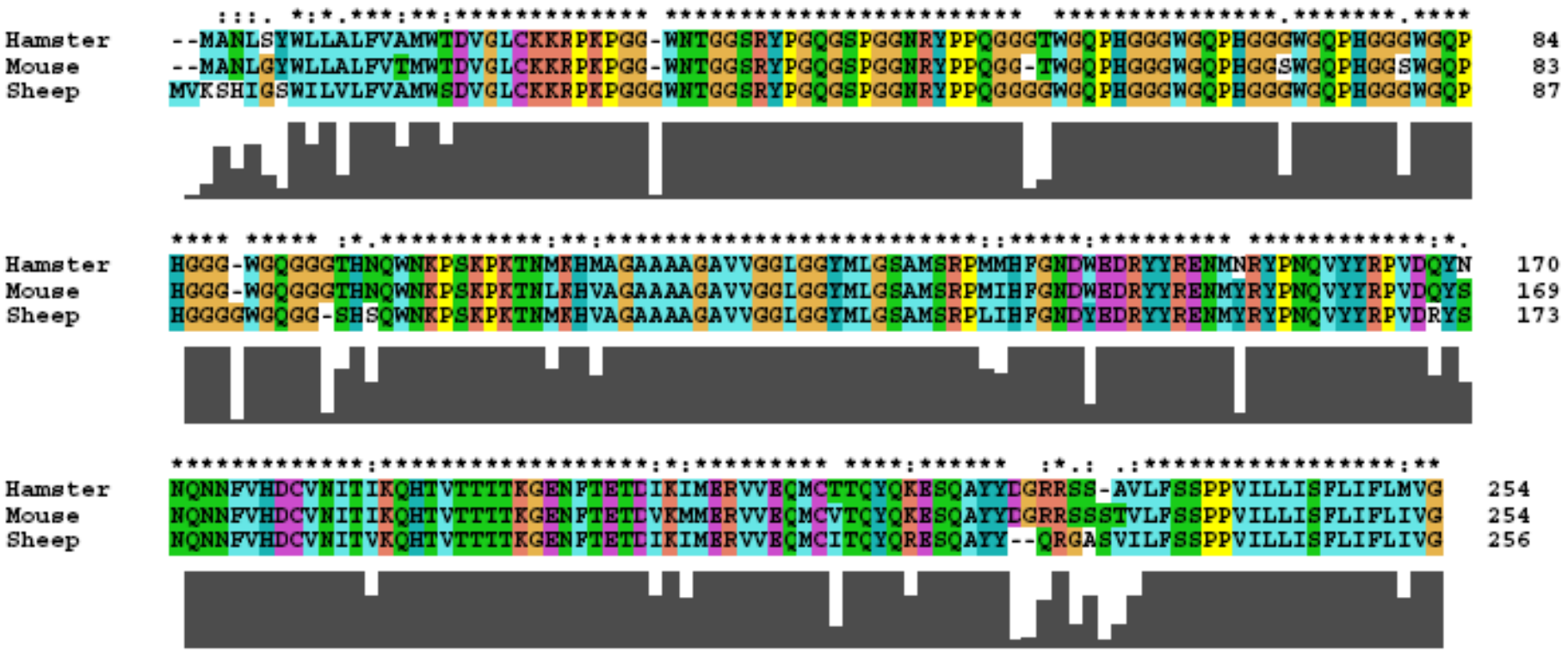

Figure 4.14: Sequence alignment for Syrian hamster, mouse and ovine PrP. Residues aligned using the nearest neighbour fit in Cluster.

4.8 Species structural stability

T-Wave ion mobility was used to investigate the structural differences between full-length Syrian hamster, mouse and ovine (OvPrP(23-230)) PrP. Figure 4.14 shows the aligned primary sequences of these three species. The PrP sequence is highly conserved throughout the mammalian species with ten different amino acid residues between the full-length hamster and mouse, 14 between hamster and ovine, and 15 between ovine and mouse. Figure 4.15 shows the mass spectra of OvPrP(23-230), MoPrP(23-230) and SHaPrP(23-231) at pH 5.5. Inset is the deconvoluted molecular mass of the corresponding oxidised sample: ovine 22872 Da, mouse 23059 Da and hamster 23102 Da. A comparison of the MS spectra indicates the charge state envelope distribution, between all three data sets, is similar. The exception to this observation is the presence of additional peaks in the OvPrP(23-230) spectrum which are a result of methionine oxidation (labelled accordingly).

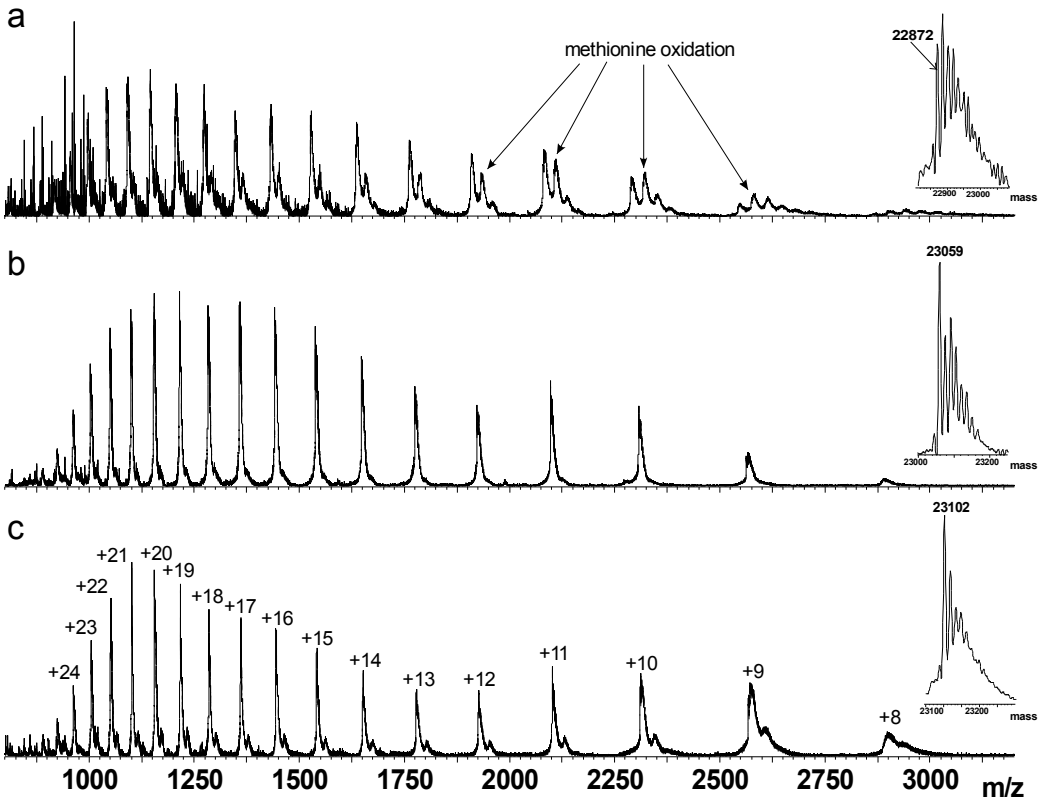

Figure 4.15(a): Mass spectrum of α OvPrP(23-230) at pH 5.5. Inset. Deconvoluted mass of the oxidised protein. (b) Mass spectrum of α MoPrP(23-230) at pH 5.5. Inset. Deconvoluted mass of the oxidised protein. (c) Mass spectrum of SHaPrP(23-231) at pH 5.5. Inset. Deconvoluted mass of the oxidised protein.

Figure 4.16 shows the estimated cross-sections for charge states +9 to +26 of the full-length prion proteins at pH 5.5 and pH 7.0. Only ATDs that are greater than 50% in relative intensity are represented in the estimated cross-section plot. Upon the addition of sequential protons the estimated cross-section of the protein increases and the higher charge states represent an extending/unfolding structure. Charge states +9, +12 to +14 and +17 to +18 have two or more distinct stable conformations whereas the remaining charge states have only one. A comparison of the three species reveals there are no significant differences in estimated cross-section at charge states +9 to +14 at pH 5.5 or between the +9 to +12 charge states at pH 7.0 (Figure 4.16 a and b). This implies that the most biologically relevant conformations are similar. The program PyMOL was used to make a comparison of the corresponding structures based on NMR spectroscopy. It showed that there was a structural similarity between the species (data not shown). No notable differences were observed between the estimated cross-section of mouse and ovine prion at either pH. This is despite the 15 different amino acid residues in their sequence and a 187 Da difference in the molecular weights. The estimated cross-sections of mouse and ovine prions are smaller than those of hamster prions of similar charge. This suggests that the hamster prion structure can adopt a more open conformation in the gas-phase. At charge states $\geq$ +15 small but distinct differences in the estimated cross-section were observed between hamster prion and mouse prion. These differences are exemplified at charge states +20 to +26 in which a 5% difference in cross-section was observed. There are data to suggest that hamster and mouse PrP fold via different mechanisms despite their high sequence and three-dimensional structure homology (Robinson and Pinheiro 2009). These mechanisms have been previously discussed in section 4.5. This difference in folding mechanisms, and presumably unfolding mechanisms, could account for the differences observed in the estimated cross-sections at higher charge states between SHaPrP(23-231) and MoPrP(23-230) in Figure 4.16. The similarity between the estimated cross-sections of mouse and ovine PrP, across the charge state distribution, suggests that ovine PrP folds via a nucleation condensation mechanism.

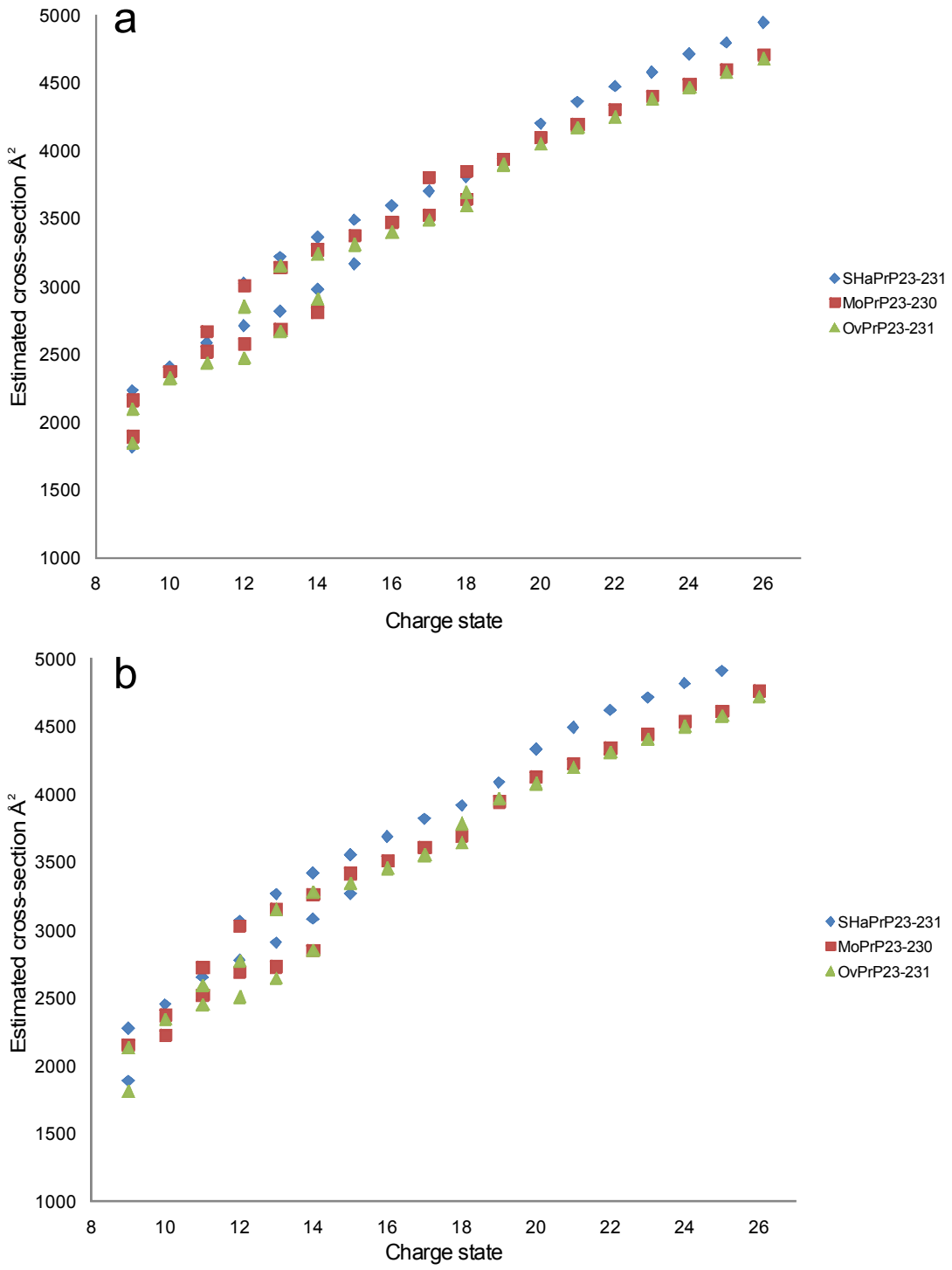

Figure 4.16: Estimated cross-section plot for α SHaPrP(23-231) (blue),α MoPrP(23-230) (red) and α OvPrP(23-231) (green) charge states +9 to +26. (a) pH 5.5. (b) pH 7.0.

Syrian hamster SHaPrP(23-231), mouse MoPrP(23-230) and ovine OvPrP(23-230) differ in their primary structure in the positions believed to be key in the structure's stability as shown in Figure 4.14. In order to investigate the hypothesis that key amino acid residues are required to stabilise the prion protein's tertiary structure, the three different recombinant mammalian prion proteins were subjected to a wide range of activating conditions. Several hypotheses have been outlined which show that the Q171R mutation present in the ovine prion can destabilise the secondary and tertiary structure of PrP (Paludi, Thellung *et al.* 2007; Robinson and Pinheiro 2009) (see Figure 4.17 magenta residue). Studies have shown polymorphisms at amino acid residues 136, 154 and 171 (ovine numbering) are associated with different degrees of scrapie susceptibility. Sheep with the genotype PrP(ARQ) [PrP(Ala136/Arg154/Gln171)] are vulnerable to scrapie, whereas those with the PrP (ARR) genotype [PrP(Ala136/Arg154/Arg171)] are scrapie resistant (Paludi, Thellung *et al.* 2007). This suggests that the amino acid residue Q171 plays an essential role in disease resistance. From co-crystallisation studies of these two variants it is believed that a hydrogen bond exists between R167 and Q171 in the ARQ variant. It is believed this interaction can stabilise the loop region between β-strand two (S2) and helix 2. This stabilisation mechanism could also be present in Syrian hamster and mouse PrP as both have the ARQ genotype. In contrast, the R167 and R171 residues in the scrapie resistant variant ARR destabilise the loop region because of electrostatic repulsion (Eghiaian, Grosclaude *et al.* 2004). Molecular dynamic stimulations have shown that destabilisation in this loop region can stimulate the opening of other domains to destabilise the overall tertiary structure (DeMarco and Daggett 2007).

The stability of a conformation in the gas-phase can be investigated by increasing the amount of energy with which the ions are injected into the mobility cell (Grabenauer, Sanghera *et al.* 2009). The injection energy studies performed by means of DCIM instrument can be mimicked in the T-Wave technology by increasing the trap voltage.

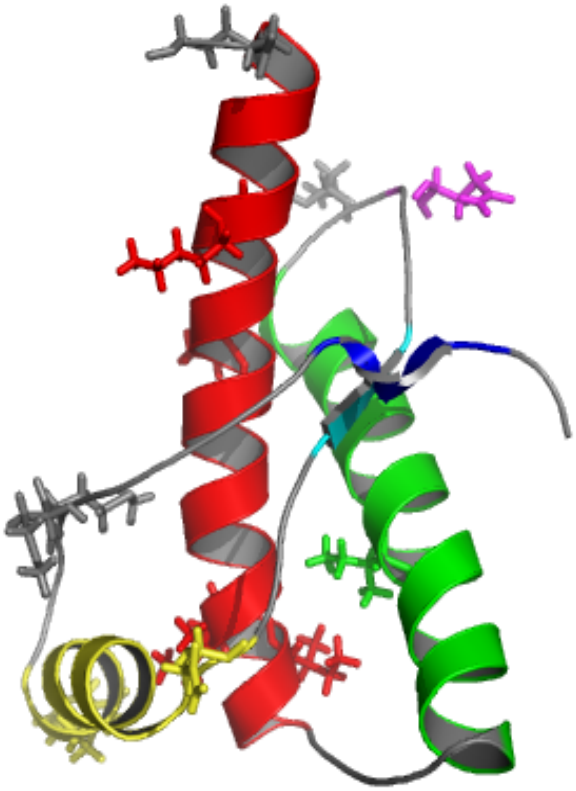

Figure 4.17: Cartoon representation of the NMR structure of recombinant SHaPrP(121-231) in aqueous solution highlighted residues and those that differ from mouse and sheep. Magenta residue R171 key mutation in sheep sequence (Q in sheep) believed to destabilise the structure. Green stick residue I184 (V in sheep) possibly essential to create interactions between helix 2 and 3. Different residues may change the kinetic pathway of folding.

The conversion from folded conformations to extended/unfolded conformations was monitored for charge state +9 by means of IM-MS for all three proteins. Figure 4.18a shows the ATDs for the +9 charge state of OvPrP(23-230) for a range of trap collision voltages. At low trap collision voltages there is a broad peak with three defined apexes corresponding to the estimated cross-sections 1624 $Å^2$, 1928 $Å^2$ and 2142 $Å^2$. As the trap collision energy was increased a number of broad but discrete peaks were observed at longer drift times. These latter peaks, assigned **D** and **E** in Figure 4.18a, can be related to the extended/unfolded conformations of the prion protein (estimated cross-section 2356 $Å^2$ and 2535 $Å^2$ respectively). The intensity of the peaks that correspond to the more compact structure, (**A**, **B** and **C**) begins to decrease at trap collision voltages 20 V, 20 V and 40 V respectively. At 60 V

onwards the extended species **D** is the most intense peak and at 50 V the most unfolded conformation (**E**) can be observed. The signal to noise ratio in the mass spectrum of charge state +9 OvPrP(23-230) decreased dramatically at a trap collision energy of 80 V and no further measurements could be obtained beyond this point. The width of the **C** and **D** peaks are considerably broader than the widths of the other peaks. This suggests that there may be multiple disparate conformations contributing to these peaks in contrast to **A**, **B** and **E**. Similar ATDs with conformational ensembles of analogous cross-section were observed for SHaPrP(23-231) and MoPrP(23-230) (data not shown).

A comparison of the gas-phase unfolding of SHaPrP(23-231), MoPrP(23-230) and OvPrP(23-230) is shown in Figure 4.18b. The relative stability of the hamster, mouse and ovine PrP conformations follow the same trend. In all three mammalian species the conformational ensemble **C** is dominant at 30 V. The intensities of the unfolded/extended conformations **D** and **E** rise in abundance at 50 V, as conformation **C** diminishes, and **D** becomes the dominant species. In the hamster and mouse sample the most unfolded form, **E**, is not observed until the compact **A** conformation has disappeared and conformation **B** accounts for less than 10% of the ion count. All conformations have similar intensities at 80 V with the notable exception of conformations **B** and **D** in ovine. The relative intensity of the **D** peak for ovine prion is approximately 10% lower than that of hamster and mouse PrP, whereas the intensity for conformation **B** is approximately 10% higher. This implies that the compact conformations are more stable in the ovine PrP than they are in the other two proteins. This is a surprising result because the ovine ARR genotype, as discussed above, contains steric hinderance between residues R167 and R171 which have the potential to destabilise the structure. Recent kinetic folding studies have shown that core mutations within human PrP have a profound effect on the protein's stability - of note were mutations in the amino acid residues V108, located in helix 2 and M206 within helix 3 (human numbering) (Hart, Hosszu *et al.* 2009). These two residues are located on the interface of the respective helices and can interact to create structural constraints (see Figure 4.17 green and red stick residues). In all the mammalian species studied here the equivalent V108 and M206 residues are

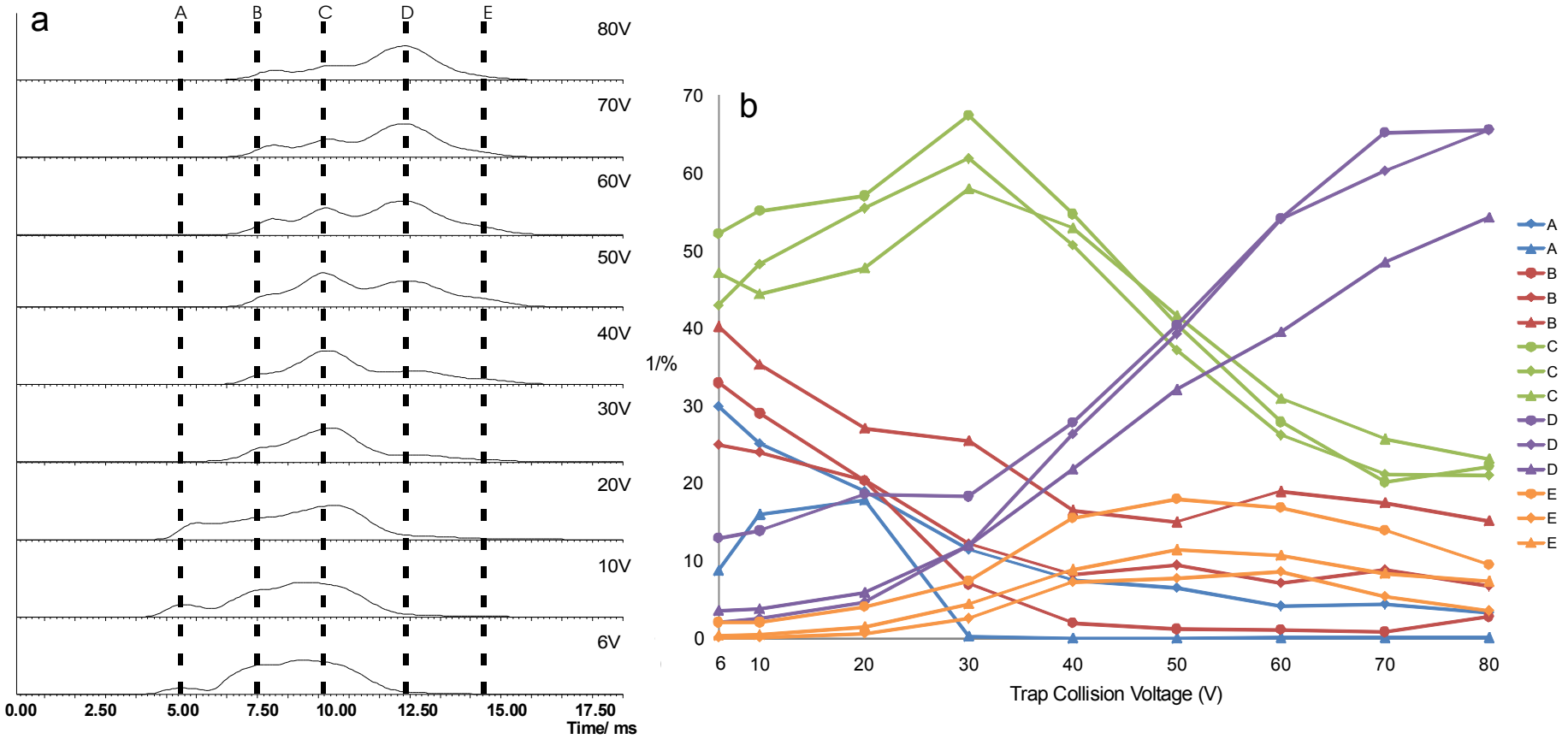

Figure 4.18: (a) The arrival time distribution of the +9 charge state of OvPrP23-230 monomer acquired at the corresponding trap collision voltage show a conformational transition from compact to extended ion conformations. The centroid estimated cross-sections of peaks are labelled A to E. (b) The relative intensities of the individual peaks calculated from the arrival time distribution of 9+ charge state of monomer SHaPrP(23-231) (circle), MoPrP(23-230) (diamond) and OvPrP(23-231) (triangle).

conserved and therefore cannot account for the difference in stability. Hart *et al*, observed that the I184V mutation had a dramatic effect on the human PrP protein's folding kinetics. Isoleucine is the equivalent amino acid residue in the hamster and mouse PrP primary sequence whereas valine is the equivalent in ovine PrP (see Figure 4.14). This mutation could account for the differences in stability observed for conformation **D**. The residue is located within helix 2 and has the ability to interact with helix 3 and S2 (see Figure 4.17 green stick residue). Kinetic experiments suggest that this single mutation can distort the native-folded structure of PrP and change the equilibrium pathway between the folded and unfolded structure, without significantly changing the global structure of the protein (Hart, Hosszu *et al.* 2009). The difference in the folding pathway may energetically favour the folded structure; hence the higher intensity of conformation **B** and the lower intensity of conformation **D** observed for ovine compared to hamster and mouse prions.

4.9 Conclusions

ESI-IM-MS has been used to study recombinant isobaric prion conformational isoforms at relevant physiological pHs: α-SHaPrP(90-231), β-sheet rich SHaPrP(90-231), α-MoPrP(90-230) and β-sheet rich MoPrP(90-230) at pH 5.5 and pH 7.0. CD and ATR FTIR information characterised the secondary structure of the proteins whilst the protein aggregations were observed by means of EM. The presence of the β-sheet rich SHaPrP(90-231) and MoPrP(90-230) was further suggested by the ready aggregation of the samples necessitating each sample solution to be sonicated prior to any IM-MS experiments. The use of ion mobility as a shape-selective separation technique has made possible the differentiation of the recombinant α-helical SHaPrP(90-231) and β-sheet rich SHaPrP(90-231) conformational isoforms at pH 5.5. While the differences in cross sections were small (~3%) the resulting ATD profiles were significantly different at this pH. No differences in cross-sections or ATD profiles were observed when the analyte was at pH 7.0. In contrast, the estimated cross-sections of the truncated mouse isoforms were distinctly different at pH 7.0 (≥ 5%) but were difficult to distinguish under the mildly acidic pH conditions. Significant differences were observed between the individual ATDs of the α MoPrP(90-230) and β-sheet rich MoPrP(90-230) at both physiological pHs. A comparison of the truncated Syrian hamster PrP cross-sections with those of mouse PrP showed that the hamster isoforms were larger in cross-section than those of the mouse PrP. It was reasoned that the differences in the folding mechanisms could account for the differences in the estimated cross-section.

The structure of full-length PrP was probed by the means of IM-MS. The estimated cross-section of α SHaPrP(23-231) indicated the presence of three different conformational families. The difference between the families was attributed to the difference in the proteins' unfolding. The first family contained the lower charge states and were considered the most compact conformations, the second family suggested that the conformations were in the folded/unfolded transition stage and the third family incorporated conformations which were fully unfolded. Further evidence that the first family contained the most compact or native-like conformations came from a comparison between the Syrian hamster constructs

SHaPrP(90-231) and SHaPrP(23-231). At the lower charge states the estimated cross-section of both constructs were similar. This similarity suggested that the N-terminal flexible tail was associated with the core structure rather than, as previous studies had suggested, being unstructured and dissociated. A comparison between the theoretically calculated and experimentally derived cross-sections also supported the hypothesis that the flexible N-terminal tail was associated with the core PrP structure. These simplistic computer model structures supported the findings of previously published work that the lowest/lower charge states are similar to the *in vivo* structure (Scarff, Thalassinos *et al.* 2008).

Three different mammalian PrP species were studied by means of IM-MS. Previous studies have shown that a species barrier exists between the three species despite their highly conserved primary sequences (Prusiner, Scott *et al.* 1990; Scott, Kohler *et al.* 1992). The estimated cross-section for the lower charge states was similar between all the species of PrP but at the higher charge states significant differences in the cross-section between hamster and mouse PrP, and hamster and ovine PrP were observed. The estimated cross-section of mouse PrP and ovine PrP were similar at all of the charge states under both physiological conditions. The lowest, most biologically relevant, charge state of each species was subjected to increasing trap collision energies and the stability of the conformations was monitored. The most compact conformations in ovine PrP were more stable than the corresponding conformations in Syrian hamster and mouse PrP. The differences in stability suggest that the I184V amino acid mutation plays an important role in the tertiary structures stability. The occurrence of the species barrier between hamster and mouse PrP, and hamster and ovine PrP, could be because of the differences in their tertiary structure and folding mechanisms. The species barrier between ovine PrP and mouse PrP could be because of the differences in the proteins' stability and the mutation of amino acid I184V in their primary sequence.

ESI-MS alone cannot distinguish between the isobaric conformational isoforms. The T-Wave device is able to operate at biologically relevant sample concentrations and with its speed and ease of use it has the ability to be used in an automated fashion.

ESI-IM-MS provides an extra dimension of fast, sensitive, gas-phase, ion separation enabling conformational changes in the protein structure to be probed. Consequently, the technique is worth evaluating as a potential method of providing an ante-mortem screening assay of bodily fluids for protein misfolding diseases such as TSEs. The T-Wave device can also be used to study the differences in structural stability of a protein and T-Wave cross-section data is comparable to NMR spectroscopy cross-section data and computer model structures.

4.10 References

Back, J. W., Sanz, M. A., De Jong, L., De Koning, L. J., Nijtmans, L. G., De Koster, C. G., Grivell, L. A., Van Der Spek, H. and Muijsers, A. O. (2002). A structure for the yeast prohibitin complex: Structure prediction and evidence from chemical crosslinking and mass spectrometry. *Protein Science* **11**, 2471-8.

Badman, E. R., Myung, S. and Clemmer, D. E. (2005). Evidence for Unfolding and Refolding of Gas-Phase Cytochrome c Ions in a Paul Trap. *Journal American Society for Mass Spectrometry* **16**, 1493-1497.

Berman, H. M., Westbrook, J., Feng, Z., Gilliland, G., Bhat, T. N., Weissig, H., Shindyalov, I. N. and Bourne, P. E. (2000). The Protein Data Bank. *Nucleic Acids Research* **28**, 235-42.

Borchelt, D. R., Scott, M., Taraboulos, A., Stahl, N. and Prusiner, S. B. (1990). Scrapie and cellular prion proteins differ in their kinetics of synthesis and topology in cultured cells. *Journal of Cell Biology* **110**, 743-52.

Castilla, J., Saa, P., Hetz, C. and Soto, C. (2005). In vitro generation of infectious scrapie prions. *Cell* **121**, 195-206.

Caughey, B., Race, R. E., Ernst, D., Buchmeier, M. J. and Chesebro, B. (1989). Prion protein biosynthesis in scrapie-infected and uninfected neuroblastoma cells. *Journal of Virology* **63**, 175-81.

Caughey, B. and Raymond, G. J. (1991). The scrapie-associated form of PrP is made from a cell surface precursor that is both protease- and phospholipase-sensitive. *Journal of Biological Chemistry* **266**, 18217-23.

DeMarco, M. L. and Daggett, V. (2007). Molecular mechanism for low pH triggered misfolding of the human prion protein. *Biochemistry* **46**, 3045-54.

Donne, D. G., Viles, J. H., Groth, D., Mehlhorn, I., James, T. L., Cohen, F. E., Prusiner, S. B., Wright, P. E. and Dyson, H. J. (1997). Structure of the recombinant full-length hamster prion protein PrP(29-231): the N terminus is highly flexible. *Proceeding of the National Academy of Sciences U S A* **94**, 13452-7.

Eghiaian, F., Grosclaude, J., Lesceu, S., Debey, P., Doublet, B., Treguer, E., Rezaei, H. and Knossow, M. (2004). Insight into the PrPC-->PrPSc conversion from the structures of antibody-bound ovine prion scrapie-susceptibility variants. *Proceeding of the National Academy of Sciences U S A* **101**, 10254-9.

Gambetti, P., Dong, Z., Yuan, J., Xiao, X., Zheng, M., Alshekhlee, A., Castellani, R., Cohen, M., Barria, M. A., Gonzalez-Romero, D., Belay, E. D., Schonberger, L. B., Marder, K., Harris, C., Burke, J. R., Montine, T., Wisniewski, T., Dickson, D. W., Soto, C., Hulette, C. M., Mastrianni, J. A., Kong, Q. and Zou, W. Q. (2008). A novel human disease with abnormal prion protein sensitive to protease. *Annals of Neurology* **63**, 697-708.

Grabenauer, M., Sanghera, N., Pinheiro, T. J., H, S. J. and Bowers, M. T. (2009). Conformational Stability of Syrian Hamster Prion Protein PrP(90-231). *Journal of the American Chemical Society* Submitted.

Hart, T., Hosszu, L. L., Trevitt, C. R., Jackson, G. S., Waltho, J. P., Collinge, J. and Clarke, A. R. (2009). Folding kinetics of the human prion protein probed by temperature jump. *Proceeding of the National Academy of Sciences U S A* **106**, 5651-6.

Hilton, G. R., Jackson, A. T., Thalassinos, K. and Scrivens, J. H. (2008). Structural Analysis of Synthetic Polymer Mixtures Using Ion Mobility and Tandem Mass Spectrometry. *Analytical Chemistry* **80**, 9720-9725.

Hosszu, L. L., Trevitt, C. R., Jones, S., Batchelor, M., Scott, D. J., Jackson, G. S., Collinge, J., Waltho, J. P. and Clarke, A. R. (2009). Conformational Properties of {beta}-PrP. *Journal of Biologcial Chemistry* **284**, 21981-90.

Maras B., B. D., Schinina M. E., Cardone F., Pocchiari (2004). Prion (PrPres) allotypes profiling: new perspectives from mass spectrometry. *European Journal of Mass Spectrometry* **10**, 371-382.

Martins, S. M., Frosoni, D. J., Martinez, A. M., De Felice, F. G. and Ferreira, S. T. (2006). Formation of soluble oligomers and amyloid fibrils with physical properties of the scrapie isoform of the prion protein from the C-terminal domain of recombinant murine prion protein mPrP-(121-231). *Journal of Biological Chemistry* **281**, 26121-8.

Mesleh, M. F., Hunter, J. M., Shvartsburg, A. A., Schatz, G. C. and Jarrold, M. F. (1996). Structural Information from Ion Mobility Measurements: Effects of the Long-Range Potential. *Journal of Physical Chemistry* **100**, 16082-16086.

Onisko, B., Dynin, I., Requena, J. R., Silva, C. J., Erickson, M. and Carter, J. M. (2007). Mass Spectrometric Detection of Attomole Amounts of the Prion Protein by nanoLC/MS/MS. *Journal of the American Society for Mass Spectrometry* **18**, 1070-1079.

Paludi, D., Thellung, S., Chiovitti, K., Corsaro, A., Villa, V., Russo, C., Ianieri, A., Bertsch, U., Kretzschmar, H. A., Aceto, A. and Florio, T. (2007). Different structural stability and toxicity of PrP(ARR) and PrP(ARQ) sheep prion protein variants. *Journal of Neurochemistry* **103**, 2291-300.

Principe, S., Maras, B., Schinina, M. E., Pocchiari, M. and Cardone, F. (2008). Unraveling the details of prion (con)formation(s): recent advances by mass spectrometry. *Current Opinion in Drug Discovery & Development* **11**, 697-707.

Prusiner, S. B. (1998). Prions. *Proceeding of the National Academy of Sciences U S A* **95**, 13363-83.

Prusiner, S. B., Scott, M., Foster, D., Pan, K. M., Groth, D., Mirenda, C., Torchia, M., Yang, S. L., Serban, D., Carlson, G. A. and et al. (1990). Transgenetic studies implicate interactions between homologous PrP isoforms in scrapie prion replication. *Cell* **63**, 673-86.

Pushie, M. J., Ross, A. R. and Vogel, H. J. (2007). Mass spectrometric determination of the coordination geometry of potential copper(II) surrogates for the mammalian prion protein octarepeat region. *Analytical Chemistry* **79**, 5659-67.

Qin, K., Yang, Y., Mastrangelo, P. and Westaway, D. (2002). Mapping Cu(II) binding sites in prion proteins by diethyl pyrocarbonate modification and matrix-assisted laser desorption ionization-time of flight (MALDI-TOF) mass spectrometric footprinting. *Journal of Biological Chemistry* **277**, 1981-90.

Requena, J. R., Groth, D., Legname, G., Stadtman, E. R., Prusiner, S. B. and Levine, R. L. (2001). Copper-catalyzed oxidation of the recombinant SHa(29-231) prion protein. *Proceeding of the National Academy of Sciences U S A* **98**, 7170-5.

Riek, R., Hornemann, S., Wider, G., Glockshuber, R. and Wuthrich, K. (1997). NMR characterization of the full-length recombinant murine prion protein, mPrP(23-231). *FEBS Letters* **413**, 282-8.

Robinson, P. J. and Pinheiro, T. J. (2009). The unfolding of the prion protein sheds light on the mechanisms of prion susceptibility and species barrier. *Biochemistry* **48**, 8551-8.

Scarff, C. A., Thalassinos, K., Hilton, G. R. and Scrivens, J. H. (2008). Travelling wave ion mobility mass spectrometry studies of protein structure: biological significance and comparison with X-ray crystallography and nuclear magnetic

resonance spectroscopy measurements. *Rapid Communications in Mass Spectrometry* **22**, 3297-3304.

Scott, M. R., Kohler, R., Foster, D. and Prusiner, S. B. (1992). Chimeric prion protein expression in cultured cells and transgenic mice. *Protein Science* **1**, 986-97.

Shelimov, K. B., Clemmer, D. E., Hudgins, R. R. and Jarrold, M. F. (1997a). Protein Structure in Vacuo: Gas-Phase Conformations of BPTI and Cytochrome c. *Journal American Chemical Society* **119**, 2240-2248.

Shelimov, K. B., Clemmer, D. E., Hudgins, R. R. and Jarrold, M. F. (1997b). Protein Structure in Vacuo: Gas-Phase Conformations of BPTI and Cytochrome c. *Journal- American Chemical Society* **119**, 2240-2248.

Shvartsburg, A. A. and Jarrold, M. F. (1996). An exact hard-spheres scattering model for the mobilities of polyatomic ions. *Chemical Physics Letters* **261**, 86-91.

Sinelnikov, I., Kitova, E. N. and Klassen, J. S. (2007). Influence of Coulombic Repulsion on the Dissociation Pathways and Energetics of Multiprotein Complexes in the Gas Phase. *Journal- American Society for Mass Spectrometry* **18**, 617-631.

Thalassinos, K. and Scrivens, J. H. (2009). Applications of Traveling Wave Ion Mobility Mass Spectrometry. *CRC Press*.

Whittal, R. M., Ball, H. L., Cohen, F. E., Burlingame, A. L., Prusiner, S. B. and Baldwin, M. A. (2000). Copper binding to octarepeat peptides of the prion protein monitored by mass spectrometry. *Protein Science* **9**, 332-43.

Wyttenbach, T., Grabenauer, M., Thalassinos, K., Scrivens J. H and Bowers, M. T. (2009). The Effect of Calcium Ions and Peptide Ligands on the Stability of the Calmodulin Dumbbell Structure. *Submitted*.

Yedidia, Y., Horonchik, L., Tzaban, S., Yanai, A. and Taraboulos, A. (2001). Proteasomes and ubiquitin are involved in the turnover of the wild-type prion protein. *Embo J* **20**, 5383-91.

Chapter 5
Results: Conformational Studies of Metal Ion Coordination to the Prion Protein

5.1 Introduction

5.1.1 Role of Copper

Copper is an essential element for life. It has numerous roles within the human body including acting as a catalyst in the transportation of iron, in the synthesis of collagen, in the coagulation of blood (Linder and Hazegh-Azam 1996) and of particular significance to prion research in the synthesis of neurotransmitters (Georgieff 2007). A deficiency of copper can lead to a variety of diseases ranging from the common blood disorder anaemia to the rarer Wilson's disease. Wilson's disease is an autosomal recessive disorder characterised by the toxic accumulation of copper in the liver and brain. The brain pathology of deceased Wilson's disease sufferers resembles the spongiform degeneration observed in PrP diseases (Tanzi, Petrukhin *et al.* 1993). It is widely accepted that PrP^{C} can bind copper in a cooperative manner with some indication that it is involved in the homeostasis of copper within the body (Brown, Qin *et al.* 1997; Viles, Cohen *et al.* 1999). In CJD patients, the levels of copper found in the brain are significantly decreased (Wong, Chen *et al.* 2001). Similar effects/changes were also found in mice infected with scrapie.

5.1.2 Copper Transport

Copper uptake, sequestration and excretion in living systems are highly regulated processes which eliminates the need for copper storage. In blood, the major protein that transports copper is ceruloplasmin. This protein is stimulated by ascorbate and other reducing agents to take up copper which it then readily deposits into tissues (Linder and Hazegh-Azam 1996). Copper can act as an electron transfer agent or as a cofactor for specific enzymes such as superoxide dismutase (SOD). The Cu/Zn SOD enzyme catalyses the disproportionation reaction of superoxide (O_2^-) to hydrogen peroxide and oxygen to protect the cell against oxygen radical damage (as described in Figure 5.1). Recombinant mouse and chicken PrP can also act as SOD enzymes but their activity is approximately 10% of the extremely potent Cu/Zn-SOD enzyme. Although low, this PrP SOD activity is believed to be significant and is observed only in the full-length species (Thompsett and Brown 2004). SOD activity

in the octarepeat peptides alone was found to be insufficient (Wong, Pan *et al.* 2000). It has been shown that knockout *Prnp* mice have lower levels of copper in their brains and reduced Cu/Zn-SOD activity (approximately 50%) compared to their wild type counterparts (Brown 2001; White, Bush *et al.* 1999). This implies that the lower SOD activity in knockout mice is due to the absence of the PrP protein. It is believed that PrP^C can behave as a sacrificial antioxidant resulting in oxidative chemical modification of the methionine and histidine residues in PrP^C (Nadal, Abdelraheim *et al.* 2007). In proteins, methionine residues can act as a reactive oxygen species (ROS) sink which scavenge for harmful ROS before they can damage the cell. The toxicity of ROS is strongly increased in the presence of copper. In Fenton chemistry, copper ions act as a catalyst to transfer a single electron and aid the formation of a free radical (see Figure 5.2) (Fenton 1995). This newly formed free radical ($^{\bullet}OH$) is toxic to the cell and can cause damage to the DNA or initiate lipid peroxidation cascades (Fernaeus, Reis *et al.* 2005). The short half life of PrP (3-6 hours) (Borchelt, Scott *et al.* 1990; Caughey, Race *et al.* 1989; Caughey and Raymond 1991; Yedidia, Horonchik *et al.* 2001) coupled with its high copper binding affinity implies that the PrP^C functional role is to act as a sacrificial quencher of free radicals, thereby protecting the cell from the Cu^{2+} toxic effects (Viles, Klewpatinond *et al.* 2008).

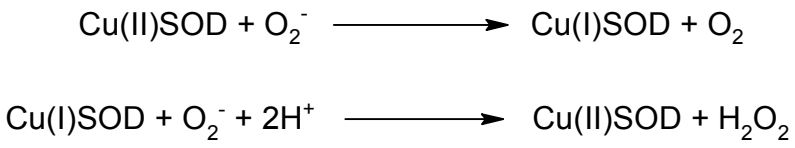

Figure 5.1: Cu/Zn-SOD reaction with superoxide.

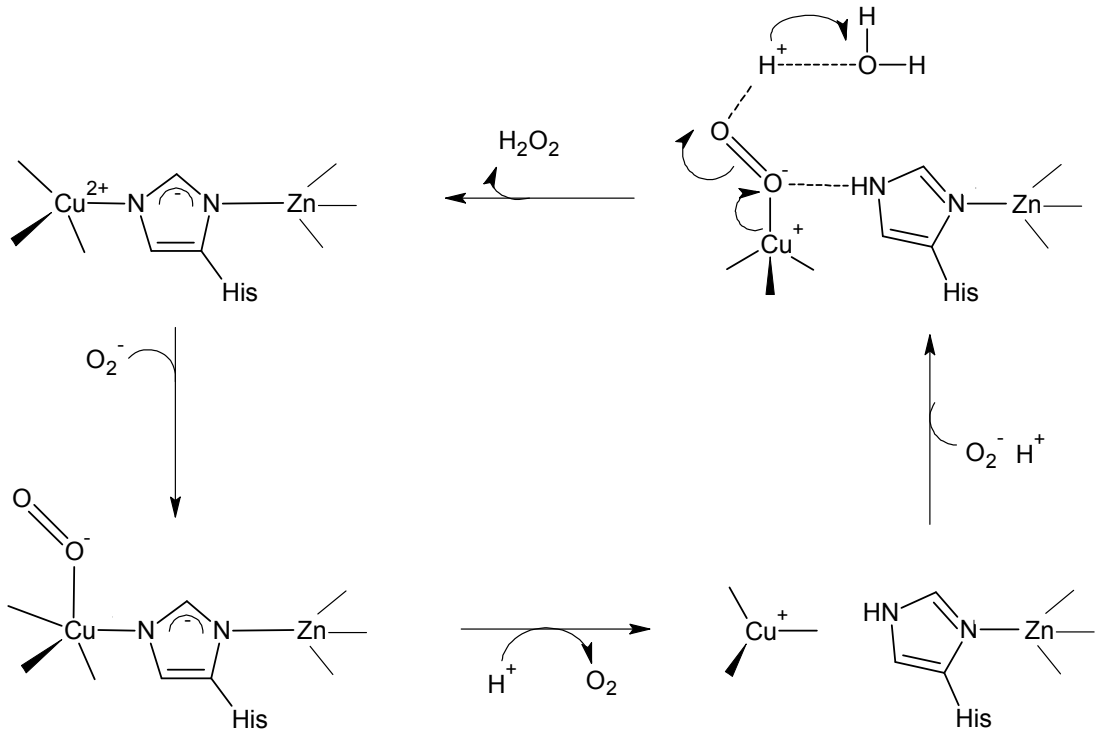

Figure 5.2: Proposed mechanism for the action of BESOD. Mechanism thought to be similar in the PrP protein (Fenton 1995). The bound superoxide reduces the copper(II) to copper (I) with simultaneous cleavage of the bond between the copper and His (this is the bridging His in Cu/Zn-SOD). Dioxygen is released and a second superoxide binds to the copper (I) positioning an oxygen atom to form a hydrogen bond with the protonated imidazole of His. Electron transfer from the copper (I) coupled with proton transfer from the His gives copper hydroperoxide which picks up the second hydrogen from the active site water to release hydrogen peroxide (Fenton 1995).

5.1.3 PrP metal binding

PrP^C may specifically bind copper, but similarities in ionic strength, hydration size and valence allow other metal ions to bind to PrP^C if present in sufficient concentrations. It has been shown that oxidative impairment in scrapie-infected mice is associated with lower levels of divalent copper, zinc, manganese, iron and calcium in the brain (Choi, Kanthasamy *et al.* 2006). This suggests that metal imbalances in infected brains can affect the structural and antioxidant functional properties of the protein. Fernaeus *et al,* have demonstrated that iron regulation is disturbed in scrapie-infected mouse neuroblastoma cells with the infected cells having a lowered intracellular iron concentration than that of their wild type cousins (Fernaeus and Land 2005). Further studies showed that an increase in excess iron weakens the cell's cytoprotective defence and leads to an increase in ROS formation and eventually cell death (Fernaeus, Reis *et al.* 2005). There is evidence to suggest that manganese, like copper, can bind to PrP^C at two distinct binding sites (Brown, Hafiz *et al.* 2000). This manganese binding results in the conversion of PrP^C to an abnormal isoform which is high in β-sheet content and has the ability to aggregate. These features are reminiscent of PrP^{Sc}. Studies of PrP manganese coordination suggests that manganese can drive the conversion of PrP^C to PrP^{Sc} *in vivo* by aiding the formation of a β-sheet rich PrP intermediate or a PrP seed (see Figure 5.3 and Chapter 2.9.1) (Brown, Hafiz *et al.* 2000; Choi, Kanthasamy *et al.* 2006). An alternative theory suggests that other divalent transition metals can inhibit the ubiquitin proteasomal pathway, causing it to be inactivated thereby leading to an increase in the concentration of PrP^{Sc} (see Figure 5.3).

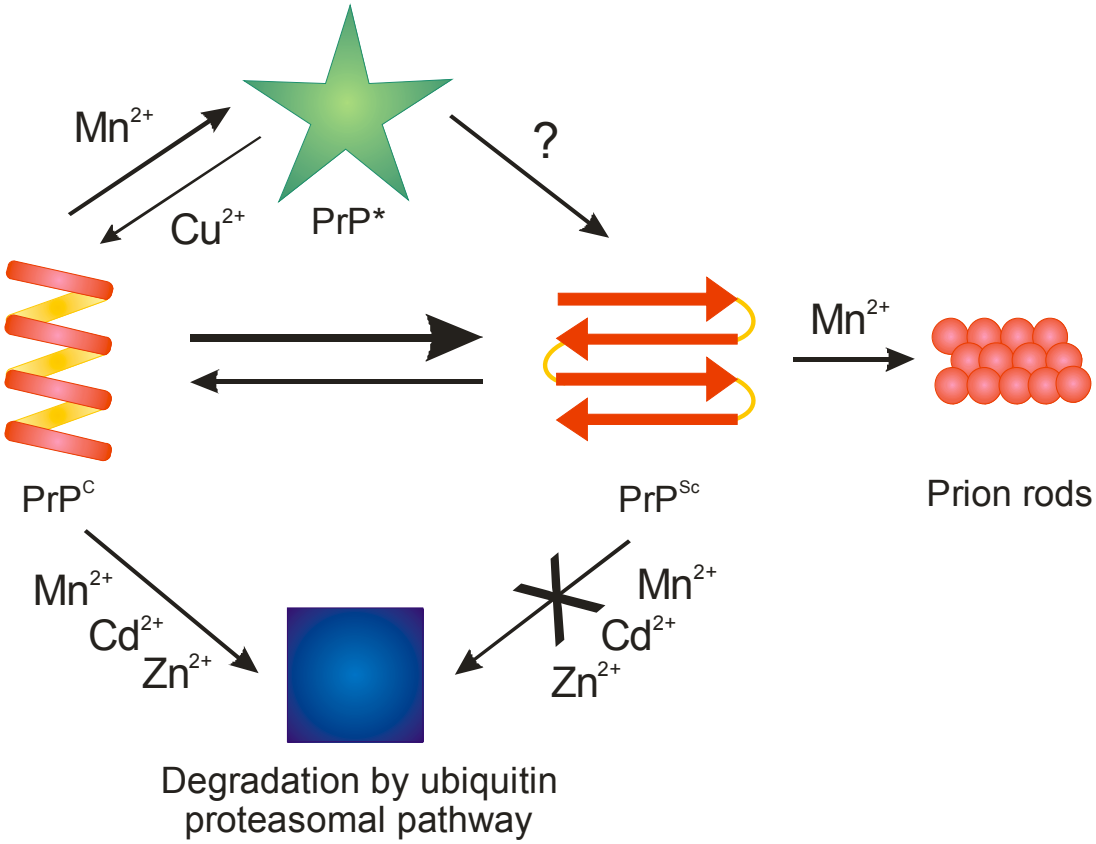

Figure 5.3: Schematic representation of the proposed metal-induced changes in the structure and function of PrP^{C}. Transition metals such as manganese, cadmium and zinc could inhibit the proteasomal activity thereby increasing the concentration of PrP^{Sc}. Manganese can induce a conformational change in PrP^{C} to create the intermediate PrP*, this reaction can be reversed with the introduction of copper. In the presence of excess manganese PrP^{Sc} can form aggregates. Adapted from (Choi, Kanthasamy *et al.* 2006).

5.1.4 PrP binding affinities

The concentration of copper varies dramatically throughout the body with the highest concentration being found in the muscles and brain (see Figure 5.4). These findings are complementary to the distribution of the prion protein. Cu^{2+} concentrations in the cerebrospinal fluid (CSF) and extracellular brain interstitial fluid are typically 0.1 µM. Concentrations of serum albumin are found at much lower levels in the CSF than in blood plasma (typically 3 µM), but much of the Cu^{2+} is still found to be in the serum albumin, which has a picomolar affinity for Cu^{2+} ions (Viles, Klewpatinond *et al.* 2008). PrP^{C} is found concentrated at the synaptic cleft with the Cu^{2+} concentration ranging from 100-250 µM depending on the cleft size (Kardos, Kovacs *et al.* 1989).

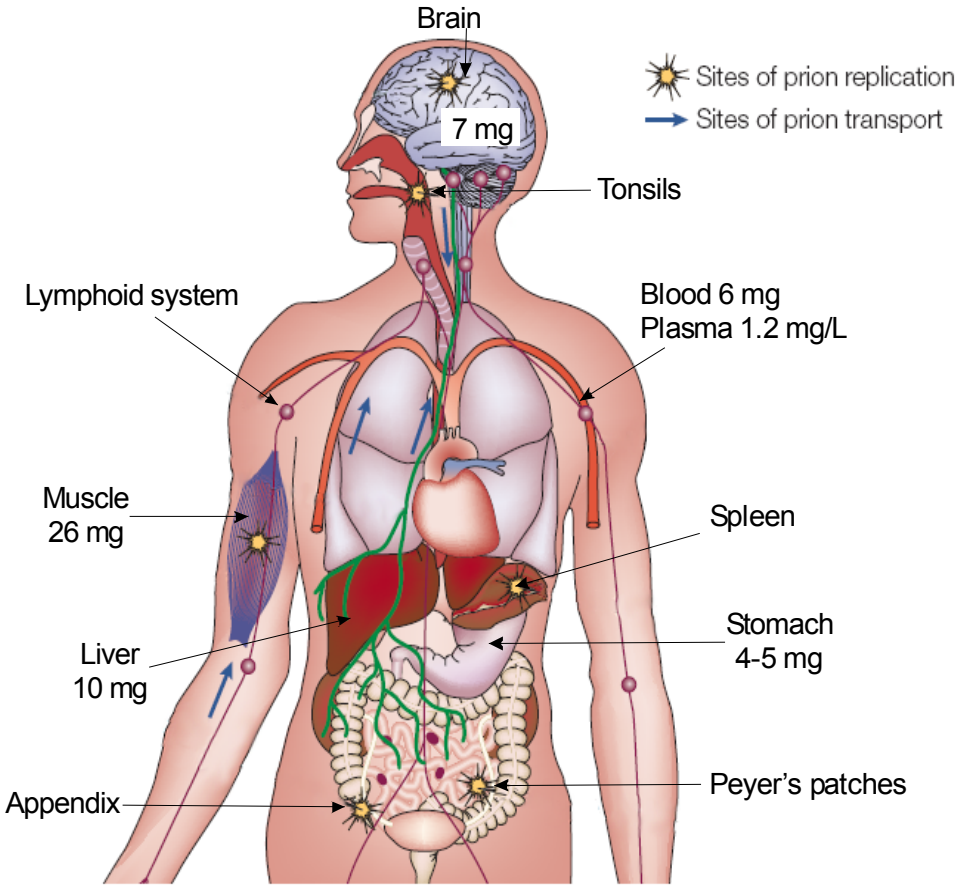

Figure 5.4: Summary of nutritional biochemistry of copper in adult humans. Values for copper indicate average daily amounts of copper concentrations in fluids and tissues. Diagram modified from (Aguzzi and Heikenwalder 2006), copper values obtained from (Linder and Hazegh-Azam 1996).

There is no general agreement concerning the binding affinities, sites and extents of copper binding within PrP (Brown 2004; Jackson, Murray *et al.* 2001). There is evidence to suggest that PrP binds up to four copper ions in the highly conserved octarepeat, and possibly a further copper at a fifth site outside this region (Brown 2004). The octarepeat is located in the N-terminal region and is rich in histidine residues. Binding of copper to the N-terminal fragment of human PrP (23-98) suggested a saturation stoichiometry of one copper per histidine residue (Brown, Qin *et al.* 1997), with dissociation constants in the micromolar range. An alternative binding mode in which four octarepeat His residues bind to one Cu^{2+} ion simultaneously has been reported with the corresponding dissociation constants ranging from 8 fM (Jackson, Murray *et al.* 2001) to 3 nM (Viles, Klewpatinond *et al.* 2008). In addition, Cu^{2+} can bind to the amyloidogenic region (residues 90-126) which, comprises His96 and His111 in humans, with binding affinities between 1-100 nM being recorded (Klewpatinond, Davies *et al.* 2008; Viles, Klewpatinond *et al.* 2008).

PrP can also bind two manganese ions, in conjunction with Cu^{2+}, to the amyloidogenic region with binding affinities of 63 μM for one Mn^{2+} ion and ~200 μM for two Mn^{2+} ions (Brazier, Davies *et al.* 2008; Jackson, Murray *et al.* 2001). The concentration of manganese in heathly human blood is approximately 22 ppb and is even lower in serum with typical values ranging from 3-18 ppb (Hesketh, Sassoon *et al.* 2008). Upon the onset of TSE diseases it has been shown that manganese levels are elevated in blood and brain tissues (Hesketh, Sassoon *et al.* 2007) but still remain within ppb range. The binding dissociation constants and the low concentration of manganese in the blood imply that PrP cannot bind manganese *in vivo*. If this observation were true, very few manganese-binding proteins would successfully chelate the metal ion. It is therefore assumed that manganese binding to proteins is regulated in a manner that is currently not understood (Brazier, Davies *et al.* 2008).

In contrast to numerous studies of Cu^{2+} binding to fragments of PrP fewer structural studies of Cu^{2+} binding to full-length PrP are available. These studies have been

restricted by the solubility of PrP^C at physiological pH required for Cu^{2+} binding. Spectroscopic techniques such as CD (Klewpatinond, Davies *et al.* 2008), NMR spectroscopy (Wells, Jackson *et al.* 2006) and EPR spectroscopy (Burns, Aronoff-Spencer *et al.* 2003) have been used to study structural details of Cu^{2+} binding to full-length and other large recombinant PrP fragments. These techniques are limited to the measurement of the average structure in solution and often require high sample concentrations and volumes. In comparison, IM-MS is able to operate at biologically relevant concentrations (as low as femto molar) and when combined with soft ionisation methods, such as ESI, detailed molecular structural information can be obtained on individual conformations in a complex mixture. Mass spectrometry is gaining in popularity as a technique for prion characterisation (Back, Sanz *et al.* 2002; Maras B. 2004; Onisko, Dynin *et al.* 2007; Pushie, Ross *et al.* 2007; Qin, Yang *et al.* 2002; Requena, Groth *et al.* 2001; Whittal, Ball *et al.* 2000) and it can be especially useful in determining the stoichiometric ratio of metal ions bound to proteins, (Becker and Jakubowski 2009) for which other techniques give ambiguous results.

5.2 Results and Discussion

For all materials and methods please refer to Chapter 3.

T-Wave ion mobility was used to investigate the structure of PrP in the presence and absence of cooper and manganese coordination. Two different constructs were studied; full-length Syrian hamster prion protein containing a structured C-terminal domain and an N-terminal fragment containing the unstructured octarepeat region. The N-terminal region of mammalian PrP contains a highly conserved sequence of five or six octapeptide repeats $(PHGGGWGQ)_n$. Previous studies have shown that copper binds to the histidine residues in the octarepeat motif with a saturation stoichiometry of one copper per histidine residue (Brown, Qin *et al.* 1997), and manganese can bind in the amyloidogenic region (Brazier, Davies *et al.* 2008). Bovine PrP and Syrian hamster PrP have complete sequence identity in their

octarepeat regions with the addition of one extra octarepeat motif in the bovine protein.

5.2.1 Copper coordination to BovPrP(57-101)

The interaction of copper with the N-terminal peptide of bovine PrP BovPrP(57-101), was studied for different stoichiometric ratios of Cu^{2+} ($PrP:Cu^{2+}$) at near-physiological pH 7.0. Figure 5.5 shows the deconvoluted mass spectra for apo-BovPrP(57-101) **[1]**, BovPrP(57-101): Cu^{2+} **[2]**, BovPrP(57-101): $3Cu^{2+}$ **[3]** and BovPrP(57-101): $5Cu^{2+}$ **[4]**. The deconvoluted peak derived from sample **[1]** corresponds to the predicted molecular mass, 4313.8 Da, of BovPrP(57-101), labelled PrP. Upon the addition of copper, unbound PrP is no longer observed which is indicative of the protein's high affinity for copper. At the 1:1 $PrP:Cu^{2+}$ molar ratio (sample **[2])** the peak at 4377 Da indicates the binding of one copper ion, in addition further peaks at 4438 Da and 4502 Da suggest binding of a further one and two Cu^{2+} ions. The masses reflect that two H^+ atoms are displaced upon Cu^{2+} coordination to the peptide. It was found that as the concentration of Cu^{2+} was increased the number of Cu^{2+} ions attached to the peptide also increased with up to three Cu^{2+} ions bound in **[2]** compared to five Cu^{2+} ions, inclusive, in samples **[3-4]**. It is observed that increasing stoichiometric ratios of Cu^{2+} decreases the relative abundance, in the gas-phase, of $PrP + 1Cu^{2+}$.

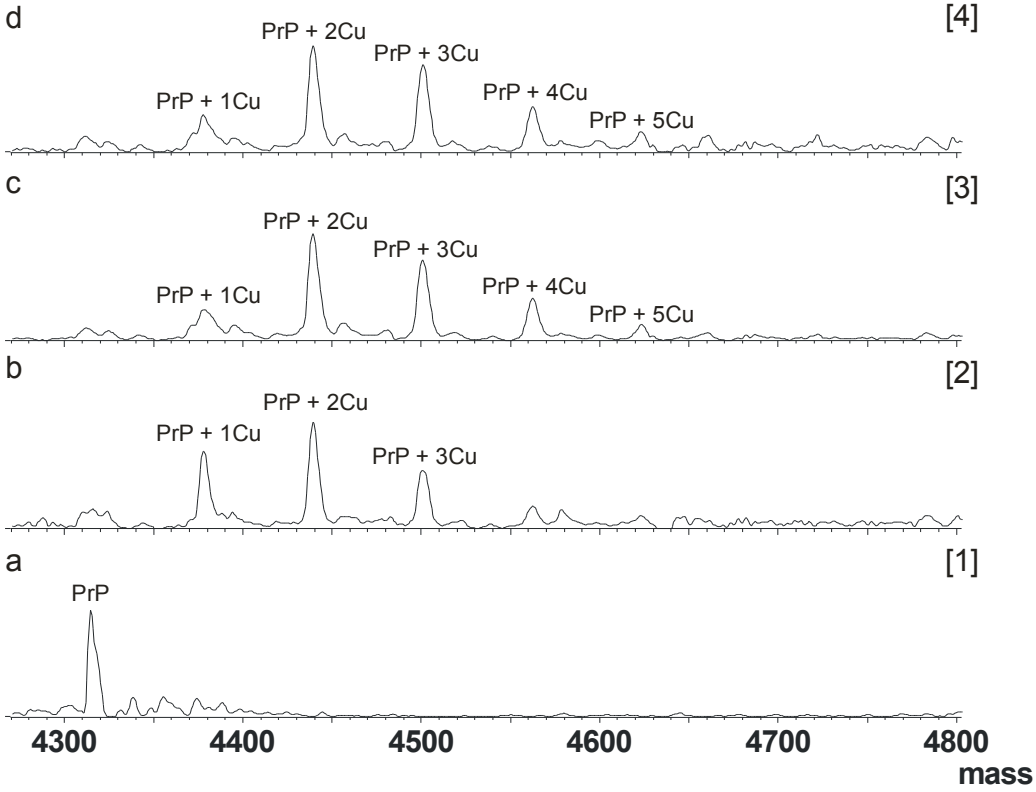

Figure 5.5: Deconvolution of the ESI spectrum for (a) BovPrP(57-101), (b) BovPrP(57-101): Cu^{2+} (c) BovPrP(57-101): $3Cu^{2+}$ and (d) BovPrP(57-101): $5Cu^{2+}$.

All experiments were repeated three times over different days and the ATDs were measured for the +3 to +5 charge states. Figure 5.6a shows the estimated cross-sections for the biologically relevant +5 charge state with 0, 1, 2, 3, 4, and 5 Cu^{2+} ions bound at physiological pH 7.0. The relatively small estimated cross-section of apo BovPrP(57-101) at the +5 charge state suggests this has a more globular structure than its copper bound counterparts. When 1-3 Cu^{2+} ions are coordinated to PrP, an increase in the estimated cross-section was observed with a 15 $Å^2$ difference measured between the average estimated cross-section of BovPrP and BovPrP+$2Cu^{2+}$. This increase in estimated cross-section suggests a more extended structure compared to the apo peptide. The coordination of three Cu^{2+} ions results in a structure that is more extended than the apo peptide but more compact than that with one and two Cu^{2+} ions bound. The observation of the attachment of a fourth and fifth Cu^{2+} ion suggests the peptide becomes more globular as a decrease in estimated cross-sections is seen (from 774 $Å^2$ to 769 $Å^2$ respectively). These findings are in good agreement with previous reports in which molecular dynamics

(Riihimaki, Martinez *et al.* 2008) and NMR studies (Zahn 2003) indicate that binding of copper ions to the human PrP octarepeat peptide can induce a conformational transition. The FWHM of the individual ATDs (Figure 5.6b) also suggests that at higher Cu^{2+} coordination the peptide becomes less flexible/more rigid. The FWHM of BovPrP is 15 scans and is reduced to 9 scans when one copper is coordinated. The width of an ATD can be related to the number of conformations contributing to the area of that peak. The relatively large width of the BovPrP ATD suggests that there are multiple conformations present which have a difference in cross-section of <5%. It is expected that individual cross-sections that are greater than 5% in difference would be resolved by this ion mobility instrument (Hilton, Jackson *et al.* 2008). In comparison, the ATD for BovPrP+1Cu^{2+} is narrower indicating fewer conformations are present when one copper ion is bound. Upon increasing the number of Cu^{2+} ions coordinated to the peptide the FWHM of the respective ATDs increases and it can therefore be presumed that the number of different conformations per ATD also increases.

Secondary structural changes of the N-terminal peptide upon Cu^{2+} coordination were determined by means of CD. CD data are a representation of the average structure in solution, whereas IM-MS can analyse individual conformations in the gas-phase. Far-UV CD spectra of BovPrP(57-101) show a single minimum at 198 nm which represents an essentially unstructured protein. This is in good agreement with previously published NMR structures which show that the amino acid residues 23-124 have features of a flexible random coil-like polypeptide (Riek, Hornemann *et al.* 1997). In the presence of copper, samples **[2-4]**, the relative abundance of random coil is reduced suggesting a profound structuring of the peptide from the unstructured conformation. This has been previously observed elsewhere (Garnett and Viles 2003) and is in good agreement with the IM-MS data.

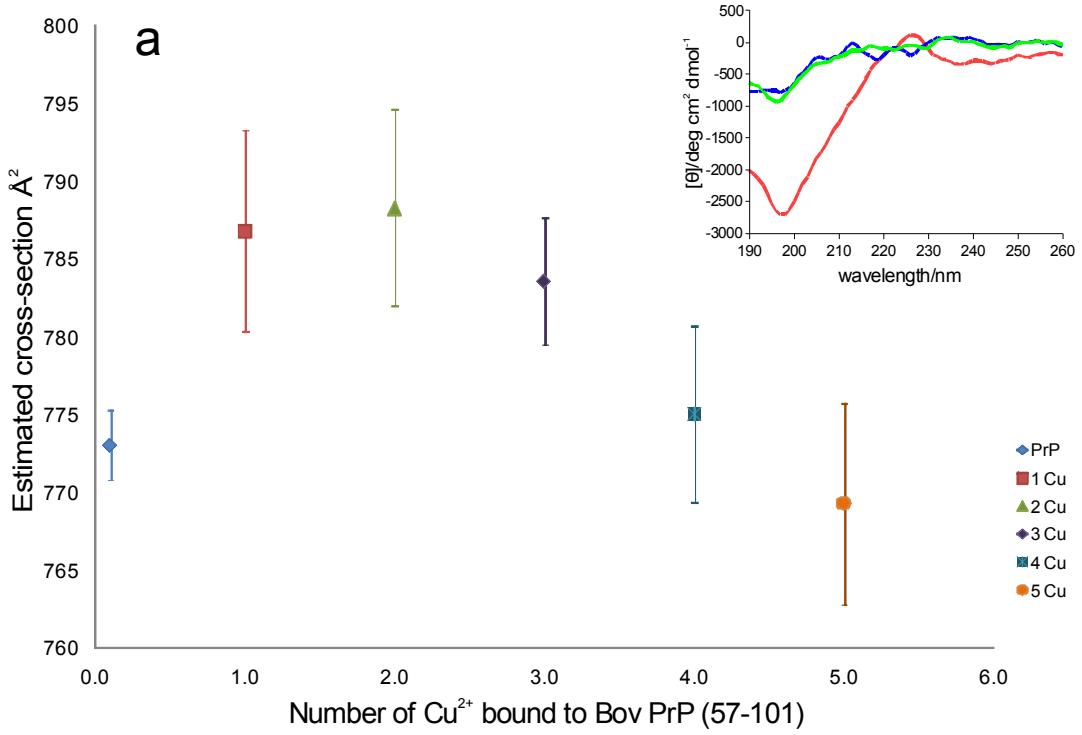

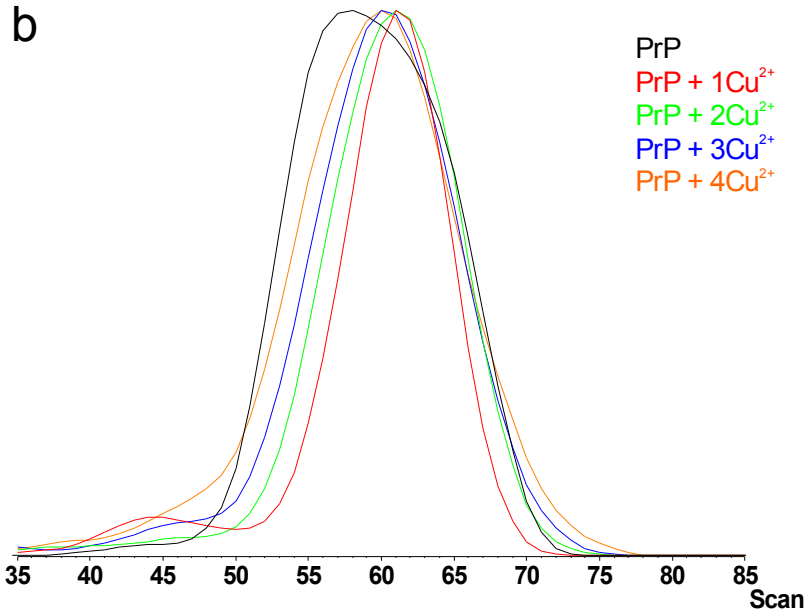

Figure 5.6a: Comparison of estimated cross-sections for charge state 5+ of BovPrP(57-101), BovPrP(57-101)+Cu^{2+}, BovPrP(57-101)+2Cu^{2+}, BovPrP(57-101)+3Cu^{2+}, BovPrP(57-101)+4Cu^{2+} and BovPrP(57-101)+5Cu^{2+}. Inset: Far-UV CD spectrum of BovPrP(57-101) (red), BovPrP(57-101): Cu^{2+} and BovPrP(57-101): 3Cu^{2+} (blue) and BovPrP(57-101): 5Cu^{2+} (green). Figure 5.6b: Comparison of full-width half-height maximum (FWHM) of the

individual arrival time distributions (ATDs) for BovPrP(57-101) (black), BovPrP+Cu^{2+} (red), BovPrP+2Cu^{2+} (green), BovPrP+3Cu^{2+} (blue) and BovPrP+4Cu^{2+} (orange) at the biologically relevant charge state $[M+5H]^{5+}$. The FWHM of BovPrP is 15 scans and is reduced to 9 scans when one copper is coordinated.

It is widely accepted that PrP^C can bind copper in a cooperative manner with several structural models suggesting that the Cu^{2+} ion stoichiometry can influence the binding mechanism of copper coordination (Burns, Aronoff-Spencer *et al.* 2003; Chattopadhyay, Walter *et al.* 2005; Riihimaki, Martinez *et al.* 2008; Viles, Cohen *et al.* 1999). It can therefore be postulated that the binding of one copper ion can change the conformation of PrP to allow the coordination of the further copper ions. The estimated cross-section plot for BovPrP(57-101) with Cu^{2+} attached, shown in Figure 5.6a, indicates that the shape of the peptide changes depending on the number of Cu^{2+} ions coordinated to BovPrP(57-101). It is observed that the apo BovPrP(57-101) has a more compact structure than that of the species with 1-3 copper ions bound. It has been previously noted that the structure of the apo octarepeat is strongly influenced by the interaction of the aromatic rings in tryptophan, histidine and proline residues (Riihimaki, Martinez *et al.* 2008). Ring-stacking initially occurs between the consecutive histidine and tryptophan residues which apply structural constraints to the peptide. These structural constraints allow further ring interactions to occur between the proline residues. It is proposed that this ring-stacking gives the octarepeat peptide a more globular structure as observed for BovPrP in Figure 5.6a. See Figure 5.7 for a schematic representation of the ring-stacking mechanism. In the presence of copper, however, the extent of ring-stacking is diminished to allow for a more extended structure, as observed in the cross-sections of PrP+1Cu^{2+} and PrP+2Cu^{2+}. The estimated cross-section of BovPrP(57-101) decreases when $\geq$3 Cu^{2+} ions are coordinated, whereas an increase in the FWHM of the respective ATDs has been observed. This apparent ring stacking phenomena that gives the peptide structure was not observed by means of far-UV CD and NMR spectroscopy. This could be because these techniques measure the average structure in solution and therefore cannot select a single conformation. The use of near-UV CD to characterise the peptide could show evidence for the aromatic ring interactions.

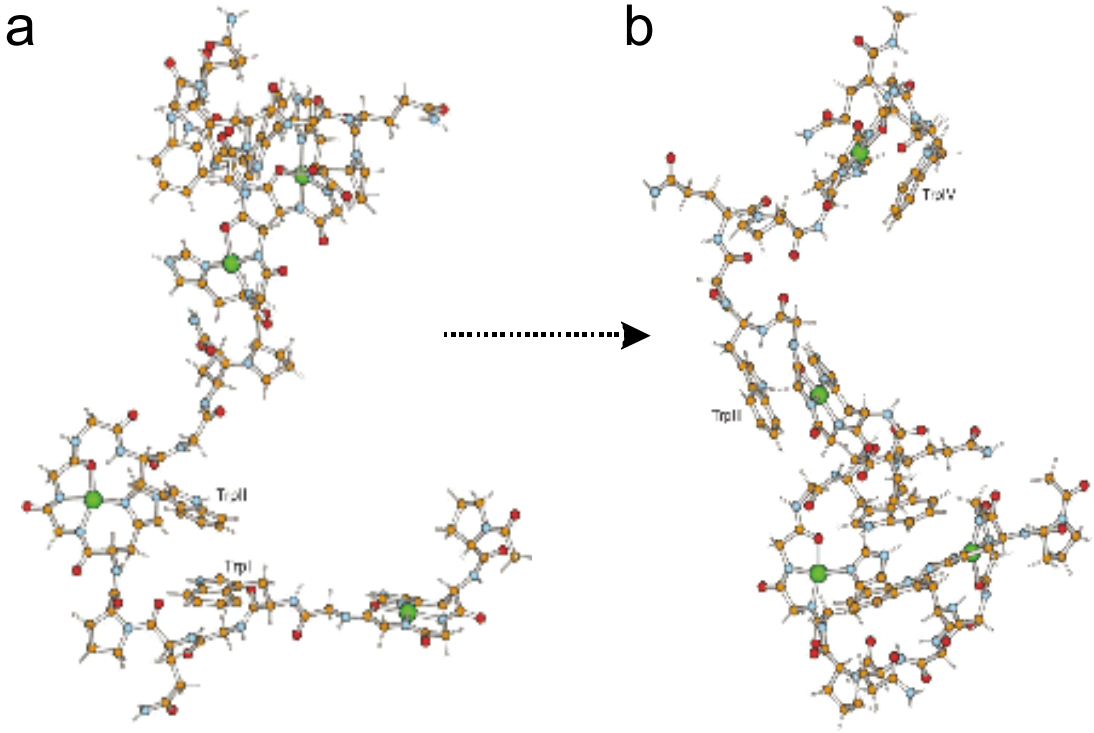

Figure 5.7: Schematic representation of the octarepeat peptide ring-stacking. (a) The indole rings of the first and second octarepeat sequence interact through ring-stacking. The proline residue has folded to the axial region of the first coordination site. (b) Globural structure formed as the indole rings of the third and fourth octarepeat sequence are in well-defined positions. Taken from (Riihimaki, Martinez *et al.* 2008)

A unique feature of IM-MS is its ability to measure individual cross-sections, calculated from the ATD, as well as the overall conformation of a protein or peptide. The width of an ATD can be related to the number or spread of conformations present at a particular charge state. An increase in the FWHM of the ATDs upon Cu^{2+} coordination implies that there are also an increased number of different conformations contributing to these peaks (Figure 5.6b). Several hypotheses have been outlined to explain copper coordination binding modes. A crystal structure has been postulated by Chattopadhyay *et al,* which shows Cu^{2+} coordinated to the octarepeat motif (HGGGW). The Cu^{2+} coordinates to three nitrogen atoms and one oxygen atom, in an equatorial plane, and an axial water oxygen atom to form a square-pyramidal coordination complex (Burns, Aronoff-Spencer *et al.* 2002;

Millhauser 2004) (see Figure 5.8a). These and other studies (Jackson, Murray *et al.* 2001) further showed that a change in coordination geometry can occur as a function of the relative Cu^{2+} concentration, suggesting that an alternative binding mechanism could take place at different copper levels. Figure 5.8b shows a further alternative binding mode in which copper can coordinate to nitrogen provided by the octarepeat histidine imidazole as well as the nitrogen present in the exocyclic backbone (Chattopadhyay, Walter *et al.* 2005). It has also been proposed that at low copper concentrations (stoichiometric equivalents <1.0 Cu^{2+}) three or four sequential HGGGW motifs are required to coordinate to one Cu^{2+} with the neutral imidazoles (see Figure 5.8c). Recent studies have shown that Cu^{2+} initially binds to full-length PrP in the amyloidogenic region at His95 and His110 inducing yet another binding mode (Klewpatinond, Davies *et al.* 2008). It is believed that Cu^{2+} ions preferentially bind to the amyloidogenic region, before the octarepeat region, until each histidine residue in the repeat is saturated with copper (Viles, Klewpatinond *et al.* 2008). The overall cross-section of the three different binding mechanisms, shown in Figure 5.8, to the octarepeat region could be similar (<5% difference in cross-section) and therefore, it would be difficult to resolve individual conformations when using ion mobility (Chattopadhyay, Walter *et al.* 2005; Malmström and Vänngård 1960). This similarity is reflected in the individual ATDs. If the cross-sections of conformations contributing to the ATD were different, greater than 5%, then several resolvable peaks would be observed. This suggests that the binding mode conformations are too similar to be fully resolved but different enough to increase the number or spread of conformations contributing to each ATD. It is unclear, at different copper concentrations, which of the three binding modes described above would be dominant; consequently all three could be present and contribute to the increased width at FWHM of the respective individual ATDs.

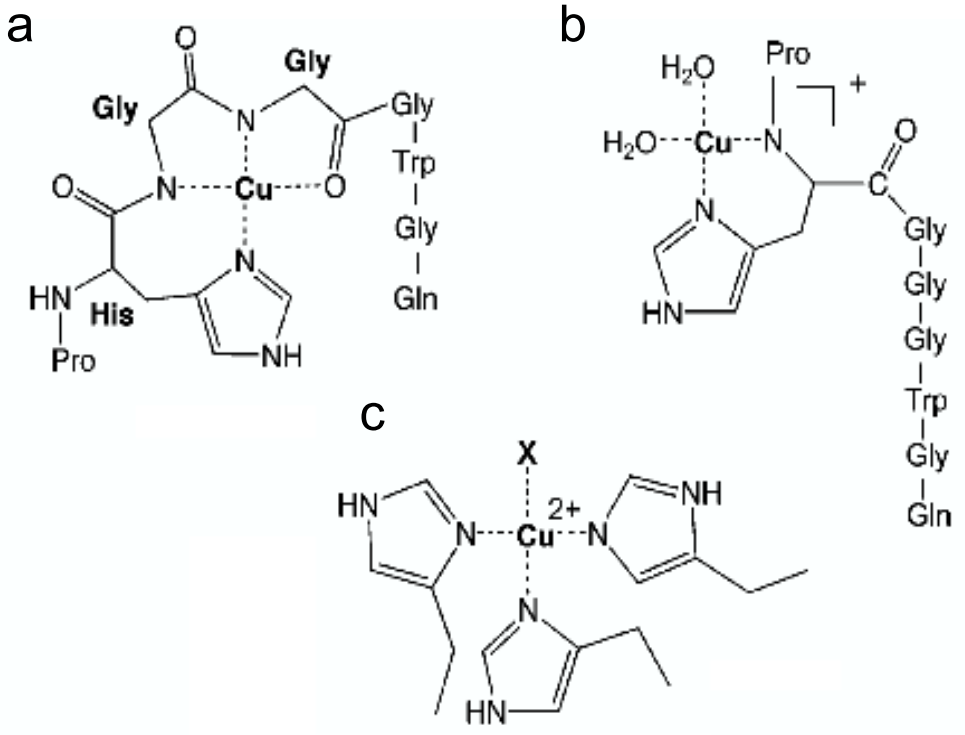

Figure 5.8: Models of the three proposed different copper binding modes. (a) Cu^{2+} ions coordinate with three nitrogen atoms and one oxygen atom, in an equatorial plane, preferred binding mode for high Cu^{2+} occupancy. (b) Cu^{2+} ions coordinate to nitrogen provided by the octarepeat histidine imidazole and nitrogen present in the exocyclic backbone. (c). Three sequential HGGGW motifs coordinate to one Cu^{2+} via the neutral imidazoles. X may represent either a fourth neutral imidazole or a water molecule. This binding mode provides the highest binding affinity. Taken from (Chattopadhyay, Walter *et al.* 2005).

5.2.2 Copper coordination to SHaPrP(23-231)

The coordination of copper with the full-length hamster PrP SHaPrP(23-231) was studied using different stoichiometric ratios of Cu^{2+} at physiological pH 7.0. Figure 5.9 shows the mass spectra of SHaPrP(23-231) and SHaPrP(23-231): Cu^{2+} at pH 7.0. The insets are an enlargement of the +11 charge state ($[M+11H]^{11+}$), with masses attributed to $[M+9H+Cu]^{11+}$ and $[M+7H+2Cu]^{11+}$, respectively. A comparison of the MS spectra indicates the charge state envelope distribution of the two data sets is similar. The exception to this observation is the presence of extra dimer peaks in the SHaPrP(23-231): Cu^{2+} spectrum. It was noted that upon increasing the concentration of copper relative to that of the prion, the sample became increasing difficult to spray. In samples with a stoichiometric ratio greater than 1:5 PrP:Cu^{2+} visible

aggregates were formed and blocked the sample tip. This prevented further mass spectrometry studies of higher stoichiometric ratios being performed. The appearance of dimer peaks in the mass spectrum supports the proposal that when copper interacts with PrP^C it can promote the protein to oligomerise (Qin, Yang *et al.* 2000). The concentration of copper used in the stoichiometric ratio experiments was biologically relevant with the highest concentration of Cu^{2+} ions not exceeding 150 μM. Kardos *et al,* calculated the concentration of copper in the synaptic cleft to be in the range of 100 – 250 μM (Kardos, Kovacs *et al.* 1989). .

A comparison of the deconvoluted mass spectra for all four samples, SHaPrP(23-231) **[5]**, SHaPrP(23-231): Cu^{2+} **[6]**, SHaPrP(23-231): $3Cu^{2+}$ **[7]** and SHaPrP(23-231): $5Cu^{2+}$ **[8]**, is shown in Figure 5.10. The dominant peak (23102 Da) derived from sample **[5]** in Figure 5.10a corresponded to the predicted molecular mass of oxidised SHaPrP(23-231), labelled PrP. The second lower intensity peak observed is due to sodium salt adducts and has not been labelled. With 1:1 PrP:Cu^{2+} (sample **[6])** the presence of unbound SHaPrP(23-231) was still observed as well as PrP+Cu^{2+} and PrP+$2Cu^{2+}$. When the stoichiometric ratio of copper was increased to 1:3 and 1:5 (PrP:Cu^{2+}) the unbound SHaPrP(23-231) and PrP+Cu^{2+} were no longer observed. The masses deconvoluted from sample **[7]** and **[8]** can be attributed to PrP+$2Cu^{2+}$, PrP+$3Cu^{2+}$ and, in sample **[8]** only, PrP+$4Cu^{2+}$. This observation of an increase in the number of copper ions coordinated to the protein as the concentration of copper is increased is in good agreement with that obtained for copper binding to BovPrP(57-101). This again agrees with previous studies which suggest copper can coordinate to the prion protein in a cooperative manner (Brown, Qin *et al.* 1997; Viles, Cohen *et al.* 1999).

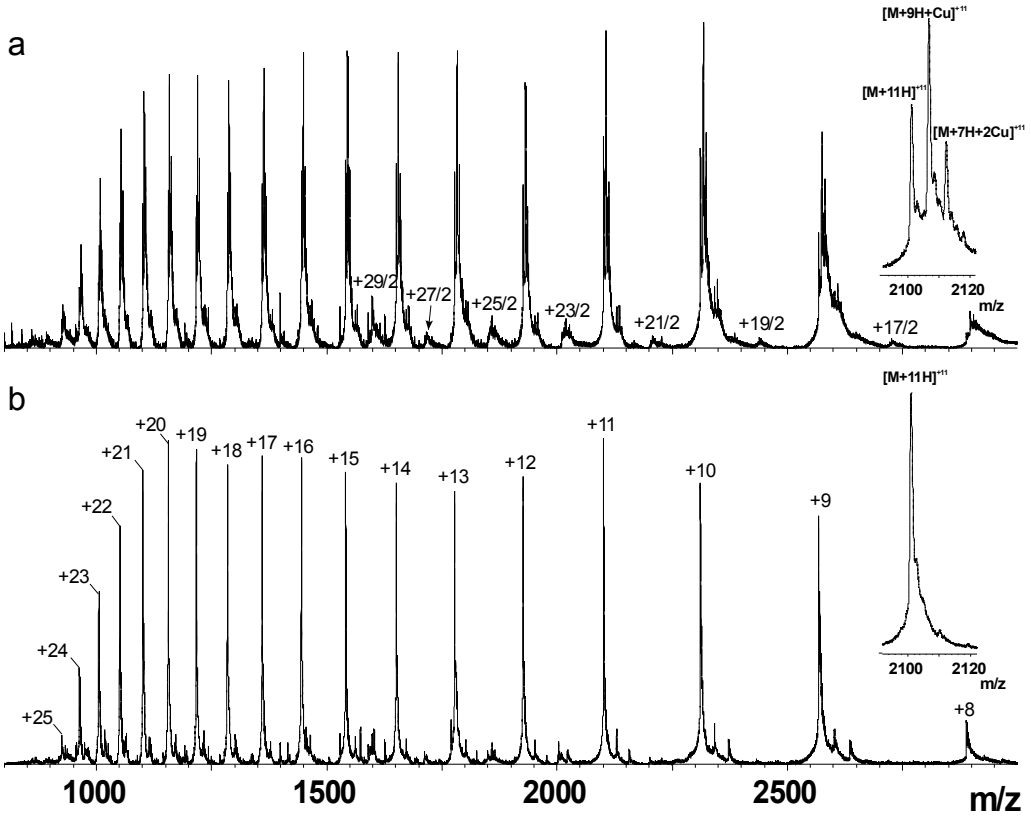

Figure 5.9: (a) Mass spectrum of SHaPrP(23-231):Cu2+ at pH 7.0. The spectrum shows two series of peaks corresponding to multiply charged ions from monomer and dimer. Inset: Enlargement of the +11 charge state showing m/z peaks due to $[M+11H]^{+11}$, $[M+9H+Cu]^{+11}$, $[M+7H+2Cu]^{+11}$. (b) Mass spectrum of SHaPrP(23-231) at pH 7.0. The spectrum shows one series of peaks corresponding to multiply charged ions from monomer. Inset: Enlargement of the +11 charge state showing *m/z* peaks due to $[M+11H]^{+11}$.

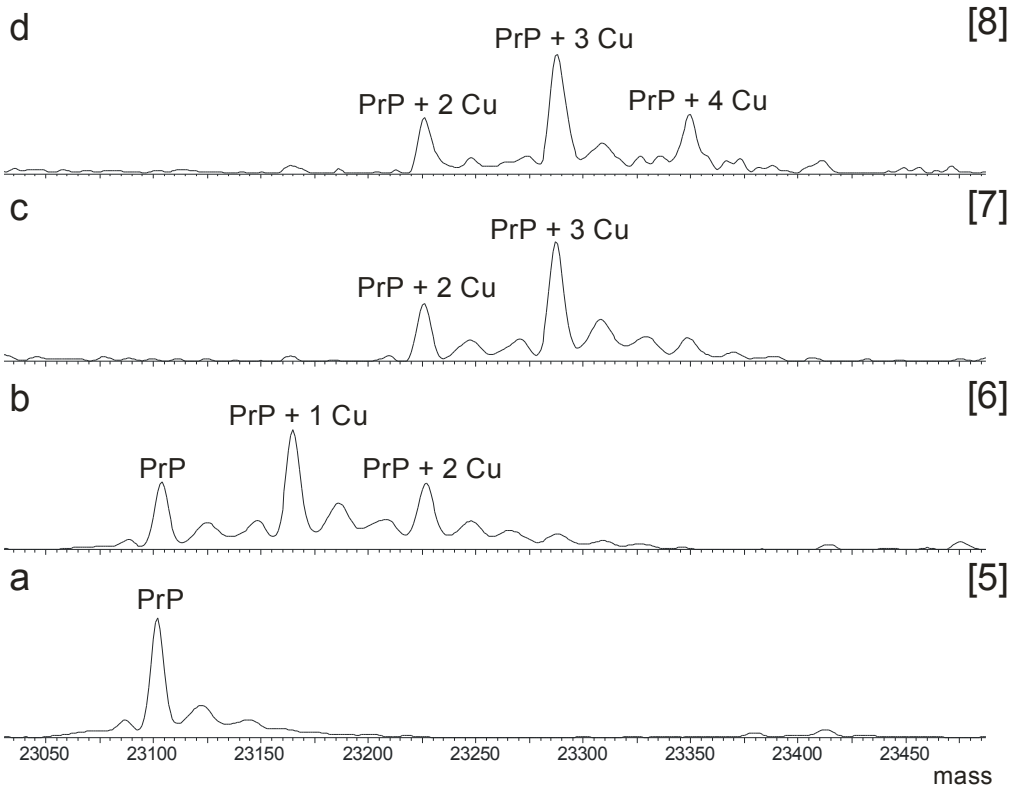

Figure 5.10: Deconvolution of the ESI spectrum for (a) SHaPrP(23-231), (b) SHaPrP(23-231): Cu^{2+}, (c) SHaPrP(23-231): $3Cu^{2+}$ and (d) SHaPrP(23-231): $5Cu^{2+}$.

Figure 5.11 shows the estimated cross-sections of the charge states of PrP, with and without Cu^{2+} ions coordinated, from (+9 to +25 charge states) obtained at pH 7.0. The samples with a higher concentration of Cu^{2+}, namely 1:3 and 1:5 PrP:Cu^{2+} (samples **[7 and 8]**) had a propensity to aggregate and were analysed immediately after the Cu^{2+} had been mixed with the prion protein. The estimated cross-section plot shows that protonation of the protein increases the cross-section measured and therefore higher charge states represent an extending/unfolding structure. Charge states +9, +12 to +14 and +17 to +19 have two or more stable conformations whereas the remaining charge states have only one conformation. Figure 5.11 also shows that there are no significant differences in the estimated cross-sections between SHaPrP(23-231) and its respective copper bound forms which suggests that copper coordination has little influence on the degree of the prion protein folding. This observation is in agreement with far-UV CD data (see inset Figure 5.11) from which a structural similarity was also detected. There is a significant difference in

the lower estimated cross-section value of charge state +12 between PrP, PrP+Cu^{2+} and PrP+≥$2Cu^{2+}$. This difference is greater than the ±3% expected from experimental error. The ATDs at this charge state (see Figure 5.12) indicate there is a significant difference in the intensity on the second conformational peak (see Figure 5.12b *) between unbound SHaPrP(23-231), PrP+Cu^{2+} and the ATDs of PrP+$2Cu^{2+}$, PrP+$3Cu^{2+}$ and PrP+$4Cu^{2+}$. The relative intensity of the ATD suggests that when zero or one Cu^{2+} ion is coordinated to the prion protein two stable conformations are preferred, compared with one significant stable conformation at higher Cu^{2+} ion concentrations.

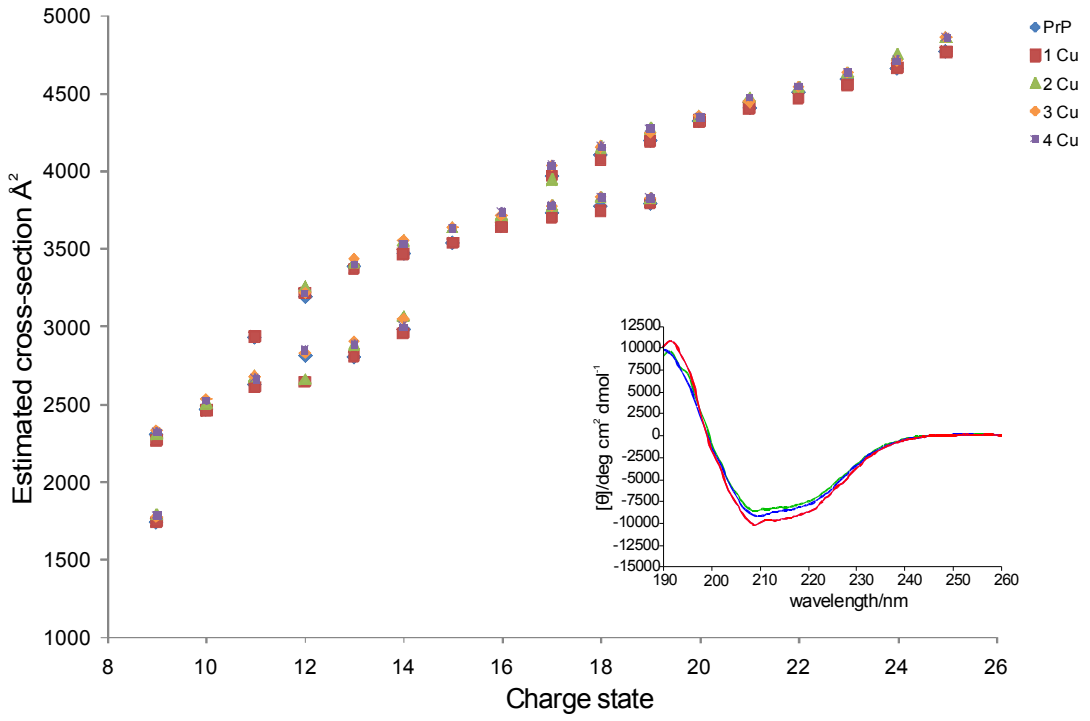

Figure 5.11: Comparison of estimated cross-sections for different charge states of SHaPrP(23-231), PrP+Cu^{2+}, PrP+$2Cu^{2+}$, PrP+$3Cu^{2+}$ and PrP+$4Cu^{2+}$. Inset: Far-UV CD spectrum of SHaPrP(23-231) (green), SHaPrP(23-231): Cu^{2+} and SHaPrP(23-231): $3Cu^{2+}$ (blue) and SHaPrP(23-231): $5Cu^{2+}$ (red).

In Chapter 4, it was observed that differences can be detected between ATDs of the same *m/z* when no significant differences were present in the estimated cross-section plots. Figure 5.12 shows a comparison of the ATDs of SHaPrP(23-231) unbound

and PrP+Cu^{2+},PrP+$2Cu^{2+}$, PrP+$3Cu^{2+}$ and PrP+$4Cu^{2+}$ at charge states +10, +12, +14 and +22. There are no significant differences between the ATDs at any charge state (except +12 charge state see above) indicating that the estimated cross-sectional plot, in this case, is an accurate representation of this data set. As the charge state increases the ATD baseline width and FWHM decreases. For the +10 charge state the FWHM is 29 scans compared to 13 scans FWHM at charge state +22. The width of an ATD can be related to the number of conformations contributing to the area of that peak. The large width at charge state +10 suggests that there is more than one conformation, of a similar shape, present which is unable to be fully resolved in the ion mobility cell. At the +22 charge state the sharp, narrow ATD suggests fewer conformations are present. This observation can be rationalised as at lower charge states, such as +10, a more native like structure is detected (Scarff, Thalassinos *et al.* 2008) (in this case globular) whereas, at higher charge states, +22, the protein has unfolded becoming denatured in structure.

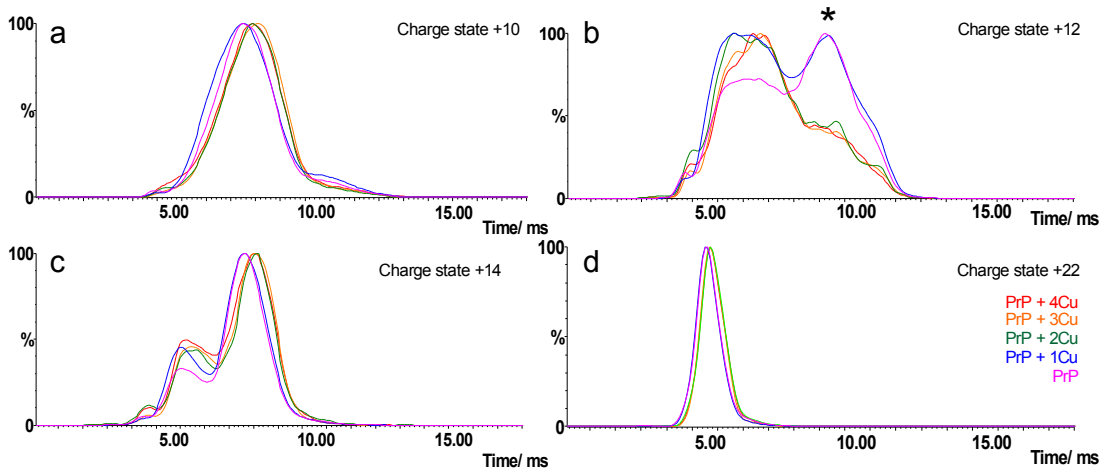

Figure 5.12: Comparison of SHaPrP(23-231) (pink), PrP+Cu^{2+} (blue), PrP+$2Cu^{2+}$ (green), PrP+$3Cu^{2+}$ (orange) and PrP+$4Cu^{2+}$ (red) selected arrival time distributions (ATDs) for the +10, +12, +14 and +22 charge states.(a) Overlaid ATDs for the +10 charge state at pH 7.0. (b) Overlaid ATDs for the +12 charge state at pH 7.0. (c) Overlaid ATDs for the +14 charge state at pH 7.0. (d) Overlaid ATDs for the +22 charge state at pH 7.0.

An X-ray crystal structure or molecular model of the complete full-length prion has not been published. The NMR structure of recombinant full-length prion protein reveals residues 125-228 comprise a global domain and the N-terminal fragment, residues 23-120, shows features of a flexible random coil-like polypeptide (Riek, Hornemann *et al.* 1997). The actual positions/structure of this flexible tail has never been defined because of missing residue assignments and exchange-broadening in the NMR spectrum. The majority of copper coordination conformational studies for PrP have used octarepeat fragments. The limited size of these fragments permits the peptides to be more flexible allowing them to fold and interact with the copper more readily than if constrained by the rest of the protein. Zahn observed a structural change in the octarepeat motif under different pH conditions and postulated that the induced conformational transition modulated PrP aggregation (Zahn 2003). In these experiments, the estimated cross-sections of the octarepeat region peptide, BovPrP(57-101) suggests that upon the addition of copper a change in estimated cross-section occurs. The most significant difference observed is between BovPrP(57-101) and BovPrP(57-101)+2Cu^{2+} with a difference of 15 $Å^2$. This difference is less than 1% in the overall estimated cross-section. In Figure 5.11, the estimated cross-sections of SHaPrP(23-231) suggests that, upon the addition of copper, no discernible change in the estimated cross-section occurs. If a similar change in cross-section, i.e. ± 15 $Å^2$, occurred when copper coordinated to full-length prion the difference in estimated cross-section between SHaPrP(23-231) and SHaPrP(23-231)+2Cu^{2+} would be <0.1%. This difference is too small to be detected by means of current IM-MS instrumentation.

It is believed that binding of copper could stimulate endocytosis by altering the conformation of PrP^C. Putative endocytic receptors that localise PrP^C in clathrin-coated pits could be stimulated by the conformational change, thereby increasing the binding affinity (Pauly and Harris 1998). Pauly *et al,* hypothesise that the attachment of PrP^C to the cell surface by a GPI anchor, results in the loss of a cytoplasmic domain which can directly bind to the intracellular components of a clathrin-coated pit. Pauly postulates, that a copper induced structural change in PrP^C could enable the protein to bind to a transmembrane receptor whose cytoplasmic domain contain signals for interacting with adapter molecules and clathrin (Harris,

Gorodinsky *et al.* 1996; Shyng, Moulder *et al.* 1995); this could aid endocytosis. These results suggest that the relatively small changes in the estimated cross-section when copper coordinates to the N-terminal fragment BovPrP(57-101) do not induce significant conformational changes in the C-terminal domain. This suggests that endocytosis is stimulated by Cu^{2+} binding that is triggered by extremely small changes in conformational structure.

Brown *et al,* have demonstrated for the prion protein to display SOD activity a minimum number of two coordinated copper ions are required (Brown, Hafiz *et al.* 2000). In the full-length protein the SOD activity can be increased when a further two copper ions are bound. It is postulated that the more ordered structure observed in the octarepeat peptide when up to five copper ions are coordinated (see Figure 5.6a) can account for the increase in the protein's SOD activity. The conformational change in the peptide was not detected in the full-length protein. Again, if this hypothesis is true, these experiments suggest that SOD activity can be induced by minor changes in the overall conformation of the full-length prion protein.

5.2.3 Manganese coordination to SHaPrP(23-231)

Recent literature indicates that manganese coordinates only to the amyloidogenic region in the prion protein (Brazier, Davies *et al.* 2008; Gaggelli, Bernardi *et al.* 2005), therefore manganese binding to the octarepeat peptide was not studied. The coordination of manganese with SHaPrP(23-231) was studied using different stoichiometric ratios of Mn^{2+} at physiological pH 7.0. Figure 5.13 shows the mass spectra of SHaPrP(23-231) and SHaPrP(23-231): $20Mn^{2+}$ at pH 7.0. The insets are an enlargement of the +11 charge state ($[M+11H]^{11+}$), with masses attributed to $[M+9H+Mn]^{11+}$ and $[M+7H+2Mn]^{11+}$, respectively. A comparison of the MS spectra indicates the charge state envelope distribution, between the two data sets, is similar. Manganese coordination was not observed to promote aggregation; this is in stark contrast to copper coordination. It was noted, however, that upon increasing the concentration of manganese with respect to prion the sample became increasingly difficult to spray. Stoichiometric ratios greater than 1:20 $PrP:Mn^{2+}$

greatly reduced data quality, and prevented further mass spectrometry studies of higher stoichiometric ratios being performed.

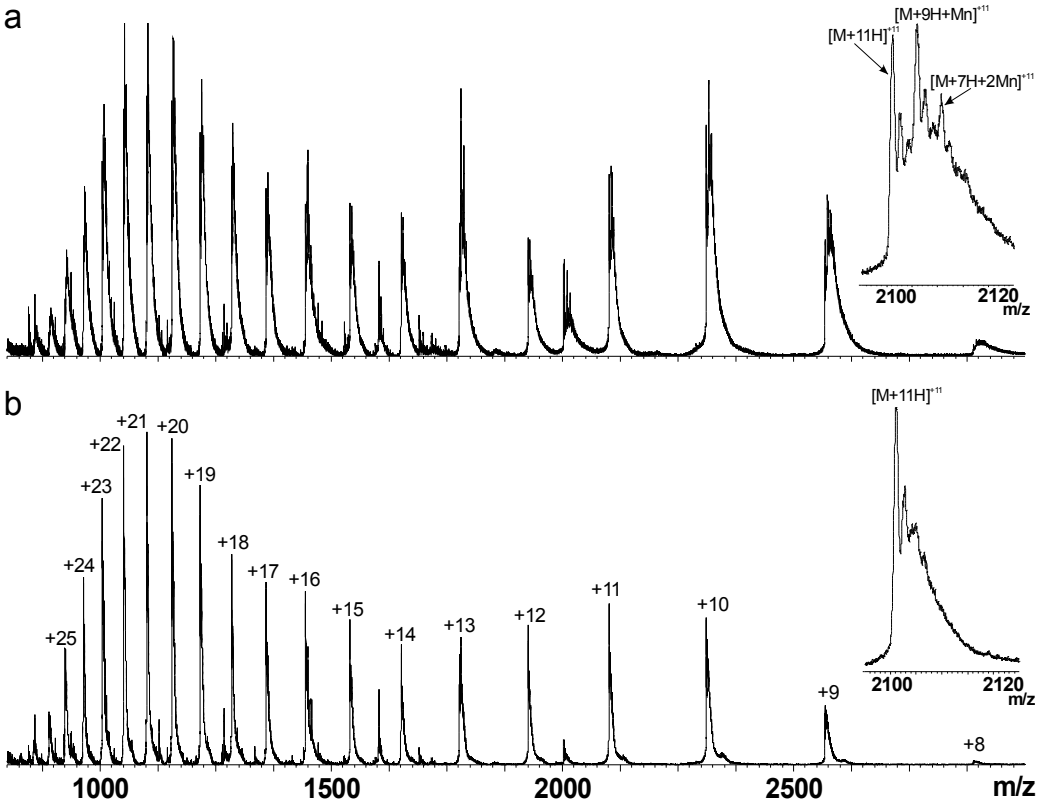

Figure 5.13: (a) Mass spectrum of SHaPrP(23-231):20Mn^{2+} at pH 7.0. The spectrum shows a series of peaks corresponding to multiply charged ions from monomer. Inset: Enlargement of the +11 charge state showing m/z peaks due to $[M+11H]^{+11}$, $[M+9H+Mn]^{+11}$, $[M+7H+2Mn]^{+11}$. (b) Mass spectrum of SHaPrP(23-231) at pH 7.0. The spectrum shows one series of peaks corresponding to multiply charged ions from monomer. Inset: Enlargement of the +11 charge state showing *m/z* peaks due to $[M+11H]^{+11}$.

A comparison of the deconvoluted mass spectra for all three samples, SHaPrP(23-231) **[9]**, SHaPrP(23-231): 10Mn^{2+} **[10]**, and SHaPrP(23-231): 20Mn^{2+} **[11]**, is shown in Figure 5.14. The dominant peak (23,102 Da) derived from sample **[9]** in Figure 5.14a corresponds to the predicted molecular mass of oxidised SHaPrP(23-231), labelled PrP. The second and third lower intensity peaks observed are due to ammonium and sodium salts adducts respectively and have not been labelled. The samples PrP: Mn^{2+}, and PrP: 5Mn^{2+} were also analysed but manganese coordination

was not observed. In contrast to the copper experiments, the deconvoluted mass spectra for all three samples (**[9-11]**) shows a continual presence of unbound SHaPrP(23-231). The masses deconvoluted from sample **[10]** can be attributed to PrP and PrP+1Mn^{2+} (23,155 Da), whereas sample **[11]** has an additional peak at mass 23,208 Da which corresponds to PrP+2Mn^{2+}. The continual presence of PrP suggests that manganese does not bind to PrP in a cooperative manner. The Mn^{2+} binding constant, to PrP, is 10 orders of magnitude lower than for copper (femto molar dissociation constant) (Jackson, Murray *et al.* 2001), this is reflected in the higher stoichiometric ratios required to coordinate the metal to the protein. Figures 5.5 and 5.10 indicate that as the concentration of copper is increased, with respect to prion, the peak intensities of the copper coordinated species (PrP+$\geq$2Cu^{2+}) also increase. In contrast, Figure 5.14 illustrates that apo-SHaPrP(23-231) is the dominant peak in the spectra whatever the manganese ion concentration used. These striking differences could be caused by the difference in binding modes and affinities.

Figure 5.15 shows the estimated cross-sections of the charge states of PrP, with and without Mn^{2+} ions coordinated, from (+9 to +25 charge states) obtained at pH 7.0. Charge states +9, +12 to +14 and +17 to +19 have only two or more stable conformations whereas the remaining charge states only have one conformation. This unfolding pattern is similar to that observed in Figure 5.11. Figure 5.15 also shows that there are no significant differences in the estimated cross-sections between SHaPrP(23-231) and those forms in which manganese is bound to the prion. This suggests that manganese coordination to the amyloidogenic region has no influence on the degree of the prion protein folding.

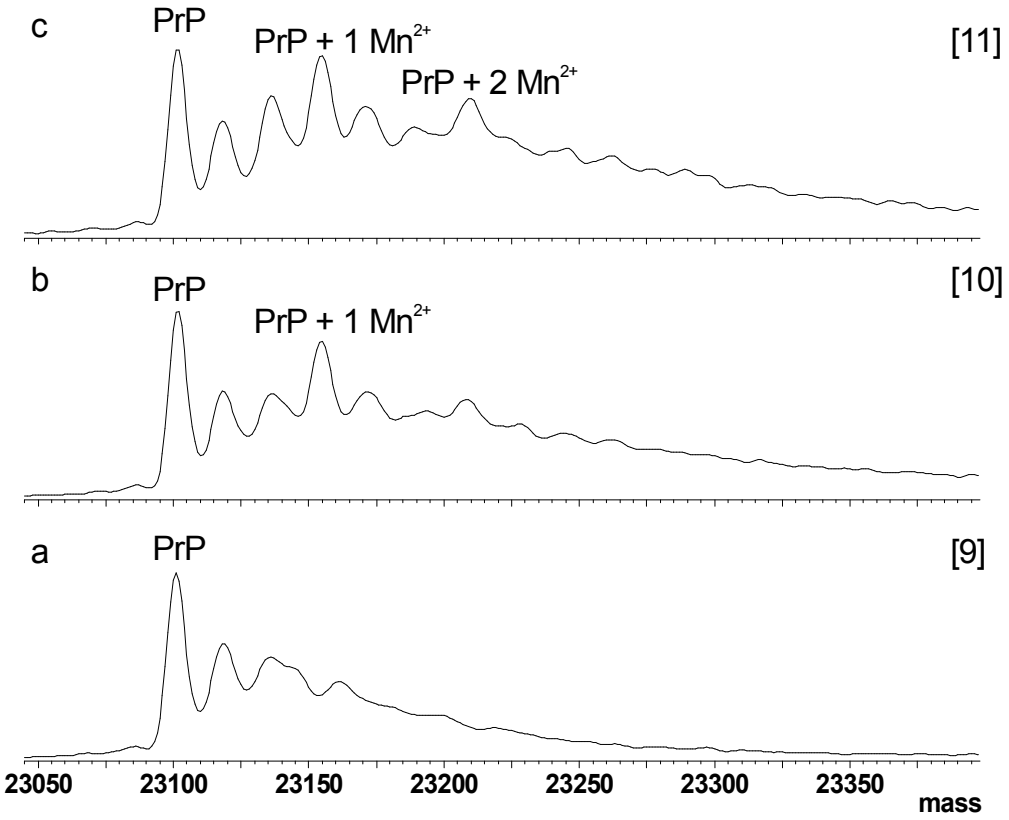

Figure 5.14: Deconvolution of the ESI spectrum for (a) SHaPrP(23-231), (b) SHaPrP(23-231): $10Mn^{2+}$, (c) SHaPrP(23-231): $20Mn^{2+}$.

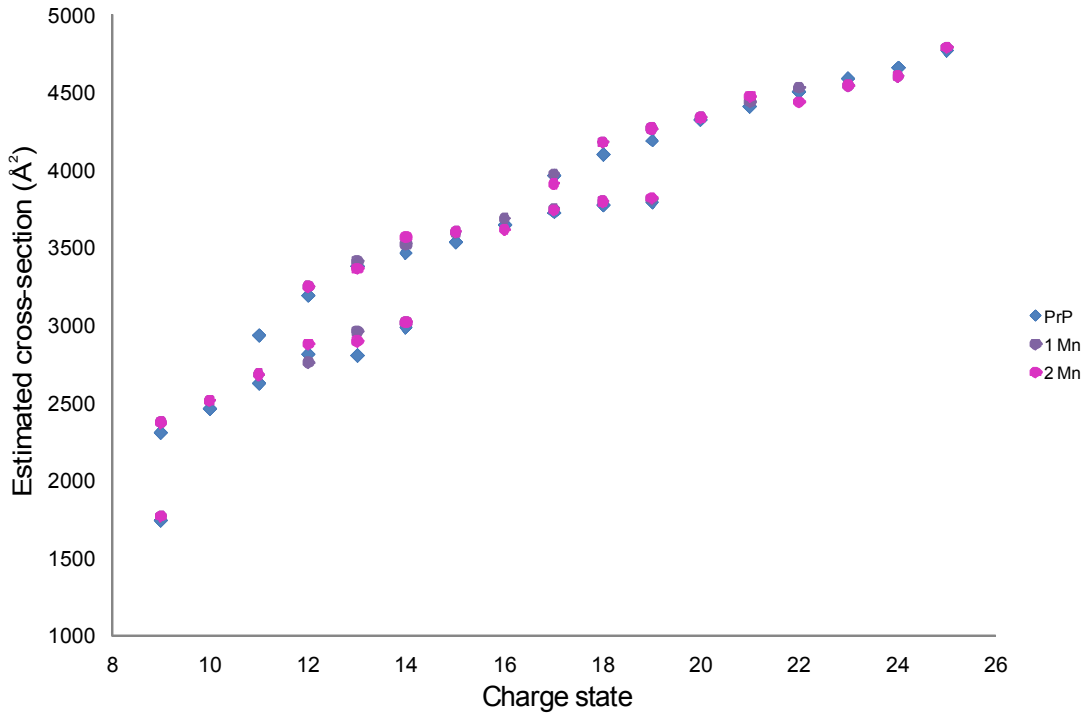

Figure 5.15: Comparison of estimated cross-sections for different charge states of SHaPrP(23-231), PrP+1Mn^{2+}, PrP+2Mn^{2+}.

5.2.4 Copper coordination vs manganese coordination to SHaPrP(23-231)

The coordination chemistry of Cu^{2+} and Mn^{2+} to the prion protein have been previously characterised and studies reveal that both metal ions coordinate to the His 111 imidazole ring at the fifth binding site (Burns, Aronoff-Spencer *et al.* 2002; Chattopadhyay, Walter *et al.* 2005; Gaggelli, Bernardi *et al.* 2005; Jackson, Murray *et al.* 2001; Klewpatinond, Davies *et al.* 2008; Millhauser 2004). Copper and manganese bind to the prion protein in two different regions; the structure of the N-terminal region is affected by Cu^{2+}, while Mn^{2+} first anchors to the Gly126 carboxylate and involves the preceding carbonyl residues from Leu125, Gly124 and His111 in the metal ion coordination (Gaggelli, Bernardi *et al.* 2005). A comparison of the estimated cross-sections for the copper and manganese coordinated species can be found in Figure 5.16. There are no significant differences in the estimated cross-sections between apo-SHaPrP(23-231) and PrP+Cu^{2+}, PrP+Mn^{2+}, PrP+2Cu^{2+} and PrP+2Mn^{2+}. This implies that the different binding sites for Cu^{2+} and Mn^{2+} do not induce a major conformational change in the protein. The difference in the prion cross-section upon metal coordination could be as small as 0.1%, as described above, and therefore IM-MS would not detect these differences.

Brown *et al* demonstrated that when the recombinant full-length prion protein is refolded in the presence of 5 mM $MnCl_2$, the protein is resistant to proteinase K digestion (Brown, Hafiz *et al.* 2000). These PrP constructs also became less stable upon manganese binding and were quickly converted to a misfolded form. From these findings Brown hypothesised that incorporation of manganese ions into PrP^{C} could produce a proteinase-resistant PrP seed which catalysed the conversion of PrP^{C} to PrP^{Sc}. In these experiments, the recombinant full-length PrP remained stable throughout and did not produce high order oligomers. A comparison of the estimated cross-sections showed there was no significant change in the overall conformation.

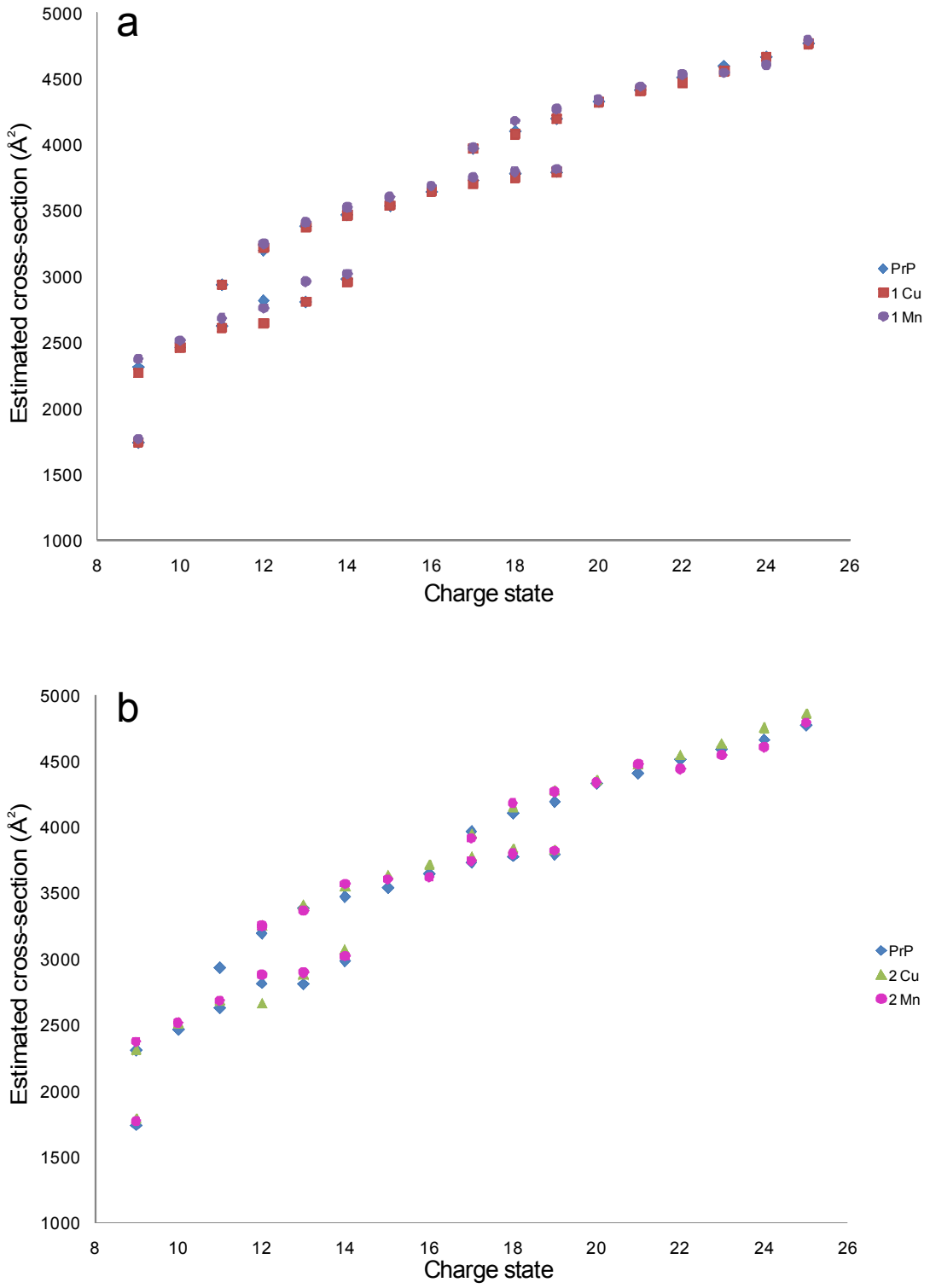

Figure 5.16: (a) Comparison of estimated cross-sections for different charge states of SHaPrP(23-231), PrP+1Cu^{2+}, PrP+1Mn^{2+}. (b) Comparison of estimated cross-sections for different charge states of SHaPrP(23-231), PrP+2Cu^{2+}, PrP+2Mn^{2+}.

5.3 Conclusions

ESI-IM-MS has been used to measure the interaction of copper and manganese with recombinant bovine peptide, BovPrP(57-101) and full-length recombinant Syrian hamster prion, SHaPrP(23-231), using different stoichiometric ratios of Cu^{2+} and Mn^{2+} at physiological pH, pH 7.0. Bovine peptide experiments show that at high copper concentrations (1:≥3 PrP: Cu^{2+}) all five octarepeat histidine residues coordinate to Cu^{2+} ions resulting in five Cu^{2+} attached to the peptide. The estimated cross-sections of the peptide suggest that the apo form may be globular in shape due to electrostatic interactions between the aromatic rings in consecutive tryptophan, histidine and proline residues. At low copper occupancy the peptide becomes less globular, as up to two Cu^{2+} ions can coordinate. The peptide becomes more globular when all five Cu^{2+} ions coordinate; this observation is also reflected in far-UV CD data as the relative abundance of random coil structure decreases upon increasing copper concentration. The largest difference in estimated cross-section upon copper coordination is 15 $Å^2$ which is observed between BovPrP(57-101) and BovPrP(57-101)+2Cu^{2+}. IM-MS can successfully detect small differences (≥1%) in the cross-section of the N-terminal octarepeat peptide.

Analysis of SHaPrP(23-231) ESI-MS data with and without ion mobility separation is in good agreement. At low Cu^{2+} ion concentrations (1:≤1 PrP:Cu^{2+} equivalents) a maximum of two Cu^{2+} are coordinated to the protein. At higher Cu^{2+} ion concentrations (1:>3 PrP:Cu^{2+} equivalents) it was observed that four Cu^{2+} coordinate to the prion in a cooperative manner. Copper binding affinities have been published elsewhere and it is noted that different binding modes occur at different copper concentrations. The mass spectrum of apo SHaPrP(23-231) shows a single series of multiply charged peaks suggesting only monomer is present and the prion sample is of a high purity. In comparison, the mass spectrum of SHaPrP(23-231):Cu^{2+} shows the presence of dimer peaks indicating that copper can induce aggregation of the prion. There are no significant differences between the estimated cross-sections of PrP, PrP+Cu^{2+}, PrP+2Cu^{2+}, PrP+3Cu^{2+} and PrP+4Cu^{2+}; the same observation can be made when comparing individual ATDs.

Manganese binding experiments to SHaPrP(23-231) show that a high excess of the metal ion is required for Mn^{2+} coordination to occur. Up to two Mn^{2+} ions coordinate to the protein at ratios PrP:≥20 Mn^{2+}. Apo SHaPrP(23-231) was observed in all the deconvoluted spectra and the mass spectra reveal a single series of peaks arising from multiply-charged ions throughout the sample set. Manganese binding to the protein did not induce the sample to aggregate. A comparison of Cu^{2+} and Mn^{2+} coordinated species shows there is no significant difference in the estimated cross-section between apo SHaPrP(23-231) and its metal bound counterparts.

It has been observed that copper coordination to the N-terminal fragment can induce conformational changes in the octarepeat fragment. These changes are relatively small and cannot be measured in the full-length prion protein. This suggests that minor structural changes in the N-terminal could stimulate endocytosis via a minor, undetected, conformational change in the C-terminal domain. It also implies that SOD activity in the full-length protein is sensitive to extremely small conformational changes.

The T-Wave device is able to operate at biologically relevant sample concentrations and with its speed and ease of use it has the ability to be used in an automated fashion. ESI-IM-MS provides an extra dimension of fast, sensitive, gas phase, ion separation enabling conformational changes in the protein structure to be probed. T-Wave technology is still in the early stages of development and it is likely that further improvements in the resolution of the technique will extend the approach into a fast, sensitive, information-rich method. This provides a technique with the potential to probe small but significant changes in structure of biological molecules.

The aim of this work was to develop and evaluate a mass spectrometry-based method to distinguish between the prion isoforms and access the technique's ability to be used as an ante-mortem diagnostic test. The work described in chapters four and five suggests that the IM-MS technique has the potential to be used as an ante-

mortem test. It was discussed that, in principle, the IM-MS technique could be used to distinguish between PrP^{C} and PrP^{Sc} and IM-MS was a useful tool to discriminate between small conformation changes in the gas-phase. Extensive further studies would, however, be required before this approach could be recognised as an effective ante-mortem test. Such studies include an amplification method of PrP in mammalian blood, de-glycosylation of the extracted PrP protein and the re-assessment of the IM-MS technique to detect PrP^{C} and PrP^{Sc} from healthy and diseased blood samples.

5.4 References

Aguzzi, A. and Heikenwalder, M. (2006). Pathogenesis of prion diseases: current status and future outlook. *Nature Reviews Microbiology* **4**, 765-75.

Back, J. W., Sanz, M. A., De Jong, L., De Koning, L. J., Nijtmans, L. G., De Koster, C. G., Grivell, L. A., Van Der Spek, H. and Muijsers, A. O. (2002). A structure for the yeast prohibitin complex: Structure prediction and evidence from chemical crosslinking and mass spectrometry. *Protein Science* **11**, 2471-8.

Becker, J. S. and Jakubowski, N. (2009). The synergy of elemental and biomolecular mass spectrometry: new analytical strategies in life sciences. *Chemical Society Reviews* **38**, 1969-83.

Borchelt, D. R., Scott, M., Taraboulos, A., Stahl, N. and Prusiner, S. B. (1990). Scrapie and cellular prion proteins differ in their kinetics of synthesis and topology in cultured cells. *Journal of Cell Biology* **110**, 743-52.

Brazier, M. W., Davies, P., Player, E., Marken, F., Viles, J. H. and Brown, D. R. (2008). Manganese binding to the prion protein. *Journal of Biological Chemistry* **283**, 12831-9.

Brown, A. R. T. a. D. R. (2004). A Functional Role for a Copper Binding Prion Protein *Horizon Bioscience*.

Brown, D. R. (2001). Prion and prejudice: normal protein and the synapse. *Trends in Neuroscience* **24**, 85-90.

Brown, D. R., Hafiz, F., Glasssmith, L. L., Wong, B. S., Jones, I. M., Clive, C. and Haswell, S. J. (2000). Consequences of manganese replacement of copper for prion protein function and proteinase resistance. *Embo J* **19**, 1180-6.

Brown, D. R., Qin, K. F., Herms, J. W., Madlung, A., Manson, J., Strome, R., Fraser, P. E., Kruck, T., vonBohlen, A., SchulzSchaeffer, W., Giese, A., Westaway, D. and Kretzschmar, H. (1997). The cellular prion protein binds copper in vivo. *Nature* **390**, 684-687.

Burns, C. S., Aronoff-Spencer, E., Dunham, C. M., Lario, P., Avdievich, N. I., Antholine, W. E., Olmstead, M. M., Vrielink, A., Gerfen, G. J., Peisach, J., Scott, W. G. and Millhauser, G. L. (2002). Molecular features of the copper binding sites in the octarepeat domain of the prion protein. *Biochemistry* **41**, 3991-4001.

Burns, C. S., Aronoff-Spencer, E., Legname, G., Prusiner, S. B., Antholine, W. E., Gerfen, G. J., Peisach, J. and Millhauser, G. L. (2003). Copper coordination in the full-length, recombinant prion protein. *Biochemistry* **42**, 6794-6803.

Caughey, B., Race, R. E., Ernst, D., Buchmeier, M. J. and Chesebro, B. (1989). Prion protein biosynthesis in scrapie-infected and uninfected neuroblastoma cells. *Journal of Virology* **63**, 175-81.

Caughey, B. and Raymond, G. J. (1991). The scrapie-associated form of PrP is made from a cell surface precursor that is both protease- and phospholipase-sensitive. *Journal of Biological Chemistry* **266**, 18217-23.

Chattopadhyay, M., Walter, E. D., Newell, D. J., Jackson, P. J., Aronoff-Spencer, E., Peisach, J., Gerfen, G. J., Bennett, B., Antholine, W. E. and Millhauser, G. L. (2005). The octarepeat domain of the prion protein binds Cu(II) with three distinct coordination modes at pH 7.4. *Journal of American Chemical Society* **127**, 12647-56.

Choi, C. J., Kanthasamy, A., Anantharam, V. and Kanthasamy, A. G. (2006). Interaction of metals with prion protein: possible role of divalent cations in the pathogenesis of prion diseases. *Neurotoxicology* **27**, 777-87.

Fenton, D. E. (1995). Biocoordination chemistry. *Oxford University Press*.

Fernaeus, S. and Land, T. (2005). Increased iron-induced oxidative stress and toxicity in scrapie-infected neuroblastoma cells. *Neuroscience Letters* **382**, 217-20.

Fernaeus, S., Reis, K., Bedecs, K. and Land, T. (2005). Increased susceptibility to oxidative stress in scrapie-infected neuroblastoma cells is associated with intracellular iron status. *Neuroscience Letters* **389**, 133-6.

Gaggelli, E., Bernardi, F., Molteni, E., Pogni, R., Valensin, D., Valensin, G., Remelli, M., Luczkowski, M. and Kozlowski, H. (2005). Interaction Of The Human Prion PrP(106-126) Sequence With Copper(II), Manganese(II), And Zinc(II): NMR and EPR Studies. *Journal- American Chemical Society* **127**, 996-1006.

Garnett, A. P. and Viles, J. H. (2003). Copper binding to the octarepeats of the prion protein. Affinity, specificity, folding, and cooperativity: insights from circular dichroism. *Journal of Biological Chemistry* **278**, 6795-802.

Georgieff, M. K. (2007). Nutrition and the developing brain: nutrient priorities and measurement. *American Journal of Clinical Nutrition* **85**, 614S-620.

Harris, D. A., Gorodinsky, A., Lehmann, S., Moulder, K. and Shyng, S. L. (1996). Cell biology of the prion protein. *Current Topics in Microbiology Immunology* **207**, 77-93.

Hesketh, S., Sassoon, J., Knight, R. and Brown, D. R. (2008). Elevated manganese levels in blood and CNS in human prion disease. *Molecular and Cellular Neuroscience* **37**, 590-8.

Hesketh, S., Sassoon, J., Knight, R., Hopkins, J. and Brown, D. R. (2007). Elevated manganese levels in blood and central nervous system occur before onset of clinical signs in scrapie and bovine spongiform encephalopathy. *Journal of Animal Science* **85**, 1596-609.

Hilton, G. R., Jackson, A. T., Thalassinos, K. and Scrivens, J. H. (2008). Structural Analysis of Synthetic Polymer Mixtures Using Ion Mobility and Tandem Mass Spectrometry. *Analytical Chemistry* **80**, 9720-9725.

Jackson, G. S., Murray, I., Hosszu, L. L., Gibbs, N., Waltho, J. P., Clarke, A. R. and Collinge, J. (2001). Location and properties of metal-binding sites on the human prion protein. *Proceeding in the National Academy of Sciences U S A* **98**, 8531-5.

Kardos, J., Kovacs, I., Hajos, F., Kalman, M. and Simonyi, M. (1989). Nerve endings from rat brain tissue release copper upon depolarization. A possible role in regulating neuronal excitability. *Neuroscience Letters* **103**, 139-44.

Klewpatinond, M., Davies, P., Bowen, S., Brown, D. R. and Viles, J. H. (2008). Deconvoluting the Cu2+ binding modes of full-length prion protein. *Journal of Biological Chemistry* **283**, 1870-81.

Linder, M. C. and Hazegh-Azam, M. (1996). Copper biochemistry and molecular biology. *American Journal of Clinical Nutrition* **63**, 797S-811.

Malmström, B. G. and Vänngård, T. (1960). Electron spin resonance of copper proteins and some model complexes. *Journal of Molecular Biology* **2**, 118-124.

Maras B., B. D., Schinina M. E., Cardone F., Pocchiari (2004). Prion (PrPres) allotypes profiling: new perspectives from mass spectrometry. *European Journal of Mass Spectrometry* **10**, 371-382.

Millhauser, G. L. (2004). Copper binding in the prion protein. *Accounts of Chemical Research* **37**, 79-85.

Nadal, R. C., Abdelraheim, S. R., Brazier, M. W., Rigby, S. E., Brown, D. R. and Viles, J. H. (2007). Prion protein does not redox-silence Cu2+, but is a sacrificial quencher of hydroxyl radicals. *Free Radical Biology & Medicine* **42**, 79-89.

Onisko, B., Dynin, I., Requena, J. R., Silva, C. J., Erickson, M. and Carter, J. M. (2007). Mass Spectrometric Detection of Attomole Amounts of the Prion Protein by nanoLC/MS/MS. *Journal of the American Society for Mass Spectrometry* **18**, 1070-1079.

Pauly, P. C. and Harris, D. A. (1998). Copper stimulates endocytosis of the prion protein. *Journal of Biological Chemistry* **273**, 33107-10.

Pushie, M. J., Ross, A. R. and Vogel, H. J. (2007). Mass spectrometric determination of the coordination geometry of potential copper(II) surrogates for the mammalian prion protein octarepeat region. *Analytical Chemistry* **79**, 5659-67.

Qin, K., Yang, D. S., Yang, Y., Chishti, M. A., Meng, L. J., Kretzschmar, H. A., Yip, C. M., Fraser, P. E. and Westaway, D. (2000). Copper(II)-induced conformational changes and protease resistance in recombinant and cellular PrP. Effect of protein age and deamidation. *Journal of Biological Chemistry* **275**, 19121-31.

Qin, K., Yang, Y., Mastrangelo, P. and Westaway, D. (2002). Mapping Cu(II) binding sites in prion proteins by diethyl pyrocarbonate modification and matrix-assisted laser desorption ionization-time of flight (MALDI-TOF) mass spectrometric footprinting. *Journal of Biological Chemistry* **277**, 1981-90.

Requena, J. R., Groth, D., Legname, G., Stadtman, E. R., Prusiner, S. B. and Levine, R. L. (2001). Copper-catalyzed oxidation of the recombinant SHa(29-231) prion protein. *Proceeding in the National Academy of Sciences U S A* **98**, 7170-5.

Riek, R., Hornemann, S., Wider, G., Glockshuber, R. and Wuthrich, K. (1997). NMR characterization of the full-length recombinant murine prion protein, mPrP(23-231). *FEBS Letters* **413**, 282-8.

Riihimaki, E.-S., Martinez, J. M. and Kloo, L. (2008). Structural effects of Cu(ii)-coordination in the octapeptide region of the human prion protein. *Physical Chemistry Chemical Physics* **10**, 2488-2495.

Scarff, C. A., Thalassinos, K., Hilton, G. R. and Scrivens, J. H. (2008). Travelling wave ion mobility mass spectrometry studies of protein structure: biological significance and comparison with X-ray crystallography and nuclear magnetic resonance spectroscopy measurements. *Rapid Communications in Mass Spectrometry* **22**, 3297-3304.

Shyng, S. L., Moulder, K. L., Lesko, A. and Harris, D. A. (1995). The N-terminal domain of a glycolipid-anchored prion protein is essential for its endocytosis via clathrin-coated pits. *Journal of Biological Chemistry* **270**, 14793-800.

Tanzi, R. E., Petrukhin, K., Chernov, I., Pellequer, J. L., Wasco, W., Ross, B., Romano, D. M., Parano, E., Pavone, L., Brzustowicz, L. M. and et al. (1993). The Wilson disease gene is a copper transporting ATPase with homology to the Menkes disease gene. *Nature Genetics* **5**, 344-50.

Thompsett, A. R. and Brown, D. A. (2004). A Functional Role for a Copper Binding Prion Protein. *Horizon Bioscience*.

Viles, J. H., Cohen, F. E., Prusiner, S. B., Goodin, D. B., Wright, P. E. and Dyson, H. J. (1999). Copper binding to the prion protein: structural implications of four identical cooperative binding sites. *Proceeding in the National Academy of Sciences U S A* **96**, 2042-7.

Viles, J. H., Klewpatinond, M. and Nadal, R. C. (2008). Copper and the structural biology of the prion protein. *Biochemical Society Transactions* **36**, 1288-92.

Wells, M. A., Jackson, G. S., Jones, S., Hosszu, L. L. P., Craven, C. J., Clarke, A. R., Collinge, J. and Waltho, J. P. (2006). A reassessment of copper(II) binding in the full-length prion protein. *Biochemical Journal* **399**, 435-444.

White, A. R., Bush, A. I., Beyreuther, K., Masters, C. L. and Cappai, R. (1999). Exacerbation of copper toxicity in primary neuronal cultures depleted of cellular glutathione. *Journal of Neurochemistry* **72**, 2092-8.

Whittal, R. M., Ball, H. L., Cohen, F. E., Burlingame, A. L., Prusiner, S. B. and Baldwin, M. A. (2000). Copper binding to octarepeat peptides of the prion protein monitored by mass spectrometry. *Protein Science* **9**, 332-43.

Wong, B. S., Chen, S. G., Colucci, M., Xie, Z., Pan, T., Liu, T., Li, R., Gambetti, P., Sy, M. S. and Brown, D. R. (2001). Aberrant metal binding by prion protein in human prion disease. *Journal of Neurochemistry* **78**, 1400-8.

Wong, B. S., Pan, T., Liu, T., Li, R., Gambetti, P. and Sy, M. S. (2000). Differential contribution of superoxide dismutase activity by prion protein in vivo. *Biochemical & Biophysical Research Communications* **273**, 136-9.

Yedidia, Y., Horonchik, L., Tzaban, S., Yanai, A. and Taraboulos, A. (2001). Proteasomes and ubiquitin are involved in the turnover of the wild-type prion protein. *Embo J* **20**, 5383-91.

Zahn, R. (2003). The octapeptide repeats in mammalian prion protein constitute a pH-dependent folding and aggregation site. *Journal of Molecular Biology* **334**, 477-88.

Chapter 6

Introduction to Synthetic Polymers

6.1 Introduction

Synthetic polymers are an integral part of everyday life. Plastic bags, medical implants, textile fibres, automobiles and children's toys are a few examples of the diverse applications of modern polymeric materials. Polymer systems can exhibit a wide range of properties. It is the differences in these physical properties that have resulted in the polymers being used for a variety of different applications. The performance of these materials is dependent on a number of factors including the initiating and/or terminating end groups, the molecular weight distribution and more importantly the monomeric units. As a consequence, there is great interest in characterising the detailed microstructure of synthetic polymers and to relate this information to their structural and functional properties (Koenig 2004).

6.2 What is a polymer?

A polymer can be a naturally-occurring, an artificially-modified or a synthetic compound. The most common and generally accepted definition of a polymer is: "a system formed by an assembly of macromolecules – that is a system of molecular entities with large dimension which are obtained by the covalent linking of a large number of constitutional repeat units, more commonly called monomeric units" (Gnanou and Fontanille 2008). The polymeric repeat units are composed from sequentially reacted monomers which are typically capped by end groups. A polymer can be characterised by the chemical composition of its repeat units, the end groups and the molecular weight distribution of the oligomers.

6.3 Function

Synthetic polymeric materials are used throughout the industrial world for a variety of different purposes within chemical, pharmaceutical and manufacturing commerce (see Table 6.1 for examples). They range from high-value commodity products such as poly(propylene) (PP) and poly(ethylene) (PE), to low tonnage speciality products such as poly(ether ether ketone) (PEEK) and carbon fibre reinforced resins (Scrivens

and Jackson 2000). Traditional polymer systems such as poly(methyl methacrylate), cellulose acetate and poly(ether urethane) are commonplace within the medical field and are regularly used as false teeth, dialysis tubing or in artificial hearts respectively (Peppas and Langer 1994). These polymer materials have helped to usher in new medical treatments but critical problems in biocompatibility, mechanical properties, degradation and numerous other areas still remain (Langer and Tirrell 2004). Developments in manufacturing and in biomedical materials have been the catalysis for the creation, and synthesis, of thousands of specialised products. For example a new polyether copolymer has been synthesised that, once formed into nanospheres, can circulate around the body mimicking the movement of cells (Langer and Tirrell 2004). This application has the potential to revolutionise drug delivery systems. The new specially synthesised polymeric materials tend to be more chemically complex and can be difficult to analyse.

Table 6.1: Examples of synthetic polymers and their function (Nicholson 2006)

Polymer class	Example	Uses
Acrylic	Poly(methyl methacrylate)	• Shatter-proof glass • Heat-proof material • Paints
Polyamide	Nylon	• Textile fibres • Engineering applications
Polycarbonate	Polycarbonate of bisphenol A	• Shatter-proof glass • Reading spectacles
Polyester	Poly(ethylene terephthalate)	• Textile fibres • Food & drink containers
Polyether	Poly(ethylene glycol)	• Electrical insulation • Cosmetics • Building and construction
Polyurethane	Elastane (Spandex/Lycra)	• Rigid or flexible foam • Protective coatings • Textile fibres
Polyvinyl	Poly(vinyl chloride)	• Adhesives • Pipes • Textile fabrics

6.4 Polymer formulations

A polymer formulation can contain several components in addition to the synthetic polymer itself. These components range from contaminants of the synthetic process which include un-reacted catalyst, low molecular weight oligomers and intact monomers, to components deliberately added to the polymer system that modify the properties of the polymeric material. These deliberately added components, known as polymer additives, can enhance the performance of a polymer system. Different types of additives can be mixed with a synthetic polymer to change its function. For example Table 6.1 shows that poly(ethylene glycol) (PEG) can be used as both an electrical insulator and in cosmetic products. The properties required for these two manufactured goods are dramatically different. An electrical wire insulator should be flexible, protect the wire from environmental factors and protect the user from receiving an electrical shock. Polymer additives such as plasticizers, flow enhancers and heat stabilisers are added to the PEG formulation to improve its insulation properties. In cosmetic applications the polymer is added as a bulk reagent to the formulation; it should be stable when exposed to light, creamy in texture and inert. Antioxidants, lubricants and fragrances are the types of additives added to cosmetic PEG formulations. Polymer additives can be complex mixtures and a variety of different analytical techniques is often required to help identify and quantify them.

6.5 Polymerisation

Synthetic polymers can be classified according to their method of synthesis. The two main methods are either step-growth or chain-growth polymerisation. Step polymerisation describes the mechanism in which the polymer backbone is generated by a step-wise reaction between two independent molecular species. Most step-growth polymers, such as Nylon 66, are produced by a reaction between two difunctional monomers (see Figure 6.1a). The majority of step-growth polymerisation mechanisms occur by simple one step condensation/addition reaction. In contrast, chain polymerisation typically consists of three phases: namely initiation; propagation and termination (see Figure 6.1b). In some cases a chain transfer agent is used to control the functionality and molecular weight of the polymer system. In the initiation stage a reactive centre is generated. These reactive

centres are usually free radicals and are formed when an initiator is heated or excited by UV light. The newly formed free radical can react with a monomer unit to create a reactive intermediate. In the propagation phase, the reactive intermediate reacts with successive monomers to create a growing polymer chain. This chain continues to grow until all the monomer units have been reacted or the end groups undergo a termination reaction. Free radical polymerisation reactions can be terminated either by combination or disproportionation. The combination mechanism involves the reaction of two radical species which form a single bond and one reaction product. In the disproportionation reaction two radical species react to yield a saturated and unsaturated reaction product (see Figure 6.1b). The polymerisation mechanisms can influence the properties of the resulting polymer. Polymers created by chain-growth polymerisation tend to have a low polydispersity and be higher in molar mass. A long chain-growth reaction time tends to increase the yield of the polymer rather than the molar mass of the individual oligomers. In contrast, a longer step-growth reaction time is required for higher molar mass oligomers to be created; during this reaction varying oligomer lengths are created which affects the polydispersity value (Montaudo and Lattimer 2002).

a

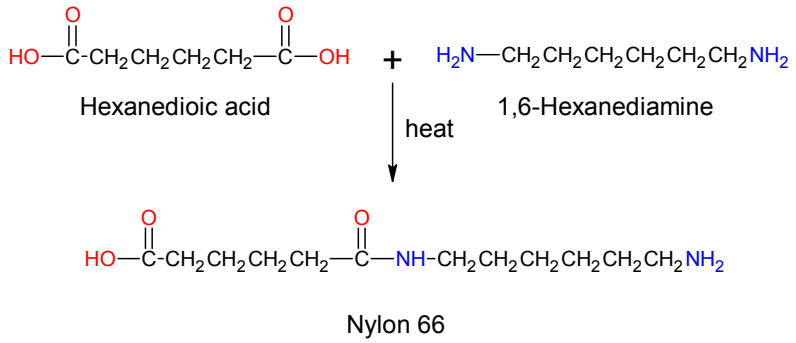

b

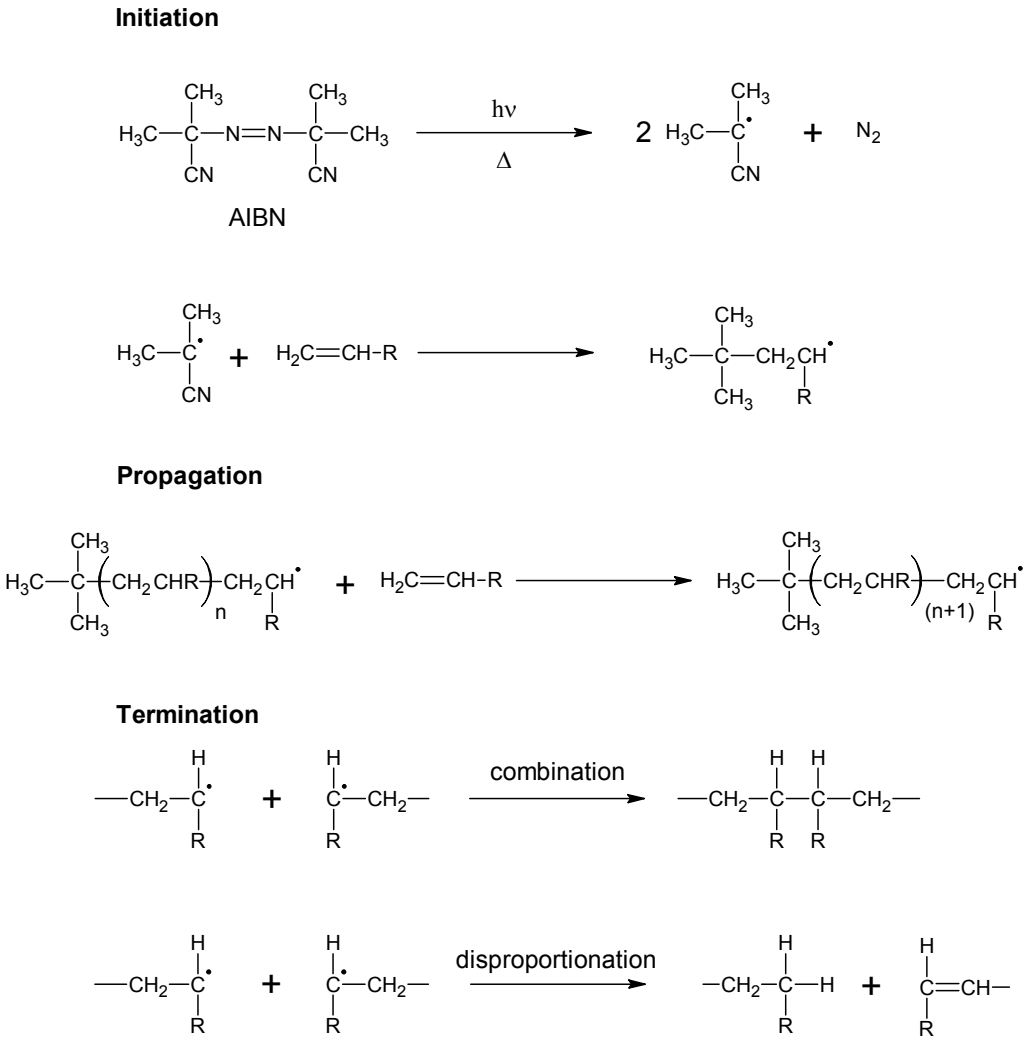

Figure 6.1: Schematic of step-growth and chain-growth polymerisation. (a) Step-growth mechanism for the formation of Nylon 66. (b) Chain-growth mechanism. Free radical reaction of a commonly used initiator azobisisobutyronitrile (AIBN). Propagation and termination stages of the chain-growth polymerisation.

6.6 Copolymers

A homopolymer is a polymer formed from polymerisation of monomer units that have the same structure; for example polyethylene is formed by polymerisation of ethylene. Copolymers are obtained from polymerisation of two different monomer units. Copolymers can be synthesised by means of step-growth polymerisation, such as Nylon 66 (see Figure 6.1a), or by chain-growth polymerisation. The propagation step in a free radical copolymerisation reaction (see Figure 6.1b *Propagation*) is the only step that differs from that of homopolymerisation. Copolymers can be classified by their statistical properties. The statistics of copolymers is defined by the distribution of monomeric units along the chain backbone (Gnanou and Fontanille 2008). The distribution of monomers can be described as alternating, block or random (see Figure 6.2). Alternating copolymers contain regular alternating comonomers (A and B). Block copolymers comprise of two or more homopolymer subunits linked together by covalent bonds. These copolymers can be further classified by the number of repeating block units each polymer contains such as di-block or tri-block. Random copolymers occur if the probability of finding a given type of monomer residue, at a particular point in the chain, is equal to the mole fraction of that monomer residue in the chain (Gnanou and Fontanille 2008). The characteristics of a copolymer are dependent on its statistical properties.

The analysis of copolymers can be considerably more challenging than that of homopolymers. In particular, the characterisation of block and random copolymers can be complex because of the additional information content. The information that can be determined from a copolymer includes the average molecular weight of the polymer, the structure of the repeat units (both A and B), the estimation of the relative abundance of macromolecular chains terminated with one type of end group or another, the average molar fraction of A and B units in the copolymer, the average length of long AAAA and BBBB blocks, the weight of copolymer chains that possess a given composition and the variation of copolymer composition as the molar mass of the macromolecular chain grows (Montaudo 2002). A variety of spectroscopic and spectrometric techniques have been used to characterise the structural properties and functions of copolymer systems (Mark, Ngai *et al.* 2004).

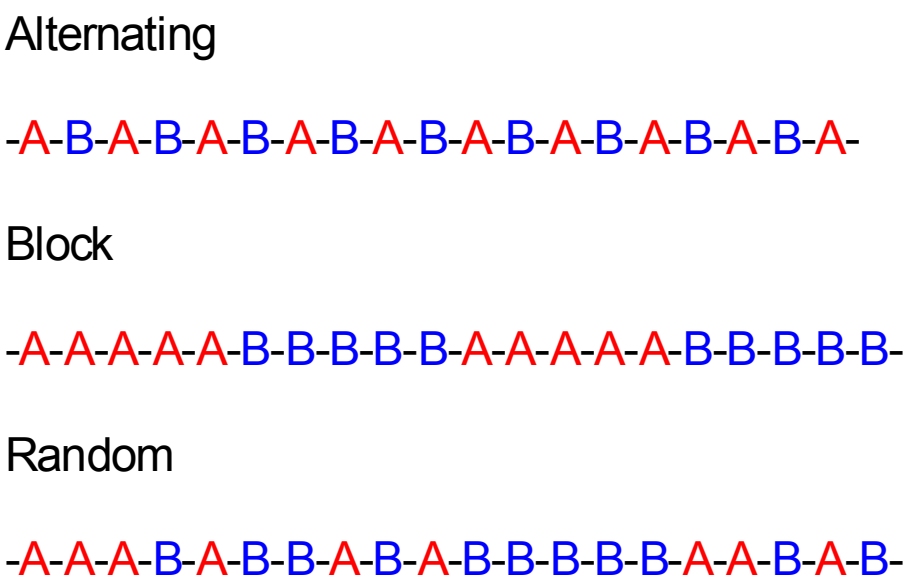

Figure 6.2: Schematic representation of statistical copolymers.

6.7 Analysis of Polymers

Assessing the performance of a polymeric material, after preparation and in its working environment, requires a fundamental understanding of the relationship between the molecular and bulk properties of a polymer system. The characterisation method chosen to analyse the polymer system depends on the information content required. The macroscopic/bulk properties of the polymeric material are typically determined by means of mechanical testing, rheology and thermal analysis. Techniques such as light scattering and microscopy are used to analyse the microscopic properties of a polymer (Nicholson 2006). The performance of a polymeric material can also be influenced by the nature of its surface and interface. Secondary ion mass spectrometry (SIMS) has been used to monitor the changes in interfacial properties (Harton, Stevie *et al.* 2006). Other techniques such as X-ray photoelectron spectroscopy (XPS) have also been used to characterise the surface defects and imperfections of a polymeric material (Briggs, Brewis *et al.* 1976).

6.7.1 Molecular Mass Distribution

Knowledge of the molecular weight distribution of a polymer is very important as a variation in this mean value and the distribution can affect the physical properties of the material. Two common measurements for the average molecular weight of a polymer are the number-average molecular weight (M_n) and the weight-average molecular weight (M_w). Equations 6.1 and 6.2 show how to calculate these parameters where m_i is the mass of an observed ion and N_i is the number of ions observed.

The number-average molar mass M_n is given by:

$$M_n = \frac{\sum m_i N_i}{\sum N_i}$$

Equation 6.1

The weight-average molar mass M_w is defined as:

$$M_w = \frac{\sum m_i^2 N_i}{\sum m_i N_i}$$

Equation 6.2

The polydispersity (D) of the polymer can be calculated from the M_n and M_w values (see Equation 6.3).

$$D = \frac{M_w}{M_n}$$

Equation 6.3

In general, the value for M_w is always larger than that of M_n except for a monodisperse system. This implies that the value for D cannot be less than 1. Narrow molecular weight distributions are characterised by D values close to 1,

whereas broad molecular weight distribution are characterised by D values ≥ 2 (Montaudo and Lattimer 2002).

6.8 Characterisation methods

Various analytical methods are available for the characterisation of synthetic polymer structures. Techniques such as gel permeation chromatography (GPC, also known as size exclusion chromatography, SEC), light scattering, osmometry, NMR spectroscopy and end group titration are used to measure the average molecular weight of the polymer. Spectroscopic techniques such as IR spectroscopy and NMR spectroscopy measure the overall average features of a polymer system rather than an individual molecular structure. In some cases, however, end group functionality can be deduced. Mass spectrometry is an established analytic tool for the characterisation of various polymer systems.

6.8.1 NMR Spectroscopy

NMR spectroscopy is frequently used to characterise polymers because of its high resolution, sensitivity and the ability to quantify polymer repeat units from the spectrum. NMR provides information on polymer structures including main-chain and microstructures (stereochemistry, regioisomerism and geometric isomerism), co-monomer composition, end- and side-group analysis, cross-linking, branching and side-chain tacticity (Mark, Ngai *et al.* 2004). Both ^{1}H and ^{13}C NMR are typically used to analyse the polymer system but the lower sensitivity of the latter means longer acquisition times are often necessary. An advantage of employing NMR spectroscopy to characterise synthetic polymers is that most polymeric phases can be analysed by means of solid-state, solution-state or hyphenated solution-state NMR methods.

6.8.2 GPC-NMR

GPC is a widely applicable chromatography technique that can help determine the molecular weight distribution of synthetic polymers. The technique is based on the separation of solvated samples based on their molecular size and shape. A sample is injected on to the GPC column, where the various components are separated according to their size and shape, and eluted from the column in order of decreasing size. The molecular size of these samples can be calculated by comparing the elution times of components of the unknown sample with the elution times of GPC calibrants. The GPC equipment should ideally be calibrated with a compound similar to that being analysed. A problem with this approach is that calibration compounds for many polymers are not available. The disadvantages of GPC are that the data generated are dependent on the calibration curve used, and the molecular shape of the compound. A difference in molecular shape can affect the elution order of a compound. For example, in a low molecular weight polymer, substitution of an aromatic end group to a long aliphatic end group could have a dramatic affect on the overall shape of the polymer. This difference could change the elution order of the polymer and therefore the predicted molecular weight of the compound (Choi, Chong *et al.* 2001; Rader, Spickermann *et al.* 1995).

The first report of GPC coupled on-line to a NMR detector was in 1988. In this initial study Hatada and co-workers demonstrated that the number-average molecular weight of isotactic poly(methyl methacrylate) (PMMA) could be directly measured by GPC-NMR (Hatada, Ute *et al.* 1988). The use of NMR as a detector removed the need to perform a GPC calibration step. Two decades later, several publications suggest that GPC-NMR is an invaluable tool for the deformulation of complex polymer mixtures (Hatada, Ute *et al.* 1990; Hatada, Ute *et al.* 1989; Kitayama, Janco *et al.* 2000; Kitayama and Ute 2006; Kramer, Pasch *et al.* 1999; Robertson, Heron *et al.* 2004; Ute, Kashiyama *et al.* 1990; Ute, Niimi *et al.* 2001). Hiller *et al,* have shown that on-line GPC-NMR can be used to analyse blends of homopolymers and copolymers at ambient and high temperatures (Hiller, Pasch *et al.* 2006). They revealed it was possible to separate a mixture of poly(ethylene) (PE) and PMMA based on their molecular masses and different chemical compositions.

6.8.3 Mass Spectrometry

Mass spectrometry is gaining in popularity as a technique that can be used to investigate the structure of polymers in the gas phase. This technique was originally used to determine the fundamental energetic and structural properties of small molecules. In more recent years, it has been applied to characterise the chemical composition and molar mass distribution of certain polymer classes. The development of soft ionisation techniques such as ESI and MALDI has permitted relatively large macromolecules to be analysed intact.

The desire for new materials and technologies has led to the creation of more complex polymer systems and mixtures. The complexity of these polymers systems makes it difficult to characterise the polymer by MS alone. To overcome this analytical challenge, many new ionisation techniques and hyphenated analytical approaches have been employed including ion mobility mass spectrometry (IM-MS) (Weidner and Trimpin 2008).

6.8.3.1 Matrix-assisted laser desorption/ionisation (MALDI)

Successful polymer analysis by means of MALDI-MS requires the polymer sample to be co-crystallised with salt and matrix molecules. The nature of synthetic polymers makes it difficult to achieve a uniform sample:salt:matrix crystal. Different sample preparation techniques are therefore required for different polymer systems or different molecular weight ranges (Peacock and McEwen 2006; Zenobi and Knochenmuss 1998). A typical MALDI mass spectrum of a low polydisperse synthetic polymer is relatively simple. The spectrum consists of peaks predominantly from singly charged, cationised polymer ions with few or no fragmentation ions present. Structural and compositional information on the polymer system can be deduced from the MALDI–MS data. This information includes repeat unit and end group identification, structural analysis of linear and cyclic oligomers, tracking of polymerisation kinetics and the determination of molecular weight distributions (Montaudo and Lattimer 2002).

Most mass spectrometry studies of synthetic polymers involve cationisation rather than protonation. Alkali metals are the preferred cationising agents but in some cases transition metals, such as silver and copper, are required. Research has shown that the molecular weight distribution of certain polymer classes can vary depending on the cation used for ionisation (Deery, Jennings *et al.* 1997; Dogruel, Nelson *et al.* 1996; Jackson, Yates *et al.* 1997a). This variation is observed because the larger cations interact less favourably with small oligomers and *vice versa*. For example, polyethers can be readily ionised when coordinated to small alkali cations such as lithium or sodium, whereas polystyrenes are more favourably ionised when they interact with larger cations such as silver (Chen and Li 2001; Deery, Jennings *et al.* 1997; Polce, Ocampo *et al.* 2008a; Polce, Ocampo *et al.* 2008b).

In recent years MALDI has developed into an invaluable tool for determining the molecular weight distributions of synthetic polymers (Bahr, Deppe *et al.* 1992; Dey, Castoro *et al.* 2002; Montaudo, Montaudo *et al.* 1995b; Montaudo, Montaudo *et al.* 1997). The advantage of analysing polymers by means of MALDI, over techniques such as SEC or light scattering techniques, is that molecular weights and molecular weight distribution can be obtained however, these values can be inaccurate. The disadvantage of the MALDI-MS technique is that the molecular weight values for polydisperse polymers (polymers with a polydispersity > 1.2 (Martin, Spickermann *et al.* 1996)) differ from known SEC values (Montaudo, Garozzo *et al.* 1995; Montaudo, Montaudo *et al.* 1995a). A number of suggestions have been made to explain these discrepancies including the mass spectrometer detector design, laser power and analyser performance (Scrivens and Jackson 2000). Hyphenation of SEC and MALDI-MS can overcome these limitations and has been demonstrated as a powerful tool for polymer characterisation (Nielen 1998).

MALDI-ToF has been used to characterise a number of copolymer systems (Malik, Trathnigg *et al.* 2009; Montaudo 2002; Van Rooij, Duursma *et al.* 1998). The analysis of copolymers is considerably more challenging than that of homopolymers. This is because, in addition to the molecular weight and end group information, copolymers can exhibit a different topological distribution. MALDI-ToF can be

used to determine the topology (either block, alternating or random) of a copolymer (Montaudo 2002). The mass spectra of copolymers can be complex and oligomeric information can be lost if ion peaks overlap. The composition of a copolymer can be determined from the *m/z* peak intensities provided that significant ion fragmentation has not taken place (Montaudo, Samperi *et al.* 2006; Montaudo 2002). Novel complex copolymer systems often require a combination of liquid chromatography separation methods and other spectroscopic techniques for complete structural analysis to be possible (Weidner and Trimpin 2008).

6.8.3.2 Electrospray ionisation (ESI)

Multiply charged species can be formed by means of ESI. The main advantage of ESI is that for instruments of limited *m/z* range the multiple charges allow one to observe ions of a higher mass at lower *m/z* values. This permits mass spectrometer systems which have limited *m/z* range analysers to characterise the polymer of interest. Separation techniques such as liquid chromatography (LC) and GPC can also be coupled to ESI. This extra dimension of separation, prior to MS analysis, can aid identification and interpretation of the data. The ESI mass spectra of synthetic polymers can be complex because of the numerous multiply charged species that are present. The interpretation of the spectra can be aided if the experiments are performed in high resolution instrumentation such as FT-ICR-MS or Orbitrap. An advantage of using FT-ICR-MS to characterise synthetic polymers is its high mass accuracy and high mass resolving power. FT-ICR-MS experiments performed in high resolution mode can provide resolutions $>10^6$ and a mass accuracy of < 1 ppm (Alber, Marshall *et al.* 1993). The high resolution enables ion peaks to be unambiguously assigned and the isotope peaks of oligomers can be distinguished in polymer systems up to 23,000 Da (O'Connor and McLafferty 2002). FT-ICR-MS is, however, usually coupled with MALDI for the analysis of synthetic polymers rather than with ESI (Buback, Frauendorf *et al.* 2007; Dey, Castoro *et al.* 2002; Easterling, Amster *et al.* 1999; Mize, Simonsick *et al.* 2003; Robinson, Garcia *et al.* 2006; Van der Hage, Duursma *et al.* 1997; Van Rooij, Duursma *et al.* 1998; van Rooij, Duursma *et al.* 1996). This is because, like MALDI, FT-ICR-MS has a limited *m/z* dynamic range and can typically characterise low polydisperse synthetic polymer systems only.

An alternative and more popular approach, to analyse synthetic polymers, is to couple ESI with an orthogonal ToF (oa-ToF) analyser (Weidner and Trimpin 2008). ESI is a soft ionisation technique and as a consequence, little or no fragmentation of the analyte molecules occurs. It is considered a softer ionisation technique than MALDI which is important for the characterisation of labile polymer systems. The advantage of coupling ESI to a Q-ToF analyser is that tandem MS experiments can be performed. These experiments enable end group and sequence information to be determined. The added advantage of ESI is that the orientation and end-group sequence can be determined from the tandem MS data. This is in contrast to MALDI data which can only suggest what the overall mass of the end-groups are.

Until recently, the majority of polymer mass spectrometry research focused on measuring the molecular weight distributions of a polymer of interest (Bahr, Deppe *et al.* 1992; Dey, Castoro *et al.* 2002; Montaudo, Montaudo *et al.* 1995b; Montaudo, Montaudo *et al.* 1997), identifying its end groups (Buback, Frauendorf *et al.* 2007; Jackson, Green *et al.* 2006; Jackson, Scrivens *et al.* 2000a; Jackson, Slade *et al.* 2004; Jackson, Yates *et al.* 1996), determining the sequence and composition of copolymers, and confirming the monomer structure in homopolymer systems (Nuwaysir, Wilkins *et al.*; Van Rooij, Duursma *et al.* 1998; Wilczek-Vera, Yu *et al.* 1999). These studies have provided information on the primary and secondary structure of the polymer, but they do not help one to deduce the tertiary structure or conformation. New methods such as tandem mass spectrometry and IM-MS can provide information on the fragmentation patterns of the polymer and the gas phase conformation respectively.

6.8.3.3 Tandem Mass Spectrometry

Most MS/MS experiments use collision-induced dissociation (CID) to induce fragmentation of the selected precursor ion (Crecelius, Baumgaertel *et al.* 2009). A different technique, namely electron capture dissociation (ECD), can also be used to achieve the fragmentation of peptides and certain types of polymers (Cerda, Horn *et al.* 1999; Syka, Coon *et al.* 2004). The production of fragment ions by means of ECD is, however, limited to FT-ICR-MS instruments. An MS/MS experiment

which makes use of metastable ion decay, called post-source decay (PSD), can be performed in MALDI-ToF instruments. This technique suffers from low selectively of the precursor ion and a lack of control of the ion activation conditions, which has prevented its widespread use in the polymer field

Pioneering tandem mass spectrometry work was first published by Craig and Derrick as a tool to analyse the microstructure of polystyrene systems (Craig and Derrick 1986). Tandem mass spectrometry experiments were originally shown by Lattimer and coworkers to be a viable method for characterising polyethers such as PEG and PPG (Lattimer 1992a; Lattimer 1992b; Lattimer 1994; Lattimer, Munster *et al.* 1989). In MS/MS experiments a specific precursor ion is mass selected, fragmented and the resulting product ions are detected to create the product ion MS/MS mass spectrum. ESI-MS/MS and MALDI-MS/MS experiments of various polymer systems have shown that valuable structural information can be gained from the fragmentation patterns observed (Jackson, Bunn *et al.* 2000; Jackson, Jennings *et al.* 1997; Jackson, Scrivens *et al.* 2000a; Jackson, Scrivens *et al.* 2000b; Jackson, Slade *et al.* 2004; Lattimer 1992a; Lattimer 1992b; Lattimer 1994; Lattimer, Munster *et al.* 1989; Polce, Ocampo *et al.* 2008a; Polce, Ocampo *et al.* 2008b). The *m/z* values in the fragment ion series produced by MS/MS experiments often enable one to identify the initiating and terminating end groups. In some polymer systems the mass of the end group can be a significant proportion of the overall molecular weight of the polymer system, especially in low molecular weight polymers. End-group analysis by means of CID has the added benefit that the orientation of the polymer can be detected; this is in contrast to high resolution mass spectrometry data. Characterisation of the end groups is therefore very important, as changes to the end group functionality could lead to significant changes in the properties of the polymer.

6.8.3.4 Fragmentation pathways

The fragmentation series produced by MS/MS experiments can enable one to determine both the sum of and the individual masses of the initiating and terminating end groups. This allows both end groups to be identified. In general, the MS/MS

spectrum of a polymer contains a series of fragment ion peaks which have either experienced the loss of repeat units containing the initiating end group (α) or have sequentially lost repeat units that contain the terminating end group (ω).

It has been demonstrated that lithiated precursor ions can generate more structural information, from the tandem mass spectra of polyethers, than other alkali metal cations (Chen and Li 2001; Lattimer 1992a; Lattimer 1994; Selby, Wesdemiotis *et al.* 1994; Williams, Hilton *et al.* 2007). Polyethers ionised by other alkali metals, such as potassium and cesium, can lead to the formation of bare cations as the dominant fragment ions. MS/MS spectra with these bare cations enable little (if any) structural information to be derived. The majority of polyether fragmentation studies have therefore used lithium ions to ionise the polymer (Chen and Li 2001; Chen, Yu *et al.* 2002; Jackson, Slade *et al.* 2008; Lattimer 1992a; Lattimer 1994; Lattimer, Munster *et al.* 1989). Figure 6.3 shows the proposed annotated fragmentation pathways for polyethers. Polyether MS/MS mass spectra are dominated by ions, which have retained the cation, from the A_x, B_x and C_x series (where x represents the partial or whole number of monomer units in the product ions). The A series describes product ions that contain newly-generated alcohol end groups, the B series contain vinyl end functionalities and the C series contains an aldehyde end group (Jackson, Green *et al.* 2006; Lattimer 1992a; Lattimer 1994). The apostrophes present in the annotation scheme in Figure 6.3 denote fragment ions that contain either the initiating end group (R') or the terminating end group (R"). Apostrophes are not used when the initiating and terminating end functionalities are the same e.g. di-hydroxyl end-capped PEG. A further series of ions have been proposed for esterified polyethers (Jackson, Green *et al.* 2006). This new series of ions A^a_x, B^a_x and C^a_x describes the loss of an acid from the remaining original end group of the A_x, B_x and C_x ion series respectively (where the superscript "a" denotes the loss of an acid). It has been shown that low-energy CID fragment ions of PPG diesters are

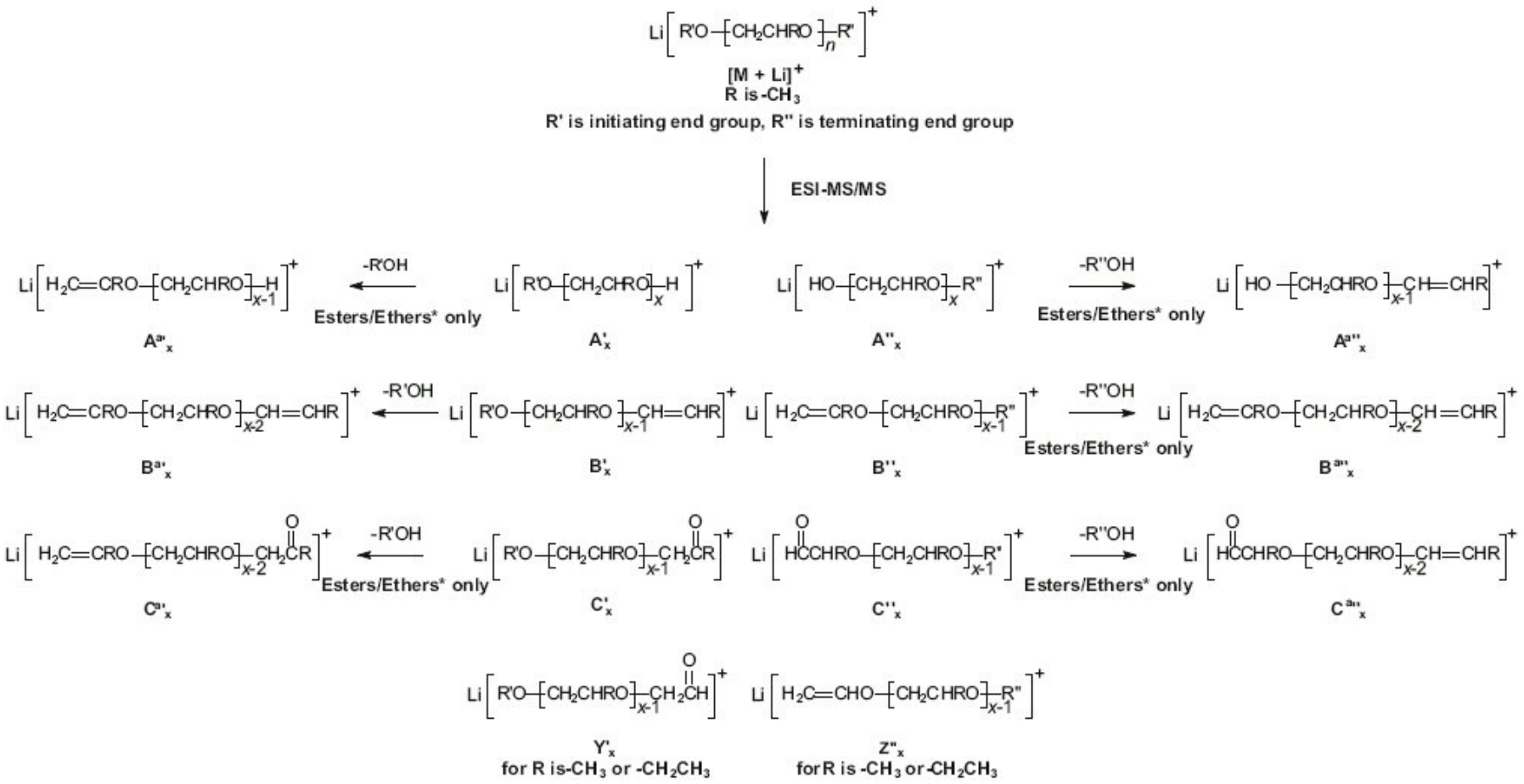

Figure 6.3: Proposed annotated fragmentation pathway for polyethers. Taken from (Jackson, Green *et al.* 2006)

analogous to high-energy CID ions of PEG diesters and that the presence of these ions are diagnostic for polyether diesters (Jackson, Slade *et al.* 2008). Additional fragment ions observed in the CID mass spectrum of 1,2-epoxide derived polyethers can be associated with the creation of the Y and Z ion series. The Y_x series is similar to the C_x ion series and the Z_x series shows similarities to the B_x ion series. The exception to this observation is that the two new ion series account for the loss of a side chain functionality from the polyether backbone. It has been proposed that the presence of the Y_x and Z_x ion series can help to differentiate between structurally similar polyethers such as poly(butylene glycol) and poly(tetramethylene glycol) (Jackson, Green *et al.* 2006). Jackson *et al,* postulated that when observing the A_x, B_x and C_x series, fragments at the higher *m/z* are the most structurally informative for the generation of end group information (Jackson, Green *et al.* 2006).

The ion series nomenclature for polymethacrylates is similar to that for polyethers. In polymethacrylates and acrylics the A series describes fragment ions which retain the cation and the terminating end group, whereas the B series retain the cation and the initiating functionality (see Figure 6.4) (Jackson, Slade *et al.* 2004). These fragment ion series tend to be the dominant fragment ion peaks in the MS/MS spectrum. There are two proposed mechanisms for the formation of the A and B ion series. The first is believed to be charged induced, with cleavage of the polymer backbone preferentially being induced in close proximity to the cation (Gidden, Jackson *et al.* 1999). This mechanism accounts for the low molecular weight fragment ions observed in polyacrylate MS/MS mass spectra (Gidden, Jackson *et al.* 1999; Jackson, Slade *et al.* 2004). The less abundant fragment ions observed in the MS/MS spectra belong to the C, D, E and F ion series (see Figure 6.4). These series of fragment ions arise from fragments that contain an intact functionality group from either the initiating- (C and F series) or terminating- (D and E series) end group. It has been demonstrated that ions from the C-F series can be used to differentiate between random and block copolymers (Jackson, Scrivens *et al.* 2000b). The second mechanism is random homolytic cleavage of the polymer backbone followed by depolymerisation. This mechanism has recently

been used to describe the fragmentation pathways of polystyrene systems (Polce, Ocampo *et al.* 2007a; Polce, Ocampo *et al.* 2007b).

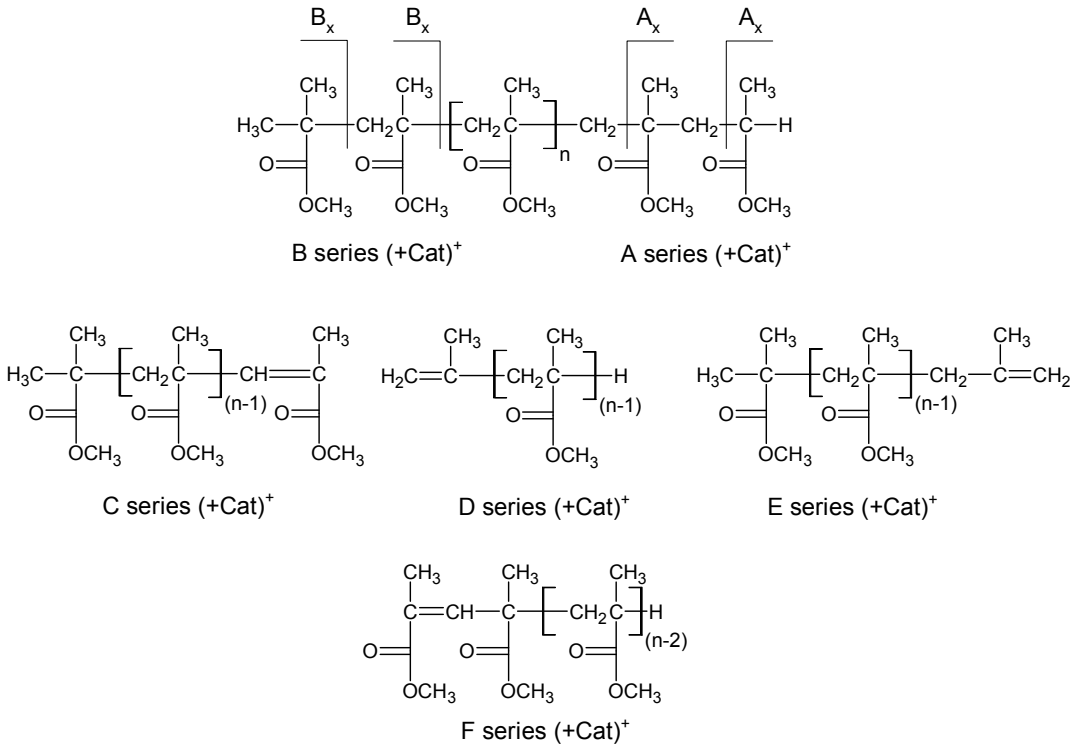

Figure 6.4: Proposed fragmentation scheme and structures for the A-E series of PMMA. Adapted from (Jackson, Slade *et al.* 2004)

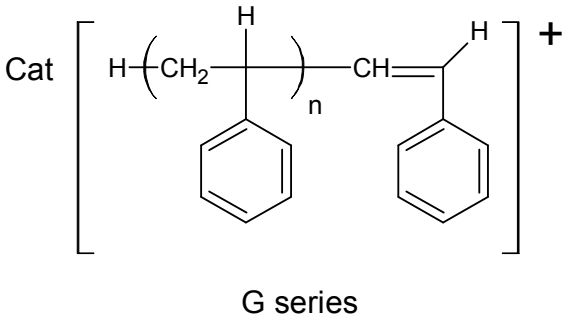

Figure 6.5: Proposed structure for ions from the G series observed for polystyrenes. (Jackson, Yates *et al.* 1998)

Another polymer that has been extensively studied by means of MS/MS is polystyrene (Jackson, Bunn *et al.* 2000; Jackson, Yates *et al.* 1998; Scrivens, Jackson *et al.* 1997). It was demonstrated that polystyrenes with a variety of different end-group functionalities could be differentiated by the intense series of peaks in the low *m/z* range (Jackson, Bunn *et al.* 2000; Polce, Ocampo *et al.* 2007a; Polce, Ocampo *et al.* 2007b). The styrene notation is similar to that used in describing the spectra of polyacrylates. The A_x and B_x polystyrene series are analogous to those noted for methacrylate polymers (see Figure 6.4). These two series dominate the mass spectrum and have been proposed to be the most useful for the identification of polystyrene end groups. The G series contains other fragment ions that are also intense in the mass spectrum from polystyrene (see Figure 6.5). These fragment ions retain the cation and are formed by rearrangement reactions rather than direct backbone cleavages. This internal fragment series is thought to be formed by a two hydrogen rearrangement reaction which is analogous to the that observed for poly(alkyl methacrylates) (Jackson, Bunn *et al.* 2000; Jackson, Yates *et al.* 1997b). The remaining series of ion fragment peaks (C, D, E and F) are proposed to be generated by means of a 1,5-hydrogen rearrangement. These reactions involve cleavage of the polymer backbone, loss of a benzene group and formation of neutrals with unsaturated end groups, and fragment ions. These ions are equivalent to the polyacrylate ion series in Figure 6.4. Recently a new mechanistic rationale has been proposed to describe the formation of CID polystyrene fragments (Polce, Ocampo *et al.* 2007b). The mechanistic rationale described above does not account for the origin of abundant internal fragments. Polce *et al,* describe a free radical chemistry mechanism that accounts for the appearance of the previously characterised, and some uncharacterised, fragment ions commonly observed in the polystyrene product ion MS/MS mass spectrum. This mechanism is referred to as random homolytic cleavage followed by depolymerisation. They propose all MS/MS polystyrene fragments, that have silver as the cation, are formed by random, charge-remote homolytic cleavages along the polymer chain, followed by typical radical site reactions (Polce, Ocampo *et al.* 2007b). The radical reactions involve a β C-C bond scission and hydrogen atom rearrangements (also known as backbiting). In the backbiting mechanism, a terminal radical can abstract a hydrogen atom from an interior position of the chain to create a

more stable radical (see Figure 6.6). Polce and co-workers believe the two mechanistic pathways, β scission and backbiting, are in competition with one another and the preferred mechanism is dependent on the chain end groups. For example it has been demonstrated that fragmentation of poly(α-methyl styrene) occurs via the β scission mechanism only. This is because hydrogen rearrangement of the benzylic hydrogen atoms cannot occur (Polce, Ocampo *et al.* 2007a). .

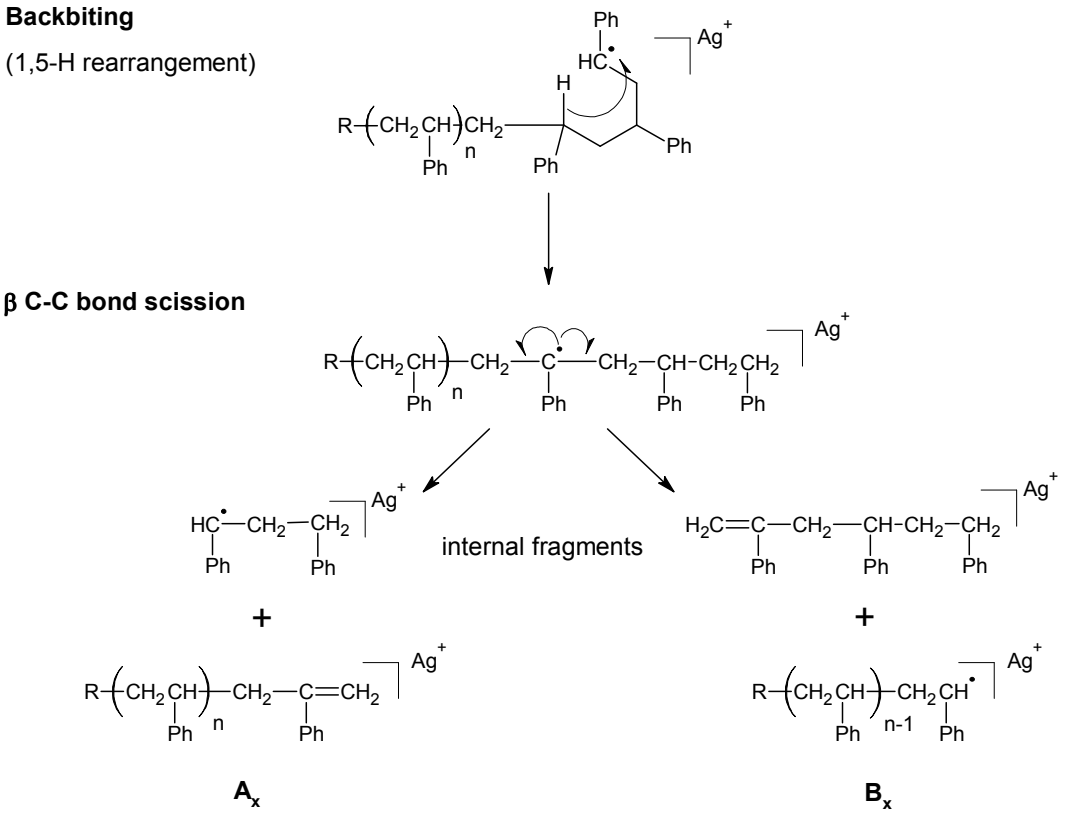

Figure 6.6: Proposed polystyrene fragmentation scheme. Adapted from (Polce, Ocampo *et al.* 2007a)

In comparison to peptides, relatively few polymer fragmentation pathways have been characterised. Possible reasons for this observation are that polymers can either undergo re-arrangement(s) after dissociation or a complex range of covalent bonds are present in the polymer system backbone. These rearrangement reactions can produce additional fragment ions or a new ion series which can make elucidation of the mass spectrum even more complicated. Tandem experiments performed by means of MALDI-MS have the added analytical challenge that the singly charged fragment ions, preferentially produced in MALDI, can be of low intensity and can lack the information-rich backbone cleavages. The majority of research has focussed on polyether, polyacrylate or polystyrene systems (as described above).

6.8.3.5 Software development

Software and databases are an inherent tool for the identification of peptides and proteins from tandem MS data (Craig and Beavis 2003; Eng, McCormack *et al.* 1994; Geer, Markey *et al.* 2004; Ma, Zhang *et al.* 2003; Perkins, Pappin *et al.* 1999; Zhang, Aebersold *et al.* 2002). Until recently, there was no development in computational programs which could aid the interpretation of MS/MS data from synthetic polymers. Thalassinos *et al,* describe the development and application of a software program that can annotate MS/MS data of synthetic polymers (Thalassinos, Jackson *et al.* 2007). This software aids the interpretation of MS/MS spectra from polymers with known fragmentation pathways (such as those described above) and can significantly reduce the spectral interpretation time. Exact mass MS/MS data were assigned by means of the Polymerator software to validate the suggested structures and to give further confidence in the interpretation of end-group structures (Thalassinos, Jackson *et al.* 2007). Figure 6.7 shows a screenshot from the Polymerator software of an annotated ESI-MS/MS spectrum. The software requires centroid MS/MS data to be imported as a text file. Knowledge of parameters such as the initiating end group, terminating end group and repeat unit empirical formulae, number of repeat units and the cation are required in order for the software to annotate the spectrum.

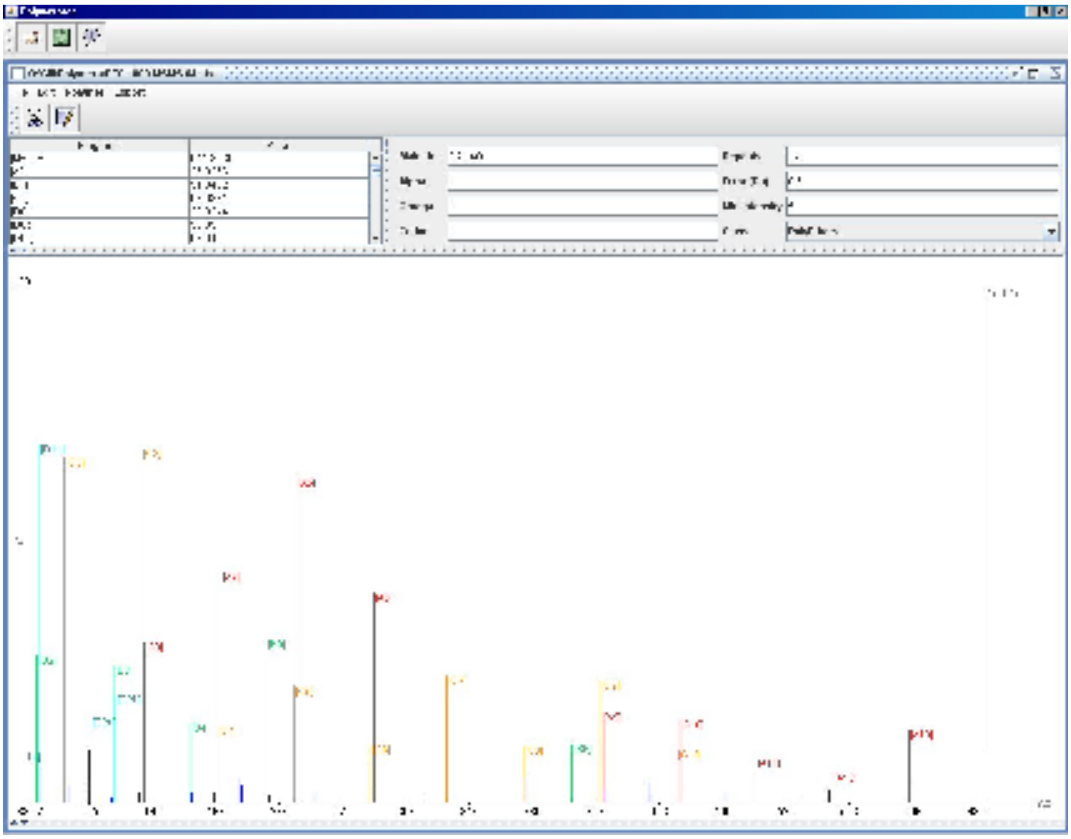

Figure 6.7: Screenshot from the Polymerator software of an annotated ESI-MS/MS spectrum from the lithiated 14mer of dihydroxyl end capped poly(ethylene glycol). Predicted fragment ions are detailed above (left) the spectrum.

Williams *et al* also implemented this software to aid the interpretation/annotation of desorption electrospray ionisation (DESI) Q-ToF MS/MS data (Williams, Hilton *et al.* 2007). Mass spectrometric sampling of DESI-generated ions is rapid and requires a minimal amount of sample preparation. These properties coupled with the automated interpretation software allowed experiments and data analysis to be performed within minutes.

6.8.3.6 Gas-phase conformations

It is believed that the structure of a synthetic polymer can be related to its performance. Structural changes can affect the physical and mechanical properties, thermal degradation and impact resistance of a polymeric material (Mark, Ngai *et al.* 2004). The development of IM-MS has enabled the gas-phase conformation of synthetic polymers to be investigated. IM-MS and molecular mechanics/dynamics have been used to probe the tertiary structure and gas-phase conformation of various polymer systems (Gidden, Bowers *et al.* 2002; Gidden, Jackson *et al.* 1999; Gidden, Wyttenbach *et al.* 1999; Gidden, Wyttenbach *et al.* 2000; von Helden, Wyttenbach *et al.* 1995a). Initial studies characterised PEG coordination to the alkali cation sodium. von Helden and co-workers demonstrated that singly charged PEG oligomers could adopt a compact structure (von Helden, Wyttenbach *et al.* 1995a; von Helden, Wyttenbach *et al.* 1995b). This was because of the preferred crown ether coordination geometry to the cation. It was observed that seven oxygen atoms in the nonamer structure could coordinate to one Na^+ ion; five oxygen atoms coordinate in the same plane, one coordinates above the Na^+ ion and the other coordinates below the Na^+ ion (von Helden, Wyttenbach *et al.* 1995a). This binding mechanism completely encases the cation. Further investigations showed that the cross-section of PEG increased linearly with oligomer size; a common observation for structurally related ions (Gidden, Wyttenbach *et al.* 2000; von Helden, Wyttenbach *et al.* 1995b). Two different polyethers, PPG and poly(tetramethylene glycol) PTMEG, were used to study the effect of repeat unit composition, flexibility and chain length on the gas-phase conformation. It was observed that all sodiated polyethers had similar structural features with each polymer coordinating to the cation via its oxygen atoms. The differences in repeat unit length and flexibility did, however, create structural changes between each polyether (see Figure 6.8). It was observed that the conformation of the polymer became more flexible as the temperature was increased. This observation was rationalised by molecular dynamic stimulations which showed that certain sections of the oligomer, that were not coordinated to the Na^+ ion, could unravel (Gidden, Wyttenbach *et al.* 2000).

The gas phase conformation of other polymer classes has been studied and found to differ from the polyethers (Gidden, Bowers *et al.* 2002; Gidden, Jackson *et al.* 1999). Oxygen atoms within PMMA can coordinate to the cation to form a horse-shoe geometry. Temperature dependence studies for PMMA showed a minimal increase in the cross-section of the oligomers. This suggests that the cation can act as an anchor to limit the thermal motion of the coordinating oligomers. Poly(styrene) conformational studies showed that the gas phase conformation is not dependent on the metal cation used. Theoretical modelling of PS predicted the conformation to be quasi-linear in structure with the metal cation sandwiched between two central phenyl groups (see Figure 6.9c). The collisional cross-sections of the theoretical model was in good agreement with experimental data (Gidden, Bowers *et al.* 2002). Figure 6.9 shows a comparison of the coordination geometry to the Na^+ cation and suggests that all three polymer classes studied (polyethers, polyacrylates and polystyrenes) have significantly different binding modes and coordination geometries. These differences in gas-phase conformation could enable IM-MS to characterise different polymer systems by their rotationally-averaged cross-section as well as their *m/z* ratio.

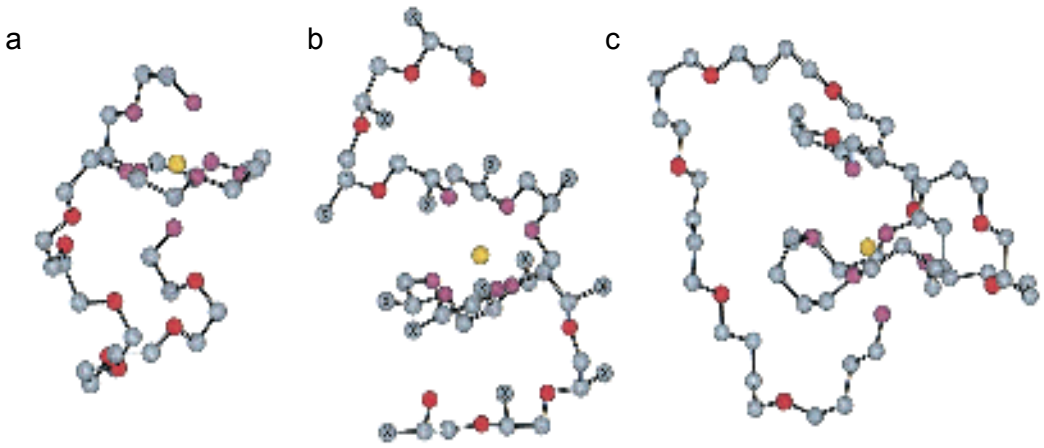

Figure 6.8: Lowest energy molecular model structures for (a) ($[PEG14 + Na]^+$) (b) ($[PPG14 + Na]^+$) and (c) ($[PTMEG14 + Na]^+$). Carbon atoms are shown in grey, oxygen atoms red and sodium yellow. The methyl group carbons in PPG are represented by X. Taken from (Gidden, Wyttenbach *et al.* 2000).

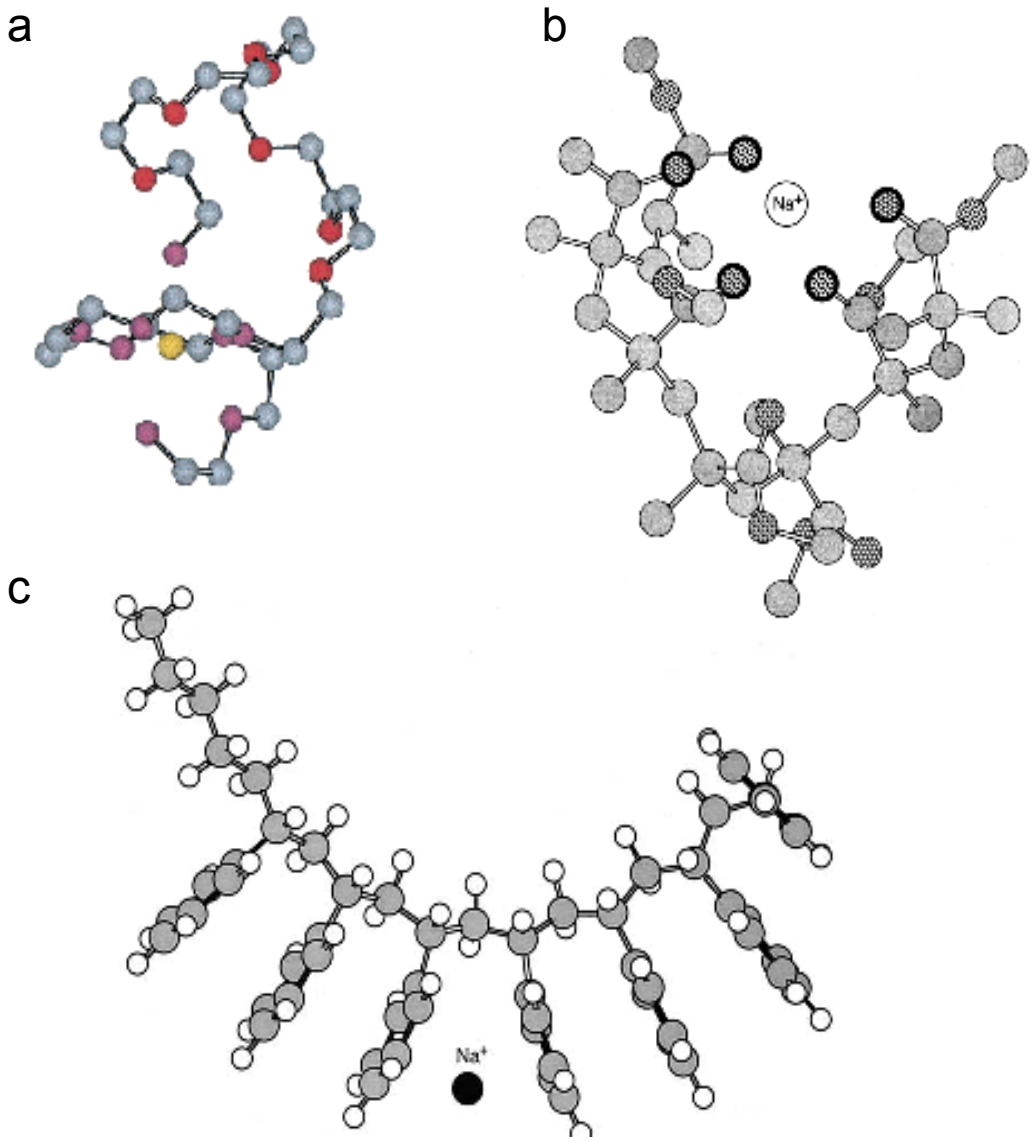

Figure 6.9: Lowest energy molecular model structures of cation coordination to synthetic polymers. (All hydrogen atoms have been omitted for clarity). (a) PEG, carbon atoms are shown in grey, oxygen red, sodium yellow (Gidden, Wyttenbach *et al.* 2000). (b) PMMA, carbon atoms are shown in grey, oxygen atoms are shown with dots, sodium labelled (Gidden, Jackson *et al.* 1999). (c) PS, carbon atoms are shown in grey, hydrogen atoms are white, sodium cation is black (Gidden, Bowers *et al.* 2002).

6.4 Aims

The aim of this work is to develop and improve methods for structural characterisation of oligomeric and monomeric mixtures. In particular, IM-MS and IM-MS/MS have been used as a rapid, information rich method of obtaining detailed structural information.

6.5 References

Alber, G. M., Marshall, A. G., Hill, N. C., Schweikhard, L. and Ricca, T. L. (1993). Ultrahigh-Resolution Fourier-Transform Ion-Cyclotron Resonance Mass-Spectrometer. *Review of Scientific Instruments* **64**, 1845-1852.

Bahr, U., Deppe, A., Karas, M. and Hillenkamp, F. (1992). Mass Spectrometry of Synthetic Polymers by UV-Matrix-Assisted Laser Desorption/Ionization. *Analytical Chemistry* **64**, 2866.

Briggs, D., Brewis, D. M. and Konieczo, M. B. (1976). X-Ray Photoelectron-Spectroscopy Studies of Polymer Surfaces .1. Chromic Acid Etching of Polyolefins. *Journal of Materials Science* **11**, 1270-1277.

Buback, M., Frauendorf, H., Günzler, F. and Vana, P. (2007). Electrospray ionization mass spectrometric end-group analysis of PMMA produced by radical polymerization using diacyl peroxide initiators. *Polymer* **48**, 5590-5598.

Cerda, B. A., Horn, D. M., Breuker, K., Carpenter, B. K. and McLafferty, F. W. (1999). Electron capture dissociation of multiply-charged oxygenated cations. A nonergodic process. *European Journal of Mass Spectrometry* **5**, 335-338.

Chen, R. and Li, L. (2001). Lithium and transition metal ions enable low energy collision-induced dissociation of polyglycols in electrospray ionization mass spectrometry. *Journal of the American Society for Mass Spectrometry* **12**, 832-839.

Chen, R., Yu, X. L. and Li, L. (2002). Characterization of poly(ethylene glycol) esters using low energy collision-induced dissociation in electrospray ionization mass spectrometry. *Journal of the American Society for Mass Spectrometry* **13**, 888-897.

Choi, D.-S., Chong, Y. S., Whitehead, D. and Shimizu, K. D. (2001). Molecules with Shape Memory Based on Restricted Rotation. *Organic Letters* **3**, 3757-3760.

Craig, A. G. and Derrick, P. J. (1986). Production and Characterization of Beams of Polystyrene Ions. *Australian Journal of Chemistry* **39**, 1421-1434.

Craig, R. and Beavis, R. C. (2003). A method for reducing the time required to match protein sequences with tandem mass spectra. *Rapid Communications in Mass Spectrometry* **17**, 2310-2316.

Crecelius, A. C., Baumgaertel, A. and Schubert, U. S. (2009). Tandem mass spectrometry of synthetic polymers. *Journal of Mass Spectrometry* **44**, 1277-1286.

Deery, M. J., Jennings, K. R., Jasieczek, C. B., Haddleton, D. M., Jackson, A. T., Yates, H. T. and Scrivens, J. H. (1997). A Study of Cation Attachment to Polystyrene by Means of Matrix-assisted Laser Desorption/Ionization and Electrospray Ionization-Mass Spectrometry. *Rapid Communications in Mass Spectrometry* **11**, 57-62.

Dey, M., Castoro, J. A. and Wilkins, C. L. (2002). Determination of Molecular Weight Distributions of Polymers by MALDI-FTMS. *Analytical Chemistry* **67**, 1575-1579.

Dogruel, D., Nelson, R. W. and Williams, P. (1996). The Effects of Matrix pH and Cation Availability on the Matrix-assisted Laser Desorption/Ionization Mass Spectrometry of Poly(methyl methacrylate). *Rapid Communications in Mass Spectrometry* **10**, 801-804.

Easterling, M. L., Amster, I. J., van Rooij, G. J. and Heeren, R. M. A. (1999). Isotope beating effects in the analysis of polymer distributions by Fourier transform mass spectrometry. *Journal of the American Society for Mass Spectrometry* **10**, 1074-1082.

Eng, J. K., McCormack, A. L. and Yates Iii, J. R. (1994). An approach to correlate tandem mass spectral data of peptides with amino acid sequences in a protein database. *Journal of the American Society for Mass Spectrometry* **5**, 976-989.

Geer, L. Y., Markey, S. P., Kowalak, J. A., Wagner, L., Xu, M., Maynard, D. M., Yang, X., Shi, W. and Bryant, S. H. (2004). Open Mass Spectrometry Search Algorithm. *Journal of Proteome Research* **3**, 958-964.

Gidden, J., Bowers, M. T., Jackson, A. T. and Scrivens, J. H. (2002). Gas-phase conformations of cationized poly(styrene) oligomers. *Journal of the American Society for Mass Spectrometry* **13**, 499-505.

Gidden, J., Jackson, A. T., Scrivens, J. H. and Bowers, M. T. (1999). Gas phase conformations of synthetic polymers: poly (methyl methacrylate) oligomers cationized by sodium ions. *International Journal of Mass Spectrometry* **188**, 121-130.

Gidden, J., Wyttenbach, T., Batka, J. J., Weis, P., Bowers, M. T., Jackson, A. T. and Scrivens, J. H. (1999). Poly (ethylene terephthalate) oligomers cationized by

alkali ions: structures, energetics, and their effect on mass spectra and the matrix-assisted laser desorption/ionization process. *Journal of the American Society for Mass Spectrometry* **10**, 883-895.

Gidden, J., Wyttenbach, T., Jackson, A. T., Scrivens, J. H. and Bowers, M. T. (2000). Gas-Phase Conformations of Synthetic Polymers: Poly(ethylene glycol), Poly(propylene glycol), and Poly(tetramethylene glycol). *Journal of the American Chemical Society* **122**, 4692-4699.

Gnanou, Y. and Fontanille, M. (2008). Organic and Physical Chemistry of Polymers. *Wiley*.

Harton, S. E., Stevie, F. A., Griffis, D. P. and Ade, H. (2006). SIMS depth profiling of deuterium labeled polymers in polymer multilayers. *Applied Surface Science* **252**, 7224-7227.

Hatada, K., Ute, K., Kitayama, T., Nishimura, T., Kashiyama, M. and Fujimoto, N. (1990). Studies on the Molecular-Weight Dependence of Tacticity of Anionically Prepared Pmmas by Online GPC/NMR. *Polymer Bulletin* **23**, 549-554.

Hatada, K., Ute, K., Kitayama, T., Yamamoto, M., Nishimura, T. and Kashiyama, M. (1989). Online Gpc Nmr Analyses of Block and Random Copolymers of Methyl and Butyl Methacrylates Prepared with Tert-C4h9mgbr. *Polymer Bulletin* **21**, 489-495.

Hatada, K., Ute, K., Okamoto, Y., Imanari, M. and Fujii, N. (1988). Online Gpc/Nmr Experiments Using the Isotactic Poly(Methyl Methacrylate) with Well-Defined Chemical-Structure. *Polymer Bulletin* **20**, 317-321.

Hiller, W., Pasch, H., Macko, T., Hofmann, M., Ganz, J., Spraul, M., Braumann, U., Streck, R., Mason, J. and Van Damme, F. (2006). On-line coupling of high temperature GPC and 1H NMR for the analysis of polymers. *Journal of Magnetic Resonance* **183**, 290-302.

Jackson, A. T., Bunn, A., Hutchings, L. R., Kiff, F. T., Richards, R. W., Williams, J., Green, M. R. and Bateman, R. H. (2000). The generation of end group information from poly(styrene)s by means of matrix-assisted laser desorption/ionisation-collision induced dissociation. *Polymer* **41**, 7437-7450.

Jackson, A. T., Green, M. R. and Bateman, R. H. (2006). Generation of end-group information from polyethers by matrix-assisted laser desorption/ionisation collision-induced dissociation mass spectrometry. *Rapid Communications in Mass Spectrometry* **20**, 3542-3550.

Jackson, A. T., Jennings, K. R. and Scrivens, J. H. (1997). Generation of Average Mass Values and End Group Information of Polymers by Means of a Combination of Matrix-Assisted Laser Desorption/Ionization-Mass Spectrometry and Liquid Secondary Ion-Tandem Mass Spectrometry. *Journal- American Society for Mass Spectrometry* **8**, 76-85.

Jackson, A. T., Scrivens, J. H., Simonsick, W. J., Green, M. R. and Bateman, R. H. (2000a). Generation of structural information from polymers and copolymers using tandem mass spectrometry. *Abstracts of Papers of the American Chemical Society* **219**, U363-U363.

Jackson, A. T., Scrivens, J. H., Simonsick, W. J., Green, M. R. and Bateman, R. H. (2000b). Generation of structural information from polymers and copolymers using tandem mass spectrometry. *Abstracts of Papers of the American Chemical Society* **219**, 50-POLY.

Jackson, A. T., Slade, S. E. and Scrivens, J. H. (2004). Characterisation of poly(alkyl methacrylate)s by means of electrospray ionisation-tandem mass spectrometry (ESI-MS/MS). *International Journal of Mass Spectrometry* **238**, 265-277.

Jackson, A. T., Slade, S. E., Thalassinos, K. and Scrivens, J. H. (2008). End-group characterisation of poly(propylene glycol)s by means of electrospray ionisation-tandem mass spectrometry (ESI-MS/MS). *Analytical and Bioanalytical Chemistry* **392**, 643-650.

Jackson, A. T., Yates, H. T., MacDonald, W. A., Scrivens, J. H., Critchley, G., Brown, J., Deery, M. J., Jennings, K. R. and Brookes, C. (1997a). Time-Lag Focusing and Cation Attachment in the Analysis of Synthetic Polymers by Matrix-Assisted Laser Desorption/Ionization-Time-of-Flight-Mass Spectrometry. *Journal-American Society for Mass Spectrometry* **8**, 132-139.

Jackson, A. T., Yates, H. T., Scrivens, J. H., Critchley, G., Brown, J., Green, M. R. and Bateman, R. H. (1996). The application of matrix-assisted laser

desorption/ionization combined with collision-induced dissociation to the analysis of synthetic polymers. *Rapid Communications in Mass Spectrometry* **10**, 1668-1674.

Jackson, A. T., Yates, H. T., Scrivens, J. H., Green, M. R. and Bateman, R. H. (1997b). Utilizing matrix-assisted laser desorption/ionization-collision induced dissociation for the generation of structural information from poly(alkyl methacrylate)s. *Journal of the American Society for Mass Spectrometry* **8**, 1206-1213.

Jackson, A. T., Yates, H. T., Scrivens, J. H., Green, M. R. and Bateman, R. H. (1998). Matrix-assisted laser desorption/ionization-collision induced dissociation of poly(styrene). *Journal of the American Society for Mass Spectrometry* **9**, 269-274.

Kitayama, T., Janco, M., Ute, K., Niimi, R., Hatada, K. and Berek, D. (2000). Analysis of poly(ethyl methacrylate)s by on line hyphenation of liquid chromatography at the critical adsorption point and nuclear magnetic resonance spectroscopy. *Analytical Chemistry* **72**, 1518-1522.

Kitayama, T. and Ute, K. (2006). On-line SEC-NMR. *Springer*.

Koenig, J. L. (2004). The application of molecular spectroscopy to characterisation of polymers. Physical properties of polymers, Cambridge University Press.

Kramer, I., Pasch, H., Handel, H. and Albert, K. (1999). Chemical heterogeneity analysis of high-conversion poly[styrene-co-(ethyl acrylate)]s by NMR and on-line coupled SEC-NMR. *Macromolecular Chemistry and Physics* **200**, 1734-1744.

Langer, R. and Tirrell, D. A. (2004). Designing materials for biology and medicine. *Nature* **428**, 487-92.

Lattimer, R. P. (1992a). Tandem Mass-Spectrometry of Lithium-Attachment Ions from Polyglycols. *Journal of the American Society for Mass Spectrometry* **3**, 225-234.

Lattimer, R. P. (1992b). Tandem Mass-Spectrometry of Poly(Ethylene Glycol) Proton-Attachment and Deuteron-Attachment Ions. *International Journal of Mass Spectrometry and Ion Processes* **116**, 23-36.

Lattimer, R. P. (1994). Tandem Mass-Spectrometry of Poly(Ethylene Glycol) Lithium-Attachment Ions. *Journal of the American Society for Mass Spectrometry* **5**, 1072-1080.

Lattimer, R. P., Munster, H. and Budzikiewicz, H. (1989). Tandem mass spectrometry of polyglycols. *International Journal of Mass Spectrometry and Ion Processes* **90**, 119-129.

Ma, B., Zhang, K., Hendrie, C., Liang, C., Li, M., Doherty-Kirby, A. and Lajoie, G. (2003). PEAKS: powerful software for peptide de novo sequencing by tandem mass spectrometry. *Rapid Communications in Mass Spectrometry* **17**, 2337-2342.

Malik, M. I., Trathnigg, B. and Saf, R. (2009). Characterization of ethylene oxide-propylene oxide block copolymers by combination of different chromatographic techniques and matrix-assisted laser desorption ionization time-of-flight mass spectroscopy. *Journal of Chromatography A* **1216**, 6627-6635.

Mark, J., Ngai, K., Graessley, W., Mandelkern, L., Samulski, E., Koenig, J. L. and Wignall, G. (2004). Physical Properties of Polymers. *Cambridge University Press*.

Martin, K., Spickermann, J., Räder, H. J. and Müllen, K. (1996). Why Does Matrix-assisted Laser Desorption/Ionization Time-of-flight Mass Spectrometry Give Incorrect Results for Broad Polymer Distributions? *Rapid Communications in Mass Spectrometry* **10**, 1471-1474.

Mize, T. H., Simonsick, W. J. and Amster, I. J. (2003). Characterization of polyesters by matrix-assisted laser desorption/ionization and Fourier transform mass spectrometry. *European Journal of Mass Spectrometry* **9**, 473-486.

Montaudo, G., Garozzo, D., Montaudo, M. S., Puglisi, C. and Samperi, F. (1995). Molecular and Structural Characterization of Polydisperse Polymers and Copolymers by Combining Maldi-Tof Mass-Spectrometry with GPC Fractionation. *Macromolecules* **28**, 7983-7989.

Montaudo, G. and Lattimer, R. P. (2002). Mass Spectrometry of Polymers. *CRC Press*.

Montaudo, G., Montaudo, M. S., Puglisi, C. and F., S. (1995a). Characterization of polymers by matrix-assisted laser desorption/ionization time-of-flight mass spectrometry: Molecular weight estimates in samples of varying polydispersity. *Rapid Communications in Mass Spectrometry* **9**, 453-460.

Montaudo, G., Montaudo, M. S., Puglisi, C. and Samperi, F. (1995b). Characterization of Polymers by Matrix-Assisted Laser Desorption Ionization-Time

of Flight Mass Spectrometry. End Group Determination and Molecular Weight Estimates in Poly(ethylene glycols). *Macromolecules* **28**, 4562.

Montaudo, G., Montaudo, M. S., Puglisi, C. and Samperi, F. (1997). Molecular weight determination and structural analysis in polydisperse polymers by hyphenated gel permeation chromatography matrix-assisted laser desorption ionization - Time of flight mass spectrometry. *International Journal of Polymer Analysis and Characterization* **3**, 177-192.

Montaudo, G., Samperi, F. and Montaudo, M. S. (2006). Characterization of synthetic polymers by MALDI-MS. *Progress in Polymer Science* **31**, 277-357.

Montaudo, M. S. (2002). Mass spectra of copolymers. *Mass Spectrometry Reviews* **21**, 108-144.

Nicholson, J. W. (2006). The Chemistry of Polymers. *RSC publishing*.

Nielen, M. W. F. (1998). Polymer Analysis by Micro-Scale Size-Exclusion Chromatography/MALDI Time-of-Flight Mass Spectrometry with a Robotic Interface. *Analytical Chemistry* **70**, 1563-1568.

Nuwaysir, L. M., Wilkins, C. L. and Simonsick Jr, W. J. Analysis of copolymers by laser desorption fourier transform mass spectrometry. *Journal of the American Society for Mass Spectrometry* **1**, 66-71.

O'Connor, P. B. and McLafferty, F. W. (2002). Oligomer Characterization of 4-23 kDa Polymers by Electrospray Fourier Transform Mass Spectrometry. *Journal of the American Chemical Society* **117**, 12826-12831.

Peacock, P. M. and McEwen, C. N. (2006). Mass spectrometry of synthetic polymers. *Analytical Chemistry* **78**, 3957-3964.

Peppas, N. A. and Langer, R. (1994). New challenges in biomaterials. *Science* **263**, 1715-20.

Perkins, D. N., Pappin, D. J. C., Creasy, D. M. and Cottrell, J. S. (1999). Probability-based protein identification by searching sequence databases using mass spectrometry data. *Electrophoresis* **20**, 3551-3567.

Polce, M. J., Ocampo, M., Quirk, R. P., Leigh, A. M. and Wesdemiotis, C. (2007a). Tandem Mass Spectrometry Characteristics of Silver-Cationized Polystyrenes:

Internal Energy, Size, and Chain End versus Backbone Substituent Effects. *Analytical Chemistry* **80**, 355-362.

Polce, M. J., Ocampo, M., Quirk, R. P., Leigh, A. M. and Wesdemiotis, C. (2008a). Tandem Mass Spectrometry Characteristics of Silver-Cationized Polystyrenes: Internal Energy, Size, and Chain End versus Backbone Substituent Effects. *Analytical Chemistry* **80**, 355-362.

Polce, M. J., Ocampo, M., Quirk, R. P. and Wesdemiotis, C. (2007b). Tandem Mass Spectrometry Characteristics of Silver-Cationized Polystyrenes: Backbone Degradation via Free Radical Chemistry. *Analytical Chemistry* **80**, 347-354.

Polce, M. J., Ocampo, M., Quirk, R. P. and Wesdemiotis, C. (2008b). Tandem Mass Spectrometry Characteristics of Silver-Cationized Polystyrenes: Backbone Degradation via Free Radical Chemistry. *Analytical Chemistry* **80**, 347-354.

Rader, H. J., Spickermann, J. and Mullen, K. (1995). Maldi-Tof Mass-Spectrometry in Polymer Analytics .1. Monitoring the Polymer-Analogous Sulfonation Reaction of Polystyrene. *Macromolecular Chemistry and Physics* **196**, 3967-3978.

Robertson, D. F., Heron, J. E. and Beckett, M. C. (2004). On-Line Gel Permeation Chromatography/Nuclear Magnetic Resonance of Complex Polymer Formulations. *Applied Spectroscopy* **58**, 1122-1127.

Robinson, E. W., Garcia, D. E., Leib, R. D. and Williams, E. R. (2006). Enhanced mixture analysis of poly(ethylene glycol) using high-field asymmetric waveform ion mobility spectrometry combined with Fourier transform ion cyclotron resonance mass spectrometry. *Analytical Chemistry* **78**, 2190-2198.

Scrivens, J. H. and Jackson, A. T. (2000). Characterisation of synthetic polymer systems. *International Journal of Mass Spectrometry* **200**, 261-276.

Scrivens, J. H., Jackson, A. T., Yates, H. T., Green, M. R., Critchley, G., Brown, J., Bateman, R. H., Bowers, M. T. and Gidden, J. (1997). The effect of the variation of cation in the matrix-assisted laser desorption/ionisation collision induced dissociation (MALDI-CID) spectra of oligomeric systems. *International Journal of Mass Spectrometry* **165**, 363-375.

Selby, T. L., Wesdemiotis, C. and Lattimer, R. P. (1994). Dissociation characteristics of [M + X]+ ions (X = H, Li, Na, K) from linear and cyclic polyglycols. *Journal of the American Society for Mass Spectrometry* **5**, 1081-1092.

Syka, J. E., Coon, J. J., Schroeder, M. J., Shabanowitz, J. and Hunt, D. F. (2004). Peptide and protein sequence analysis by electron transfer dissociation mass spectrometry. *Proceeding in the National Academy of Sciences U S A* **101**, 9528-33.

Thalassinos, K., Jackson, A. T., Williams, J. P., Hilton, G. R., Slade, S. E. and Scrivens, J. H. (2007). Novel Software for the Assignment of Peaks from Tandem Mass Spectrometry Spectra of Synthetic Polymers. *Journal of the American Society for Mass Spectrometry* **18**, 1324-1331.

Ute, K., Kashiyama, M., Oka, K., Hatada, K. and Vogl, O. (1990). Online GPC NMR Analysis of the Mixture of Chloral Oligomers. *Makromolekulare Chemie-Rapid Communications* **11**, 31-35.

Ute, K., Niimi, R., Matsunaga, M., Hatada, K. and Kitayama, T. (2001). On-line SEC-NMR analysis of the stereocomplex of uniform isotactic and uniform syndiotactic poly(methyl methacrylate)s. *Macromolecular Chemistry and Physics* **202**, 3081-3086.

Van der Hage, E. R. E., Duursma, M. C., Heeren, R. M. A., Boon, J. J., Nielen, M. W. F., Weber, A. J. M., De Koster, C. G. and De Vries, N. K. (1997). Structural Analysis of Polyoxyalkyleneamines by Matrix-Assisted Laser Desorption/Ionization on an External Ion Source FT-ICR-MS and NMR. *Macromolecules* **30**, 4302-4309.

Van Rooij, G. J., Duursma, M. C., De Koster, C. G., Heeren, R. M. A., Boon, J. J., Wijnand Schuyl, P. J. and Van der Hage, E. R. E. (1998). Determination of Block Length Distributions of Poly(oxypropylene) and Poly(oxyethylene) Block Copolymers by MALDI-FT-ICR Mass Spectrometry. *Analytical Chemistry* **70**, 843-850.

van Rooij, G. J., Duursma, M. C., Heeren, R. M. A., Boon, J. J. and de Koster, C. G. (1996). High resolution end group determination of low molecular weight polymers by matrix-assisted laser desorption ionization on an external ion source fourier transform ion cyclotron resonance mass spectrometer. *Journal of the American Society for Mass Spectrometry* **7**, 449-457.

von Helden, G., Wyttenbach, T. and Bowers, M. T. (1995a). Conformation of Macromolecules in the Gas Phase: Use of Matrix-Assisted Laser Desorption Methods in Ion Chromatography. *Science* **267**, 1483-1485.

von Helden, G., Wyttenbach, T. and Bowers, M. T. (1995b). Inclusion of a MALDI ion source in the ion chromatography technique: conformational information on polymer and biomolecular ions. *International Journal of Mass Spectrometry and Ion Processes* **146-147**, 349-364.

Weidner, S. M. and Trimpin, S. (2008). Mass Spectrometry of Synthetic Polymers. *Analytical Chemistry* **80**, 4349-4361.

Wilczek-Vera, G., Yu, Y., Waddell, K., Danis, P. O. and Eisenberg, A. (1999). Detailed Structural Analysis of Diblock Copolymers by Matrix-assisted Laser Desorption/Ionization Time-of-flight Mass Spectrometry. *Rapid Communications in Mass Spectrometry* **13**, 764-777.

Williams, J. P., Hilton, G. R., Thalassinos, K., Jackson, A. T. and Scrivens, J. H. (2007). The rapid characterisation of poly(ethylene glycol) oligomers using desorption electrospray ionisation tandem mass spectrometry combined with novel product ion peak assignment software. *Rapid Communications in Mass Spectrometry* **21**, 1693-1704.

Zenobi, R. and Knochenmuss, R. (1998). Ion formation in MALDI mass spectrometry. *Mass Spectrometry Reviews* **17**, 337-366.

Zhang, N., Aebersold, R. and Schwikowski, B. (2002). ProbID: A probabilistic algorithm to identify peptides through sequence database searching using tandem mass spectral data. *Proteomics* **2**, 1406-1412.

Chapter 7
Results: Structural Analysis of Synthetic Polymer Mixtures

7.1 Introduction.

Mass spectrometry is gaining in popularity as a technique that can be used to investigate the structure of polymers in the gas-phase. An analytical challenge is introduced when MS is used to analyse polymers containing oligomers of differing structures, but isobaric molecular weights. Polymer systems with oligomers of the same empirical formulae, that have different structures, cannot be easily differentiated by direct MS analysis without introducing a time consuming chromatographic step. High resolution MS is required to differentiate between oligomers of the same nominal molecular weight, but differing empirical formulae. Conventional MS resolution is defined as ($m/\Delta m$) at a certain *m/z* ratio with the value calculated at FWHM of the peak. Quadrupole mass spectrometers can reach unit mass resolution (up to approximately 3000 FWHM), ToF analysers can exceed 12,000, Orbitraps have a resolving power of 100,000 and FT-ICR mass spectrometers can have a resolving power of 1,000,000 or larger (Alber, Marshall *et al.* 1993; Kind and Fiehn 2006).

When conducting MS/MS experiments, consideration should be given to the resolution under which the precursor ion has been selected, which form of activation has occurred, and the resolution at which the product ion spectrum has been acquired. MS/MS experiments can either take place in space (Q-ToF, ToF-ToF, QQQ) or in time (Iontrap, Orbitrap, FT-ICR-MS). The resolution available to select a precursor ion is normally much lower than that of the detecting analyser. Commercial triple quadrupole or Q-ToF instruments have the ability to select ions at unit mass resolution over the mass range of the quadrupole. In ToF-ToF instruments precursor ion resolution can be as low as ± 2.5 Da, however, when post source decay experiments are used the precursor ion window can increase to 10 Da or more (Lin, Campbell *et al.* 2003). In contrast, hybrid instruments with a magnetic sector device as the first analyser such as sector oa-ToF or four sector instruments were capable of precursor resolutions of > 10,000 FWHM. These machines are no longer widely in use because of cost, ease of use and other performance limitations. Many modern instruments are capable of product ion resolutions in the tens of thousands, or in the case of FT-ICR-MS > 1 million; the

precursor ion selection does, however, not match this performance (Alber, Marshall *et al.* 1993). Trapping technologies such as FT-ICR-MS instruments can rely on ion ejection approaches to select ions for their MS/MS experiments. With FT-ICR-MS instrumentation, precursor ion selection prior to MS/MS experiments can be carried out in two main ways. For example, ions can be selected for subsequent ion activation within the FT-ICR-MS instrument by means of an additional analyser such as a quadrupole or an ion trap device. The capability of these technologies to resolve precursor ions rarely exceeds unit mass resolution. Ions may also be selected for subsequent activation within the FT-ICR-MS cell itself by means of stored waveform inverse Fourier transform (SWIFT) or pulse shaping. Routine, high sensitivity, precursor ion selection using these methods is again limited to unit mass precursor ion resolution. More specialised non-routine experiments have been used, which demonstrate higher precursor ion resolution with values up to 20,000 for SWIFT and 50,000 in correlated sweep excitation (COSE) experiments (Heck and Derrick 1997). In FT-ICR mass spectrometry, the parent ion can be mass selectively trapped in the cell by ejecting all ions with different *m/z* values using appropriate RF ejection fields. The mass resolution by FT-ICR parent ion selection is lower than the resolution at the detection stage of a FT-ICR mass spectrometer. This is because parent ions can be unintentionally excited and/or ejected by an RF frequency (off-resonance) used to eject all other ions from the cell. The SWIFT technique can minimise the unintentional off-resonance effects by providing an excitation magnitude spectrum of a desired, "nearly" arbitrary, shape. This reduces the amount of unintentional excitation the parent ion experiences (Heck and Derrick 1997).

For some MS/MS experiments it is necessary to select more than one precursor and use the power of the analyser to characterise the mixture from the product ion spectrum (or further MS/MS experiments). Unit mass precursor ion selection is not sufficient to select pure components for subsequent characterisation of complex mixtures of the type described here. The potential of ion mobility has been evaluated for the shape-directed selection of unique precursor ions in a complex mixture.

The combination of ESI with ion mobility and MS/MS, in the same experiment, was used to generate structural information on polyethers, specifically poly(ethylene glycol) (PEG). Separation of PEGs with the same nominal *m/z* ratio but differing structure was possible by means of ion mobility. This allowed IM-MS/MS data to be obtained from individual components, in a mixture, with the same nominal *m/z*. The MS/MS data obtained allowed structural identification of the separate components. Separation of an isobaric polyether mixture by means of GPC coupled on-line to a NMR detector has also been demonstrated.

7.2 Results and Discussion.

The polyether mixtures studied were di-hydroxyl end capped poly(ethylene glycol) (PEG) 1000 (**1**), PEG mono-oleate (**2**), stearyl alcohol initiated PEG (**3**) and PEG bis(2-ethyl hexanoate) (**4**). NMR data from all four compounds indicated that the structures of the polymers were those shown in Figure 7.1. For all materials and methods please refer to Chapter 3.

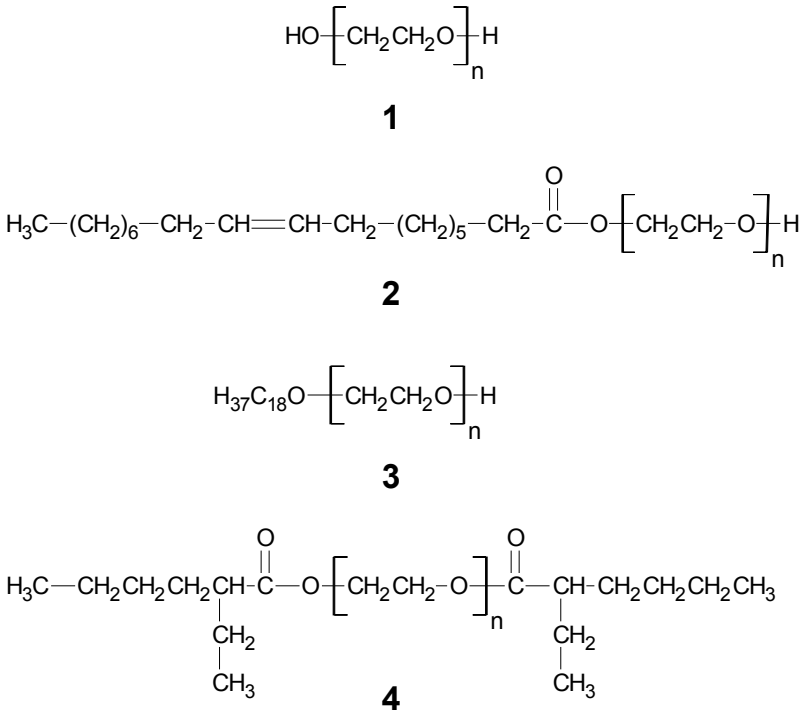

Figure 7.1: Structures of di-hydroxyl end capped poly(ethylene glycol) (PEG) 1000 (1), PEG mono-oleate (2), stearyl alcohol initiated PEG (3) and PEG bis(2-ethyl hexanoate) (4).

7.2.1 GPC-NMR

It has been demonstrated that GPC coupled on-line to a NMR detector can separate complex synthetic polymer mixtures (Robertson, Heron *et al.* 2004). Previous studies have employed this method to separate polymer formulations (Robertson, Heron *et al.* 2004), to distinguish tacticity distributions of pure and mixed stereocomplexes (Hatada,

Ute *et al.* 1990; Ute, Niimi *et al.* 2001) and to characterise the structure and molecular mass of polymers in one experiment (Hatada, Ute *et al.* 1990; Hatada, Ute *et al.* 1989; Hatada, Ute *et al.* 1988; Kramer, Pasch *et al.* 1999; Ute, Niimi *et al.* 1999). It is believed GPC-NMR can be an invaluable tool for the deformulation of complex mixtures. Here GPC-NMR has been used to characterise a mixture of isobaric polyether samples and the results have been compared to IM-MS data.

Figure 7.2 shows a GPC-^{1}H NMR contour plot of stearyl alcohol initiated PEG (M_n 711) (green) overlaid with the contour plot of PEG bis(2-ethyl hexanoate) (M_n 650) (yellow). The y-axis shows the retention time, in seconds, with each graduation on the scale corresponding to four NMR data scans. The x-axis shows the chemical shift of the compounds. The proton density curve (y'-axis) is equivalent to the GPC chromatogram. The magnitude of the curve, relative to the baseline, is representative of the number of protons in the free induction decay (FID) at a particular retention time. A 1D slice from the apex of each curve is shown at the top of the contour plot and the enlarged ^{1}H NMR spectra of stearyl alcohol initiated PEG and PEG bis(2-ethyl hexanoate) are shown above and below the contour plot respectively. The contour plot shows a continuous signal at 1.5 ppm for both the stearyl alcohol initiated PEG and PEG bis(2-ethyl hexanoate). The presence of this signal is because of water in the $CDCl_3$ solvent. GPC separates compounds according to their size and shape. In general, larger molecular weight compounds elute before smaller compounds. This suggests that stearyl alcohol initiated PEG with a M_n 711 should elute before PEG bis(2-ethyl hexanoate) (M_n 650). The opposite is observed in Figure 7.2. The retention time of the individual apexes is 110 s for PEG bis(2-ethyl hexanoate) and 116 s for stearyl alcohol initiated PEG. The reversed elution order, to that of the expected, could be because of hydrophobic/hydrophilic effects in the solution phase. The stearyl alcohol initiated PEG has a hydroxyl end group. This hydroxyl group could interact with water molecules in the $CDCl_3$ solvent thereby prolonging its retention time in the GPC column.

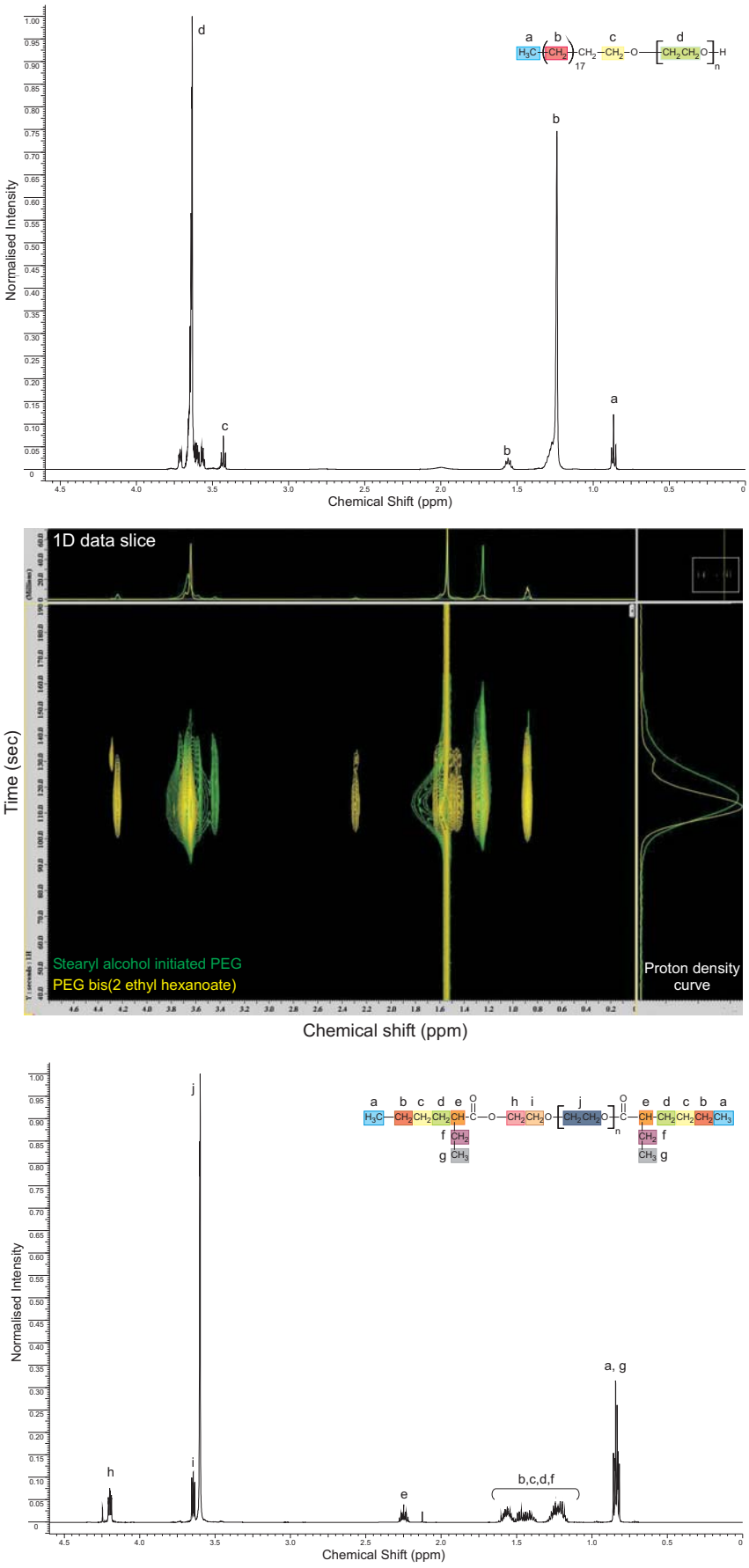

Figure 7.2: GPC-^{1}H NMR contour plot of stearyl alcohol initiated PEG (Mn 711) (green) overlaid with the contour plot of PEG bis(2-ethyl hexanoate) (Mn 650) (yellow). ^{1}H NMR spectra of stearyl alcohol initiated PEG and PEG bis(2-ethyl hexanoate) are shown above and below the contour plot respectively.

[Insert Figure 7.2]

Figure 7.2: GPC-^{1}H NMR contour plot of stearyl alcohol initiated PEG (M_n 711) (green) overlaid with the contour plot of PEG bis(2-ethyl hexanoate) (M_n 650) (yellow). ^{1}H NMR spectra of stearyl alcohol initiated PEG and PEG bis(2-ethyl hexanoate) are shown above and below the contour plot respectively.

The shape of the polymers will also have an effect on the elution order. In the solution phase, PEG bis(2-ethyl hexanoate) may be more globular in structure than the stearyl alcohol initiated PEG. This would also account for a faster elution time. Molecular modelling would be required to verify this.

NMR spectroscopy data are a representation of the average structure in solution for a polymeric mixture. Online GPC-NMR can, however, analyse individual conformations in the solution-phase. The proton density curve shows the molecular weight distribution of the individual polymer systems. Characterisation by means of NMR spectroscopy represents the average number of repeat units in the polymer system. Each data point on the GPC-NMR proton density curve corresponds to a 1D ^{1}H NMR spectrum. These data can be manipulated and the molecular weight distribution of the individual polymer systems can be calculated. Figure 7.3 shows the integrated 1D ^{1}H NMR spectrum of stearyl alcohol initiated PEG extracted from retention time 116 s (apex of curve). From the integrated spectrum, the number of repeat units and the length of the stearyl alcohol initiator can be quantified. The signal at 0.85 ppm corresponds to the three protons in the terminal methyl group from the stearyl alcohol initiator (labelled **a** in Figure 7.2 (top) and Figure 7.3). All other integrals on the spectrum are measured with respect to this methyl group. The chemical shift signal ranging from 3.5-3.8 ppm corresponds to the four protons per ethylene oxide repeat unit (labelled **d**) (see Figure 7.3). The number of repeat units can be calculated from dividing the integral value of **d** by the number of protons contributing to this signal – four. An example calculation is shown in Figure 7.3. The number of repeat units (n) calculated from 1D ^{1}H NMR spectra, shown in Figure 7.2, for stearyl alcohol initiated PEG is n=10 and n=8 for PEG bis(2-ethyl hexanoate). The stearyl alcohol initiated PEG proton density curve represents a molecular weight distribution of n=1 to n=23 (inclusive) and the proton density curve for PEG bis(2-ethyl hexanoate) represents a molecular weight distribution of n=1 to n=21. These molecular weight distributions are in good agreement with MALDI-MS data (not shown).

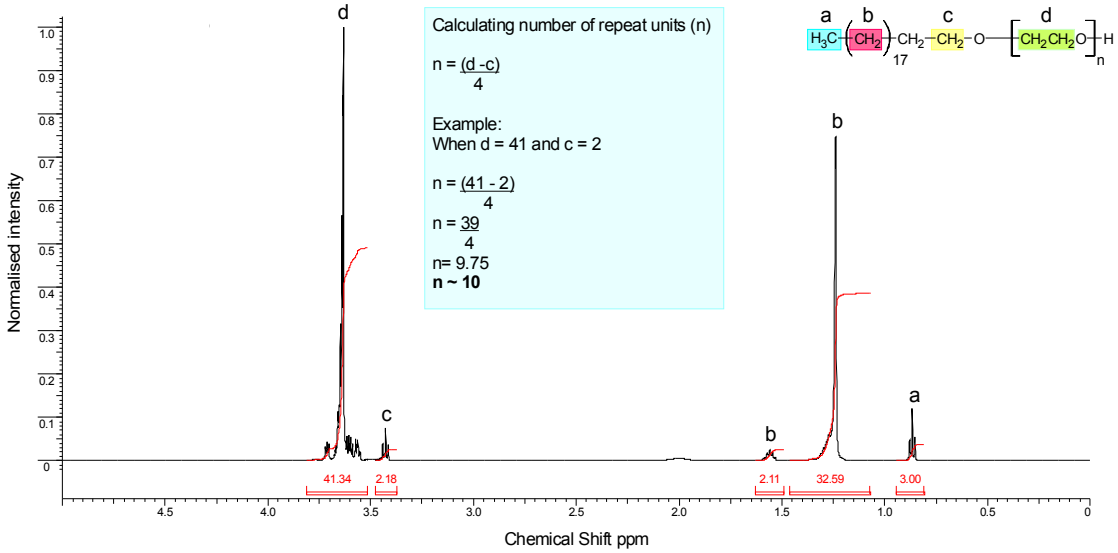

Figure 7.3: ^{1}H NMR spectrum of stearyl alcohol initiated PEG. Insert: Example of how to calculate number of repeat units.

The overlaid GPC-^{1}H NMR contour plots of stearyl alcohol initiated PEG and PEG bis(2-ethyl hexanoate) are very similar (see Figure 7.2). The major differences between the plots are the additional chemical shift signals at 2.25 ppm and 4.2 ppm for PEG bis(2-ethyl hexanoate) (labelled **e** and **h** respectively Figure 7.2 (bottom)). The retention times and peak width of the proton density curve are similar. The apex of the individual polymer systems are separated by a 6 s retention time difference. Figure 7.4 shows the GPC-^{1}H NMR contour plot of a mixture of stearyl alcohol initiated PEG and PEG bis(2ethyl hexanoate). The presence of the chemical shift signals at 2.25 ppm and 4.2 ppm, and the signal at 3.4 ppm suggests that PEG bis(2-ethyl hexanoate) and stearyl alcohol initiated PEG are present in the mixture respectively. The proton density curve contains one maximum. This suggests that the PEG samples are too similar in mass, size and shape to be separated by means of GPC. van Gorken and co-workers showed that GPC-NMR with insufficient chromatographic separation could still be used to characterise a complex polymer mixture (Kitayama and Ute 2006; Van Gorkom and Hancewicz 1998). They demonstrated that the GPC-NMR data could be manipulated by means of multivariate curve resolution and that this technique could extract the

individual components of the mixture according to their proton intensity profiles. Their data did, however, show significantly better separation than that observed in Figure 7.4. The data shown here was not subject to multivariate analysis.

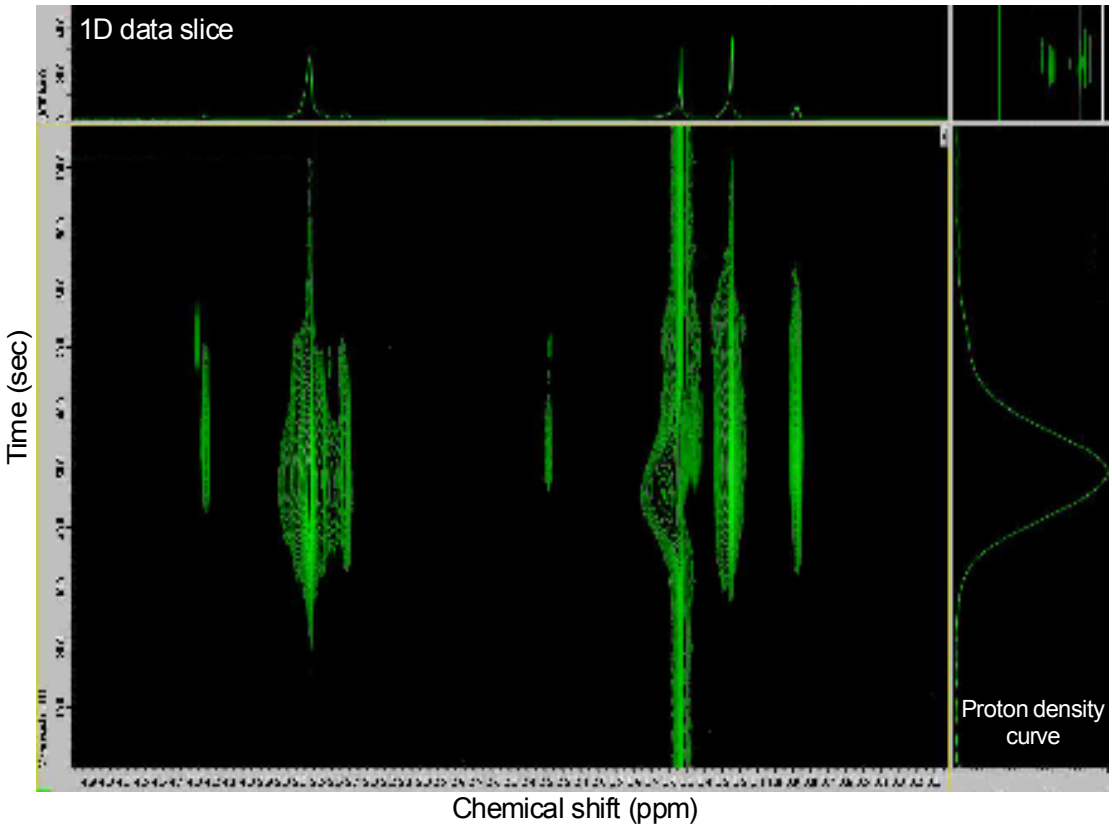

Figure 7.4: GPC-^{1}H NMR contour plot of a mixture of stearyl alcohol initiated PEG and PEG bis(2-ethyl hexanoate).

Figure 7.5 shows a GPC-^{1}H NMR contour plot of PEG 1000 (M_n 1000) (yellow) overlaid with the contour plot of PEG mono-oleate (M_n 860) (green). The y-axis shows the retention time with each graduation on the scale corresponding to four NMR data scans. The x-axis shows the chemical shift of the compounds. The proton density curve (y'-axis) is equivalent to the GPC chromatogram. A 1D slice from the apex of each curve is shown at the top of the contour plot and the enlarged ^{1}H NMR PEG mono-

oleate and PEG 1000 are shown above and below the contour plot respectively. The chemical signal at ~1.5 ppm in both the PEG 1000 and PEG mono-oleate contour plot is because of water present in the $CDCl_3$ solvent (similar to Figure 7.2). The proton density curve of the two polymer systems shows that PEG mono-oleate has a shorter apex of distribution (47 s) compared to PEG 1000 (50 s). This elution order suggests that PEG mono-oleate is larger, on average, than PEG 1000. The prolonged retention time of chemical signals on the contour plot and the relative width of the baseline in the proton density curve also indicate that PEG 1000 has a lower polydispersity than PEG mono-oleate. This observation was confirmed by MALDI analysis (data not shown). The reversed elution order of stearyl alcohol initiated PEG and PEG bis(2-ethyl hexanoate) was proposed to be because of hydrophobic/hydrophilic effects in the solution phase. These same hydroxyl group:water interactions could occur in both the PEG 1000 and PEG mono-oleate samples, however, because both of these compounds contain a free hydroxyl end group the effect of the hydrophilic interactions is assumed to be equivalent. It was demonstrated that the mixture of stearyl alcohol initiated PEG and PEG bis(2-ethyl hexanoate) could not be separated by GPC-NMR despite a 6 s difference in their average proton density curve retention times (see Figure 7.4). There is a 3 s difference in the retention time between the proton density curve of PEG 1000 and PEG mono-oleate. The GPC-NMR proton density curve of these compounds showed one peak maximum (data not shown). This suggests that GPC-NMR has insufficient resolution, in this case, to separate the mixture of isobaric polymer systems into their individual components.

In contrast to NMR and GPC-NMR, IM-MS has the advantage that it can analyse individual polymer oligomer conformations in the gas-phase as well as the overall average structure. This ability to select oligomers may aid the separation and identification of the individual components in an isobaric polymer mixture.

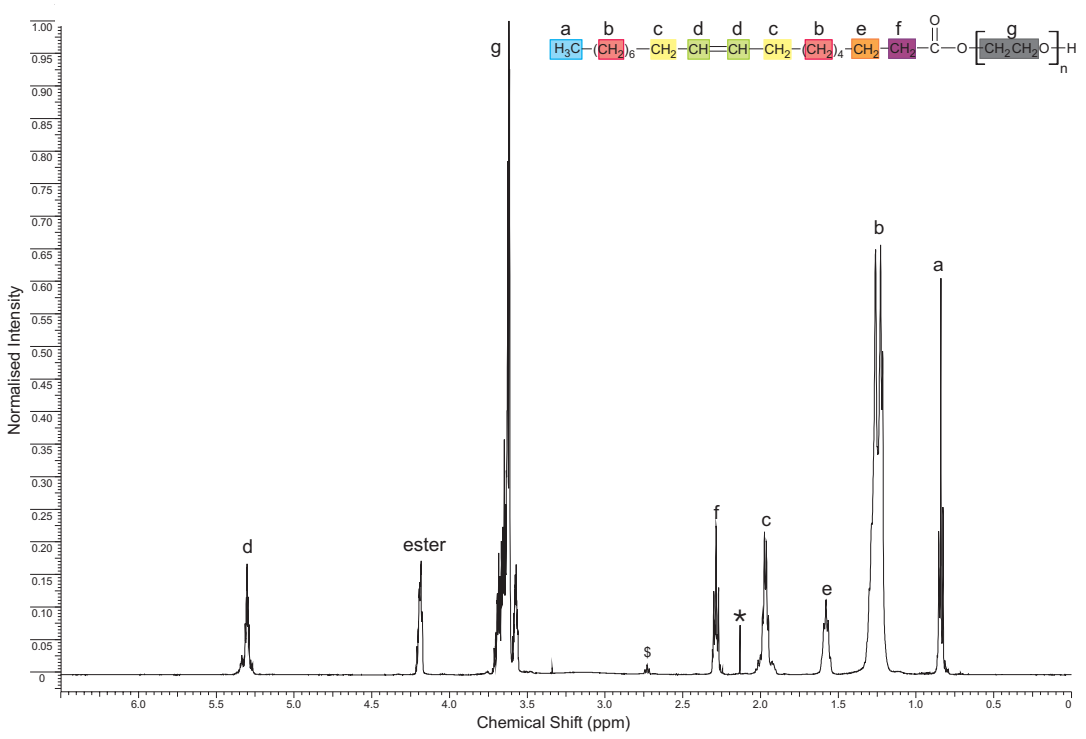
Normalised Intensity
Chemical Shift (ppm)
g
d
ester
f
c
b
a
e
*
$

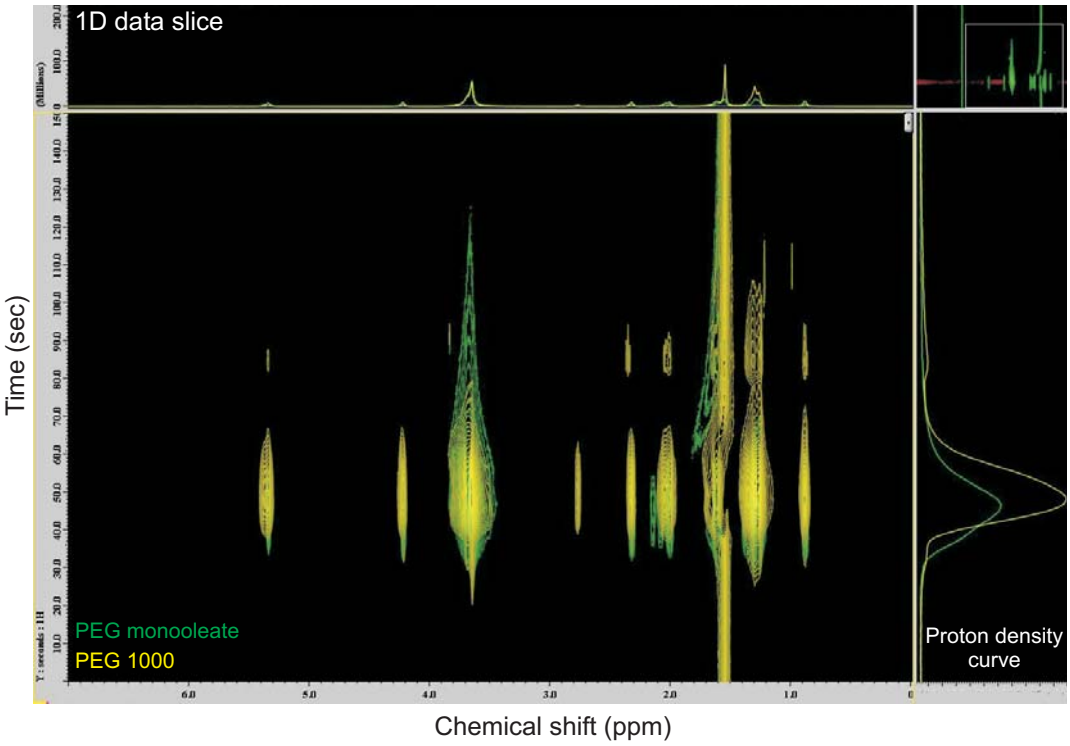
1D data slice
Time (sec)
PEG monooleate
PEG 1000
Proton density curve
Chemical shift (ppm)

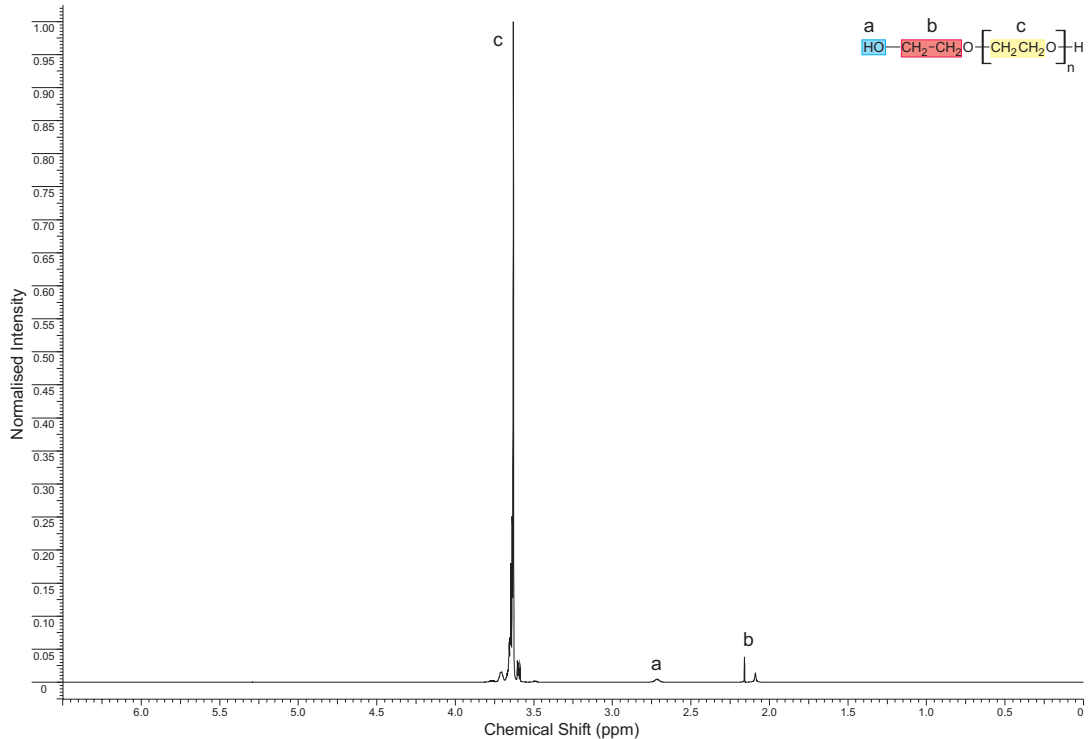
Normalised Intensity
Chemical Shift (ppm)
c
a
b

[Insert Figure 7.5]

Figure 7.5: GPC-^{1}H NMR contour plot of PEG 1000 (M_n 1000) (yellow) overlaid with the contour plot of PEG mono-oleate (M_n 860) (green). ^{1}H NMR PEG mono-oleate and PEG 1000 are shown above and below the contour plot respectively.

7.2.2 Mass Spectrometry

Oligomers of **1** and **2** have the same nominal *m/z* ratio but contain a different number of moles of ethylene oxide (EO) units. An oligomer, for example, of **1** with 12 repeat units (*n*) of EO has the same nominal molecular weight as **2** with 6 repeat units (*n*) of monomer. Oligomers of **3** and **4** have the same nominal *m/z* ratio and also have the same number of moles of EO units. MS/MS data have been shown to provide structural information that can aid identification of unknown end groups in PEG (Jackson, Scrivens *et al.* 2000; Lattimer 1992a; Lattimer 1992b; Lattimer 1994; Lattimer, Munster *et al.* 1989). This MS/MS methodology will not help for these mixtures of polyethers as the resolution of the quadrupole, ion trap, sector or ToF analyser typically used for precursor ion selection is not able to resolve the oligomers with the same nominal *m/z* ratio. The combination of IM with MS/MS was employed to both provide the possible extra resolving power of the former with the possibility of structural identification and/or differentiation from the latter. It was hoped that the isobaric oligomers could be separated using the difference in their rotationally-averaged cross-sections.

All individual polyether samples were characterised by means of ^{1}H and ^{13}C NMR and MALDI-MS (data not shown) prior to IM-MS/MS analysis. This confirmed that the samples had the expected structures (**1**-**4**,see Figure 7.1) and were of high purity. A mixture of PEG 1000 and PEG mono-oleate was directly infused by means of ESI into the Synapt mass spectrometer. Figure 7.6 shows the full separation of two isobaric oligomers (*m/z* 553) by ion mobility. The IM-MS/MS product ion spectra from the lithiated oligomer, from PEG 1000 ($[\mathbf{1} + Li]^+$) containing 12 moles of EO and PEG mono-oleate ($[\mathbf{2} + Li]^+$) containing 6 moles of EO, are also displayed. These three sets of data were all derived in the same experiment. There is a clear differentiation of the two isobaric species, as observed from the IM arrival time distribution. The IM-MS/MS data obtained from the separated components in the mixture enabled end group analysis and confirmation of the structure of the two oligomeric species. The MS resolution required to separate these two oligomers (differing by *m/z* 0.0880 for $[\mathbf{1} + Li]^+$ at *m/z* 553.3411 and $[\mathbf{2} + Li]^+$ at *m/z* 553.4292) is approximately 6,300. This would not be

possible using standard quadrupoles for the first mass spectrometer in a MS/MS instrument, but the IM capability used here allows separation for structural analysis of this mixture of polyethers. Good separation (but with slightly lower resolution of isobaric oligomers) was also obtained for higher molecular weight oligomers in this mixture of samples and the concurrent MS/MS data were used to differentiate between **1** and **2**. The resolving power of IM-MS/MS is insufficient to resolve the higher molecular weight oligomers as shown in Figure 7.7. The oligomers of $[\mathbf{2} + Li]^+$, which are isobaric with $[\mathbf{1} + Li]^+$, appear to have significantly larger rotationally averaged cross-sections. This is probably because of the presence of the long oleate chain in the former oligomers, but modelling of the structures would be required to confirm this. It is expected that cross-sections that are greater than 5% in difference would be resolved by the IM approach (Gidden, Wyttenbach *et al.* 2000).

Lattimer initially demonstrated that MS/MS could be used to generate structural information from polymers such as PEG (Lattimer 1992a; Lattimer 1994). Lattimer and coworkers and Jackson *et al.* have proposed mechanisms to account for the fragment ions generated, when lithium is used as the cation, in polyglycol spectra (Jackson, Scrivens *et al.* 2000; Lattimer 1992a; Lattimer 1992b; Lattimer 1994; Lattimer, Munster *et al.* 1989). Four dominant series of fragment ions, notated $\mathbf{A}_n$, $\mathbf{B}_n$, $\mathbf{C}_n$ and $\mathbf{D}_n$, were proposed to be generated from CID of polyglycols. Jackson *et al.* postulated that, when observing the $\mathbf{A}_n$, $\mathbf{B}_n$ and $\mathbf{C}_n$ series, fragments at the higher *m/z* are the most structurally informative for the generation of end group information (Jackson, Green *et al.* 2006). Additional fragment ions were also noted to be important for end group identification in the case of some functionalised polyglycols. Similar fragmentation is noted for the poly(ethylene glycol)s studied here, with end group information proposed to be gleaned from peaks of the $\mathbf{A}_n$, $\mathbf{B}_n$ and $\mathbf{C}_n$ series, plus initiator fragments from the oleate chain of **2**, at higher mass-to-charge ratios (selected peaks are labelled in Figure 7.6, following the notation proposed by Jackson *et al.* (Jackson, Green *et al.* 2006))

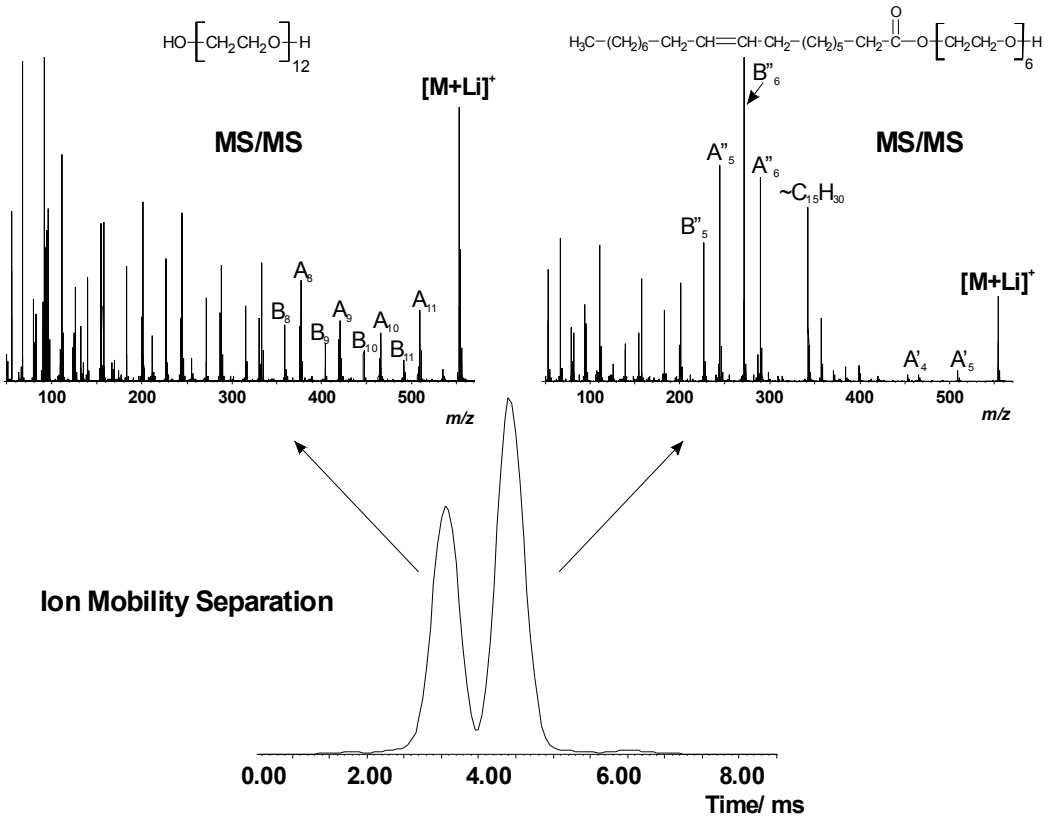

Figure 7.6: Arrival time distribution (bottom) of *m/z* 553 from a mixture of PEG 1000 and PEG mono-oleate and IM-MS/MS spectra (top) from the two peaks noted. Peaks in the IM-MS/MS spectra are partially annotated as described previously by Jackson *et al.* (Jackson, Green *et al.* 2006). IM-MS/MS spectra are very similar to those noted from MS/MS data (without ion mobility separation) of the same oligomers, obtained from PEG 1000 and PEG mono-oleate separately (see Figure 7.10).

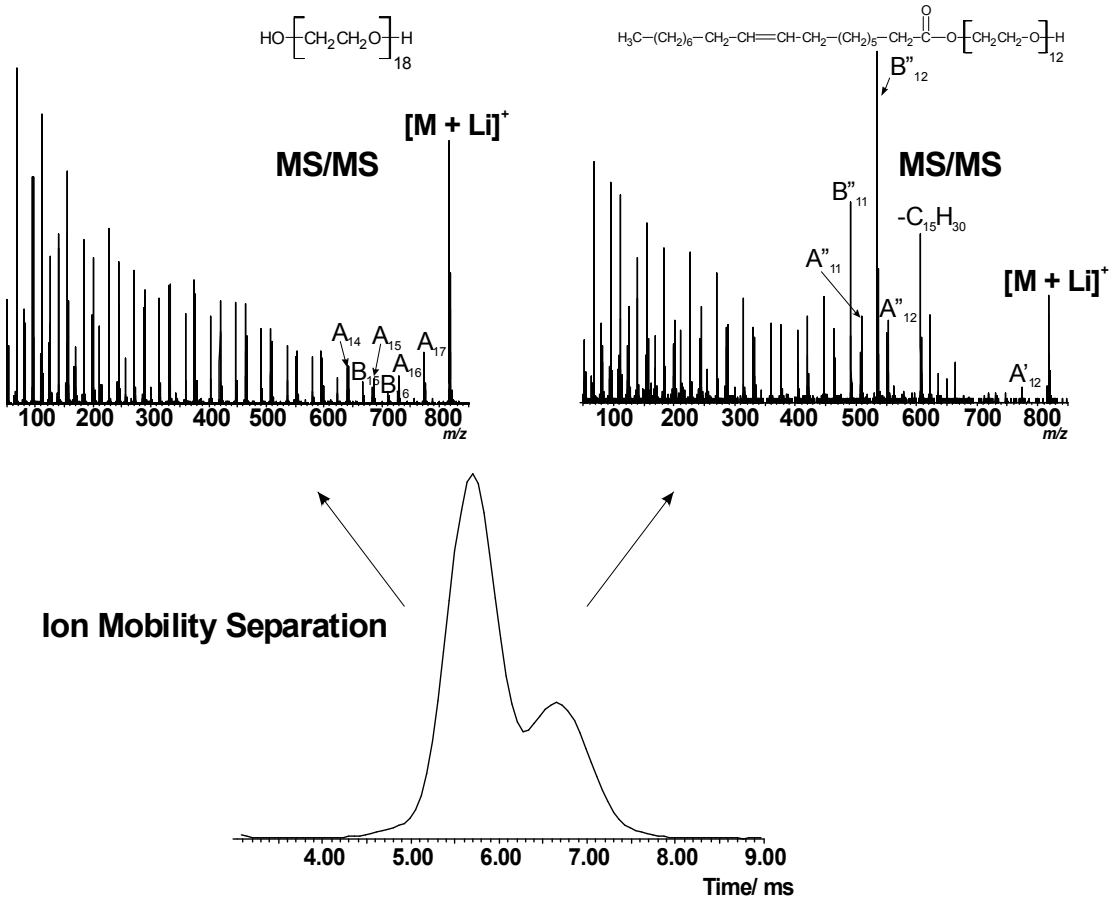
HO-[CH2CH2O]-H
18
[M + Li]+
MS/MS
A14
A15
A17
B15
A16
B16
100 200 300 400 500 600 700 800
m/z
H3C-(CH2)6-CH2-CH=CH-CH2-(CH2)5-CH2-C(=O)-O-[CH2CH2-O]-H
12
B"12
MS/MS
B"11
-C15H30
A"11
A"12
[M + Li]+
A'12
100 200 300 400 500 600 700 800
m/z
Ion Mobility Separation
4.00 5.00 6.00 7.00 8.00 9.00
Time/ ms

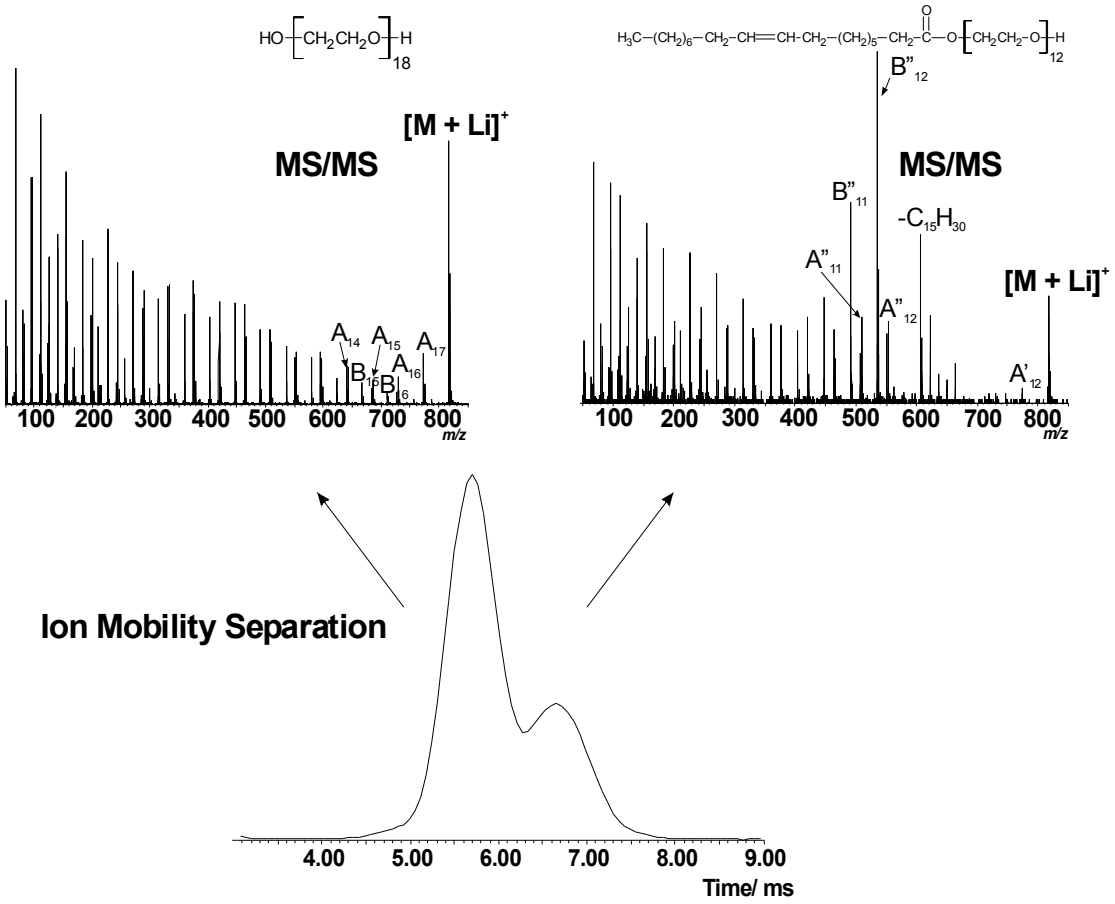

Figure 7.7: Arrival time distribution (bottom) of *m/z* 817 from a mixture of PEG 1000 and PEG mono-oleate and IM-MS/MS spectra (top) from the two peaks noted. Peaks in IM-MS/MS spectra are partially annotated as described previously by Jackson *et al.*[8]. IM-MS/MS spectra are very similar to those noted from MS/MS data (without ion mobility separation) of the same oligomers, obtained from PEG 1000 and PEG mono-oleate.

Figure 7.8 shows the full separation of two isobaric oligomeric species (*m/z* 497), from stearyl alcohol initiated PEG and PEG bis(2-ethyl hexanoate) by ion mobility. Also shown are the IM-MS/MS product ion spectra, which were generated in the same experiment, from the lithiated oligomers ([**3** + Li]$^+$ and [**4** + Li]$^+$) from stearyl alcohol initiated PEG and PEG bis(2-ethyl hexanoate), both of which contain 5 moles of EO. The arrival time distribution, combined with the IM-MS/MS, indicates that lithiated oligomers of PEG bis(2-ethyl hexanoate) have a more compact rotationally-averaged cross-section than those of the isobaric stearyl alcohol initiated PEG species. The coordination to the lithium ion is likely to be stronger in PEG bis(2-ethyl hexanoate) due to the presence of two additional oxygen atoms when compared with stearyl alcohol initiated PEG. This includes two carbonyl oxygen atoms which could show stronger interaction with the cation (Gidden, Wyttenbach *et al.* 2000; von Helden, Wyttenbach *et al.* 1995; Wyttenbach, von Helden *et al.* 1997). Stearyl alcohol initiated PEG has a long alkyl chain from the initiating group; this may induce the polymer to have a larger rotationally averaged cross-section (Robinson, Sellon *et al.* 2007; Ude, FernandezdelaMora *et al.* 2004). Modelling of gas-phase oligomeric structures would be required to confirm this. A MS resolution of approximately 6,800 would be required to fully separate lithiated pentamers of **3** and **4** (these oligomers have a difference of *m/z* 0.0728 for [**3** + Li]$^+$ at *m/z* 497.4393 and [**4** + Li]$^+$ at *m/z* 497.3666). A quadrupole would not be able to separate these oligomers for MS/MS experiments, but the ion mobility separation allows differentiation of the two oligomers. Separation of higher molecular weight isobaric oligomers of **3** and **4** was also achieved, allowing end group identification by MS/MS, albeit with an increased overlap of the two peaks observed in the arrival time distribution (with increasing molecular weight of the oligomers).

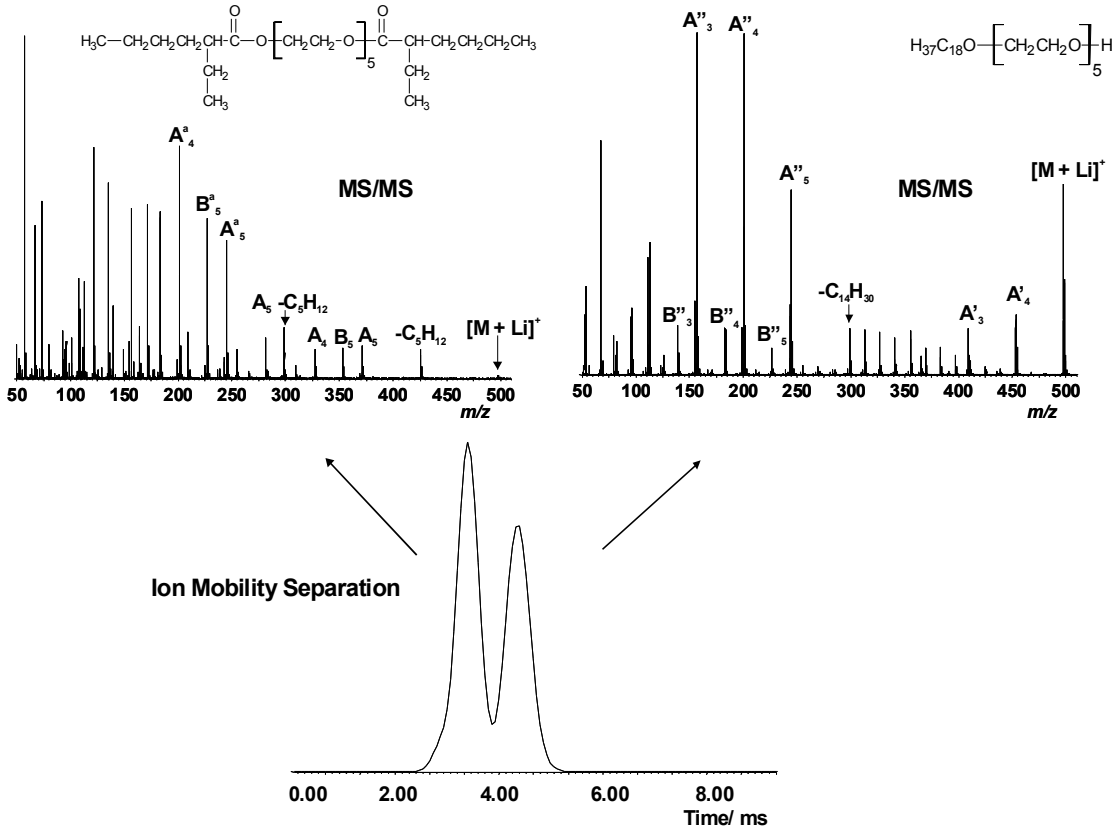

Figure 7.8: Arrival time distribution (bottom) of *m/z* 497 from a mixture of stearyl alcohol initiated PEG and PEG bis(2-ethyl hexanoate) and IM-MS/MS spectra (top) from the two peaks noted. Peaks in the IM-MS/MS spectra are partially annotated as described previously by Jackson *et al.* (Jackson, Green *et al.* 2006). IM-MS/MS spectra are very similar to those noted from MS/MS data (without ion mobility separation) of the same oligomers, obtained from stearyl alcohol initiated PEG and PEG bis(2-ethyl hexanoate) separately (see Figure 7.10c and Figure 7.9 respectively).

The IM-MS/MS data obtained from the individual components in the mixture enabled end group analysis to be performed for the two polymers. Fragmentation to form the $\mathbf{A}_n$, $\mathbf{B}_n$ an $\mathbf{C}_n$ series of fragment ions (as partially annotated in Figure 7.8), along with characteristic losses of part or whole of the end groups, allows differentiation between the alcohol initiated PEG and the PEG di-ester. Characteristic losses of both of the ester end groups, for example, is as expected from previous data from PEG (Jackson, Green *et al.* 2006). Also, loss of the whole alkyl chain (losses of part of the stearyl chain in sequence are also noted), from the stearyl initiated PEG, would be expected from this previous work, as is noted in Figure 7.8 (see peak annotated as $\mathbf{A''}_5$). The annotation of fragment ion peaks is again as that proposed previously (Jackson, Green *et al.* 2006). The IM-MS/MS and ESI-MS/MS data (see Figure 7.9) shows an unusual ion differing by *m/z* 72 from the precursor ion. This loss could correspond to C_5H_{12} although more detailed work would be needed to confirm this. The ^{1}H and ^{13}C NMR data, however, clearly indicate that **4** is the major structure of the di-ester. Further work would be required to elucidate the fragmentation mechanism for this loss.

ESI-MS/MS experiments were carried out for all four individual polyethers (without any ion mobility separation) using a standard quadrupole oa-TOF tandem mass spectrometer. A comparison of the MS/MS data, with and without ion mobility separation, indicates that there is good agreement between the two sets of spectra (see Figure 7.9 and Figure 7.10). Figure 7.10a shows a comparison of product ion spectra from the lithiated dodecamer of PEG 1000, acquired with IMS-MS/MS (Synapt HDMS, Waters, Manchester, UK) and ESI-MS/MS (Q-ToF I, Waters, Manchester, UK). The data are very similar, with identical fragment ions (e.g. labelled $\mathbf{A}_n$ and $\mathbf{B}_n$) observed in both spectra. A slight variation in distribution is seen because of differences in experimental parameters (i.e. difference in collision energy and low mass cut off). The similarity of both spectra validates the quality of the data obtained and the separation power of IMS. This is indicative of full separation of the oligomers in the ion mobility cell and that good quality MS/MS data can be obtained using IM-MS/MS experiments (that enables end group information to be obtained).

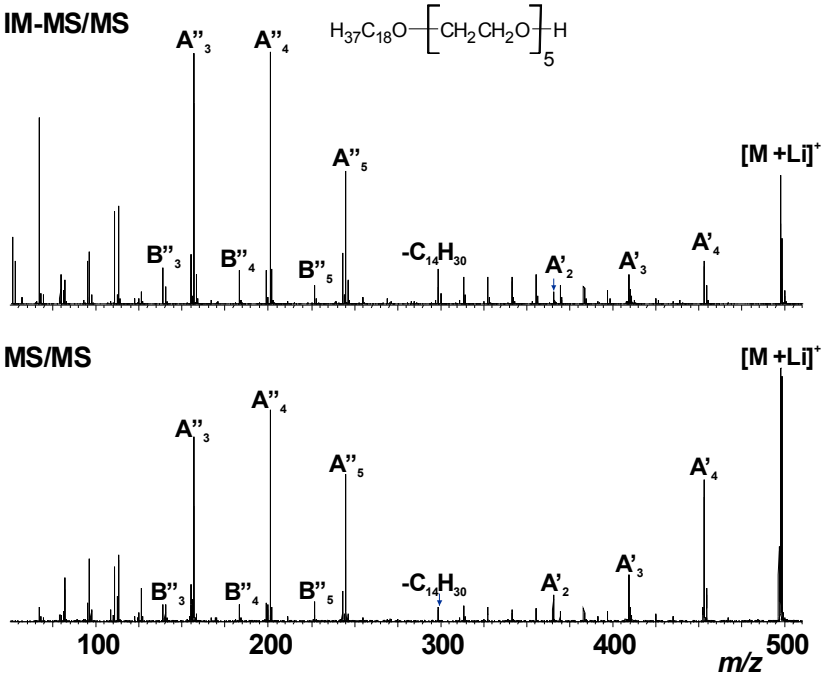

Figure 7.9: A comparison of product ion spectra from the lithiated pentamer of PEG bis(2-ethyl hexanoate), acquired with IMS-MS/MS (Synapt HDMS, Waters, Manchester, UK) and ESI-MS/MS (Q-ToF I, Waters, Manchester, UK). Characteristic fragmentation of di-esters is observed, with a partial loss of the ester end group (**-C_5H_{12}**) and the entire end group (**A_5**) seen. The ion annotated as **A_5 - C_5H_{12}** indicates the loss of one ester end group with the partial loss of the other, whilst **A^a_5** identifies loss of both end groups.

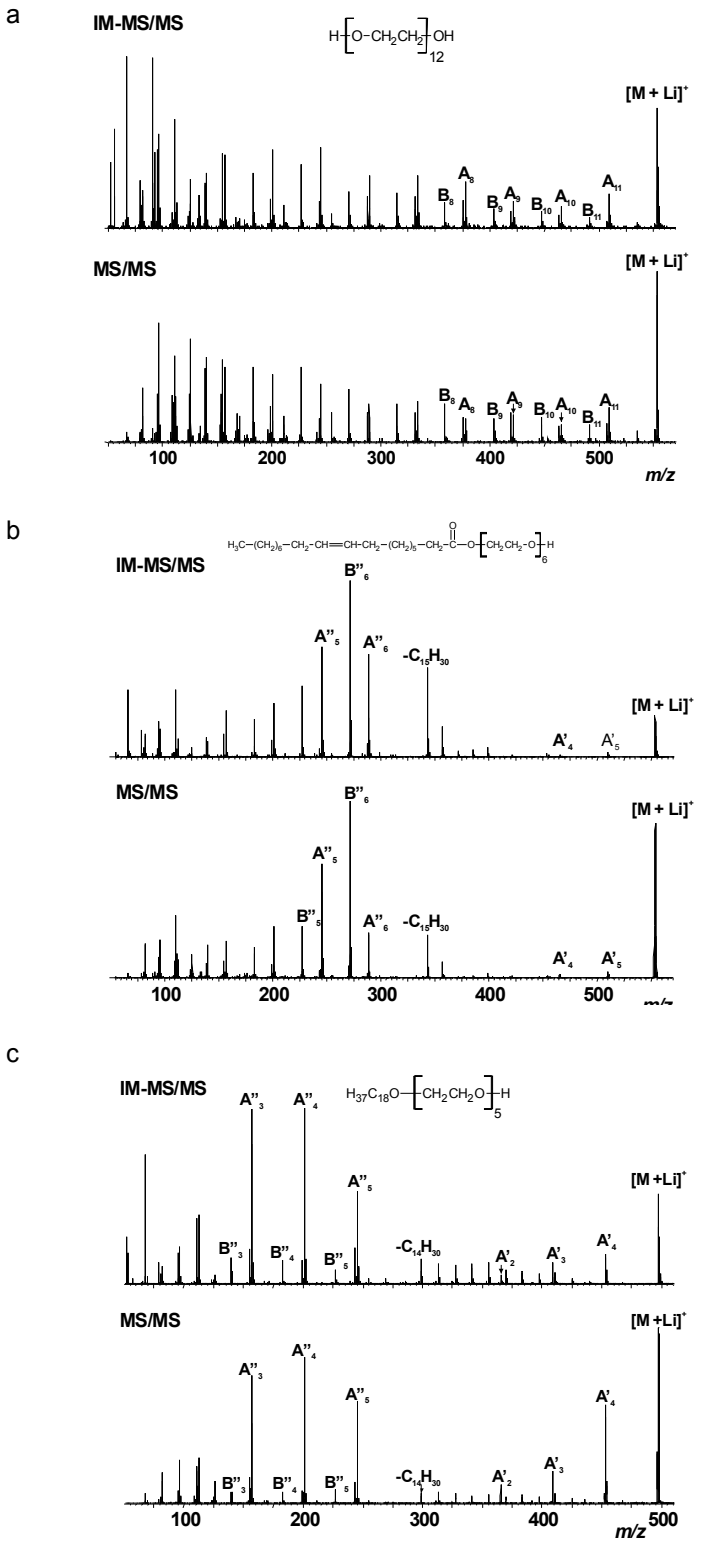

Figure 7.10: (a) A comparison of product ion spectra from the lithiated dodecamer of PEG 1000, acquired with IMS-MS/MS (Synapt HDMS, Waters, Manchester, UK) and ESI-MS/MS

(Q-ToF I, Waters, Manchester, UK). The data are very similar, with identical fragment ions (e.g. labelled $\mathbf{A}_n$ and $\mathbf{B}_n$) observed in both spectra. (b) A comparison of product ion spectra from the lithiated hexamer of PEG mono-oleate, acquired with IMS-MS/MS (Synapt HDMS, Waters, Manchester, UK) and ESI-MS/MS (Q-ToF I, Waters, Manchester, UK). The same fragmentation series (e.g. $\mathbf{A}_n$ and $\mathbf{B}_n$ series) are observed in both spectra indicating the good quality of the data obtained and the separation power of IMS. (c) A comparison of product ion spectra from the lithiated pentamer of stearyl alcohol initiated PEG, acquired with IMS-MS/MS (Synapt HDMS, Waters, Manchester, UK) and ESI-MS/MS (Q-ToF I, Waters, Manchester, UK). Characteristic fragmentation to form the $\mathbf{A}_n$ and $\mathbf{B}_n$ series, and the loss of the whole alkyl chain (losses of part of the stearyl chain in sequence are also observed) from the stearyl initiated PEG is noted.

7.2.3 IM-MS Poly(propylene glycol)

The poly(propylene glycol) (PPG) mixtures studied were PPG mono butyl ether (**5**) and PPG bis (2-amino propyl ether) (**6**). NMR data from the compounds indicated that the structures of the polymers were those shown in Figure 7.11.

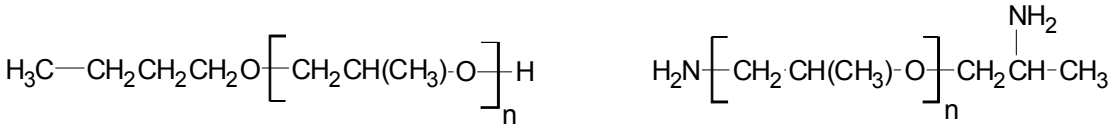

5 **6**

Figure 7.11: Structures of poly(propylene glycol) (PPG) mono butyl ether (**5**) and PPG bis(2-amino propyl ether) (**6**).

Oligomers of **5** and **6** have the same nominal *m/z* ratio and contain the same number of moles of propylene oxide (PO) units. For example, an oligomer of **5** with 3 repeat units (*n*) of PO has the same nominal molecular weight as **6** with the same number of repeat units of monomer. Figure 7.12 shows the lithiated mass spectra of PPG mono butyl ether, PPG bis (2-amino propyl ether) and a mixture of both polymer systems. The ion series labelled with dots, in the PPG mono butyl ether mass spectrum, are the sodiated oligomers and have not been considered in this investigation. In comparison to PPG bis (2-amino propyl ether), PPG mono butyl ether has a narrow charge state envelope distribution *m/z* range. The number of isobaric oligomers present in the mixture is therefore limited to the lower *m/z* range. The ATD at *m/z* 255 are inset in the respective mass spectra in Figure 7.12. The dotted and dashed lines represent the apex of each ATD peak. The ATD of the individual polymers are separated by two scan numbers. This suggests that PPG mono butyl ether and PPG bis (2-amino propyl ether) have a similar rotationally averaged cross-section. The ATD for the PPG mono butyl ether and PPG bis (2-amino propyl ether) mixture cannot distinguish between the isobaric oligomers. The MS resolution required to separate these two oligomers (differing by *m/z* 0.0368 for $[\mathbf{5} + Li]^+$ at *m/z* 255.2984 and $[\mathbf{6} + Li]^+$ at *m/z* 255.2616) is approximately 7,000. A quadrupole would not be able to separate these oligomers for MS/MS experiments, and ion mobility cannot aid the separation which would allow differentiation of the two oligomers. Previous ion mobility studies have shown isomers with a collision cross-section that differ by 5-10% appear as a shoulder or distinct separate peak in the ATDs (Gidden, Jackson *et al.* 1999; Gidden, Wyttenbach *et al.* 1999; Gidden, Wyttenbach *et al.* 2000; von Helden, Hsu *et al.* 1991; von Helden, Wyttenbach *et al.* 1995). This suggests that the cross-section of PPG mono butyl ether and PPG bis (2-amino propyl ether) differ by less than 5%.

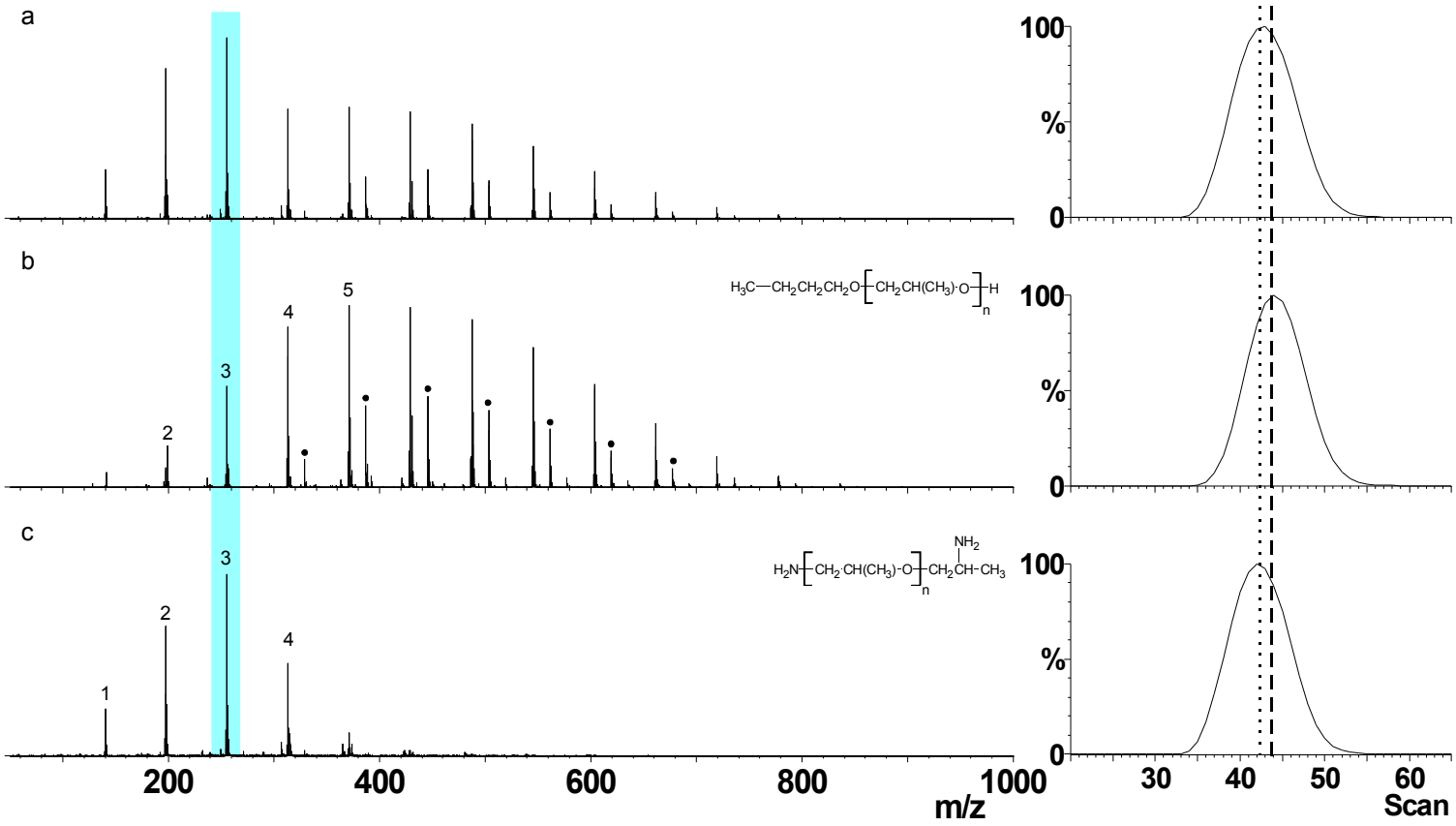

Figure 7.12: A comparison of lithiated mass spectra of polypropylene glycol (PPG) mono butyl ether and PPG bis(2-amino propyl ether). Blue highlighted region indicates 255 *m/z* (a) Mass spectrum of lithiated PPG mono butyl ether and PPG bis(2-amino propyl ether) mixture. Inset arrival time distribution (ATD) for 255 *m/z*. (b) Mass spectrum of lithiated PPG mono butyl ether, series of peaks marked with dots are the sodiated oligomers. Inset ATD for 255 *m/z*. (c) Mass spectrum of lithiated PPG bis(2-amino propyl ether). Inset ATD for 255 *m/z*.

7.2.4 GPC-NMR vs IM-MS/MS

GPC-NMR and IM-MS/MS were used to separate isobaric polyether mixtures of PEG 1000 and PEG mono-oleate, and stearyl alcohol initiated PEG mixed with PEG bis(2ethyl hexanoate). The elution order of PEG 1000 and PEG mono-oleate were the same when characterised by means of GPC-NMR and IMS-MS/MS. It was observed that the elution order of stearyl alcohol initiated PEG and PEG bis(2-ethyl hexanoate) differed between the two techniques. IMS-MS suggested that oligomers of PEG bis(2-ethyl hexanoate) have a more compact rotationally-averaged cross-section than those of the isobaric stearyl alcohol initiated PEG species. In contrast, the elution order of GPC-NMR implies that PEG bis(2-ethyl hexanoate) is larger than stearyl alcohol initiated PEG. A possible explanation for these contradicting observations is that the GPC-NMR elution order could be affected by hydrophobic/hydrophilic interactions between the polymer and solvent. It was postulated that the hydroxyl end group in stearyl alcohol initiated PEG could interact with water molecules in the $CDCl_3$ solvent which could prolong its retention time in the GPC column. The experiment could be repeated with a different solvent system to investigate if this phenomena was solvent related. It was observed that IM-MS had a greater separation power of both isobaric PEG mixtures than GPC-NMR. This is because IM-MS can analyse individual polymer oligomer conformations in the gas-phase as well as the overall average structure. This study suggests that IM-MS/MS would be the preferred technology to successfully separate and identify synthetic isobaric polyether systems; especially when taking speed and sensitivity into account.

7.3 Conclusions.

GPC-NMR has been used to study two mixtures of synthetic isobaric polyether systems, PEG 1000 mixed with PEG mono-oleate, and stearyl alcohol initiated PEG with PEG bis(2-ethyl hexanoate). It was observed that the overall mass, size and shape of the isobaric mixtures could not be separated by GPC-NMR. Manipulation of individual ^1H NMR spectra allowed the number of repeat units in the polymer to be calculated. Previous studies have demonstrated that this technique can aid the

deformulation of complex polymer systems (Robertson, Heron *et al.* 2004), however, this study has shown it cannot separate isobaric mixtures.

ESI-IM-MS/MS has been used to study three mixtures of synthetic polymers: PEG 1000 and PEG mono-oleate (with different concentrations of EO in isobaric oligomers), stearyl alcohol initiated PEG and PEG bis(2-ethyl hexanoate) (isobaric oligomers containing the same number of moles of EO), plus PPG mono butyl ether and PPG bis (2-amino propyl ether) (isobaric oligomers containing the same number of moles of PO). The effective use of ion mobility as a high resolution separation device for precursor ions, in MS/MS experiments, has allowed the clear differentiation of isobaric polyether species. The resolving power of IM-MS/MS is insufficient to resolve the higher molecular weight oligomers with limited separation observed with precursor ion resolution > 10,000. ESI-MS/MS alone was not able to significantly resolve these isobaric species, due to the inherent limitations in precursor ion resolution of the quadrupole analyser used. It has been observed that the MS/MS data with and without ion mobility separation are in good agreement. This indicates that oligomers can be fully separated by ion mobility. The MS/MS data from the resolved oligomers enabled full structural characterisation, with different end groups being identified. The fragment ion peaks observed are similar to those proposed previously by Lattimer (Lattimer 1992a; Lattimer 1994) and Jackson *et al.* (Jackson, Green *et al.* 2006). ESI-IM provides an extra dimension of fast, sensitive, gas phase, ion separation enabling isobaric synthetic polymers to be differentiated by their size, shape and charge (Trimpin, Plasencia *et al.* 2007). The approach is still in the early stages of development and it is likely that further improvements in resolution of the technique will extend the approach into a fast, sensitive, information-rich method for studying complex polymer mixtures. This will help to quickly and effectively identify other isobaric synthetic polymer species.

7.4 References.

Alber, G. M., Marshall, A. G., Hill, N. C., Schweikhard, L. and Ricca, T. L. (1993). Ultrahigh-Resolution Fourier-Transform Ion-Cyclotron Resonance Mass-Spectrometer. *Review of Scientific Instruments* **64**, 1845-1852.

Gidden, J., Jackson, A. T., Scrivens, J. H. and Bowers, M. T. (1999). Gas phase conformations of synthetic polymers: poly (methyl methacrylate) oligomers cationized by sodium ions. *International Journal of Mass Spectrometry* **188**, 121-130.

Gidden, J., Wyttenbach, T., Batka, J. J., Weis, P., Bowers, M. T., Jackson, A. T. and Scrivens, J. H. (1999). Poly (ethylene terephthalate) oligomers cationized by alkali ions: structures, energetics, and their effect on mass spectra and the matrix-assisted laser desorption/ionization process. *Journal of the American Society for Mass Spectrometry* **10**, 883-895.

Gidden, J., Wyttenbach, T., Jackson, A. T., Scrivens, J. H. and Bowers, M. T. (2000). Gas-Phase Conformations of Synthetic Polymers: Poly(ethylene glycol), Poly(propylene glycol), and Poly(tetramethylene glycol). *Journal of the American Chemical Society* **122**, 4692-4699.

Hatada, K., Ute, K., Kitayama, T., Nishimura, T., Kashiyama, M. and Fujimoto, N. (1990). Studies on the Molecular-Weight Dependence of Tacticity of Anionically Prepared Pmmas by Online GPC/NMR. *Polymer Bulletin* **23**, 549-554.

Hatada, K., Ute, K., Kitayama, T., Yamamoto, M., Nishimura, T. and Kashiyama, M. (1989). Online Gpc Nmr Analyses of Block and Random Copolymers of Methyl and Butyl Methacrylates Prepared with Tert-C4H9MgBr. *Polymer Bulletin* **21**, 489-495.

Hatada, K., Ute, K., Okamoto, Y., Imanari, M. and Fujii, N. (1988). Online Gpc/Nmr Experiments Using the Isotactic Poly(Methyl Methacrylate) with Well-Defined Chemical-Structure. *Polymer Bulletin* **20**, 317-321.

Heck, A. J. R. and Derrick, P. J. (1997). Ultrahigh Mass Accuracy in Isotope-Selective Collision-Induced Dissociation Using Correlated Sweep Excitation and Sustained Off-Resonance Irradiation: A Fourier Transform Ion Cyclotron Resonance Mass Spectrometry Case Study on the [M + 2H]2+ Ion of Bradykinin. *Analytical Chemistry* **69**, 3603-3607.

Jackson, A. T., Green, M. R. and Bateman, R. H. (2006). Generation of end-group information from polyethers by matrix-assisted laser desorption/ionisation collision-induced dissociation mass spectrometry. *Rapid Communications in Mass Spectrometry* **20**, 3542-3550.

Jackson, A. T., Scrivens, J. H., Simonsick, W. J., Green, M. R. and Bateman, R. H. (2000). Generation of structural information from polymers and copolymers using tandem mass spectrometry. *Abstracts of Papers of the American Chemical Society* **219**, U363-U363.

Kind, T. and Fiehn, O. (2006). Metabolomic database annotations via query of elemental compositions: Mass accuracy is insufficient even at less than 1 ppm. *BMC Bioinformatics* **7**.

Kitayama, T. and Ute, K. (2006). On-line SEC-NMR. *Springer*.

Kramer, I., Pasch, H., Handel, H. and Albert, K. (1999). Chemical heterogeneity analysis of high-conversion poly[styrene-co-(ethyl acrylate)]s by NMR and on-line coupled SEC-NMR. *Macromolecular Chemistry and Physics* **200**, 1734-1744.

Lattimer, R. P. (1992a). Tandem Mass-Spectrometry of Lithium-Attachment Ions from Polyglycols. *Journal of the American Society for Mass Spectrometry* **3**, 225-234.

Lattimer, R. P. (1992b). Tandem Mass-Spectrometry of Poly(Ethylene Glycol) Proton-Attachment and Deuteron-Attachment Ions. *International Journal of Mass Spectrometry and Ion Processes* **116**, 23-36.

Lattimer, R. P. (1994). Tandem Mass-Spectrometry of Poly(Ethylene Glycol) Lithium-Attachment Ions. *Journal of the American Society for Mass Spectrometry* **5**, 1072-1080.

Lattimer, R. P., Munster, H. and Budzikiewicz, H. (1989). Tandem mass spectrometry of polyglycols. *International Journal of Mass Spectrometry and Ion Processes* **90**, 119-129.

Lin, M., Campbell, J. M., Mueller, D. R. and Wirth, U. (2003). Intact protein analysis by matrix-assisted laser desorption/ionization tandem time-of-flight mass spectrometry. *Rapid Communications Mass Spectrometry* **17**, 1809-1814.

Robertson, D. F., Heron, J. E. and Beckett, M. C. (2004). On-Line Gel Permeation Chromatography/Nuclear Magnetic Resonance of Complex Polymer Formulations. *Applied Spectroscopy* **58**, 1122-1127.

Robinson, E. W., Sellon, R. E. and Williams, E. R. (2007). Peak deconvolution in high-field asymmetric waveform ion mobility spectrometry (FAIMS) to characterize macromolecular conformations. *International Journal of Mass Spectrometry* **259**, 87-95.

Trimpin, S., Plasencia, M., Isailovic, D. and Clemmer, D. E. (2007). Resolving Oligomers from Fully Grown Polymers with IMS-MS. *Analytical Chemistry* **79**, 7965-7974.

Ude, S., FernandezdelaMora, J. and Thomson, B. A. (2004). Charge-Induced Unfolding of Multiply Charged Polyethylene Glycol Ions. *Journal American Chemical Society* **126**, 12184-12190.

Ute, K., Niimi, R., Hatada, K. and Kolbert, A. C. (1999). Characterization of ethylene-propylene-diene terpolymers (EPDM) by 750 MHz on-line SEC-NMR. *International Journal of Polymer Analysis and Characterization* **5**, 47-59.

Ute, K., Niimi, R., Matsunaga, M., Hatada, K. and Kitayama, T. (2001). On-line SEC-NMR analysis of the stereocomplex of uniform isotactic and uniform syndiotactic poly(methyl methacrylate)s. *Macromolecular Chemistry and Physics* **202**, 3081-3086.

Van Gorkom, L. C. M. and Hancewicz, T. M. (1998). Analysis of DOSY and GPC-NMR Experiments on Polymers by Multivariate Curve Resolution. *Journal of Magnetic Resonance* **130**, 125-130.

von Helden, G., Hsu, M.-T., Kemper, P. R. and Bowers, M. T. (1991). Structures of carbon cluster ions from 3 to 60 atoms: Linears to rings to fullerenes. *The Journal of Chemical Physics* **95**, 3835-3837.

von Helden, G., Wyttenbach, T. and Bowers, M. T. (1995). Conformation of Macromolecules in the Gas Phase: Use of Matrix-Assisted Laser Desorption Methods in Ion Chromatography. *Science* **267**, 1483-1485.

Wyttenbach, T., von Helden, G. and Bowers, M. T. (1997). Conformations of alkali ion cationized polyethers in the gas phase: polyethylene glycol and bis[(benzo-15-crown-5)-15-ylmethyl] pimelate. *International Journal of Mass Spectrometry and Ion Processes* **165-166**, 377-390.

Chapter 8
Conclusions and Future Work

Travelling-wave IM-MS in conjunction with other biophysical techniques was used to characterise the structure of various prion proteins and synthetic polymer systems.

8.1 Prion Proteins

Recombinant prion proteins were expressed in *E. coli* and purified prior to their structural analysis. Truncated conformational isoforms, representative of PrP^{C} and PrP^{Sc}, which had the same nominal *m/z* ratio but differing secondary structure, were distinguished between by means of IM-MS. The differences in ATD and estimated cross-section were more prominent in the mouse PrP species than the Syrian hamster PrP. A greater difference was observed between the two conformational isoforms at acidic pH than at pH 7.0.

The structure of the full-length prion protein was probed by means of IM-MS. A comparison of the estimated cross-sections of truncated prion protein constructs and full-length constructs suggested that the N-terminal flexible tail was associated with the core structure. Computer modelled structures and their respective theoretical cross-sections also supported the hypothesis that the N-terminal flexible tail is associated with the core PrP structure.

Three different full-length mammalian PrP constructs were studied by means of IM-MS. It was observed that all three species had similar compact conformations at the lower (native) charge states, whereas each species had distinctive estimated cross-sections at the higher charge states. It was shown that ovine PrP structure was more stable than the corresponding Syrian hamster and mouse PrP counterparts. It was proposed that the differences in structural stability were because of key amino acid mutations in the PrP primary sequence.

Metal binding to two different prion protein constructs was investigated. It was observed that Cu^{2+} ions could coordinate to all histidine residues in the octarepeat

region in both the prion peptide and full-length protein. It was shown that different stoichiometric ratios of PrP:Cu^{2+} resulted in a different number of Cu^{2+} ions coordinated to the octarepeat region. The estimated cross-section of copper coordination to the bovine peptide suggested that different conformations were present at different levels of copper occupancy. The difference in estimated cross-section between the apo PrP peptide and copper bound counterparts was significant. In contrast, there was no significant different in estimated cross-section or ATDs between the apo full-length PrP and the copper or manganese bound species. Experiments suggested that copper coordination was favoured over manganese coordination.

8.1.1 Future directions

The field of prion protein research is vast and numerous key questions still remain unanswered. The new emerging IM-MS technique could aid the study and understanding of the *in vivo* prion structure. At present, little is known about the *in vivo* prion structure because of its complex natural environment and post-translational modifications such as glycosylation. In order to study the *in vivo* protein by means of IM-MS, a de-glycosylation and amplification protocol will need to be developed. Although there are several hypotheses for the conversion of PrP^{C} to PrP^{Sc}, the essential misfolding event has yet to be observed. IM-MS has been used to investigate the key steps involved in the amyloid assembly pathway for other amyloidosis such as Alzheimer's disease (Bernstein, Dupuis *et al.* 2009; Bernstein, Wyttenbach *et al.* 2005; Clemmer and Valentine 2009) and a plausible mechanism for the formation of Aβ oligomers was proposed from IM-MS data. The amyloid assembly pathway for the prion protein has been investigated using size-exclusion chromatography (Rezaei, Eghiaian et al. 2005) but, to date, mass spectrometry analysis on these oligomeric states has not been published. IM-MS could have the potential to define the amyloid assembly pathway and may also be used to study the higher order oligomers which form the symptomatic fibrillar structures in the brain.

Chapter 4 discussed that the 1D estimated cross-section plot did not fully represent the ATD data. The development of a three-dimensional contour plot would help to visualise the estimated cross-section data.

8.2 Synthetic polymers

The ion mobility device was used as a high resolution separation technique to distinguish between mixtures of isobaric synthetic polymers. It was observed that the resolving power of IM-MS/MS is insufficient to resolve the higher molecular weight oligomers. In comparison, GPC-NMR analysis of the same isobaric mixture could not separate the two components. It was observed that IM-MS was better than GPC-NMR at separating isobaric PEG mixtures, especially when taking speed and sensitivity into account.

8.2.1 Future directions

Polymer chemistry is evolving. Interest in the polymer research field is moving away from high-value commodity products and low tonnage specialty products such as PP and PEEK, to lower molecular weight materials that can be used in manufacturing and biomedical research. An example of these new developments is the creation of a polyether copolymer that, once formed into nanospheres, can circulate around the body mimicking the movement of cells (Langer and Tirrell 2004). In contrast to natural macromolecules, the three-dimensional structure of synthetic polymer systems have not been characterised by means of X-ray crystallography or NMR spectroscopy. IM-MS and computer modelling could be used to characterise the structure of these new lower molecular weight materials. The resulting data could suggest the three-dimensional structure of synthetic polymer systems and conclusions could be drawn on how these new polymeric materials can interact with one another and, in the case of biomedical research, how these materials interact with the natural ligand or cofactor.

Recently, a new T-Wave device has been developed called the Synapt G2 (Waters, Manchester, UK) which became commercially available in December 2009. This

instrument has been described as the "next generation" in IM-MS, by its manufacturer, and has considerable advantages over the previous Synapt instrument. The Synapt G2 has improved mobility resolution (upto x4 of the Synapt), a hybrid TDC/ADC detector and improved ToF detector resolution. The improved T-Wave mobility resolution has allowed a greater separation of isobaric polymer systems (see Figure 8.1). It was observed that the resolving power of IM-MS/MS (by means of the Synapt) was insufficient to resolve higher molecular weight oligomers in an isobaric PEG 1000, PEG monooleate mixture (see Figure 7.6 and 7.7). In contrast, the resolving power of the Synapt G2, has allowed all isobaric oligomers in the PEG 1000, PEG monooleate mixture to be separated, as shown in Figure 8.2. All isobaric oligomers were separated by means of the Synapt G2 and had baseline resolution. An example of the Synapt G2 data is shown in Figure 8.1.

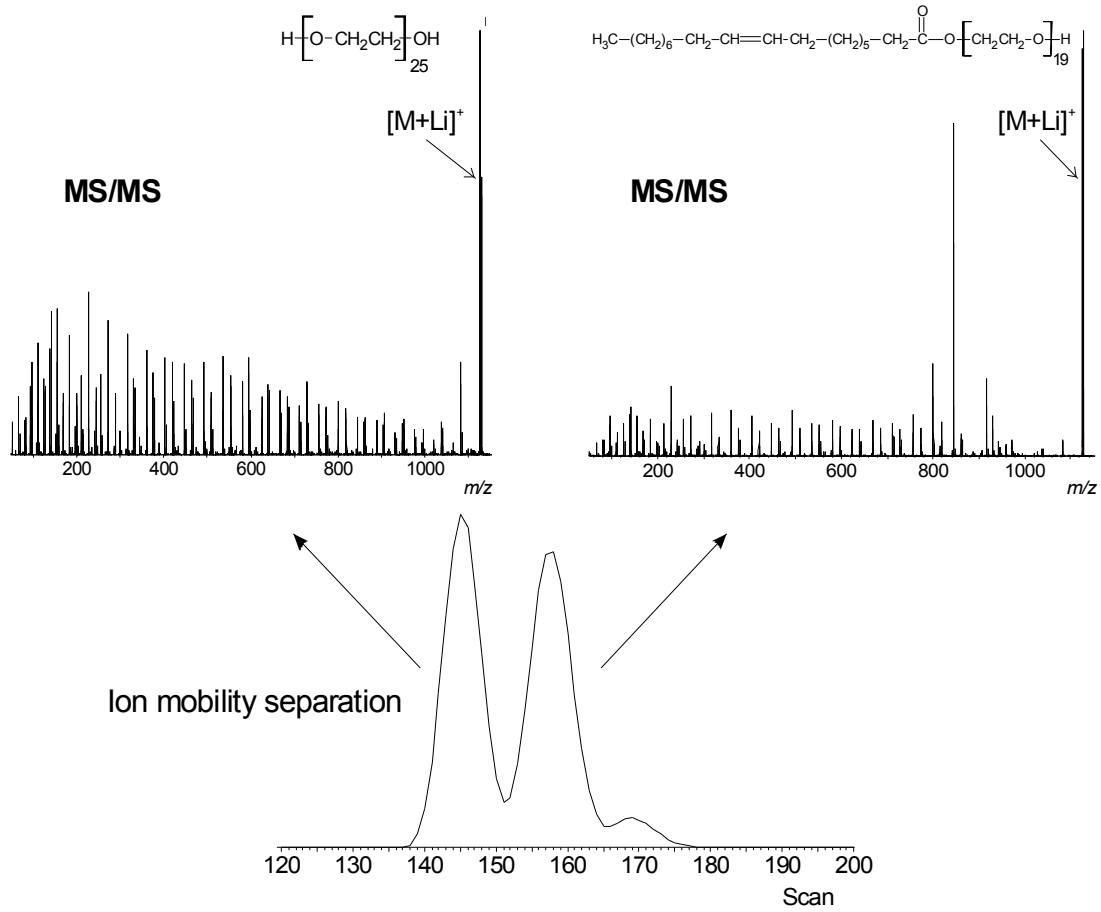

Figure 8.1: Arrival time distribution (bottom) of *m/z* 1126 from a mixture of PEG 1000 and PEG mono-oleate and IM-MS/MS spectra (top) from the two peaks noted. Data obtained by means of Synapt G2 (Waters, Manchester, UK).

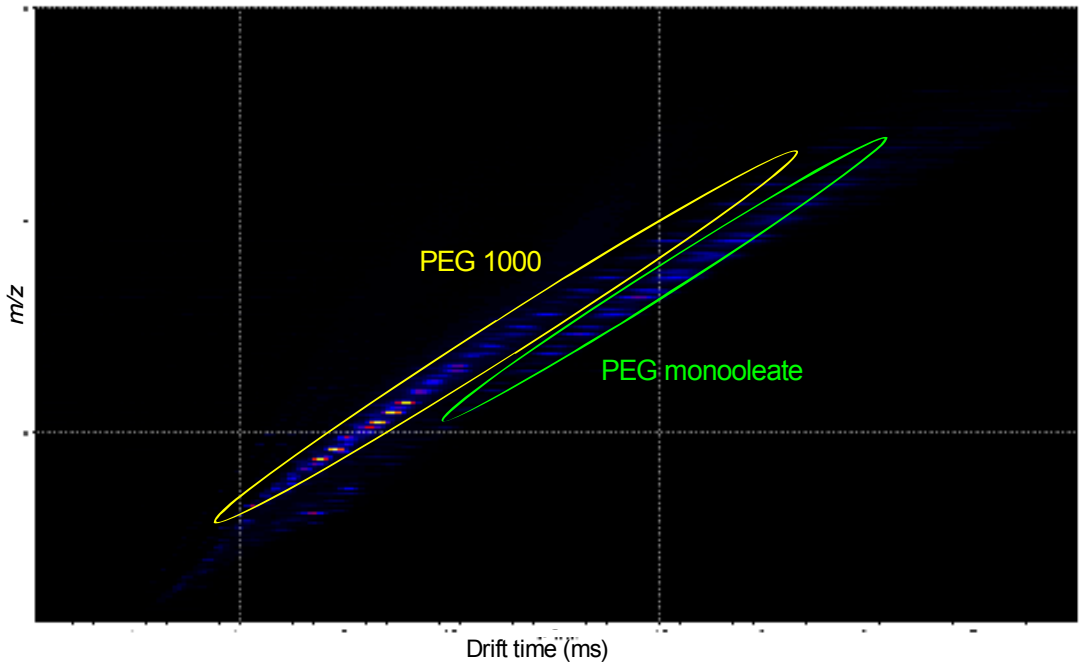

Figure 8.2: Mobilogram showing the total separation of PEG 1000 and PEG monooleate oligomers. Data obtained by means of Synapt G2 (Waters, Manchester, UK).

The development of the new IM-MS device brings with it the opportunity to perform many novel and exciting experiments, in which both natural and synthetic macromolecules can be characterised.

8.3 References

Bernstein, S. L., Dupuis, N. F., Lazo, N. D., Wyttenbach, T., Condron, M. M., Bitan, G., Teplow, D. B., Shea, J.-E., Ruotolo, B. T., Robinson, C. V. and Bowers, M. T. (2009). Amyloid-beta protein oligomerization and the importance of tetramers and dodecamers in the aetiology of Alzheimer's disease. *Nature Chemistry* **1**, 326-331.

Bernstein, S. L., Wyttenbach, T., Baumketner, A., Shea, J.-E., Bitan, G., Teplow, D. B. and Bowers, M. T. (2005). Amyloid beta-Protein: Monomer Structure and Early Aggregation States of A-beta42 and Its Pro19 Alloform. *Journal of the American Chemical Society* **127**, 2075-2084.

Clemmer, D. E. and Valentine, S. J. (2009). Bioanalytical chemistry: Protein oligomers frozen in time. *Nature Chemistry* **1**, 257-258

Langer, R. and Tirrell, D. A. (2004). Designing materials for biology and medicine. *Nature* **428**, 487-92.

Rezaei, H., Eghiaian, F., Perez, J., Doublet, B., Choiset, Y., Haertle, T. and Grosclaude, J. (2005). Sequential generation of two structurally distinct ovine prion protein soluble oligomers displaying different biochemical reactivities. *Journal of Molecular Biology* **347**, 665-79.